



HAL
open science

Functional brain imaging techniques bridging the gap between microscopic and mesoscopic vascular measurements

Ali-Kemal Aydin

► **To cite this version:**

Ali-Kemal Aydin. Functional brain imaging techniques bridging the gap between microscopic and mesoscopic vascular measurements. Neuroscience. Université Paris Cité, 2021. English. NNT : 2021UNIP5103 . tel-03647669

HAL Id: tel-03647669

<https://theses.hal.science/tel-03647669v1>

Submitted on 20 Apr 2022

HAL is a multi-disciplinary open access archive for the deposit and dissemination of scientific research documents, whether they are published or not. The documents may come from teaching and research institutions in France or abroad, or from public or private research centers.

L'archive ouverte pluridisciplinaire **HAL**, est destinée au dépôt et à la diffusion de documents scientifiques de niveau recherche, publiés ou non, émanant des établissements d'enseignement et de recherche français ou étrangers, des laboratoires publics ou privés.

THÈSE DE DOCTORAT
EN NEUROSCIENCES

Functional brain imaging techniques:
bridging the gap between microscopic and
mesoscopic vascular measurements

Défendue publiquement le 10 Septembre 2021 à Paris par
Ali-Kemal AYDIN

Préparée à
Laboratory of Neurophysiology and New Microscopy,
INSERM, Université de Paris
et
Institut de la Vision, Sorbonne Université, INSERM, CNRS

Sous la direction de Serge CHARPAK
et co-encadré par Davide BOIDO

Jury :

<i>Rapporteurs :</i>	Emilie MACÉ	Docteur Max Planck Institute of Neurobiology
	Brice BATHELIER	Docteur Institut Pasteur, INSERM, Institut de l'Audition
<i>Directeur de thèse :</i>	Serge CHARPAK	Docteur Sorbonne Université, INSERM, CNRS, Institut de la Vision
<i>Présidente :</i>	Claire LEGAY	Professeure Université de Paris, CNRS

UNIVERSITÉ DE PARIS
DOCTORAL SCHOOL FIRE - N°474
FRONTIÈRES DE L'INNOVATION EN RECHERCHE ET ÉDUCATION

PHD THESIS
IN NEUROSCIENCES

**Functional brain imaging techniques:
bridging the gap between microscopic and
mesoscopic vascular measurements**

Defended on September 10, 2021 in Paris by
Ali-Kemal AYDIN

Prepared at
Laboratory of Neurophysiology and New Microscopy,
INSERM, Université de Paris
and
Institut de la Vision, Sorbonne Université, INSERM, CNRS

Under the direction of Serge CHARPAK
and co-supervised by Davide BOIDO

Jury:

<i>Reviewers:</i>	Emilie MACÉ	Group leader Max Planck Institute of Neurobiology
	Brice BATHELIER	Group leader Institut Pasteur, INSERM, Institut de l'Audition
<i>Advisor:</i>	Serge CHARPAK	Group leader Sorbonne Université, INSERM, CNRS, Institut de la Vision
<i>President:</i>	Claire LEGAY	Professor Université de Paris, CNRS

Abstract

Functional brain imaging techniques: bridging the gap between microscopic and mesoscopic vascular measurements

BOLD-fMRI is the preferred technique to study brain activity in humans. Recently, functional ultrasound (fUS) was introduced as a novel technique to record blood volume changes while overcoming the poor spatiotemporal resolution of BOLD-fMRI. BOLD-fMRI and fUS both report signals related to changes in blood flow to determine activated brain areas, although through different physical mechanisms. Indeed, neuronal activation systematically triggers an increase in blood flow, through a cascade of molecular, cellular, and mechanical reactions named neurovascular coupling. Thus, the interpretation of vascular-based functional imaging techniques requires a thorough understanding of neurovascular coupling to recover the spatiotemporal dynamics of neuronal activation from blood flow changes. During my PhD, I linked microscopic measurements of neuronal and vascular responses to odor to the mesoscopic signal detected with functional ultrasound imaging in the mouse. My first project evaluates the correspondence between neuronal activation in a single specific olfactory bulb glomerulus, measured with two-photon microscopy and the fUS output from the voxel containing the same glomerulus through a variety of odorant stimuli. This study also allowed me to model the neurovascular coupling, between neuronal activation and the increase of red blood cell velocity in nearby capillaries. I showed that, at high stimulus strength, neurovascular coupling is no longer linear with the appearance of a delayed vascular component independent of neural activity. To achieve these results, I developed ‘Iliski’, an analysis software that is provided in a GitHub repository and is described in detail in a second article. During the second part of my thesis, I focused on a long-lasting controversy in the BOLD-fMRI field: do neuronally activated areas generate a local transient decrease in brain oxygenation that precedes the increase in oxygenated blood flow? It has been hypothesized that this oxygen decrease would be spatially more specific than the oxygen increase and allows a more precise interpretation of the BOLD-fMRI output. Previous studies reported this “initial dip” in oxygenation, but it was mainly measured in acute animal preparations, where neurovascular coupling is impaired by anesthesia and the invasiveness of the preparation. Here we report that the initial dip is barely visible in the capillaries of anesthetized chronic animals, and only in the most sensitive glomerulus to the odor. It is mainly seen in the capillary plasma rather than in individual RBCs. According to these results, we suggest that the initial dip is not the way to enhance BOLD-fMRI spatial specificity. Overall, this corpus of work helps to better interpret functional imaging techniques based on blood flow changes by shedding light on the microscopic mechanisms underlying the mesoscopic signals.

Abstract en français

Étude de l'origine microscopique des signaux vasculaires mésoscopiques observés par imagerie fonctionnelle du cerveau

L'IRM fonctionnelle BOLD est aujourd'hui la technique de prédilection pour étudier l'activité cérébrale chez l'être humain. Récemment, l'échographie fonctionnelle ultrasonore (fUS) a été décrite comme une nouvelle technique d'imagerie fonctionnelle pouvant supplanter l'imagerie BOLD. Ces deux approches ne mesurent pas directement l'activité neuronale mais l'augmentation réflexe du flux sanguin qui en résulte et que l'on appelle hyperémie fonctionnelle. Ce réflexe vasculaire met en jeu le couplage neurovasculaire, un ensemble complexe de voies de signalisation et de types cellulaires. L'imagerie fUS ou IRMf-BOLD nécessite une très bonne compréhension de la dynamique spatio-temporelle de l'hyperémie fonctionnelle pour correctement construire les cartes d'activation cérébrale. Pendant ma thèse, j'ai voulu mieux comprendre la relation entre les variations microscopiques du flux sanguin déclenchées par une activation sensorielle et les variations mésoscopiques mesurées par ces techniques. Dans mon premier projet, j'ai étudié le lien entre l'activation neuronale, déclenchée par un stimulus odorant dans un glomérule, micro-réseau neuronal du bulbe olfactif de la souris et mesurée en microscopie biphotonique, avec les réponses vasculaires mesurées en fUS dans un voxel unique comprenant ce réseau neuronal. J'ai ensuite modélisé une fonction de transfert permettant de prédire l'hyperémie fonctionnelle à partir d'une activation neuronale. Cela m'a permis de montrer qu'à de hautes concentrations d'odeur, l'hyperémie fonctionnelle n'est plus linéaire et qu'apparaît une deuxième composante vasculaire indépendante de l'activité neuronale. Pour ce travail théorique, j'ai développé 'Iliski', un logiciel d'analyse qui est disponible sur GitHub et est décrit dans un second article. Dans la deuxième partie de ma thèse, je me suis concentré sur une controverse du domaine de l'IRMf-BOLD : peut-on mesurer une diminution transitoire et localisée de l'oxygénation cérébrale au cours d'une activation neuronale ? Hypothétiquement, cette diminution, connue sous l'appellation « initial dip », serait spatialement plus spécifique que l'hyperémie fonctionnelle, ce qui permettrait d'améliorer les cartes d'activation d'IRMf-BOLD. Cette diminution a été rapportée précédemment à une échelle microscopique mais uniquement chez des modèles animaux préparés de façon aiguë, c'est-à-dire au cours de chirurgies invasives qui impactent l'hyperémie fonctionnelle. Ici, je montre que la diminution n'est que très légèrement visible dans les capillaires d'animaux anesthésiés et préparés chroniquement. La diminution est portée par la pression plasmatique en oxygène, et non par l'oxygénation intra globulaire. Par ailleurs, il est seulement visible dans le glomérule le plus sensible à l'odeur utilisée. Ceci semble indiquer que l'« initial dip » n'est pas l'outil espéré pour améliorer la spécificité spatiale de l'IRMf-BOLD. Mes résultats soulignent qu'une meilleure compréhension des données microscopiques permet d'améliorer l'interprétation des signaux détectés avec les techniques mésoscopiques d'imagerie fonctionnelle cérébrale.

Résumé de la thèse en français

Dans le cerveau, toute activation neuronale est suivie d'une augmentation locale du flux sanguin qui apporte oxygène et glucose, refroidit les tissus et collecte les déchets métaboliques. Cette augmentation, que l'on appelle hyperémie fonctionnelle (HF), est la conséquence du couplage neurovasculaire, c'est-à-dire l'ensemble des acteurs cellulaires et des mécanismes moléculaires qui relient neurones et vaisseaux cérébraux et régulent le débit cérébral sanguin. Les travaux de cette thèse ont pour sujet principal la caractérisation de l'HF qui, outre son altération dans certaines maladies neurodégénératives, est le paramètre physiologique utilisé par l'IRMf-BOLD ou l'échographie ultrasonore ultrarapide (fUS) pour explorer l'activation cérébrale. Ces deux techniques mesurent en fait les changements hémodynamiques ou leurs conséquences, que médecins et chercheurs interprètent ensuite pour en déduire les zones cérébrales activées. Ce résumé va revenir séquentiellement sur les quatre articles scientifiques issues de cette thèse, dont trois en position de premier auteur.

Transfer functions linking neural calcium to single voxel functional ultrasound signal

Une précédente étude de notre équipe a montré que toute activité neuronale, même petite, engendre une réponse vasculaire. Néanmoins, l'amplitude de la réponse vasculaire varie avec l'activation neuronale qui la génère. Nous avons recherché si la dynamique temporelle de l'HF était conservée à travers un éventail large de stimulations sensorielles et d'un individu à l'autre. Pour répondre à cette question, nous avons utilisé un modèle neurovasculaire particulier, le glomérule du bulbe olfactif du rongeur. Le bulbe olfactif est le premier relai de l'information olfactive et le glomérule est le micro-réseau contenant la synapse entre les terminaisons des neurones sensoriels olfactifs et les cellules principales du bulbe olfactif, les cellules mitrales. L'activation neuronale du glomérule est très facilement contrôlable, puisqu'elle est proportionnelle à la concentration d'odeur et à la durée d'exposition à l'odeur. Associée à une importante densité vasculaire, ces caractéristiques font du glomérule un très bon modèle pour étudier l'HF. L'activation neuronale peut être mesurée en microscopie biphotonique en suivant la dynamique du calcium intracellulaire, chez des souris exprimant l'indicateur calcique GCaMP6f dans les cellules mitrales. La vitesse des globules rouges est mesurée dans les capillaires glomérulaires après l'injection intra-veineuse d'un fluorophore rouge. Par souci de reproductibilité entre les animaux, nous avons étudié dans l'ensemble du travail un glomérule spécifique : le glomérule le plus sensible à un odorant particulier, l'Ethyl tiglate.

Dans la première partie du travail, j'ai acquis simultanément les réponses neuronales et vasculaires aux odeurs chez des souris anesthésiées, en faisant varier la concentration et la durée de l'odeur. Pour une stimulation donnée (Ethyl tiglate à 1%, 5 secondes), j'ai modélisé l'HF grâce à l'optimisation d'une fonction de transfert, dont la convolution avec le signal GCaMP6f permet de prédire la réponse vasculaire. Nous avons observé qu'une seule fonction de transfert représentant la dynamique de l'HF était suffisante pour prédire les réponses vasculaires de toutes les souris (Figure 1). Ainsi, le couplage neurovasculaire et l'HF qui en découle semblent identiques d'un individu à l'autre. De plus, cette fonction de transfert reste valide pour l'ensemble des durées testées, de 5 secondes à 120 millisecondes (une inspiration unique, Figure 2). Néanmoins, pour de très hautes concentrations d'odeur, la réponse vasculaire change et montre une deuxième composante tardive que la fonction de transfert initiale ne peut prédire (Figure 2). Enfin, nous avons également vérifié que notre approche restait valide chez la souris éveillée : dans ce cas, les réponses calciques et vasculaires ont été collectées chez des souris habituées à la contention et entraînées aux stimula-

tions olfactives pendant plus de deux semaines. La première partie de cette étude montre donc que l’hyperémie fonctionnelle a un comportement similaire entre les individus et est linéaire sur une grande plage d’activation neuronale. Un deuxième phénomène est mis en jeu quand l’activation devient très importante, et résultant probablement de la mise en jeu des astrocytes.

Dans la deuxième partie de l’étude, nous avons analysé la précision et l’interprétation des données acquises avec le fUS. Cette technique est encore récente et aucun travail n’avait précisément analysé la corrélation entre l’activation neuronale et vasculaire microscopique et les signaux fUS. En effet, le fUS rapporte les changements de volume sanguin générés par le couplage neurovasculaire. Nous avons adapté avec précision nos deux systèmes d’imagerie, le fUS et l’imagerie microscopique biphotonique, afin de mesurer le signal fUS exactement dans le voxel où je mesurais l’activation neuronale et la réponse vasculaire avec le microscope biphotonique (Figure 3). J’ai montré que le signal fUS, dont la résolution spatiale était de $100 \times 100 \times 200 \mu\text{m}$, corrélait très bien avec les mesures vasculaires microscopiques réalisées au même endroit (Figure 4). Cette corrélation était robuste pour des stimulations brèves (une inhalation) ou longues, faibles ou intenses. Néanmoins, j’ai observé que le voxel contenant le glomérule le plus sensible à l’odeur, n’était pas nécessairement celui le plus actif (Figure 5). En effet, notre approche a permis de comparer les réponses du voxel co-registré avec ceux des voxels voisins. A notre surprise, dans certains cas les signaux des voxels périphériques étaient plus importants que ceux du voxel spécifique. Ceci résulte vraisemblablement de la propagation rétrograde des signaux vasculaires au cours de l’HF. Ces résultats soulèvent les limites de l’imagerie fUS, quant à la précision des zones activées.

Iliski, a software for robust calculation of transfer functions

Comme décrit précédemment, ma première étude a nécessité le calcul de fonctions de transfert. J’ai ainsi développé une série de scripts pour faciliter le calcul et permettre de précisément paramétrer le traitement des données et les conditions initiales de l’optimisation. Pour valoriser ce travail et faciliter sa dissémination, nous l’avons mis à disposition sur GitHub et publié sous la forme d’un article. Après une description et une présentation de l’interface d’Iliski (Figure 1), nous avons détaillé les caractéristiques des méthodes d’optimisation proposées, dont certaines sont non-déterministiques et donc sujettes au « hasard » (Figure 2-4). Enfin, nous avons proposé un arbre décisionnel pour faciliter le choix des techniques de calcul (Figure 5).

Par ailleurs, j’ai utilisé Iliski pour l’étude en annexe de cette thèse. Nous avons étudié la dynamique spatio-temporelle de l’HF dans le cortex somatosensoriel de souris anesthésiées et éveillées. Un travail précédent de l’équipe avait analysé la dynamique de l’HF dans le bulbe olfactif et démontré que les dilatations et les changements de vitesse des globules rouges suivaient un patron temporel précis : les dilatations démarraient au niveau des artérioles pénétrantes et des premiers $50 \mu\text{m}$ du premier branchement capillaire, puis se propageaient en amont dans la pie-mère et en aval dans un segment actuellement défini comme le segment transitionnel. Dans le néocortex, nous avons observé que la dynamique de l’HF n’est pas stéréotypique, variant énormément au niveau des premiers branchements capillaires. Nous avons établi cette diversité fonctionnelle tant chez l’animal anesthésié qu’éveillé. D’autre part, grâce à Iliski j’ai pu calculer les fonctions de transfert de l’HF corticale. J’ai montré que ces fonctions varient énormément selon l’état cérébral de l’animal : elles sont brèves avec un front de montée rapide chez la souris éveillée, et lentes et prolongées au cours de l’anesthésie. Dans la mesure où cette différence est tenue au niveau du bulbe olfactif, nos résultats soulignent le fait que le couplage neurovasculaire varie selon les régions cérébrales. On

peut en conclure, qu'il est fondamental d'appliquer diverses fonctions de transfert pour établir les cartes d'activation cérébrale en imagerie fonctionnelle basée sur les signaux vasculaires.

Characterization of the oxygen initial dip in capillaries of chronically prepared mice

Cette étude n'est pas encore publiée mais est présente sous la forme d'un preprint dans la thèse.

L'interprétation de l'imagerie vasculaire fonctionnelle du cerveau se base sur la localisation de l'HF pour en déduire les zones cérébrales activées. Néanmoins, nous savons que la résolution spatiale de l'HF est moindre que celle de l'activation neuronale, c'est-à-dire que l'afflux sanguin augmente dans un volume cérébral nécessairement plus grand que la zone activée, du fait de la dilatation des artères et artérioles en amont. Pour cette raison, les techniques sensibles à l'oxygénation cérébrale, telles l'imagerie IRMf-BOLD et l'imagerie optique des signaux intrinsèques, se sont intéressées très tôt à un signal particulier, l'*initial dip*, une diminution transitoire et précoce de l'oxygénation tissulaire. L'idée était que cette diminution était locale, résultait de l'augmentation du métabolisme oxydatif et pouvait être détectée avant l'HF. Sa détection aurait donc pu permettre d'améliorer la résolution spatiale de ces techniques. Aujourd'hui, la détection par l'imagerie intrinsèque ou l'IRMf-BOLD de l'*initial dip* n'est plus acceptée par la communauté scientifique, le dip étant considéré comme un artefact d'analyse. Néanmoins, cette remise en cause, justifiée, n'explique pas pourquoi plusieurs études ont rapporté un « *initial dip* » en mesurant directement la Po_2 tissulaire chez des animaux préparés de manière aiguë, c'est-à-dire observés au cours d'une chirurgie. Mon dernier projet de thèse a donc été d'étudier ce paradoxe, en effectuant des mesures de la Po_2 chez des souris plusieurs semaines après toute chirurgie.

J'ai utilisé le même modèle que précédemment, le glomérule le plus sensible à l'Ethyl tiglate dans le bulbe olfactif de la souris. J'ai déterminé la valeur absolue de la Po_2 en mesurant la demi-vie de décroissance de phosphorescence de l'Oxyphor 2P, un capteur de l'oxygène. Chez la souris anesthésiée, j'ai observé que le *dip* vasculaire était bien présent, mais seulement pour d'importantes activations neuronales et avec une amplitude bien inférieure au bruit (Figure 1 et 2). Ce *dip* est présent dans $\approx 50\%$ des souris, celles présentant une HF tardive. À la suite d'une hypothèse de la littérature, j'ai essayé d'augmenter l'amplitude du *dip* en diminuant l'oxygénation cérébrale. Ceci a effectivement augmenté l'amplitude mais de façon très limitée (Figure 3). J'ai ensuite démontré que le dip était exclusif au glomérule le plus sensible à l'Ethyl tiglate (Figure 4). Enfin, chez les souris éveillées, j'ai établi l'absence de *dip* aussi bien tissulaire que vasculaire (Figure 5). Il semble donc que l'*initial dip* résulte soit d'une altération de l'homéostasie cérébrale chirurgicale soit de l'anesthésie. Ces résultats réconcilient de fait les données de l'imagerie macroscopique et les mesures précises de la Po_2 cérébrale.

Conclusion

Les résultats de cette thèse permettent de mieux comprendre les caractéristiques de l'hyperémie fonctionnelle. La modélisation par la fonction de transfert montre les limites de la linéarité du système et interroge la façon d'interpréter les signaux d'imagerie lors d'une activation neuronale intense. Par ailleurs, ces résultats soulignent la difficulté de localiser précisément les zones actives avec l'échographie ultrasonore ultrarapide : il est indispensable d'être conscient de ces limites pour ne pas surinterpréter les résultats obtenus en imagerie fonctionnelle. La dernière partie de la thèse élimine l'*initial dip* comme marqueur de l'activation neuronale et souligne le fait que toute altération des fonctions physiologiques générales d'un animal modifie les réflexes touchant au métabolisme

cellulaire, telle l'HF.

Remerciements

La thèse est une aventure, scientifique évidemment mais aussi humaine. J'espère réussir à rendre hommage ici à tous ceux qui ont contribué à mon aventure, et qui ont fait de ces 4 années une expérience que je réitérerais sans hésiter.

Pour commencer, je tiens à remercier mon jury de thèse de m'avoir fait l'honneur d'évaluer mon travail. Je ne me rendais pas compte, avant d'y être confronté, de la portée de cette évaluation et de ce qu'elle peut représenter pour le candidat. Je remercie particulièrement **Emilie Macé** et **Brice Bathellier** d'avoir relu ce manuscrit jusque dans ses moindres recoins. Merci pour vos critiques et vos avis experts¹, surtout dans les délais que vous avez eu. Merci à **Claire Legay** d'avoir accepté de faire partie du jury également. Merci à **Charlie Demené**, qui a courageusement suivi mes travaux durant cette thèse, en compagnie de Brice. Vos critiques constructives et vos visions m'ont été indispensables.

J'ai eu la chance d'être encadré par 2 chercheurs durant cette thèse, que je ne saurais remercier et reconnaître à leur juste valeur, **Serge Charpak** et **Davide Boido**. Je pourrais difficilement imaginer un autre duo que celui-ci pour diriger mon travail, un duo très complémentaire dont j'ai allègrement profité ces dernières années. Serge, je te remercie d'abord de m'avoir accepté dans ton équipe pour cette thèse alors même que l'on ne se connaissait pas vraiment. Aujourd'hui, j'espère que tu considères que le jeu en valait la chandelle. Tu m'as énormément appris, expérimentalement mais aussi en termes de vision scientifique. La rigueur que tu exiges, et que j'ai appris à exiger tant des autres que de moi-même, est une des choses qui me restera. Nous avons tous les deux une appétence particulière pour la physiologie plutôt que la pathologie, pour comprendre quels sont les mécanismes biologiques quand tout va bien avant de se pencher sur quand tout va mal. Malgré ça, tu m'as montré que l'on pouvait avoir en tête l'intérêt du patient avant tout, en choisissant bien les questions. Comme si tout cela n'était pas suffisant, tu as également été très présent pour moi sur le plan humain et ton soutien a été important à des moments clés. Une pensée ici pour la machine à café que tu m'as offerte pendant le premier confinement, et qui sera mis à grande contribution dans la suite de mes études médicales. Je te remercie également de m'avoir permis, non sans rechigner parfois, de m'investir de façon importante dans mes fonctions associatives et électives en parallèle de la thèse. Par ailleurs il faudra que l'on fasse le bilan de tous nos paris un jour, je crois qu'il nous faudra plus d'une seule soirée pour respecter nos engagements respectifs. Bref, merci pour tout.

Celui qui m'a encadré dès la première minute, et est vite devenu un ami en sus d'un chef, est Davide. Je n'aurais pas le quart des connaissances et compétences que j'ai si tu n'avais pas été là pour me les prodiguer. Ta persistance devant les problèmes expérimentaux, ta capacité à toujours trouver un moyen de les résoudre et de profiter de chaque instant pour récupérer des données, sont des aspects que j'ai toujours en tête. Ta bonne humeur malgré toutes les emmerdes que l'on a vues passer a été salvatrice. Ton soutien, ta disponibilité en toute circonstance m'ont été primordiaux. Je n'aurais pas réussi à faire passer tout le laboratoire de MATLAB à Python au cours de cette thèse, mais je n'oublie pas que tu me soutenais dans cette entreprise. En revanche, pas merci pour m'avoir fait découvrir et travailler sur LabVIEW, c'est l'œuvre du démon ce truc. Je me souviendrai de nos chants dans l'obscurité du setup pendant les 3 minutes qui séparaient chaque acquisition. Je me souviens un peu moins de mes siestes pendant nos bien trop longues manip' IRMf à Saclay,

¹Que je n'ai pas encore vu à l'heure où j'écris ces lignes, mais leur pertinence ne fait aucun doute.

mais merci de m'avoir laissé les faire. Par-dessus tout, je retiendrais ta passion pour la recherche, qui a su me mener également jusqu'ici. Encore une fois, merci pour tout.

La recherche est un travail d'équipe, tant pour s'assurer que plusieurs laboratoires à travers le monde arrivent au même résultat que pour aboutir au résultat en question dans un seul laboratoire. Je n'aurais rien pu faire sans mes collègues, et je tiens à le reconnaître. **Yannick Goulam Houssen**, tu as toujours été disponible pour résoudre mes soucis avec les microscopes et tu n'as jamais hésité à prendre de ton temps pour m'aider. On aura réussi à introduire l'humour premier degré dans l'équipe², et à fatiguer tout le monde avec nos interprétations littérales de la moindre expression. On se retrouvera quoiqu'il en soit sur les blocs d'escalade ! **Manon Omnes**, merci pour ta bonne humeur tout au long de cette thèse et pour avoir courageusement accepté de faire mes craniotomies à ma place. Je ne sais pas trop comment j'aurais fait sans toi honnêtement. **Marine Tournissac**, bien que pas officiellement chez nous, tu fais bien partie de notre équipe et c'était un plaisir de discuter chaque jour avec toi, du beau temps, d'Uber ou de sciences. Nul doute que tu sauras rendre CADASIL et le CO₂ passionnant, même pour moi. **Emmanuelle Chaigneau**, tes compétences et ton aide auront été très importantes pour la réussite du projet oxygène, merci d'avoir pris le temps de résoudre tous les petits soucis qu'on soulevait régulièrement avec Serge. **Esteban Suarez**, *keep being yourself during your PhD, I have no doubt you will be quite successful*. **Camille Verdier**, dernière arrivée dans l'équipe mais pas des moindres, merci pour ta motivation, ton travail de qualité et ton sourire en toutes circonstances. Je te souhaite toutes les réussites que tu attends, académiques comme personnelles, et j'espère que je ne t'aurais pas trop mal vendu la perspective de faire une thèse !

D'autres personnes du laboratoire sont parties depuis, mais auront marqués cette thèse. **Ravi Rungta**, on aura finalement collaboré après ton départ mais j'espère que ça se reproduira ! **Coralie-Anne Mosser**, ma grande sœur expatriée, je regrette beaucoup nos sorties sur le toit des Saints-Pères le vendredi soir alors qu'il ne restait que nous ! Ta bonne humeur, tes coups de gueules, ton regard sur la vie, tu manques terriblement ici, reviens vite *wsh*. **Morgane Roche**, dire que la thèse aurait été différente sans toi est un euphémisme à faire pâlir une souris albinos. Que ce soient les blocs d'Arkose ou les calibrations du PTG, il n'y a pas grand-chose qui nous aura résisté. J'espère que tu seras fière de ce qu'est devenu le projet que tu m'as légué en nous quittant.

Si l'on remonte dans le temps, à un soir d'octobre au début de la 2e année de médecine³, on me retrouvera sur les berges du Rhône avec **Amélie Bouvier** et **Tacien Petithomme**. Il n'aura suffi que d'un « Vas-y, tente le concours de l'Ecole de l'INSERM avec nous ! », pour me lancer avec eux dans l'aventure qui a abouti à cette thèse. On ne s'est plus quittés depuis, malgré la distance. Amélie, on a fini par être coloc' cette année et je n'aurais pas pu rêver mieux pour me supporter dans les moments difficiles qui l'ont parsemé. Tu es une amie exceptionnelle. Tacien, celui que tous mes proches connaissent comme le « futur Prix Nobel pour avoir guéri le cancer, sisi j'vous assure », tu as toujours été une oreille attentive et un conseil avisé. On aura vécu nos thèses ensemble, place à nos externats de médecine maintenant sans oublier qu'*il n'y a aucune raison que ça se passe bien*.

Je n'aurais jamais réussi le concours de l'Ecole de l'INSERM sans le précieux mentorat de

²Qu'est-ce qui est plus con qu'une poule ? ... Une table.

³Il y a 7 ans maintenant...

Yoann Grimaud. De tuteur à ami plus que proche, ma gratitude et mon admiration n'ont pas de limite. La formation que tu m'as prodiguée n'est dépassé que par l'humanité que tu montres chaque jour auprès de tes patients. N'oublie pas de toujours vérifier sous ton oreiller si un oignon ne s'y cache pas... **Clémentine Granger**, tu m'as toujours soutenu à ses côtés, et ton amitié m'est tout aussi chère.

Claudia Aoun, évidemment, je n'aurais pas commencé cette thèse si tu n'avais pas été là.

Claire Caillot, **Thomas Papazyan**, **Robin Zagala**, **Guilhem Thierry**, **Victor Morel**, nos trop rares soirées auront su compenser le temps qui les sépare par leur qualité. **Maxence Mouille**, le coloc' intermittent cette année, je n'attends que ton emménagement à Paris pour qu'on continue à être d'accord et pas d'accord à la fois sur l'industrie pharmaceutique et la nécessité d'une industrie publique du médicament. Reste comme tu es bb. **Paul Baudin**, ma tristesse infinie de ne pas t'avoir dans ma promo de médecine n'est égalée que par la perspective de ne pas pouvoir refaire la politique nationale et de jouer aux échecs ensemble régulièrement.

Ma qualité de vie durant cette thèse aura été bien moindre sans toutes les personnes que j'ai rencontrées durant mon investissement à l'ANEMF⁴. **Clara Bonnavion**, ta présidence ne saura être remplacée. **Anatole Le Guillou** et **Thomas Iampietro**, vous êtes plus gauchos que moi, et ça se remercie. **Pierre-Adrien Girard**, je n'ai toujours pas compris sur quoi tu travaillais, si tu peux écrire une contribution sur la question en 24 heures s'il-te-plaît, ce sera peut-être plus clair (ou pas). **Raphaël Sturm**, arrête d'être de droite. **Loïc Lemoine**, merci pour l'appart' en face des Fauvettes. **Killian L'Helgouarc'h**, merci de m'avoir remboursé mes TGVMax alors que je n'étais pas dans le bureau *askip*. Une mention spéciale pour **Solène Parabère**, **Margaux Delhomme**, **Alice Sioniac**, **Valentin Bannholtzer** et **Pierre Scoarnec** qui ont supporté mes venues intempestives chez eux, ont toujours su me faire rire, me changer les idées quand il le fallait. Être Tocard est un mode de vie, et on le vit bien.

Antonin Verdier, BaM 18h ?

Merci à ma famille, qui m'a soutenu malgré les inévitables questions sur mon retour en médecine. Oui c'est bon, j'y retourne enfin.

Je finis ces remerciements avec une pensée pour mes mentors scientifiques passées, qui ont inévitablement menés à ces pages : **Jean-Louis Bessereau**, **Bérangère Pinan-Lucarré**, **Laurent Seugnet** et **Boris Barbour**. Une profonde gratitude également pour **Barro Sow** et **Christine Tanga**, qui ont géré administrativement l'Ecole de l'INSERM Liliane Bettencourt et m'ont permis d'arriver jusqu'ici.

⁴Association Nationale des Etudiants en Médecine de France

CONTENTS

Abstract	
Abstract en français	i
Résumé de la thèse en français	ii
Remerciements	vi
Acronyms	xvii
I Introduction	1
1 General introduction	3
2 The brain vasculature	7
2.1 The brain's special needs	8
2.2 Vascular organization of the brain	8
2.2.1 Circle of Willis	8
2.2.2 From the surface to the parenchyma	10
2.2.3 The way back	13
2.3 Histology of the brain vessels	13
2.4 Vascular resistance	14
3 The neurovascular unit	17
3.1 Origin of the concept	18
3.2 A Hitchiker's guide to neurovascular coupling	20
3.2.1 A roadmap to functional hyperemia	22
3.2.2 What does functional hyperemia brings to the brain parenchyma?	23
3.3 Modeling the neurovascular coupling	26
3.3.1 Physical representation of a vascular network	26
3.3.2 Effect of a single actor	27
3.3.3 Holistic approach	29

3.4	Measuring the neurovascular coupling in two-photon microscopy	32
3.4.1	Neuronal changes	32
3.4.2	Vascular changes	34
3.5	Conclusion	38
4	Functional brain imaging	39
4.1	Imaging the brain	40
4.2	BOLD-fMRI	40
4.2.1	Physical principle	41
4.2.2	Analysis process	42
4.2.3	The hemodynamic response function	44
4.2.4	The initial dip: improving the spatial specificity of the vascular responses	46
4.2.5	Conclusion	50
4.3	Functional Ultrafast Ultrasound	51
4.3.1	Physical principle	51
4.3.2	Analysis process: extracting a map from the echoes	53
4.3.3	Experimental considerations	56
4.3.4	Results	58
5	The olfactory bulb, a neurovascular model	61
5.1	Introduction	61
5.2	Neuronal organization	62
5.2.1	General organization	62
5.2.2	The glomerular layer	64
5.3	Vascular organization	64
5.4	A neurovascular coupling model	65
6	Summary	67
6.1	Linking microscopic neuronal activation to mesoscopic fUS response	67
6.2	Iliski	68
6.3	The initial dip: solving a controversy	68
II	Results	69
7	Transfer functions linking neural calcium to single voxel functional ultrasound signal	71
8	Iliski, a software for robust calculation of transfer functions	87
9	Characterization of the oxygen initial dip in capillaries of chronically prepared mice	103
III	Discussions & Perspectives	125
10	Linking microscopic neuronal activation to mesoscopic fUS response	127

10.1 Summary	127
10.2 Discussion	128
10.2.1 Transfer function computation	128
10.2.2 Co-registration	129
10.2.3 Functional ultrasound activation maps	129
10.3 Perspectives	130
10.3.1 Transfer function to dissect NVC	130
11 Iliski	131
11.1 Summary	131
11.2 Discussion	132
11.3 Perspectives	133
12 To dip or not to dip	135
12.1 Summary	135
12.2 Discussion	136
12.2.1 Delay between RBCs flow and hyperemic responses	136
12.2.2 Changes in vessel dynamic upon hypoxia	137
12.3 Perspectives	137
IV Appendices	139
A Iliski: User Manual	141
B Diversity of neurovascular coupling dynamics along vascular arbors in layer II/III somatosensory cortex	163
Bibliography	181

LIST OF FIGURES

2.1	Vessels at the entry of the human brain	9
2.2	The Circle of Willis in the human brain	10
2.3	The pial network	11
2.4	Summary of the cellular characteristics of the various vessel types in the brain . . .	14
2.5	Vascular resistance in the brain mainly comes from parenchymal vessels and large arteries	15
3.1	The first clue for the neurovascular coupling	19
3.2	The first wide scale vascular-based mapping of brain function	20
3.3	Schematic representation of the cellular actors of the neurovascular unit	21
3.4	Summary of the local effect of functional hyperemia	22
3.5	Schematic representation of the vascular arbor	24
3.6	CO ₂ acts on functional hyperemia	26
3.7	Artificial vascular networks	28
3.8	RBC density does not change upon functional hyperemia in the mouse olfactory bulb	28
3.9	A TF representing the NVC	30
3.10	Holistic model of NVC shows that functional hyperemia dynamic is conserved across neural activation ways	31
3.11	An electrode placed in the brain parenchyma can measure neuronal responses through local field potential changes	33
3.12	Coronal slice of our GCaMP6-expressing model of OB	34
3.13	Simultaneous RBC velocity and Ca ²⁺ measurement with linescan acquisition . . .	35
3.14	Measuring RBC flow with a pointscan acquisition	36
3.15	Measuring Po ₂ from a pointscan acquisition in a capillary	37
4.1	Main brain functional imaging techniques	41
4.2	The BOLD has a very poor SNR	43
4.3	The GLM approach for BOLD analysis	44
4.4	Schematic representation of the HRF use	45
4.5	The initial dip in the HRF	47
4.6	Measure of the initial dip in the visual cortex by Thompson and colleagues	48
4.7	Measure of the initial dip in the olfactory bulb of the mouse	49

4.8	The BOLD initial dip depends on the lateness of the positive response	50
4.9	The Doppler effect	52
4.10	Functional Ultrafast Ultrasound	54
4.11	The fUS signal comprises both RBCs and tissue motions	55
4.12	Filtering the fUS signal allows for focusing on specific RBC velocities	56
5.1	Schematic coronal slice of a mouse head	62
5.2	Schematic laminar organization of the OB	63
11.1	Open Science Taxonomy	132

ACRONYMS

ACA anterior cerebral artery. 8, 64

BOLD blood oxygen level dependent. 18, 20, 30, 41, 42, 44–47, 49, 136, 137

CaM Cadmoduline. 34

CBF cerebral blood flow. 18

CBV cerebral blood volume. 30

CoW Circle of Willis. 8, 10

COX Cyclooxygenase. 13

CSF cerebrospinal fluid. 10

dHb deoxyhemoglobin. 41, 46, 47

EAT erythrocyte-associated transient. 38

EC endothelial cell. 13, 14, 23, 32

ESL endothelial surface layer. 16

ET Ethyl tiglate. 127

FH functional hyperemia. 23, 25, 130

FITC fluorescein. 38

fMRI functional magnetic resonance imaging. 51

fUS Functional ultrasound. 38, 51, 53, 56–58, 65, 67, 68, 128, 130

GFP Green fluorescent protein. 34

GL glomerular layer. 64, 65

-
- GLM** General Linear Model. 42, 44
- Hb** oxyhemoglobin. 41, 46, 47
- HRF** hemodynamic response function. 45–47, 131
- ID** initial dip. 46, 47, 49–51, 135–137
- IOS** Intrinsic optical imaging. 31, 46, 130
- LFP** Local field potential. 32
- MC** mitral cells. 62, 64, 65, 127, 135
- MCA** middle cerebral artery. 8
- MRI** nuclear magnetic resonance imaging. 18, 41, 42
- MSG** most sensitive glomerulus. 135, 136
- NO** Nitric oxide. 22, 23, 29
- NOS** Nitric oxide synthase. 29
- NVC** neurovascular coupling. 20, 23, 25–27, 29–32, 38, 68, 127–130, 136, 137
- NVU** neurovascular unit. 20
- OB** olfactory bulb. 55, 57, 62, 64, 65, 68, 130, 136
- ONL** olfactory nerve layer. 62
- OR** odorant receptor. 62, 64
- OSN** olfactory sensory neurons. 62, 64
- PA** penetrating arteriole. 10–12, 14, 46
- PCA** posterior cerebral artery. 8
- PD** Power doppler. 53, 55, 57
- RBC** red blood cell. 12, 25, 27, 35, 38, 52, 53, 55, 57, 68, 127, 135–137
- ROS** reactive oxygen species. 23
- SNR** Signal-to-noise ratio. 35, 38, 128, 129
- SVD** single value decomposition. 55
- TC** tufted cells. 64
- TF** transfer function. 29–31, 45, 68, 127–131, 133
- US** ultrasound. 51, 53, 57
- VSMC** vascular smooth muscle cell. 13, 14, 16, 23

Part I

Introduction

CHAPTER 1

GENERAL INTRODUCTION

Dear reader,

Welcome to my playground. I am AliKé, an MD-PhD student and your host for the next dozens of pages. I know reading a thesis is not the funniest time you can have (a few bad puns have been inserted here and there to ease the reading), so thank you for your interest. I hope you'll find what you're looking for.

This general introduction aims at introducing myself and this PhD, feel free to skip it. You may know it, but the relationship between the PhD and its candidate can be tricky. Many "old" PhD candidates, your host included, are tired at the end and do not want anything but to give up and rest, play, travel or count sheeps, rather than keep sacrificing every ounce of their time to think about science. We do it nonetheless, but why is that? Of course, we are kindly pushed by our advisors to keep up the work. Nonetheless, all PhD candidates I know are passionate about their work. I think I have the same passion. Is it intrinsically linked to my topic or do I love scientific inquiry in general? It is hard to say at this time, probably both. Most of all, looking back, I sure had a lot of fun during this PhD.

I learned a lot during these 4 years, as much about myself than about scientific knowledge in general. The two most important things are probably critical thinking and how to stand up for yourself. Science is collaborative, but collaboration does not wipe off individuality. A student can sometimes know better, and he should be aware of it. Note that it can be hard to separate rightful arguing and hopeless convictions: it has a lot to do with both oneself and who you're arguing with. These arguments may have been the most useful parts, although it didn't seem so right after: breaking every assumption I have about a matter, through arguing again and again, can be the best way to learn and fully integrate a concept. Then, every work has flaws. I am quite an idealist regarding the scientific process, and learning to get over it to accept the necessary imperfections of any work was harsh.

Funnily enough, if these may be important lessons for a scientist, it might be a dangerous habit

when I will get back to my medical studies as I was told a few times. Ask me in a few years how it went!

Before getting into the actual matter, let me explain why I chose to write my PhD thesis by making a detour by a keen interest of mine, philosophy of science. Michael Strevens in his recent book “The Knowledge Machine” [Strevens 2020] criticizes the canonical ways to think about scientific progress, as laid out by Karl Popper and Thomas Kuhn. Popper describes scientific work as formulating many hypotheses and trying as hard as possible to falsify them all through experimental work, the last one standing being the closest to reality, until a new experiment manages to falsify it. Still today, many define a scientific proposal as being subject to falsification, otherwise being nothing but belief. Strevens main criticism against popperian thought is that every experiment has underlying assumptions and that every scientist may have different plausibility ranking for these assumptions. A single result can thus be interpreted quite differently by different researchers.

Kuhn’s main work is “The Structure of Scientific Revolutions” [Kuhn 1962], where he defines the scientific process as some kind of staircase to the ultimate truth. Scientists rely on a given paradigm, a corpus of beliefs they accept as scientific truths, to design experiments and produce knowledge. When the current paradigm is contradicted too many times by experimental results, a revolution occurs when a new paradigm is laid out. Scientists move on to the next stair, and so on. Kuhn sees scientific progress as tedious work, requiring the majority of scientists “to give up the intellectual pleasures of continual speculation and debate, theorizing and arguing, and to turn instead to a life consisting almost entirely in the production of experimental data” as Strevens puts it. Kuhn himself writes “A paradigm can change only because the scientists working within it cannot imagine it changing”. However, as scientists, we can hardly describe our work as he does¹.

Strevens goes on and proposes his own conception of the scientific process. He lays out the “iron rule of explanation”, which underlies our interactions as scientists in order to advance knowledge. This rule comprises four principles, and I would like to focus on one of them. According to him, scientists are free and even incited to hold beliefs to pursue their work. Indeed, who never designed and did an experiment to prove something one believed to be true or false? Beliefs are paramount for scientists to pursue their work. However, it is strictly forbidden for them to express these beliefs in public communication, whether it be scientific articles or conference talks. He sees no problem with doing so in a lab retreat, or in any informal conversation, but scientific argumentation should solely rely on empirical evidence.

This thesis is the way to prove that I am able to pursue scientific work by myself, that I became an actual scientist through the years of training provided by my advisors. It comprises scientific articles respecting the iron rule. But the scientific process is also believing, and it is part of being a scientist. That is why I chose to express my own beliefs at the time of writing in this introduction, and to criticize what I think I should in that regard. Being a scientist is also being human and doing science is interacting with other scientists in a formal but most importantly in an informal way. So please forgive the few jokes, mainly bad puns, I may have disseminated in this introduction². It is part of my way of being myself, and a scientist!

As with any research project and probably as many students, I had no idea what the course of this PhD would actually be when I first stepped in my research team. During the first months I learned the techniques I would have to use, two-photon microscopy and functional ultrasound

¹Although PhD sometimes can feel like experimental slavery.

²As it happens, I had to refrain myself quite some times.

imaging, I learned how to analyse and interpret data, I read about our model, the mouse olfactory bulb, and about the fundamentals of neurovascular coupling. I had the chance to be closely tutored by Davide, my postdoc co-advisor, for the first project of this PhD: investigating the link between the functional ultrasound signal and the neuronal activation it supposedly reports in the brain, at a microscopic and mesoscopic scale. His physics background and experimental knowledge, along with Serge's invaluable pertinence regarding the goal and the impact of our work, as well as his love of details (from the experimental perfection to the slightest shift between two axes in publication figures), were key points for the completion of this project.

This project led to the next one, smaller but useful nonetheless. We gave everyone access to the software I developed during the first project, to compute transfer functions between any two signals. Although this particular paper did not yield any new biological findings, I firmly believe that sharing pieces of software and data is part of our contribution to scientific knowledge. As it happens, the project was perfect for a time where all work had to be done away from the microscopes, due to the COVID-19 pandemic.

The last year of my PhD has been about finding out about a long-standing controversy in our field: does the oxygen pressure in brain capillaries show an "initial dip", a transient decrease before functional hyperemia in response to a neuronal activation? To do so, I learned a new technique, life-time phosphorescence measurements, and had to manage the subsequent analysis pipeline.

Overall, the projects of this PhD all revolved around the same question: how can we improve the interpretation of vascular-based functional imaging of the brain to faithfully extract neuronally activated areas?

The following introduction is built to present the necessary background to discuss my results and this question, more generally. I start by introducing the vascular organization of the brain, as it is a main structural basis of vascular functional imaging. The changes measured by these techniques are due to the relationship between neurons and vessels, namely the neurovascular coupling. The second chapter reviews this relationship. Next in order is a description of the functional imaging of the brain techniques I worked on, which is the focus of the third chapter. I close the review of the state-of-the-art by focusing on our model, the olfactory bulb of the mouse, and its characteristics regarding this work.

Finally, I quickly review the outstanding questions of the field and provide a summary of how my projects fit in this landscape. Following the introduction, I get directly into the results since the methods and main technical developments are all described in the different articles.

This thesis is the summary of 4 years of experiments, of development, of thinking, arguing, laughing and growing. I sincerely hope that some of these will be found in the next pages.

CHAPTER 2

THE BRAIN VASCULATURE

We all need a daily check-up from the neck up to avoid stinkin' thinkin' which ultimately leads to hardening of the attitudes.

Zig Ziglar

Contents

2.1	The brain's special needs	8
2.2	Vascular organization of the brain	8
2.2.1	Circle of Willis	8
2.2.2	From the surface to the parenchyma	10
2.2.2.1	The surface network	11
2.2.2.2	Penetrating arterioles	12
2.2.2.3	The capillary bed	12
2.2.3	The way back	13
2.3	Histology of the brain vessels	13
2.4	Vascular resistance	14

A good review of the matter is [\[Cipolla 2016\]](#).

2.1 The brain's special needs

The average human weighs around 62 kg [Walpole *et al.* 2012] while his brain is about 1.3 kg [Stephan *et al.* 1981, Erwin *et al.* 2001]. This makes the brain north of 2% of the body mass, while it is the organ that consumes the most energy at rest, 20% of the total body use [Rolfe & Brown 1997, Attwell & Laughlin 2001]¹. However, the brain lacks an efficient energy reservoir and it heavily relies on the constant blood income to receive its primary energy substrates, oxygen and glucose [Diemel 2019]. Because of that, a few minutes are enough for neuronal death to occur when the supply is completely interrupted, e.g. after a stroke [Iadecola 2017]. The brain is so fragile that even a reduced blood flow is enough to cause damage to the tissues [Iadecola 2013]. A constant blood flow and a reactivity to increased energy consumption are thus paramount to a healthy brain function. In the meantime, the brain is surrounded by the skull, a rigid structure, which can put pressure on the brain in case of increased intracranial pressure due to vascular hypertension.

In this chapter, I will describe the structural and functional organization of the brain vasculature that allows for a healthy brain function. I will mainly describe the state of the art, and voluntarily stay away from the technical advances leading to its results. First, I will detail the anatomy of the brain vessels, which is the physical basis of the blood supply. Then I describe the cellular characteristics of arteries and capillaries, since they are the main actors of blood flow regulation. I will finish by introducing a major concept regarding blood flow regulation in the brain.

2.2 Vascular organization of the brain

Given its energy needs, the brain is heavily supplied in blood. The input comes from the carotid and the vertebral arteries, on the right and left side. Both vertebral arteries anastomose distally to form the basilar artery (Figure 2.1). After having gone through the brain, deoxygenated blood drains into the jugular veins.

2.2.1 Circle of Willis

The Circle of Willis (CoW)² is an anastomotic system supplied by the carotid and basilar arteries from both sides (Figure 2.2). On each side, the carotid artery divides into the anterior cerebral artery (ACA), the middle cerebral artery (MCA) and the posterior communicating artery. Both ACA anastomose in the anterior portion of the CoW in the anterior communicating artery. The posterior communicating artery joins the basilar artery in the posterior portion of the CoW to form the posterior cerebral artery (PCA). The ACA, the MCA and the PCA feed respectively the anterior, the lateral and the posterior parts of the cerebrum. Overall, there is a continuity between these vessels forming the CoW which rests at the basis of the brain.

¹This introduction is widely used in papers and dissertations. To try and be more original, I'll add that we have here the actual proof that *size does not matter*.

²First described by Sir Thomas Willis in 1664 [Willis 1664], he duly acknowledged his colleagues' help for the work: Sir Christopher Wren, Thomas Millington and Richard Lower. We also owe him the prefix 'neuro-' and the corresponding terminology, which first appeared in English in his treatises [Mehta *et al.* 2019].

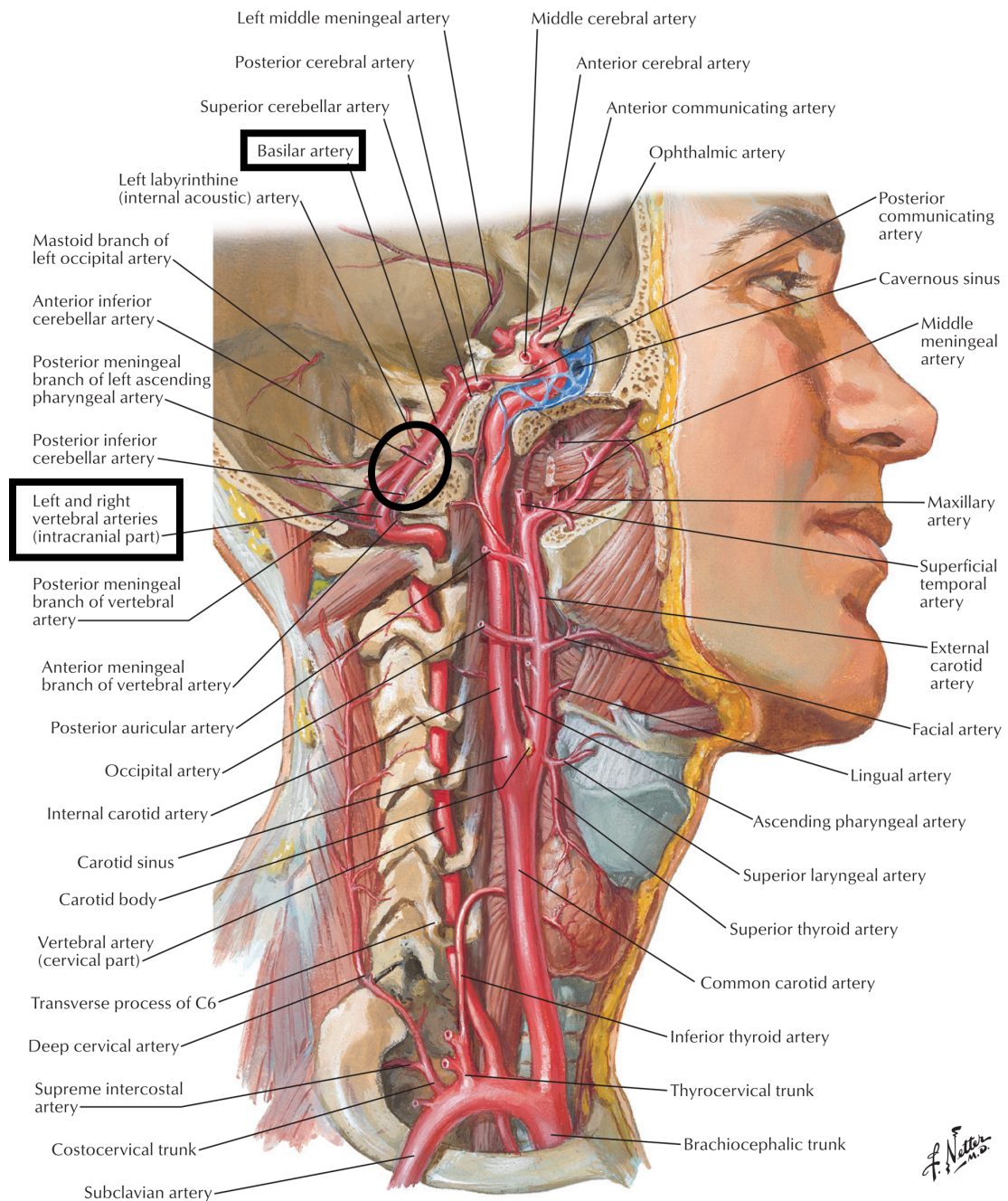


Figure 2.1: Vessels at the entry of the human brain.

Circled in black on the drawing is the anastomose of the vertebral arteries into the basilar artery.

Adapted from [Netter 2019], Plate 147.

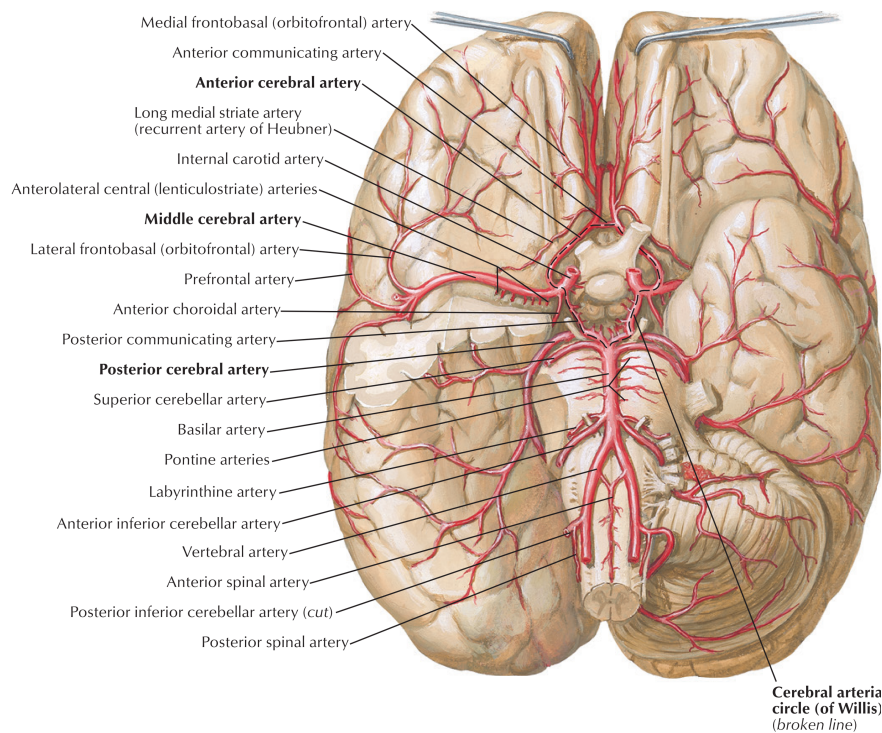


Figure 2.2: The Circle of Willis in the human brain. From [Netter 2019], Upper part of Plate 152.

This anastomotic organization allows for an equilibrium of the blood pressure in both sides of the brain. In the case of a stenosed vessel upstream or in the CoW, this anastomotic system makes sure that the brain stays sufficiently vascularized, although the blood flow can be reduced³.

The main arteries originating from the CoW divide into pial arteries at the surface of the brain, which then penetrate the brain and vascularize the parenchyma.

2.2.2 From the surface to the parenchyma

Pial arteries lie at the surface of the brain, either within the subarachnoid space or at the surface of the cortex, below the pia mater [Jones 1970]. They are surrounded by cerebrospinal fluid (CSF) and have to go through the meninges to enter the brain radially as penetrating arteriole (PA) [Nishimura *et al.* 2007]. PA will branch into capillaries, which are the main location of the vascular volume: $80\% \pm 20\%$ (mean \pm SD) [Ji *et al.* 2021]. Andy Shih and colleagues [Shih *et al.* 2015] thus describes the cerebral vasculature as 3 parts: the surface network, the subsurface microvascular network and the penetrating vessels network connecting both of them.

Below, I review some of the anatomical characteristics of these parts, which allow them to face the needs of the cerebral parenchyma.

³It may not be enough if the stenosis is in the aorta though.

2.2.2.1 The surface network

The pial network comprises a two-dimensional architecture making a robust compensation system to any PA in case of a surface stenosis [Blinder *et al.* 2010, Schaffer *et al.* 2006]. Such an interconnected network (Figure 2.3) makes possible the redistribution of blood from areas of excess to areas in need. Although they are in the brain, pial arteries are innervated by the peripheral nervous system, being as such “extrinsically” innervated as opposed to intrinsic innervation by the central nervous system [Cipolla *et al.* 2004].

The smallest pial vessels show a diameter less than 25 μm while the bigger exceeds 90 μm [Xiong *et al.* 2017] in a mouse brain. While these figures and results, as the majority of the ones in this thesis, regard the rodent brain, the organ-specific vascular organization is well conserved between vertebrates [Larrivée *et al.* 2009].

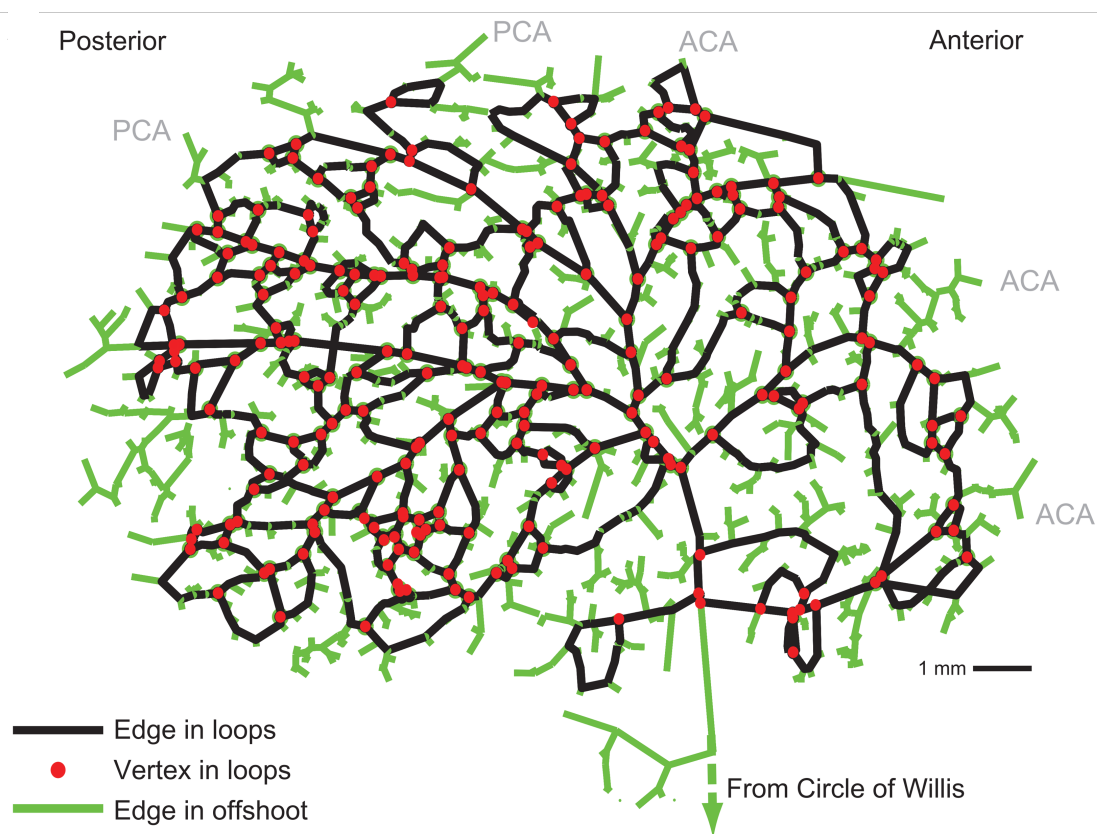


Figure 2.3: The pial network.

The pial network at the brain surface is a 2D network where vessels (edges, green or black lines) are widely connected to each other (vertex, red points). Loops are formed by these connections (black lines), while other vessels stay unconnected to these loops (green lines). From Figure 2 in [Blinder *et al.* 2010].

2.2.2.2 Penetrating arterioles

PAs are defined as the pial artery bifurcating perpendicularly into the brain [Nishimura *et al.* 2007]. When they dive, they keep a mantle of subarachnoid space creating the Virchow-Robin space. It will eventually become virtual, i.e. a space between adjacent structures that is normally pressed together, before being replaced by neuroglial processes as the PA divides into capillaries [Jones 1970]. As opposed to the pial vessels, PAs are innervated by the brain itself - thus named “intrinsic” innervation [Cipolla *et al.* 2004]. Median diameter of PA is 11 μm [Blinder *et al.* 2013].

Although the upstream pial network is highly redundant, it is not the case of the PA network. Photo-thrombolysis of a single PA in the rat cortex impaired the blood flow over a radius of 350 μm around the PA. Until 10 branches downstream, red blood cell (RBC) flow stayed below 30% of its baseline value. This is why PAs have been called the “bottleneck” in cerebral perfusion [Nishimura *et al.* 2007].

2.2.2.3 The capillary bed

The capillary network has recently been described thoroughly by multiple teams [Tsai *et al.* 2009, Xiong *et al.* 2017, Kirst *et al.* 2020, Todorov *et al.* 2020, Ji *et al.* 2021]. Until recently, a challenge upon the description of the capillary network was the size of the capillaries and their density in the parenchyma: technical advances overcame them and allowed us to better describe the capillary bed. As many physio- and pathological questions rely on a good understanding of the brain vasculature at its finest scale, we will review some of them in this part.

The definition of the capillary bed is a prerequisite before further questions. Over the years, many definitions have been given to capillaries. Blood vessels are capillaries if: (i) they do not have any Virchow-Robin space [Jones 1970], (ii) based on the vessel diameter - with various thresholds [Borowsky & Collins 1989, Chaigneau *et al.* 2003, Stefanovic *et al.* 2007, Ji *et al.* 2021] - , or (iii) considering cellular characteristics. The definition of the transitional part between arterioles and capillaries is also debated. This uncertainty makes the confirmation of findings across research teams difficult, as the same term is used to describe different vascular compartments. I will get back to this debate below (see section 3.2.1).

Similarly to the surface network, the capillary bed is highly interconnected and presents many loops. Topologically, one can quantify the loops by the number of branches needed to return to the same node: while it is 4 branches at the surface network [Blinder *et al.* 2010], it is around 9 in the capillary network [Ji *et al.* 2021].

While the PA network is on a single dimension and the pials rely on a two-dimensional network, the subsurface microvasculature comprises a three-dimensional network since it feeds the brain in its tridimensional volume [Blinder *et al.* 2013]. The density of this network is highly heterogeneous across brain areas [Craigie 1945, Michaloudi *et al.* 2005, Schmid *et al.* 2019]. An old hypothesis was that the density of the vasculature, and especially the capillaries, is highly correlated with its main purpose⁴: feeding the neurons [Klein *et al.* 1986]. As it happens, the density of capillaries is homogenous across layers of the rodent cortex [Tsai *et al.* 2009, Blinder *et al.* 2013, Kirst *et al.* 2020,

⁴The notion of purpose of a physiological mechanism is quite weak, and I only use it here for clarity *purposes*.

[Ji *et al.* 2021] while the neuronal density varies greatly [Tsai *et al.* 2009], which contradicts that hypothesis. However, a correlation appears when replacing the neuronal density by the metabolic demand: Weber and colleagues showed that the capillary density follows the activity of Cyclooxygenase (COX), an enzyme intervening in synaptic activity, in the somatosensory cortex of primates [Weber *et al.* 2008]. Combined with the fact that synapses are the most energy-consuming part of the brain [Harris *et al.* 2012], this indicates that vascular density matches synaptic density, rather than somatic density, in a way that it can supply synaptic metabolic needs. This is particularly true in the olfactory bulb [Lecoq *et al.* 2009].

2.2.3 The way back

There is no anastomosis between the arterial and venous systems other than the capillary bed: the blood path is thus necessarily arteries-capillaries-veins throughout the brain [Shih *et al.* 2015]. There are, on average, 7 capillary branches between the last arteriole and the first venule [Ji *et al.* 2021]. Venues participate in two different drainage systems: the superficial and the deep ones [Hassler 1966, Schaller 2004, Kılıç & Akakin 2007, Cipolla 2016]. The superficial system drains the cortical and subcortical volumes, while the deep system drains the central part of the brain. Both converge into the Superior Sagittal Sinus, other sinuses and finally drain into the jugular veins.

To be noted is the absence of a strict parallelism between the arteries and veins in the brain, even for the larger vessels, i.e. each artery or arteriole is not next to a vein or venule following the same path.

Compared to the arterial system, the venous system lacks attention and thorough description [Schaller 2004, Xiong *et al.* 2017, Ross *et al.* 2020]. Indeed, veins are not considered as having an active behavior in the blood flow regulation since they lack a regular paving of muscular cells in their walls [Kılıç & Akakin 2007].

2.3 Histology of the brain vessels

I will here focus on a simplified view of the arterial and capillary systems since they are responsible for the occurrence of neurovascular coupling.

Internally, pial arteries are composed by a layer of endothelial cell (EC) forming the endothelium (Figure 2.4). Externally, they are separated from the subarachnoid space by the *glia limitans* forming the perivascular space, also known as the Virchow-Robin Space [Jones 1970, Zhang *et al.* 1997]. Below are the nerves innervating the pial arteries from the peripheral nervous system [Iadecola *et al.* 1993, Hamel 2006]. Layers of vascular smooth muscle cell (VSMC) surround the endothelium of the surface arteries [Roggendorf & Cervós-Navarro 1977, Iadecola 2017]. This allows for a very precise control of the dilation and contraction of these vessels, either via a peripheral control of the VSMC tension or via the neurovascular coupling. The presence and the number of layers of VSMCs are a good indicator of the location in the arterial vascular network as it decreases while going down the hierarchy of vessels, towards capillaries.

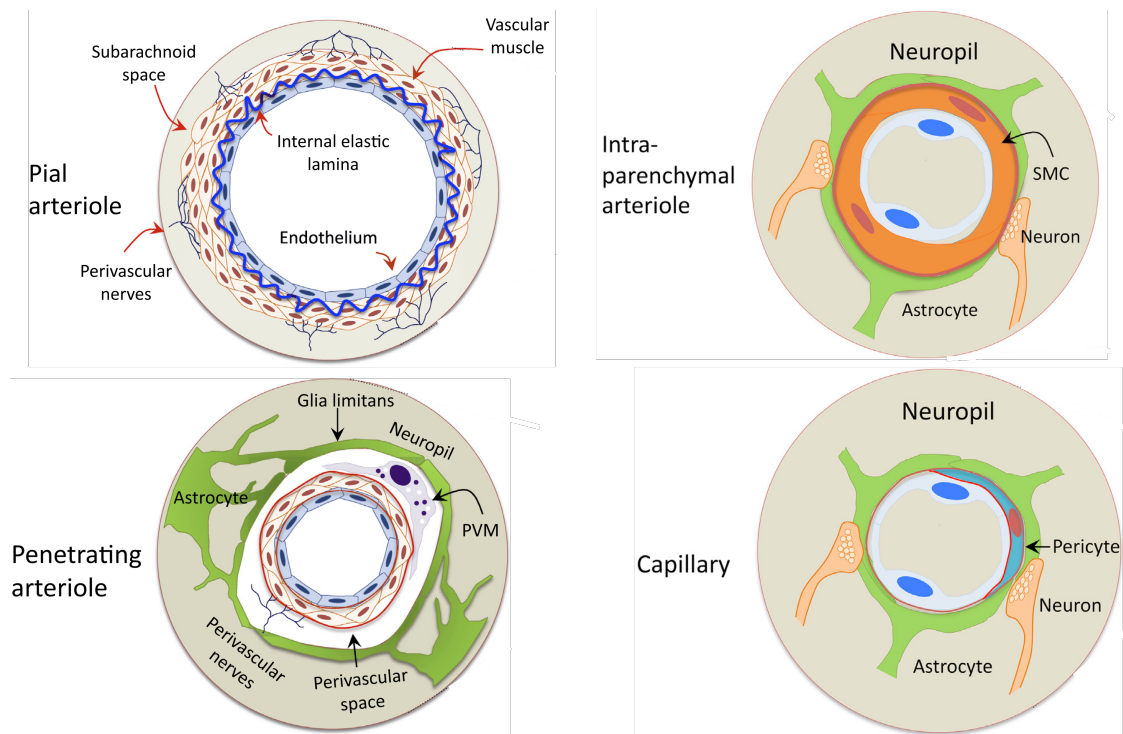


Figure 2.4: Summary of the cellular characteristics of the various vessel types in the brain. Adapted from [Iadecola 2017].

PAs keep a virtual Virchow-Robin space, eventually losing it in depth [Jones 1970, Zhang *et al.* 1997]. While the perivascular space disappears, another one is formed by multiple types of perivascular macrophages [Iadecola 2017]. As opposed to the extrinsic innervation of the pial arteries, PAs are intrinsically innervated, i.e. by fibers from the brain itself [Roggendorf & Cervós-Navarro 1977]. Being below the pials, PAs is composed of a thinner layer of VSMCs, eventually down to a single one [Dahl 1973, Roggendorf & Cervós-Navarro 1977]. ECs can physically connect to VSMCs by means of protrusions [Dahl 1973, Longden *et al.* 2015].

As previously mentioned, one of the capillary definitions is cellular: pericytes replace VSMCs, covering around 30% of the vascular walls [Dahl 1973, Damisah *et al.* 2017]. As at the level of arterioles, astrocytic end-feets are found around capillaries too [Iadecola 2017].

Overall, these cells are the physical actors of blood flow regulation in the brain.

2.4 Vascular resistance

A main concept in cerebral blood flow regulation is vascular resistance, although counter-intuitive as one could think a vessel dilation would decrease the flow at a constant pressure.

Each blood vessel fights against its own flow with a specific resistance. The ability of the vessel to change its resistance is what allows the blood income to stay constant over a wide range of

input arterial pressure, from 60 to 150 mmHg [Phillips & Whisnant 1992, Jordan & Powers 2012, Filosa *et al.* 2016]. This characteristic is crucial for brain tissue survival, due to the lack of energy reservoir [Cipolla 2016].

How can we model the resistance of a given vessel? Ohm's law applied to fluid dynamics, states that the resistance (R) is equal to the pressure difference at both ends (ΔP) over the flow (φ):

$$R = \Delta P \div \varphi \quad (2.1)$$

This allows for an estimation of the overall resistance of the brain and the contribution of the different types of vessels to this resistance. Large arteries at the entry of the brain account for 40% of the total brain vascular resistance [Stromberg & Fox 1972, Faraci & Heistad 1990, Iadecola 2017] (Figure 2.5) which coupled with auto-regulatory mechanisms, grants a highly constant blood flow input to the brain. Once in the brain itself, the biggest resistance comes from the capillary bed [Gould *et al.* 2016].

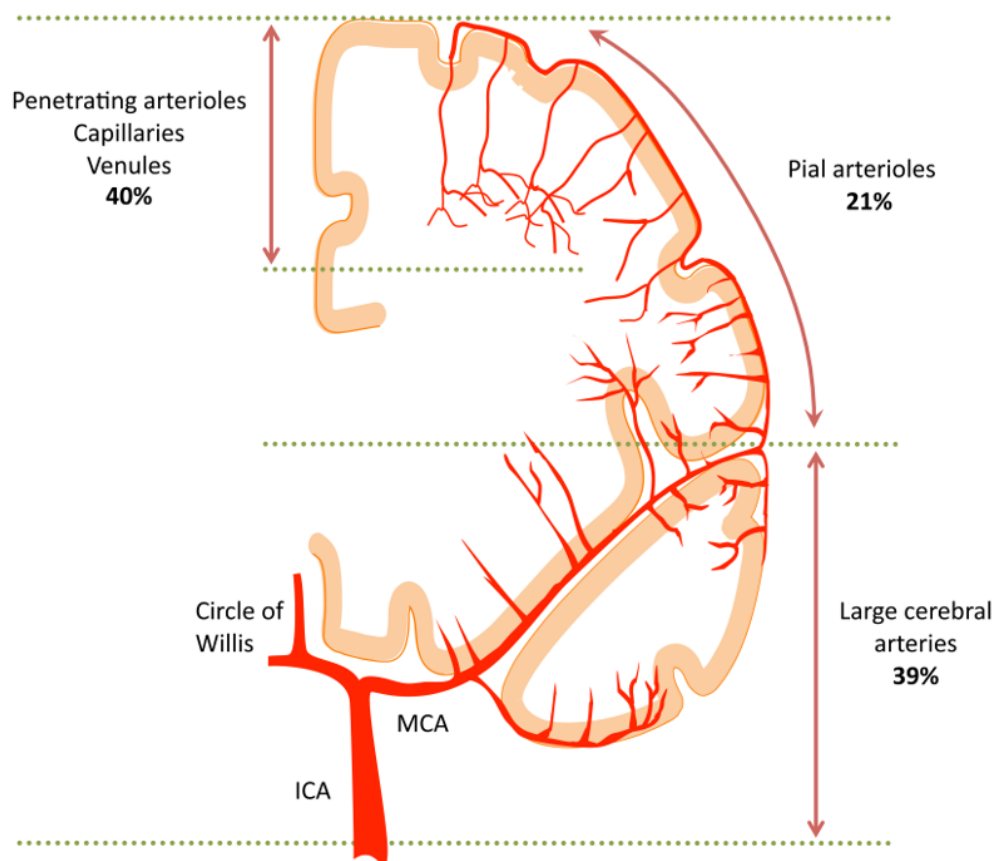


Figure 2.5: Vascular resistance in the brain mainly comes from parenchymal vessels and large arteries.

From [Iadecola 2017].

Smaller vessels, the microvasculature, have physical characteristics compatible with a newtonian

blood flow and thus, the application of the Poiseuille Law [Hirsch *et al.* 2012, Cipolla 2016]:

$$\Delta P = \frac{8\nu L}{\pi R^4} D_v \quad (2.2)$$

with ΔP the difference in pressure between the extremities of a vessel of length L and radius R , ν the viscosity of the liquid and D_v the flow.

This formula shows that for small vessels, the parameter most contributing to the resistance is the radius. This suggests that the easiest way to modulate the resistance and thus the flow in small vessels is by changing their diameter, e.g. via VSMC-mediated dilation. Interestingly, the radius importance is also highlighted by the impact of the endothelial surface layer (ESL). Discrepancies between in vitro and in vivo measurements made scientists wonder whether the ESL, a thick layer of tissue on the endothelium, increases resistance. Indeed, it does [Pries & Secomb 2005] and since the proportion of the blood in contact with the vessel walls is greater in smaller vessels, precise control of the microvasculature radii is of importance. Another resistance factor is the hematocrit, the latter being proportional to the last [Pries & Secomb 2005, Hirsch *et al.* 2012].

CHAPTER 3

THE NEUROVASCULAR UNIT

*All for one and one for all, united we
stand and divided we fall*

Alexandre Dumas in
The Three Musketeers, 1844

Contents

3.1	Origin of the concept	18
3.2	A Hitchiker's guide to neurovascular coupling	20
3.2.1	A roadmap to functional hyperemia	22
3.2.2	What does functional hyperemia brings to the brain parenchyma?	23
3.3	Modeling the neurovascular coupling	26
3.3.1	Physical representation of a vascular network	26
3.3.2	Effect of a single actor	27
3.3.3	Holistic approach	29
3.4	Measuring the neurovascular coupling in two-photon microscopy	32
3.4.1	Neuronal changes	32
3.4.2	Vascular changes	34
3.5	Conclusion	38

Noticeable reviews on this topic are [Iadecola 2017, Kaplan *et al.* 2020]¹.

¹Good luck to me trying to avoid plagiarism eh.

3.1 Origin of the concept

Blood vessels and their content are major actors of the energy delivery system of our body. We know it now and it was already known back in the XVIIIth or XIXth centuries. What we discovered only recently is that the blood vessels "listen" to the brain. Indeed, before the end of the XIXth century, the common paradigm was that the brain tissue has no influence on its own blood supply [Friedland & Iadecola 1991].

The first results to shake this idea were obtained on injured humans, with skull defects allowing for measurements of brain pulsations. In 1878, an Italian physiologist named Angelo Mosso measured and reported, for the first time, a change in the brain pulsations over the cortex, when his subject made calculations [Mosso 1880]. A few years later, Roy and Sherrington injected brain by-products in the bloodstream and reported that the brain volume increased greatly due to a variation in its vessels diameter (Figure 3.1) [Roy & Sherrington 1890]. They suggested that "the brain possesses an intrinsic mechanism by which its vascular supply can be varied locally in correspondence with local variations of functional activity", what we call today neurovascular coupling. They also reported that vascular changes following stimulation of the peripheral nervous system lasted for seconds. From our perspective, a century later, their stimulation paradigms were very crude and probably involved more stress and nociceptive pathways than a real local brain stimulation however, the neurovascular hypothesis has become reality.

Unfortunately, the hype around these results and their physiological implications never got to rise. They were even somehow replicated in the 1930's by Schmidt and Hendrix who observed an increase in the cat's brain temperature after illuminating his eyes. This increase was reported as a proxy for an increase in blood flow subsequent to neuronal activation [Schmidt & Hendrix 1938], and thus the relation between neurons and vessels was found, again. A few years later, as already mentioned in the previous chapter, Craigie proposed that the vascular density in the brain varies with the neuronal density, to account for the energy expenses [Craigie 1945]. Although he was wrong, both functional and static relationships between neurons and vessels were already subjects of interest at this time [Kety 1950].

Thanks to the development of the X-Rays and the use of radioactive inert gas, scientists in the 50's tested the hypothesis that "visual stimulation might [...] increase the blood flow in those areas of the brain associated with this function, [...] in view of the possible relationship between local cerebral blood flow (CBF) and local functional activity" [Freygang & Sokoloff 1959]. Indeed, increases of the radiographic contrast were seen in the superior colliculi and the calcarine cortex of the cat brain after flashing light at 6 Hz for 5 min, demonstrating an increase in blood flow in these regions. The later use of intra-carotidian injected radioactive isotopes and external γ -camera provided a precise - for the time - mapping of the brain functions at a regional level (Figure 3.2) [Lassen *et al.* 1978].

Now that the functional relationship between neurons and vessels has been established, let's speed up to the next big step: BOLD-fMRI. The technique is presented and discussed in a future chapter (see section 4.2), so I will only mention the milestones here. The first result with nuclear magnetic resonance imaging (MRI) dates back to 1991 in Massachusetts where blood volume was measured thanks to the contrast-enhancing injection of gadolinium [Belliveau *et al.* 1991, Raichle 2000]. It was not BOLD-fMRI yet, as the blood oxygen level de-

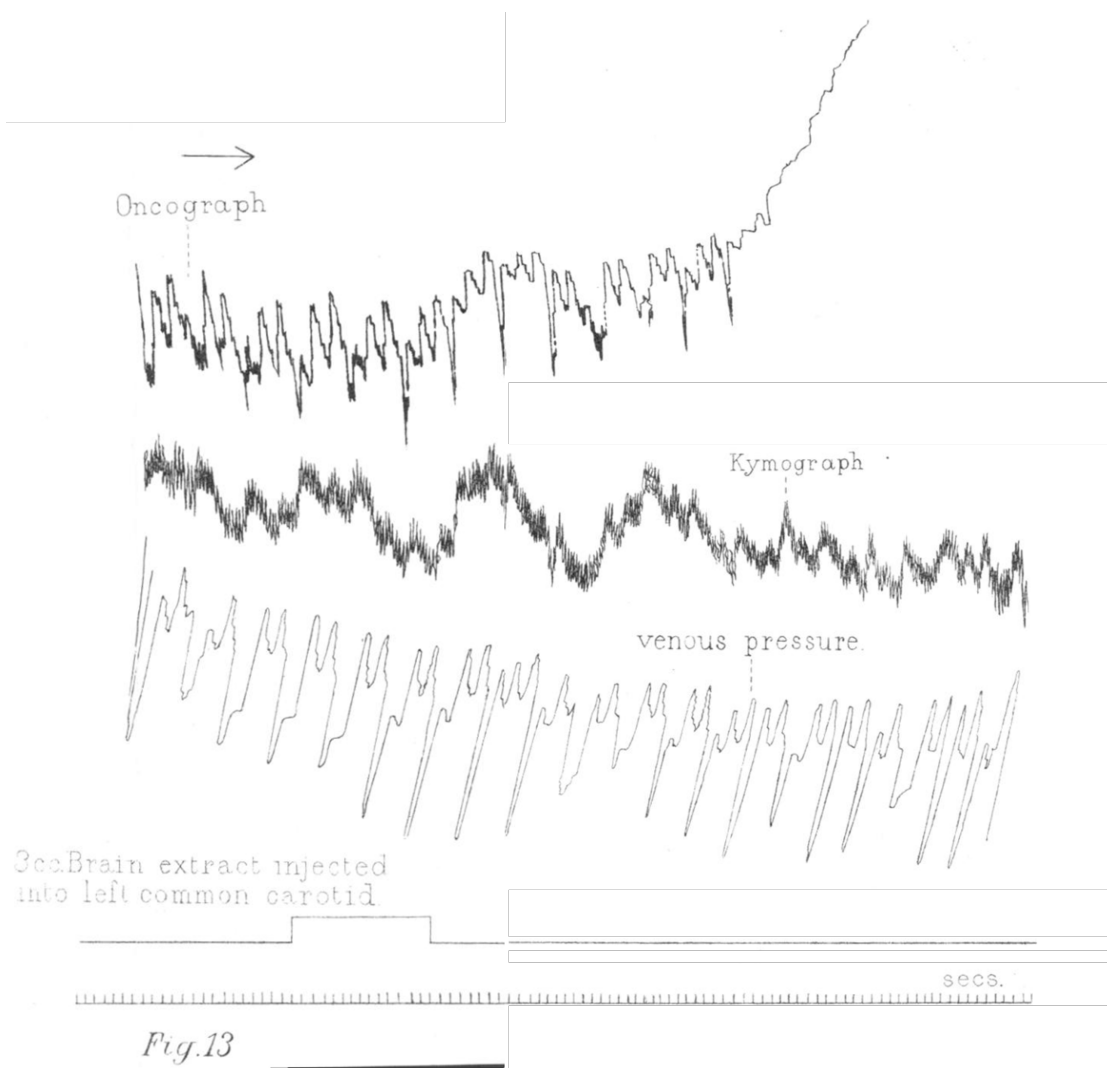


Figure 3.1: The first clue for the neurovascular coupling.

Authors injected brain by-products into the left common carotid of a dog. They observed an increase in brain volume (upper curve), measured with an oncograph placed above a craniotomy, without increases of neither arterial pressure (middle curve) in the femoral arteries nor venous pressure (bottom curve) in the jugular veins. It suggests that brain blood volume specifically reacts to the injected products. Adapted from [Roy & Sherrington 1890].

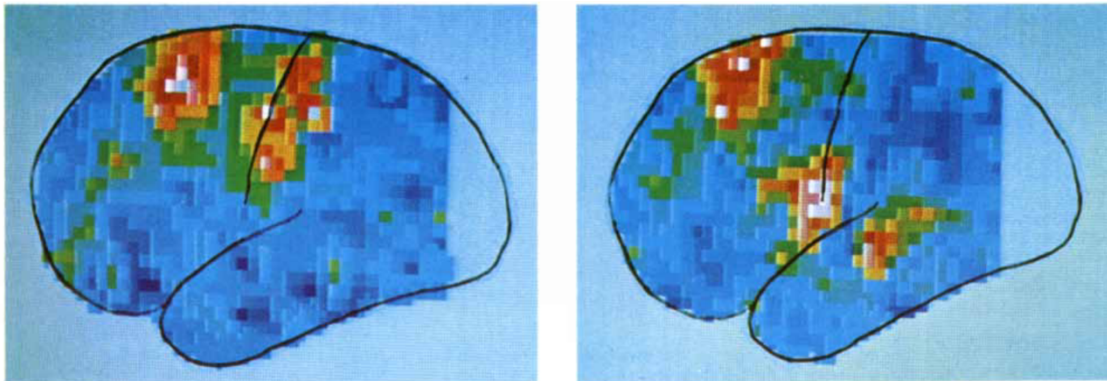


Figure 3.2: The first wide scale vascular-based mapping of brain function.

Blood flow changes in humans, compared to resting state, is measured with a Gamma-Camera reporting radioactivity from an injected xenon isotope. Mean flow rate is green, shades of blue are used for decreases up to 20% while red shades are used for increases up to 20%. On the left, the subject moves his left fingers on the opposite side of observed hemisphere, activating the motor cortex and the supplementary motor area. On the right, the subject counts repeatedly to 20, activating the famous Broca's area along with the auditory cortex. From [Lassen *et al.* 1978].

pendent (BOLD) effect was discovered around the same time [Ogawa *et al.* 1990a]. BOLD-fMRI is to this day the most used technique to study brain functions in humans, both in physiological and pathological conditions [Raichle & Mintun 2006, Logothetis 2008].

Last but not least in this story is the publication of the seminal paper on Functional Ultrafast Ultrasound in 2011 [Macé *et al.* 2011], describing this new technique which overcomes some caveats of BOLD-fMRI in animal models. I will get back to it in the next chapter.

I tried to portray here the history of the neurovascular unit, from how it came to be to how it is used today with functional brain imaging. I left out many things, the many controversies about its cellular components, how they interact with each other, etc.

As depicted by Figure 3, the neurovascular unit (NVU) comprises neurons, astrocytes, vascular cells among which endothelial cells, pericytes and vascular smooth muscle cells, and even microglia [Filosa *et al.* 2016, Iadecola 2017]. These cells cooperate to ensure that brain homeostasis is maintained. They form the blood-brain barrier, to protect the brain tissue from dangerous molecules in the bloodstream, assure a sufficient blood flow at any time, an immunitary surveillance, etc. We will now focus on how the NVU ensures the “mechanism by which its vascular supply can be varied locally in correspondence with local variations of functional activity”. That is, how neurovascular coupling (NVC) works.

3.2 A Hitchiker's guide to neurovascular coupling

A local increase of blood flow systematically follows neuronal activation (Figure 3.4), a phenomenon called “functional hyperemia” (FH), which is a consequence of the neurovascular coupling. NVC

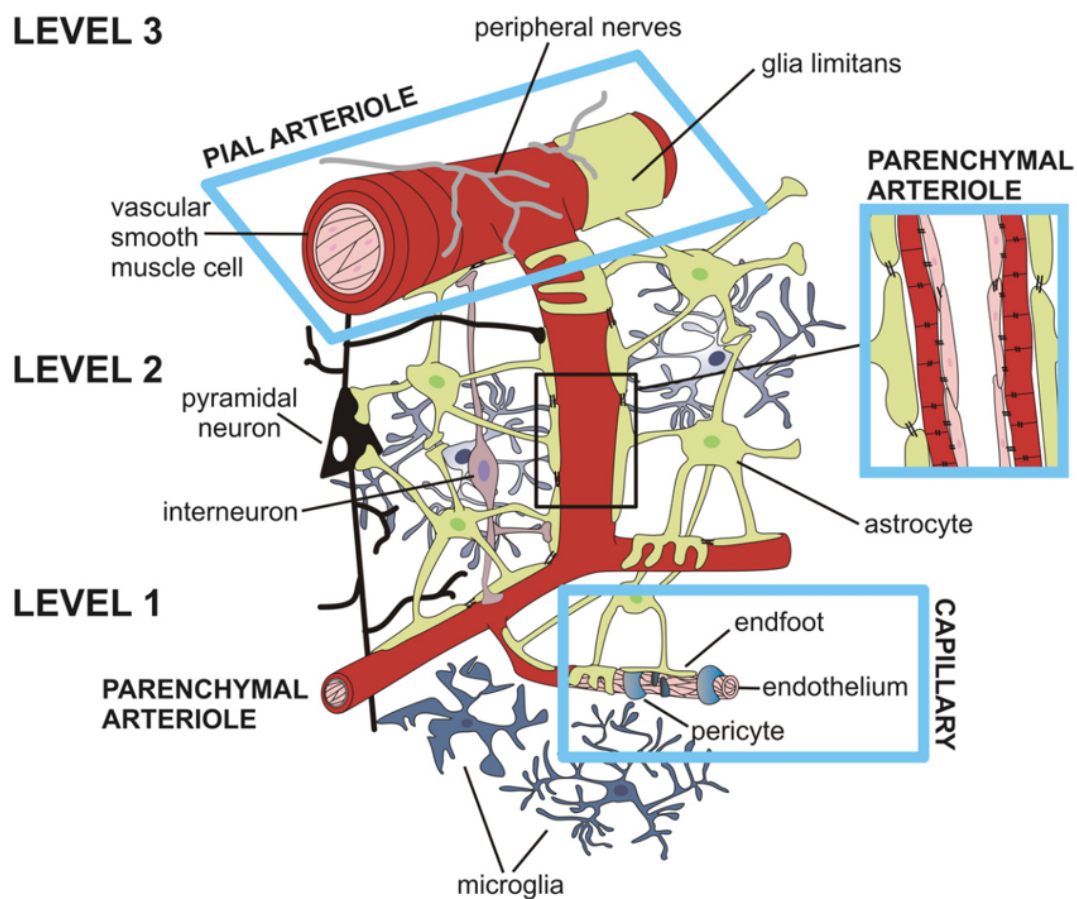


Figure 3.3: Schematic representation of the cellular actors of the neurovascular unit. Note that the spatial organization is simplified and does not faithfully represent reality. From [Filosa *et al.* 2016].

occurs thanks to the communication between neurons and vessels, forming the neurovascular unit with other cell types.

First, I will get into how a neuronal activation induces a change in blood flow, and then discuss the current experimental paradigm on NVC.

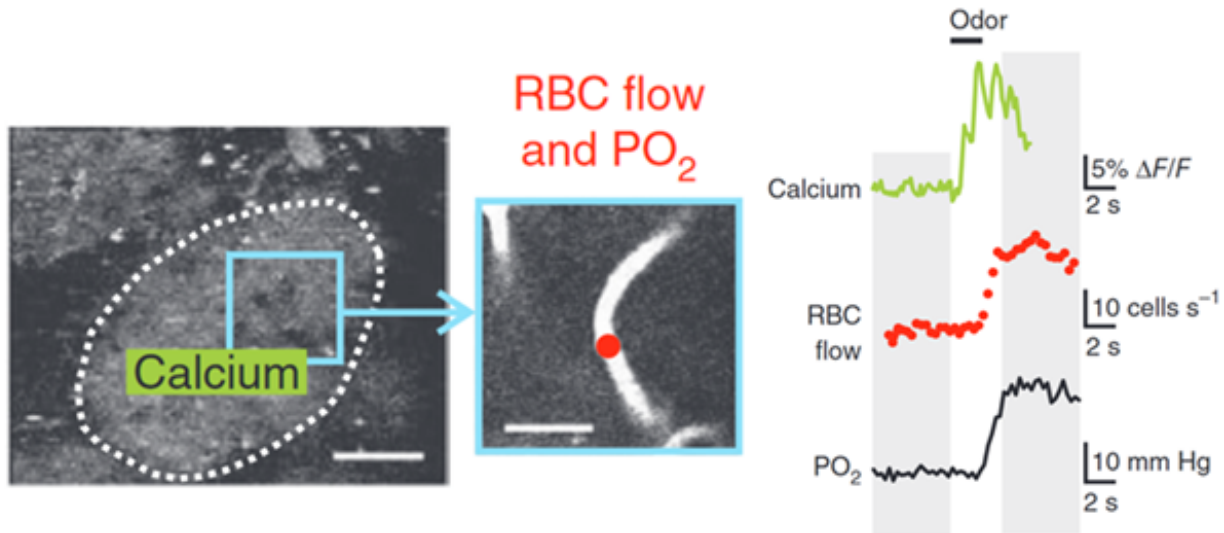


Figure 3.4: Summary of the local effect of functional hyperemia.

An anesthetized mouse receives an odor, which triggers a neuronal response in a glomerulus of the olfactory bulb (left panel). The subsequent vascular reaction is observed in a capillary located in the same glomerulus (middle panel) where red blood cell flow and partial pressure in oxygen is measured. Neuronal activation is observed through calcium dependent GCaMP2 fluorescence. As post-synaptic calcium increases, red blood cell flow and partial pressure in oxygen increase too, although with a delay, due to neurovascular coupling. Shaded areas are from the original study and should be disregarded. From [Parpaleix *et al.* 2013].

3.2.1 A roadmap to functional hyperemia

My work aims at better understanding the consequences of FH and how they relate to the original neuronal activation. I did not dissect NVC during my projects but focused only on the input and output of the system. Thus, I will only mention the main steps of FH as we know them today to answer the following question: how does a local neuronal activation generate a vessel dilation upstream, sometimes hundreds of micrometers away? What is its dynamic across the vascular arbor?

Neurons can release vasodilatory components, like Nitric oxide (NO) or prostaglandins, upon increase of intracellular Ca^{2+} [Attwell *et al.* 2010, Lacroix *et al.* 2015, Lecrux & Hamel 2016, Tasic *et al.* 2018]. However, this release is local while the capillaries in the parenchyma are not able to actively dilate. Thus, there must be other mechanisms to generate a vasodilation in upstream vessels.

One of the main hypotheses for eliciting the vessel dilation is via K^+ released upon action poten-

tials [Longden *et al.* 2017]. Neuronally-released K^+ leads to an inflow of K^+ and a hyperpolarization of the ECs. This local hyperpolarization can regenerate itself via K^+ -sensitive K^+ channels and propagates upstream the vascular arbor through the gap junction of ECs [Segal 2015].

Interestingly, a recent study proposes that depolarization rather than hyperpolarization of ECs can induce FH [Thakore *et al.* 2021]. TRPA1 channels are expressed by ECs and are sensitive to reactive oxygen species (ROS), a by-product of neuronal activation. Upon binding of ROS, they Ca^{2+} increases in ECs. The inhibition of these channels impairs NVC, indicating an important role.

Apart from ECs, which got a lot of attention in the last years, astrocytes are also proposed as important actors on the FH pathway [Tran *et al.* 2018]. However, their implication has been highly debated over the years [Filosa *et al.* 2016, Cauli & Hamel 2018] and it becomes clear that their role may differ according to their location [Mishra 2017] and that astrocyte process activation has the right timing to be involved in NVC [Otsu *et al.* 2015]. As of today, their exact contribution is unknown.

Overall, neuronal activation can generate the transmission of a signal upstream along the vascular arbor. How does this signal turns into vessel dilation? First, ECs can release NO onto the VSMCs of arteries and arterioles [Andresen *et al.* 2006, Ashby & Mack 2021]. Secondly, VSMCs are not the only proposed effector of vessel dilation. Pericytes can also elicit vasodilation [Peppiatt *et al.* 2006, Fern *et al.* 2010, Krueger & Bechmann 2010, Hall *et al.* 2014]. This is the source of a current debate in the NVC field, regarding whether capillaries can dilate. This debate essentially came from a bad definition of what is a true pericyte. Enwrapping pericytes are located on larger capillaries, express actin and can generate a capillary dilation. This vascular compartment was previously named precapillary arterioles and is now defined as the transitional segment. Thin-strand pericytes cover the smallest capillaries (the most numerous) and do not generate dilation.

Our team performed a complete study on how pericyte activation relates to FH in the olfactory bulb [Rungta *et al.* 2018]. By measuring the Ca^{2+} changes along the vascular arbor, we showed that thin-strand pericytes are reliable markers of local neuronal activation, however they are not involved in the generation of FH. In contrast, upstream enwrapping pericytes and VSMCs, show a rapid decrease of intracellular calcium before FH. Precise measurements of the neural and vascular response onsets were key in this study. In summary, FH starts upstream at the level of the primary unit comprising the descending arteriole and the first 50 μm the first capillary branch. Dilation then propagates upstream (pial arteriole) and downstream (transitional segment), actively reducing the vasculature resistance (Figure 3.5).

3.2.2 What does functional hyperemia brings to the brain parenchyma?

The first idea that comes to mind is that FH compensates for energy consumption, mainly O_2 and glucose, upon neuronal activation as the brain's energy store is scarce. Is this idea correct?

The canonical question, citing Iadecola [Iadecola 2017], would have been "What is FH for?" or "Why does CBF increase during Brain Activity", but that is not how I chose to formulate it here. Indeed, the form of the question directly supposes that there is a purpose for FH. Although there

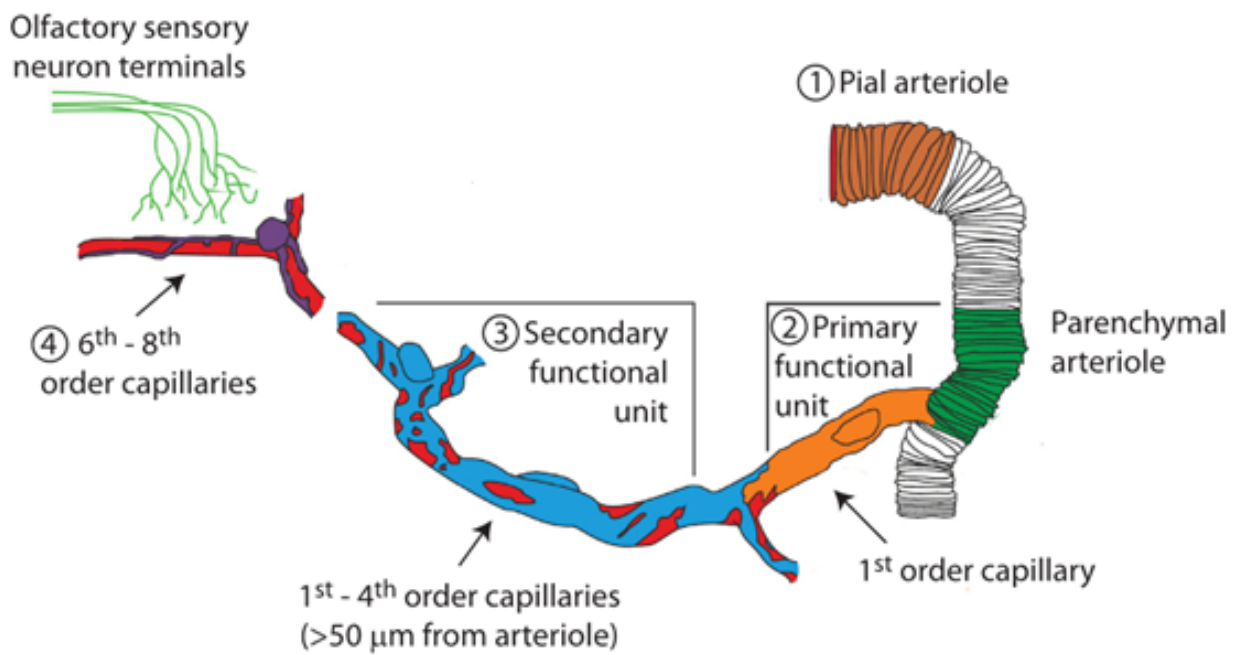


Figure 3.5: Schematic representation of the vascular arbor.

Neuronal activation occurs on the left. An electrical signal goes upstream the vascular arbor, with the primary unit being the first one to dilate. Then, the secondary functional unit dilates. From [Rungta *et al.* 2018].

may be such thing as a purpose for a physiological phenomenon, since natural selection's precept is that species and functions evolve to account for biological challenges, there is no chance to find back this purpose with certainty but by going back to the time where it appeared .

As far as I can tell, any experiment designed to study the NVC has one of two huge limitations. The first one is the impossibility to completely cancel FH. Many teams, including ours, have inactivated one of many supposed pathways of NVC to try and understand its point. However, the known presence of compensatory mechanisms, either from the developmental stage or acute, renders the results hardly 100% truthful unless the whole NVC is canceled. This leads me to the second limitation: a short-term bias. These experiments only cancel FH for a limited amount of time and thus cannot show any long-term effect of NVC impairment. And we know that many neurodegenerative diseases, known to exacerbate across years, show NVC defects quite early [Farkas & Luiten 2001, Iadecola 2004, Girouard & Iadecola 2006, Winkler *et al.* 2013, Iadecola 2013, Halliday *et al.* 2015, Iadecola 2017, Huneau *et al.* 2018]. Whether these defects are causes or consequences is unknown, but the current experimental paradigm may not be sufficient to answer it. Nonetheless, note that short-term cancelling of FH is necessary to avoid compensatory mechanisms.

That is why I formulate the title of this part as it is: that is the only one we can actually answer.

As vessel dilation occurs, blood flow increases along with the RBC velocity [Chaigneau *et al.* 2003]. This increases the partial pressure of oxygen in the blood, that is the quantity of O₂ dissolved in the plasma, but also the quantity of O₂ in the RBC [Lecoq *et al.* 2011, Parpaleix *et al.* 2013]. By effect of the increased gradient of O₂ and glucose, due to the consumption in the parenchyma and the increase in the vessel, both will diffuse more from the bloodstream to the tissue.

The increase in speed also allows for a better clearance of the by-products of the neural metabolism, which may be toxic. One recent paper by Hosford and colleagues proposes that CO₂ clearance is the key player in FH (Figure 3.6) [Hosford *et al.* 2021]. Reactive oxygen species, lactate, the infamous amyloid- β peptid are produced and also need to be removed to avoid defects, among which the Alzheimer disease (Tarasoff-Conway *et al.*, 2015). Another by-product of neural metabolism is heat, and functional hyperemia helps maintain a constant temperature [Zhu *et al.* 2006].

Although there is evidence of the consequences of functional hyperemia, can we infer that the decrease of oxygen initiates FH? Raichle and Mintun extensively discuss contradictory results which show that oxygen increases are not equivalent to the actual consumption or that the lack of oxygen in the air, and thus in the blood, does not modify functional hyperemia [Raichle & Mintun 2006]. These findings suggest that FH may not be driven by a demand for oxygen by the tissue, and thus does not have a feedback mechanism based on oxygen. Whether there is feedback through other mechanisms, such as CO₂ or lactate is still debated [Iadecola 2017].

Iadecola discusses other hypotheses I will not get into here, among which a possible effect of the vessels onto the neuronal activity, a so-called "vasculo-neuronal coupling" [Kim *et al.* 2016, Iadecola 2017].

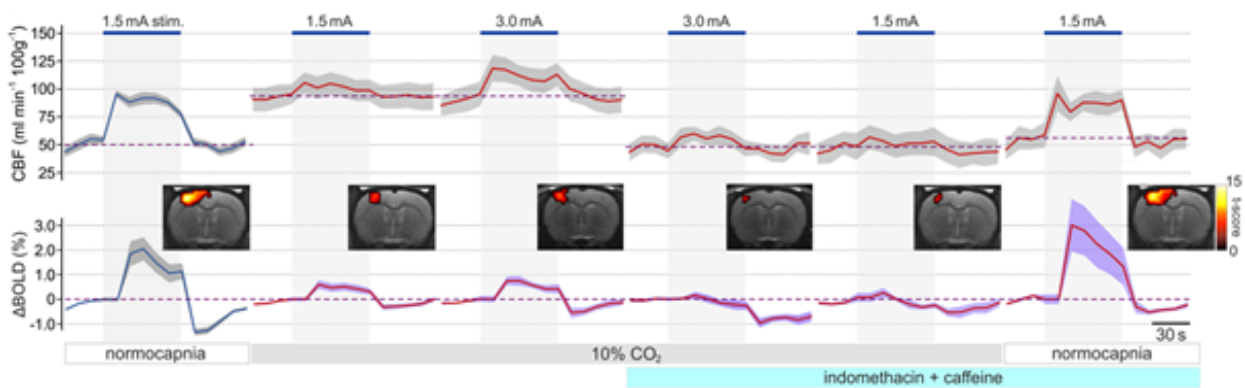


Figure 3.6: CO₂ acts on functional hyperemia.

Cerebral blood flow, through ASL, and BOLD responses are recorded while applying electrical stimuli to the mouse forepaw. Stimulus application is shown by the shaded grey areas. CO₂ application dilates vessels, which raises the CBF baseline level while reducing functional hyperemia. Intravenous injection of indomethacin and caffeine returns CBF to its baseline level and further cancels functional hyperemia. To be noted in this study is use of wide-scale vascular imaging rather than microscopic measurements of the induced effects, and the fact that CO₂ inhibits neuronal response (not shown here) forcing authors to double their stimulus strength. Overall, this result suffers from flaws which need further exploration, especially regarding the effect on neuronal activity and what happens at a microscopic level in the vasculature. From [Hosford *et al.* 2021].

3.3 Modeling the neurovascular coupling

Neurovascular coupling is a complex cascade of reactions, with interactions between many cellular and molecular actors [Attwell *et al.* 2010, Andreone *et al.* 2015, Iadecola 2017]. Getting a grasp of its overall function or understanding the precise involvement of a given actor is tricky. Modelization is a valuable tool to overcome these difficulties, and I will shortly review it in this part. I distinguish and describe three ways of modeling the neurovascular coupling, and I will give a few examples of the insights they provided. Note that some studies actually mix these types into their model. Obviously, none of them is perfect and each of them present various limitations. I do not dive into the details of all these models, e.g. I do not describe the equations underlying them, as this would be out of the scope of this introduction. A good review of the NVC modelization in the microvasculature can be found in the second part of Franca Schmid's PhD thesis introduction [Schmid 2017]. Another interesting review is from Huneau and colleagues, who go deeper into neurovascular models used in humans [Huneau *et al.* 2015].

3.3.1 Physical representation of a vascular network

The most obvious, though not the simplest, way to model NVC is to reproduce how it is at the macroscale. Such a model will describe connections between vessels, define diameters for them, introduce known fluid dynamics equations to model the flow inside, etc. The more they fit reality, the more one can expect them to faithfully predict biological behavior. However, describing reality supposes to know every single actor of the phenomenon and how all actors interact, which is

impossible to this day. This is a major limitation. As I will describe below, models usually describe physical changes in the vessel shape, e.g. dilation, or in the blood characteristics, e.g. hematocrit.

Our team described such a model in a previous work [Rungta *et al.* 2018]. The main result of this study was about the backpropagation of the vascular signal through the vascular arbor, and about the dilation dynamics of the different vascular compartments, i.e. pial, 1st and 2nd functional unit of arterioles and capillaries. Modelization, based on experimental data, allowed for the extrapolation of the results to situations we did not measure experimentally. By interacting with the model, we showed that active dilations of the upstream compartments can explain the increase of blood flow, which can passively dilate small capillaries, an effect that further contributes to a decrease of vascular resistance. This underlines that even the smallest change in capillary diameter is enough to ease blood flow changes [Blinder *et al.* 2013, Gould *et al.* 2016, Epp *et al.* 2020].

An interesting corpus of work in this domain is made by the publications of Franca Schmid and colleagues. They developed a model where both interconnected vessels and red blood cells are represented by the hematocrit (Figure 3.7), allowing for precise flow measurements and avoiding the pitfall of the interdependence between the flow and the RBC distribution. Amongst other things, they show that capillary dilation can alter the distribution of the RBC, namely the density of RBC, rather than the flow. The current paradigm focuses mainly on the RBCs flow, i.e. the number of RBC per unit of time, and we tend to forget the impact of RBCs density changes ; i.e. the number of RBC per unit of distance, on energy supply [Schmid *et al.* 2015]. Their work is based on experimental measurements done in the somatosensory cortex of the mouse. In the rat olfactory bulb, we found that the linear density varied in only 25% of non-dilating capillaries upon odor stimulation. Interestingly, I have contradictory experimental results in the mouse olfactory bulb, where RBC density seldom changes in capillaries after a nearby neuronal activation. Figure 3.8 shows some acquisitions I have made, where the density is constant, although in some cases it can quickly vary around the stimulus time. More recently, the same team showed that capillary dilation is paramount to a localized functional hyperemia [Epp *et al.* 2020]. As could be expected by the important vascularization radius for a given penetrating arteriole [Shih *et al.* 2015], if there is only arteriolar dilation the increase in blood flow would be spatially non-specific .

To be noted is that modeling vessels through their physical characteristics suffers a major flaw: the measurement of these characteristics. As stated above, even the tiniest change of capillary diameter can induce major changes in flow. Thus, the model parameters have to be very close to reality to allow for extrapolation to biology. Yet, to this day, it is cumbersome to get good measurements of vessel diameters in depth *in vivo*, as light scattering limits the application of models to real vascular arbors.

3.3.2 Effect of a single actor

The second category of models I would like to introduce are those focusing on a single actor of the NVC. Based on known physical interactions and effects, these models will explore how a single actor, a molecule for instance, will act on functional hyperemia. These models have to account precisely for the interactions between the actor and the overall studied mechanism to draw pertinent conclusions. The ability to predict known effects *in silico* is the only marker of the pertinence of the model. It allows for the exploration of experimentally difficult biological measurements as I

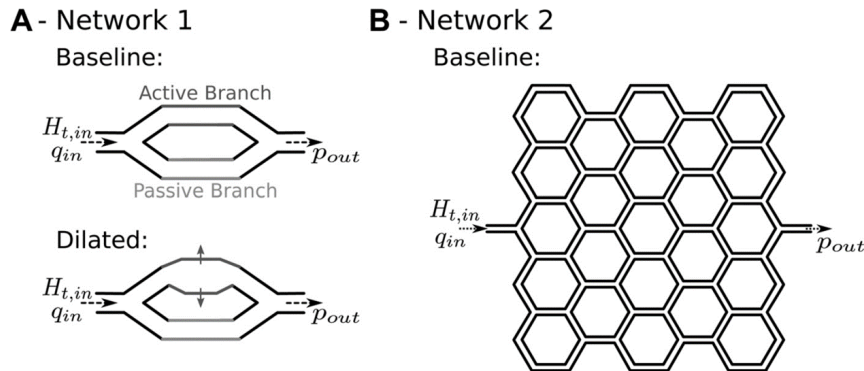


Figure 3.7: Artificial vascular networks.

Panels show two types of artificial vascular network which allow to study hematocrit (H), flow (q) and pressure (p).

A. This is a two-branch capillary with one branch actively dilating.

B. This one is called "honeycomb network", and comprises many two-branch networks.

From [Schmid *et al.* 2015].

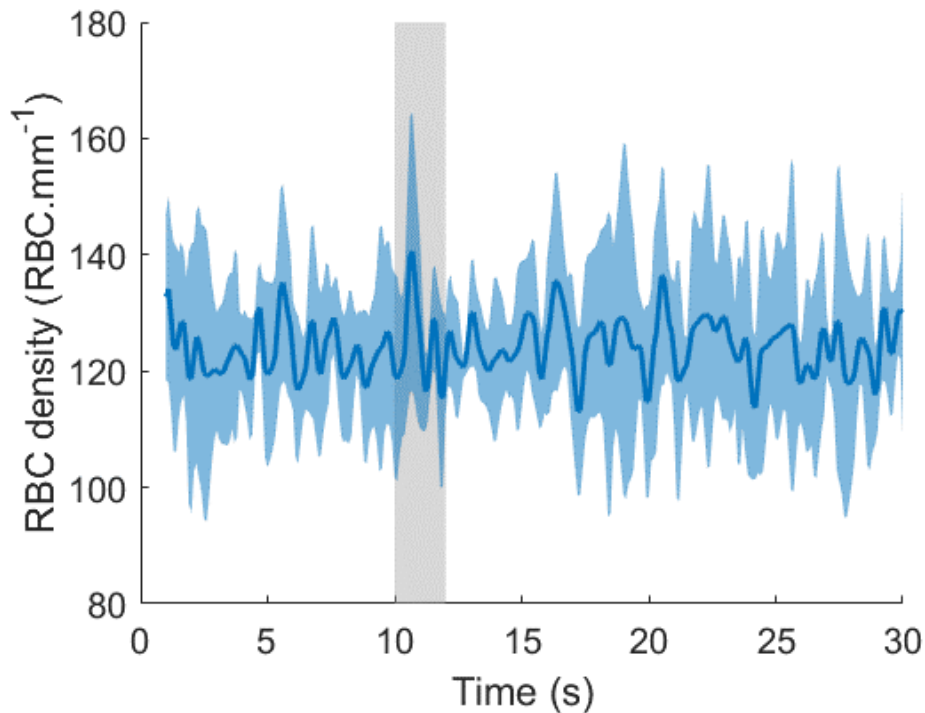


Figure 3.8: RBC density does not change upon functional hyperemia in the mouse olfactory bulb. Red blood cell density is measured as the division of the the RBC flow by the RBC velocity in a capillary nearby neuronal activation ($n = 4$ acquisitions, mean \pm SD). Both are measured instantaneously. Odorant stimulus (ET 6%, 2 s) is applied at 10 second (shaded area).

will describe below.

Nitric oxide (NO) is a well-known actor of NVC [Dirnagl *et al.* 1993, Iadecola *et al.* 1993, Stefanovic *et al.* 2006, Attwell *et al.* 2010, Iadecola 2017]. However, it has different origins, either neuronal or endothelial [Alderton *et al.* 2001, Forstermann & Munzel 2006]) and many synthesis pathways [Knowles & Moncada 1994]. Moreover, it has numerous interactions with the vasculature, eliciting dilation [Furchgott & Zawadzki 1980] or even with neurons [Lancaster 1994, Kim *et al.* 2016]. Given all these interactions, the interdependency between each actor, and the various metabolic parameters underlying each interaction, simulations are perfectly suited to try and make sense of the effects of NO. One study simulated the release of NO around arterioles and studied how its increase and decrease, considering washout by the blood flow, impacts vascular reactions. The authors showed that NO dynamic can explain the presence of the undershoot in functional hyperemia, the decrease in blood flow following the increase, and also be responsible for vasomotion in resting state [Haselden *et al.* 2020]. Of course, these findings require empirical evidence, through optogenetic control of NOS enzymes for instance, but these studies give important insights on interactions and effects we can hardly imagine on our own.

A recent study focused on oxygen availability after showing that the hippocampus has lower increases in blood flow following neuronal activations, coupled with a reduced capillary density, compared to the visual cortex V1. Modeling the characteristics of the hippocampal network and the oxygen diffusion, they show that oxygen concentrations in the tissue are much lower upon consumption, compared to V1 [Shaw *et al.* 2021]. These findings help understand how some brain areas can be more sensitive to hypoxia or be damaged early in neurodegenerative diseases.

3.3.3 Holistic approach

The main tool of this approach is the transfer function (TF). A transfer function is a function of time or frequency that models the output of a given system given an input via the convolution operation (Figure 3.9) [Dijk 2013]. In other words, given a time serie of neuronal activation, the transfer function representing the NVC can theoretically predict the blood flow response². I used “holistic approach” as the TF comprises all mechanisms between the input and the output and merges them all into a single representation: a mathematical function. Both the advantages and limitations of this approach are many.

Let NVC be our unknown system. We can devise many inputs, although all from neurons, and many outputs, at the vascular level. One can study the TF between the spike rate and the blood flow, or between the neuronal Ca^{2+} measured by GCaMP6f (see section 3.4.1) and the blood oxygenation, measured with a dye. Each of these TFs may be different, while they all represent a step of the NVC path. This makes the comparison of TF across studies quite difficult, as well as their interpretation. Their computation can also be tricky, as I will describe in the second part of the results. Once computed, using a TF implies important assumptions. A given TF cannot be simply extrapolated to signals with different sources, as described above with GCaMP and the spike rate. Moreover, the main assumption when using TF as a biologist is that the studied system is linear time-invariant. Linear invariant means that for an input multiplied by 2, the output is

²In other other words, for a neuronal activation shaped like a Dirac function, the blood flow will have the shape of the TF. This is why the TF is also named “impulse response”.

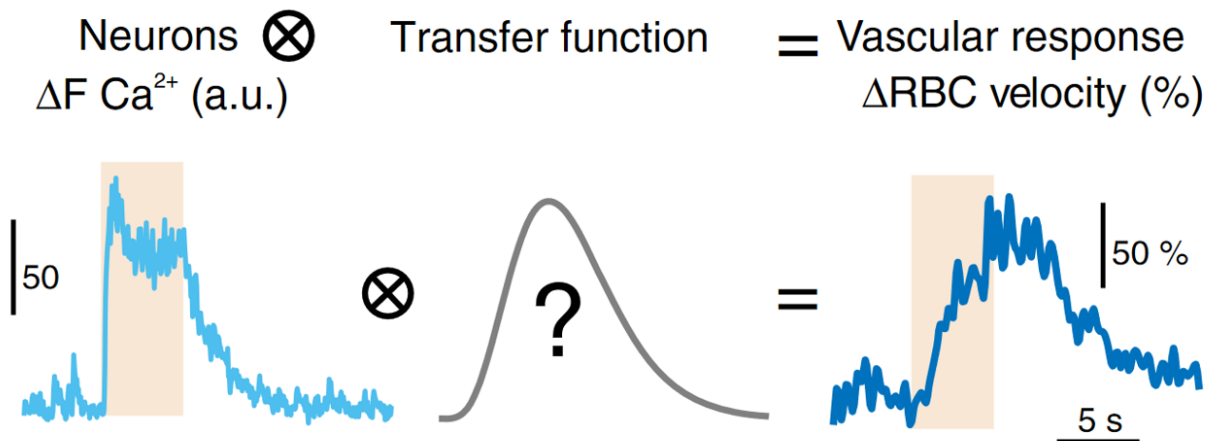


Figure 3.9: A TF representing the NVC.

The transfer function represents the dynamic relationship between two signals. Here, by using neuronal activation as input and red blood cell velocity as output, we model functional hyperemia. From [Aydin *et al.* 2020]

scaled likewise, e.g. there is no adaptation mechanism. Time invariance means that the system does not change between any two given timepoints, e.g. the brain state is identical. These are major assumptions, and they put constraints both on the experimental setup and on the animal model used.

However, a TF also has important advantages. It captures the complex dynamics of a system into the simple form of a time-dependent function, and it is a valuable tool to interpret the system dynamic. Regarding NVC it has been used for a few decades now, mainly for interpreting the output from BOLD-fMRI [Silva *et al.* 2007, Hirano *et al.* 2011]. Indeed, its obvious use is to find back the neuronal activation which generated the vascular signal measured with BOLD-fMRI. I will discuss the specific TF used in BOLD studies in the next chapter.

Our first work mainly relies on the use of a transfer function to study NVC and the output of functional ultrasound (see chapter 7), so I will quickly review some interesting results from previous works here to introduce how I used it for my research. A burning question in our field, is how NVC varies across brain states, mainly resting state and stimulus-evoked activity or across stimulus types, natural stimulus, i.e. what the mouse may feel in its environment, or forced, i.e. experimental stimuli that seldom represent the reality of everyday sensory stimuli. A recent study computed the TFs between electrophysiological recordings in resting state, whisker stimulation or volitional whisking, and blood volume changes measured with intrinsic optical imaging, in the mouse somatosensory cortex [Winder *et al.* 2017]. They show that the dynamic of the TF is similar between these 3 states (Figure 3.10A) and that they can reliably predict the neuronal activation from the cerebral blood volume (CBV) changes in stimulus-evoked cases. To be noted is that due to the high noise level of biological data, prediction of the neuronal activation requires averaging of vascular responses. And since averaging requires time-locking between onset of stimuli, they have not been able to predict resting state activity. Moreover, they also show that CBV variations during resting state is partially conserved while pharmacologically inhibiting neuronal activity

(Figure 3.10B). This last result shows that the NVC system is not a simple linear-invariant system, as the vascular output does not scale down to zero with the neuronal activation.

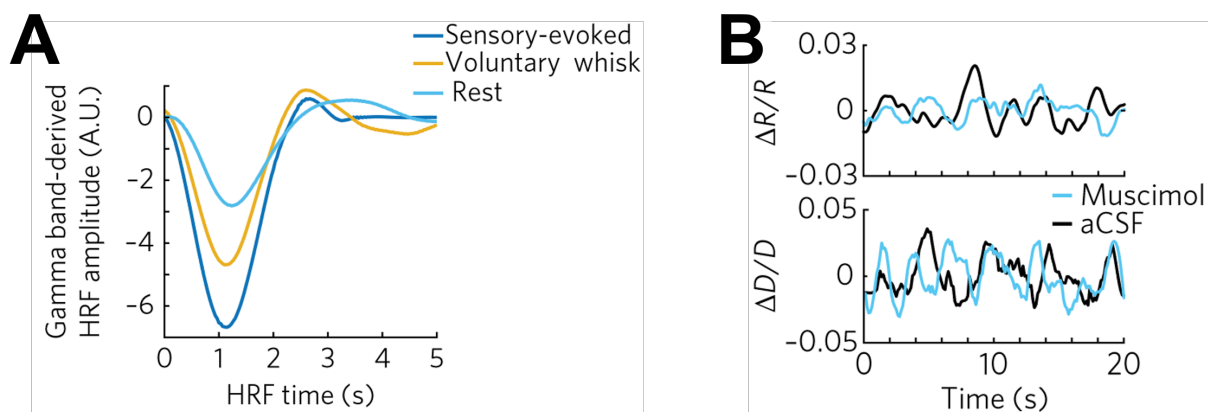


Figure 3.10: Holistic model of NVC shows that functional hyperemia dynamic is conserved across neuronal activation ways.

A. A transfer function (HRF) is computed between neuronal activation, as measured by the Gamma-band in LFP, and vascular reaction, measured as total hemoglobin with IOS. The HRF dynamic across neuronal activation types is alike.

B. Either Muscimol, to inhibit neuronal activity, or aCSF, as control, is applied over the brain. (top) Total hemoglobin shows cyclic variations in both states, (bottom) as does the diameter of a pial artery at the surface of the brain.

From [Winder *et al.* 2017].

Another important question in the NVC field is how neuronal activity influences veins, as the main belief is that they react solely passively to blood flow changes up in the vascular arbour. As I describe in the BOLD-fMRI part (see section 4.2), BOLD-fMRI relies on signals coming mainly from the veins [Kim & Ogawa 2012]. However, there is little literature on veins contributions to NVC, whether it be passive or active. In their study, Huo and colleagues model the spatial and temporal dynamics of both arteries and veins dilations, measured in two-photon microscopy, in response to locomotion-induced neuronal activation using TFs. Afterwards, they show that Intrinsic optical imaging (IOS) response to these same stimuli, at a much greater scale, can be predicted as the sum of the fast arterial response and the slow venous response [Huo *et al.* 2015]. Unbiased interpretation of IOS signals thus requires to take into account the venous contribution. They also show that the venous signal is spatially larger than the arterial one, underlying the importance of focusing on the spatial dynamics of vascular responses [Gardner 2010].

In this part, I reviewed the different ways to model NVC which I separated into three different types: the physical representation of the vascularization at the macroscale, the modelization of a single actor and the holistic approach. Each one has its own limitations, but all of them bring important insights into the function and mechanism of NVC. I will get back to modeling the NVC with TF in the next chapter, which is also important for the analysis of BOLD-fMRI data.

3.4 Measuring the neurovascular coupling in two-photon microscopy

Studying neurovascular coupling is a tedious task since it comprises not only the neuronal OR the vascular field but both, at the same time. Of course, depending on the scientific question, the experimental design does not necessarily involve measuring both. As an example, the paper on the TRPA1 channel in ECs and their involvement in the retrograde transmission did not report any kind of neuronal activity [Thakore *et al.* 2021], nor did one of the seminal papers on the pericytes role in NVC [Hall *et al.* 2014].

In my case, it was necessary to measure both, and simultaneously as much as possible. The first project was about modeling NVC and checking whether it is linear: only acquiring from the blood vessels would mean to suppose neuronal activation to be constant, both across animals and across stimuli. The next one was about the oxygen “initial dip”, supposedly reporting local neural consumption of oxygen. Measuring neural activation was mandatory in both studies.

From a historical perspective, one of our team’s work underlines in its introduction that “studies have generally assumed that the vascular compartment that regulates blood flow is controlled by the local activation of neurons but have failed to locate the precise site of neuronal activation in their in vivo preparations” [Rungta *et al.* 2018]: neglecting the spatio-temporal characteristics of neuronal activation may have led the scientific community to lose quite some time³.

3.4.1 Neuronal changes

Neuronal activation has multiple meanings. Canonically, one would think of it as the generation of an action potential, following a depolarisation which eventually goes over the cell voltage threshold. These changes in membrane potential are due to a net inflow of positive ions, mainly Na^+ and Ca^{2+} through neurotransmitter-dependent ion channels. However, they do not always trigger an action potential, as the membrane potential can stay below the threshold in the soma. Thus, dendritic potential changes do not necessarily reflect the axonal output.

While studying neurovascular coupling, do we want to focus on pre- or on postsynaptic potential changes? First, as explained above, vascular density seems to be related to the synaptic density, rather than the somatic one. Second, previous studies have shown that functional hyperemia better correlates with Local field potential (LFP) [Logothetis *et al.* 2001], i.e. subthreshold variations of neuronal membrane potentials. These results point out to the fact that postsynaptic changes are more related to functional hyperemia than presynaptic ones.

Thus we need an indicator of neuronal activation that can faithfully report dendritic potential changes. We do have other requirements that will reduce our choices. Our model is based on chronically implanted mice, as acute preparations are known to impair neurovascular coupling [Gao *et al.* 2017]. Mice are implanted with a cranial window over the bulb [Rungta *et al.* 2017, Boido *et al.* 2019, Roche *et al.* 2019, Aydin *et al.* 2020] because we also need to make simultaneous microscopic vascular measurements. As I will describe below, microscopic

³It would not be fair not to precise that our model, the olfactory bulb, is superior in that aspect, as one can control very easily the neuronal activation induced by natural stimuli. I discuss it further in the corresponding Chapter.

vascular measurements are best achieved through light microscopy, which requires a transparent window for precise measurements.

To precisely measure local changes in neuronal activation, we have two possibilities: taking advantage of intrinsic or extrinsic optical indicators, visually accessible through the window, or using electrophysiological recordings.

Extracellular measurements are achieved by means of an electrode which is placed in the brain parenchyma (Figure 3.11) [Souza *et al.* 2019]. This electrode measures both action potentials and postsynaptic potentials. However, surgeries and implants are inflammation triggering procedures, which are known to act on both microglia [Hirbec *et al.* 2019] and neurovascular coupling [Brezzo *et al.* 2020]. In our case, placing an electrode through the window and targeting it to a specific glomerulus would have been extremely difficult and we decided to focus on calcium signals to report neuronal activity.

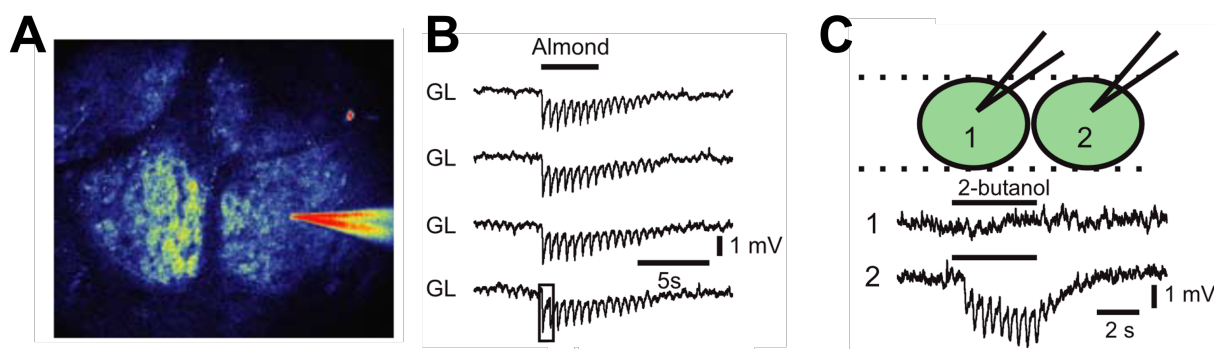


Figure 3.11: An electrode placed in the brain parenchyma can measure neuronal responses through local field potential changes.

A. Two-photon imaging of an electrode, filled with Oregon-Green, placed in a glomerulus of a mouse olfactory bulb.

B. Upon odor application, LFP responses are measured with the electrode. Each response is a single acquisition, neuronal responses in the glomerular layer are very reproducible and time-locked with the respiration.

C. Placing the electrode in two different glomeruli shows that each one responds differently to a given odor.

Adapted from [Chaigneau *et al.* 2007]

Regarding our studies, we had to be able to measure the activity over the whole bulb, which makes optical indicators more suited. They are easily operable through a transparent window, as long as measurements are done not too deep, since two-photon imaging allows for up to hundreds of μm depth imaging before light scattering impairs acquisitions. Note that this depth depends on the wavelength used, as longer wavelengths scatter less than shorter ones. In our case, the glomerular layer of the olfactory bulb is around 60 μm deep (see chapter 5). There are many types of optical indicators, either genetically-encoded or injected before and, either voltage-dependent or ion-specific. Below, I will quickly describe GCaMP and especially GCaMP6f which we used to report neuronal activation.

Genetically encoded calcium indicators have become increasingly used since their first introduction in 2001 [Nakai *et al.* 2001, Lin & Schnitzer 2016, Masatoshi 2020]. GCaMP is one of these, composed of Calmodulin (CaM), a Ca^{2+} -binding protein, and Green fluorescent protein (GFP). Upon Ca^{2+} binding to CaM, GFP changes its conformation and starts emitting fluorescence upon illumination with specific wavelengths. Further studies optimized GCaMP, until the GCaMP6 [Chen *et al.* 2013] that we used, and most recently jGCaMP8 [Zhang *et al.* 2020]. Each subsequent version improved either the signal-to-noise ratio, or the sensitivity and the dynamic range of detection, eventually all these features.

Genetically encoded calcium indicators can be expressed either in transgenic mice or after the injection of a viral transgene. Regarding the work exposed in this thesis, I exclusively used transgenic mice expressing GCaMP6f under control of the Thy1 promoter, and more specifically the Thy1-GCaMP6 5.11 lineage described in [Dana *et al.* 2014]. These mice express GCaMP6f in mitral cells of the olfactory bulb (Figure 3.12), which is perfect to measure calcium changes in the glomerular layer which contains mitral cell dendritic tufts. Notably, some transgenic lines of GCaMP mice have shown to have aberrant neuronal activity, but our mice genotype is not reported in this study [Steinmetz *et al.* 2017].

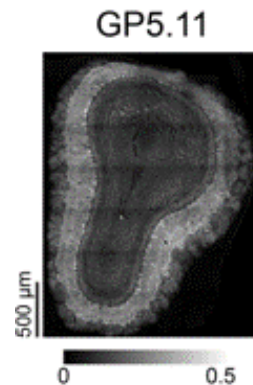


Figure 3.12: Coronal slice of our GCaMP6-expressing model of OB.

Confocal image of fixed coronal sections of the olfactory bulb, using a GFP filter. Labeled cells are mitral cells, they express GCaMP6f from the mitral layer (soma) up to the glomerular layer (dendrites). From [Dana *et al.* 2014].

Overall, GCaMP6 is a complex proxy of neuronal activation, which measures Ca^{2+} changes associated with neuronal depolarisation, firing and second messengers. It is efficient but also imperfect as additional limitations linked to photomultiplier tubes and electronics need to be considered.

3.4.2 Vascular changes

As with neuronal activity, there are multiple ways to measure vascular activity. Microscopic measurements allow single-capillary measurement of the vessel diameter or the velocity of single red blood cells. At a mesoscopic scale, intrinsic optical imaging can report hemoglobin-related changes, since oxygenated or deoxygenated hemoglobin does not reflect light in the same way. At a bigger scale, BOLD-fMRI and functional ultrasound are available, the next chapter describes them in detail.

Here I focus on microscopic measurements of vascular changes, something I had to do for each experimental study of this thesis. These measurements required the intravenous injection of several dyes, either fluorescent or a phosphorescent, and which labelled the plasma. Inside a capillary, RBCs are forced to pass through one by one, which creates a “black and white” pattern since RBCs do not uptake the dye (Figure 3.13). In two-photon microscopy, scanning a broken line repeatedly inside the capillary and outside in the neuropil allow measurements of RBC velocity and neuronal activity. Part of the time-image scanned through the vessel is used to measure the RBC shadow angle which directly reports blood speed [Dirnagl *et al.* 1992, Kleinfeld *et al.* 1998, Chaigneau *et al.* 2003]. The part of the line scanning the parenchyma of GCaMP expressing mice is used to detect the Ca^{2+} signal from neurons.

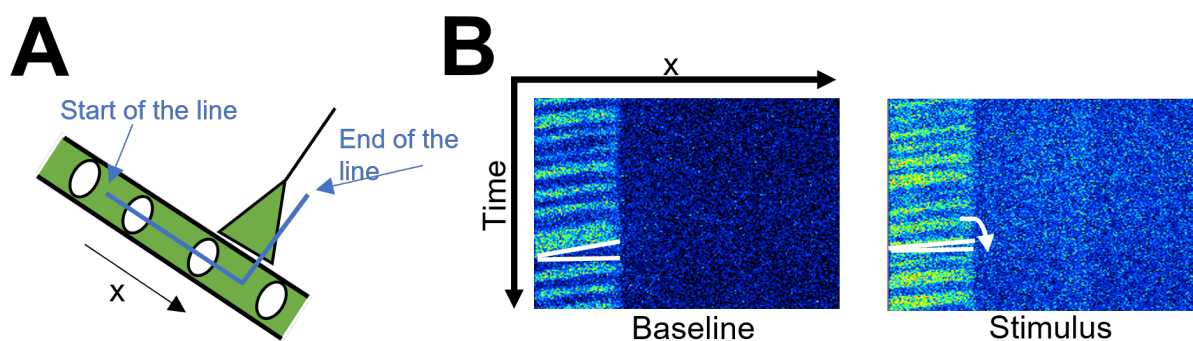


Figure 3.13: Simultaneous RBC velocity and Ca^{2+} measurement with linescan acquisition.

A. Schematic of the linescan acquisition. The vessel is filled FITC, fluorescein in green, and the parenchyma contains GCaMP-expressing neurons.

B. Scanning the line (x) over time creates shadow-patterns in the vessel part of the line. Left panel is part of the baseline, right panel is during the stimulus. The number of RBCs (shadows) increased, their angle decreased showing an increase in velocity. The right part of the line shows an increase in fluorescence, due to Ca^{2+} increasing in the neurons.

One way of measuring the flow of RBC, that is the number of RBC passing by per unit of time, is by determining the number of shadows. However, this requires an acquisition with a high signal-to-noise ratio, to get a perfect binarization of the shadows over the plasma. Experimentally, another way to measure the flow is to scan over a single point in the vessel, during Po_2 measurements. This will create a multiple boxcar-like signal, with the up state being plasma and the down-state being RBC (Figure 3.14). The Signal-to-noise ratio (SNR) is better as more points are scanned for a single RBC, which allows for a better binarization. However, in theory, this technique does not provide the user with both calcium and vascular measurements, simultaneously, as the scanned point is in the vessel. In practice, given a point-spread function z-projection bigger than the vessel diameter, changes in fluorescence above and below the vessel can be extracted. Further details about this are given in the third article of this manuscript (see chapter 9).

The last point I want to explore here is oxygen measurements. At a microscopic scale, the first techniques used Clark electrodes. This approach reports absolute values of partial pressure in oxygen (Po_2) with great spatial resolution and SNR. However, as with neuronal activity, they are not able to measure Po_2 at various locations. A few years ago, a phosphorescent

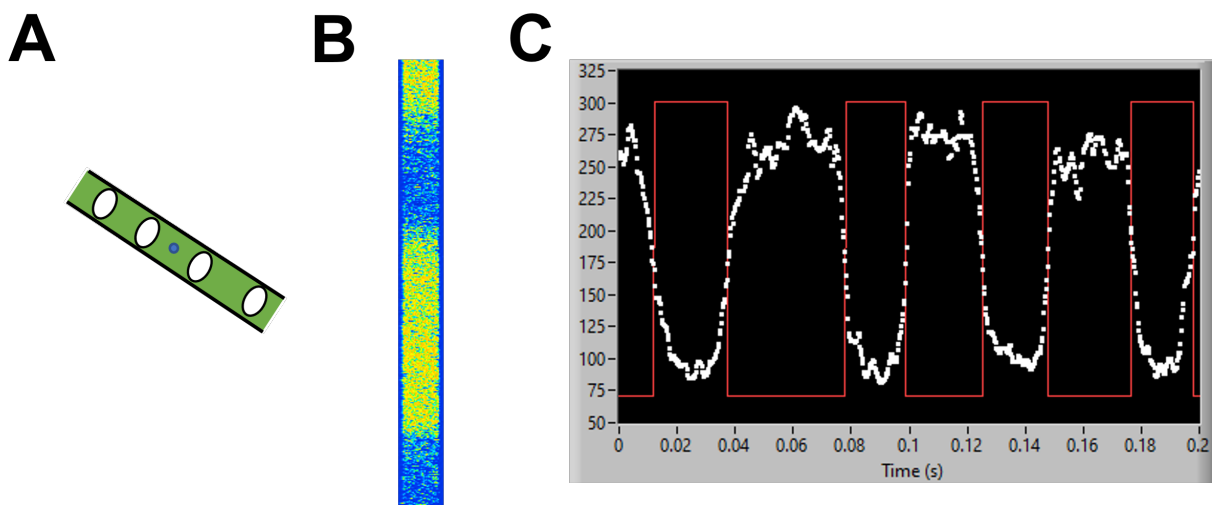


Figure 3.14: Measuring RBC flow with a pointscan acquisition.

A. A point placed in a capillary (blue dot) is scanned over time.

B. Passing of RBC creates shadows since they do not uptake the fluorescent dye. Each horizontal line represents ≈ 25 μ s of fluorescence from the point, the next line is scanned after a rest period of ≈ 250 μ s. The image represents the first 100 ms of the panel C.

C. Averaging fluorescence (white points) from each line creates up and down states that can be turned into a suite of box-car functions (red line). Upstate of the red function means there is a RBC. 4 RBCs are counted for a period of 200 ms, which is a flow of $20 \text{ RBC}\cdot\text{s}^{-1}$.

probe was designed, whose decay time at a given temperature was specific of the absolute P_{O_2} [Sakadžić *et al.* 2010, Lecoq *et al.* 2011, Roche *et al.* 2019] and which was optimized to be used with two-photon excitation [Mik *et al.* 2004, Estrada *et al.* 2008]. By scanning over the same point, alternating illumination period, to reach the excited state of the phosphorescent molecule, and dark period, to record the decay, we can measure P_{O_2} changes over time (Figure 3.15A, B). The measured decay has to be fitted with an exponential decay function whose half-life can be translated into a P_{O_2} value in mmHg.

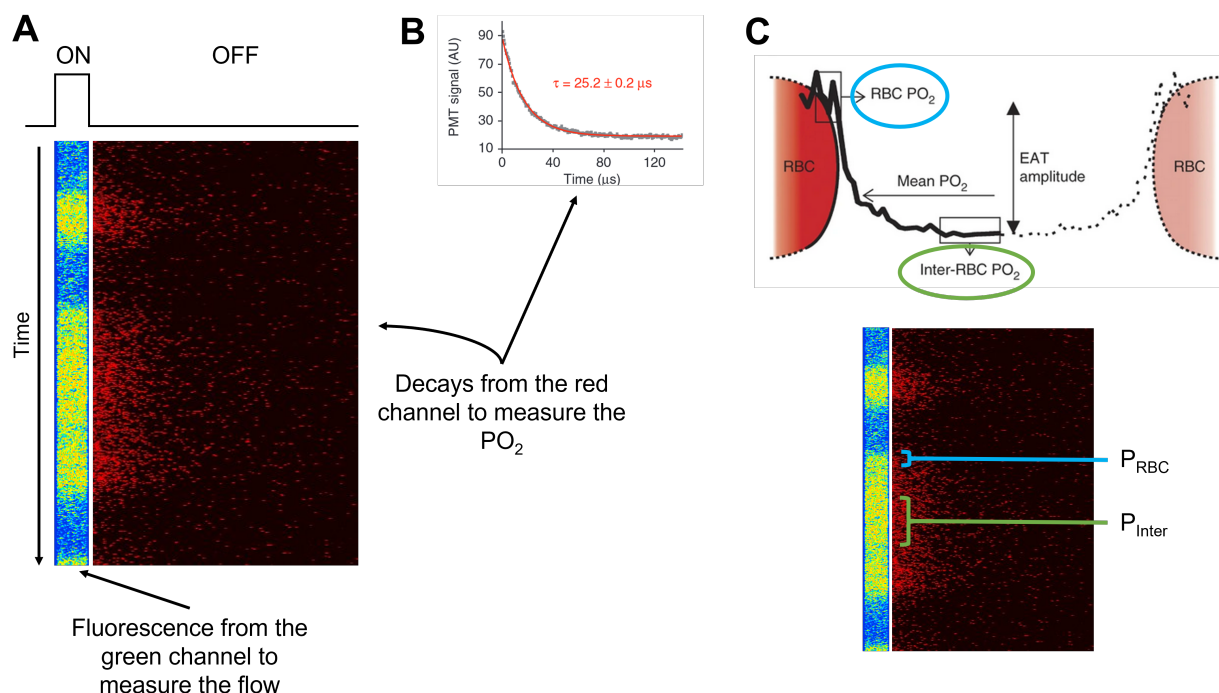


Figure 3.15: Measuring P_{O_2} from a pointscan acquisition in a capillary.

FITC and Oxyphor 2P are injected IV. FITC is used as a fluorophore to detect RBC and Oxyphor 2P is the phosphorescent probe whose decay depends on the partial pressure of O_2 .

A. Alternating illumination (ON) and rest (OFF) periods while collecting photons allows for simultaneous measurement of RBC flow in the green channel and P_{O_2} in the red channel.

B. Fitting the average of decays from the red channel computes a τ which values corresponds to a partial pressure of O_2 in the capillary.

C. Separating RBC from the plasma thanks to the green channel renders possible the computation of either the P_{O_2} around RBC or in between (Inter-RBC). The difference is called Erythrocyte-Associated Transient (EAT).

Having a good fit of the decay is crucial for a faithful measurement of the P_{O_2} , and hundreds of decays have to be averaged to make sure of the fit. Indeed, the first phosphorescent probe we used in the lab, PtP-C343 had a lower SNR than the one we are using now, Oxyphor 2P [Esipova *et al.* 2019]. The new probe allows for less laser power but also for a temporally more accurate measurement: since less decays have to be averaged, we can afford less fits per time unit. As of today, we usually average around 1000 decays to get a good evaluation of the P_{O_2} , which gives one point every 250 ms.

Remarkably, we can use point scan for both flow and Po_2 measurements. We do it by injecting both the phosphorescent Oxyphor 2P (red channel) and a fluorescent dye (green channel), as the SNR of the fluorescent dye is better for RBC detection. In my study, I used fluorescein (FITC), which emits green light to avoid polluting the red light emission of Oxyphor 2P. Notably, separating RBC from plasma while measuring Po_2 in a capillary allows for separating Po_2 around RBC from Po_2 in the plasma (Figure 3.15C). Namely, erythrocyte-associated transient (EAT) have first been modeled [Hellums 1977] and then experimentally demonstrated [Tsai *et al.* 2005, Golub & Pittman 2005, Parpaleix *et al.* 2013]. Thanks to this separation, our team previously reported that resting perivascular Po_2 in the tissue can be estimated by the plasmatic Po_2 in the capillaries of acute mice [Parpaleix *et al.* 2013].

3.5 Conclusion

Neurovascular coupling is the cascade of cellular and molecular reactions linking neuronal activation to the subsequent vascular one. Nearly every cellular type of the central nervous system appears to be implicated in functional hyperemia, the local increase in vascular flow following a neuronal activation. It has been studied for decades now, and our understanding of the topic is increasing. Notably, the development of models to get insights into the complex interactions underlying NVC and the new technical tools allowing non-invasive measurements in behaving animals will help continue in this way. Although its mechanism is far from being fully understood, it has been used for decades as the physiological basis for BOLD-fMRI interpretation, a vascular-based functional imaging technique, to determine activated brain areas. Together with Functional ultrasound (fUS), these techniques are the focus of the next chapter.

CHAPTER 4

FUNCTIONAL BRAIN IMAGING

One must guess the painter in order to understand the picture.

Friederich Nietzsche in
Schopenhauer as Educator, 1874

Contents

4.1	Imaging the brain	40
4.2	BOLD-fMRI	40
4.2.1	Physical principle	41
4.2.2	Analysis process	42
4.2.3	The hemodynamic response function	44
4.2.4	The initial dip: improving the spatial specificity of the vascular responses	46
4.2.4.1	What is the initial dip?	46
4.2.4.2	Does it really exist?	49
4.2.5	Conclusion	50
4.3	Functional Ultrafast Ultrasound	51
4.3.1	Physical principle	51
4.3.1.1	The Doppler effect	51
4.3.1.2	What if the object is a red blood cell?	52
4.3.1.3	The fUS setup	53
4.3.2	Analysis process: extracting a map from the echoes	53
4.3.3	Experimental considerations	56
4.3.3.1	Voxel size and spatial specificity	56
4.3.3.2	Heating the tissue	57

4.3.3.3	Vessel orientation	57
4.3.3.4	Impact of the surgical preparation	57
4.3.4	Results	58

4.1 Imaging the brain

The human brain is a conundrum, still to this day. The numerous interactions between neurons, between neurons and astrocytes, between neurons and vessels, between astrocytes and vessels makes its understanding an utopia at the moment. As researchers, we mainly focus on animal models to advance on the path of understanding. This allows us to measure neuronal activity precisely, with invasive techniques, and we genetically modify our model to test our hypotheses. For obvious ethical reasons, it is impossible to do so with a human subject. We shall thus rely on the conservation of the physiological mechanisms across the evolutionary tree to extrapolate our findings to ourselves, a concept which has been put to harm a few times now. I cited in the first chapter that the overall structure of the mammalian brain is conserved: this means that given a section of olfactory bulb, we could not differentiate whether it is from the mouse or from the human only by looking at the layer organization. However, at a smaller scale and from a functional perspective, things are much more complicated. Oberheim and colleagues reported anatomical and functional differences between astrocytes from mice and humans [Oberheim *et al.* 2009], and we know that astrocytes greatly interact with both neurons and vessels. More recently, an RNA-sequencing study of mouse and human brain slices showed that while there is a high homology between cell types, as anatomically defined, the expression of RNA widely differs, especially regarding neurotransmitters and ion receptors [Hodge *et al.* 2019]. This may easily explain why pharmacological preclinical studies hardly pass the clinical phase, with up to 90% of failure at this phase [Hingorani *et al.* 2019].

Validating in humans results acquired in animal models, is an essential part of the biomedical research process. How can we study the human brain function? The most popular technique to do so is BOLD-fMRI. This will be the subject of the first section. I will not get into all the other techniques, such as EEG, MEG or other fMRI modalities (Figure 4.1), since they are not directly linked to my work.

The second section is about a novel technique, functional ultrasound imaging, which we used in my first study. It shows promising applications both in fundamental research, clinical research and potentially at the patient bedside.

4.2 BOLD-fMRI

I do not present any BOLD-fMRI experiment in this thesis, although I did some for a side project. However BOLD-fMRI is a widely used technique in neuroscience and especially in the human, due to its non-invasive nature, and it solely relies on neurovascular coupling to be well interpreted. Moreover, my projects had some relationship with BOLD analysis. The first one studied one of the linearity assumptions of the HRF while the starting point of the last project was based on the hope of improving the spatial specificity of the signal.

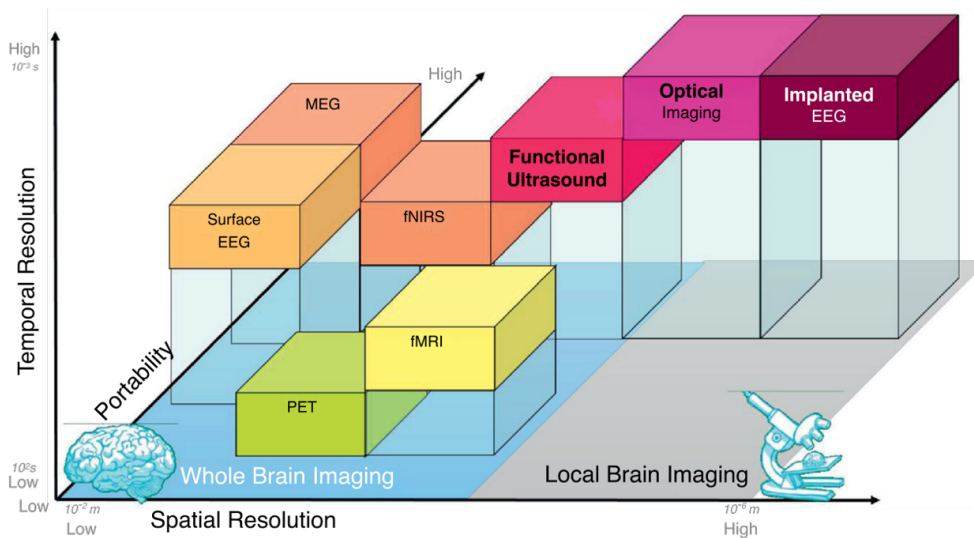


Figure 4.1: Main brain functional imaging techniques.

Imaging techniques are presented on account of their spatial resolution, temporal resolution and portability. From [Deffieux *et al.* 2018].

4.2.1 Physical principle

The blood oxygen level dependent (BOLD) signal is acquired through a nuclear magnetic resonance imaging (MRI)¹. Grossly, the MRI machine acts on subatomic particles in our body which are magnetic, i.e. dipoles, which are mainly protons from the hydrogen nucleus. The MRI scanner produces a constant and homogeneous electromagnetic field called B_0 , which sets the dipoles of the subject to a baseline state. Then, another electromagnetic field, B_1 , is applied transiently. B_1 “excites” the dipoles which will change their orientation. When B_1 disappears the dipoles get back to their original alignment as determined by B_0 , they “relax”, with different spatiotemporal characteristics depending on their surroundings. The MRI machine picks up these spatiotemporal characteristics by measuring the electrical signal produced by the movement of the magnetic dipoles returning to their baseline state. Upon excitation, multiple relaxation characteristics are measurable to get anatomical or functional maps of the brain. They are called T_1 , T_2 or T_2^* for the most famous ones. I don’t get into more details here, there are great reviews on the topic [Huettel *et al.* 2014].

The physical principle underlying the BOLD signal was discovered in 1990 by Ogawa and colleagues. In their seminal papers [Ogawa *et al.* 1990a, Ogawa & Lee 1990, Ogawa *et al.* 1990b], they show that the presence of deoxygenated hemoglobin alters the T_2 relaxation characteristic of nearby hydrogen nuclei. Indeed, deoxyhemoglobin (dHb) is paramagnetic as opposed to oxyhemoglobin (Hb). An increase in dHb, e.g. through neuronal oxygen consumption, will decrease the contrast by altering the relaxation characteristics of H^+ . Conversely, increased Hb increases T_2 relaxation time and results in better contrast. Functional hyperemia will reduce the relative quantity of dHb compared to Hb thus increasing the contrast and BOLD signal. In other words, in BOLD-fMRI imaging, the signal is related to the ratio $\frac{Hb}{dHb}$ rather than the absolute quantities of either one.

¹The N from “nuclear” is left out to avoid scaring patients off with radioactivity when talking about MRI exams.

Before going further into the analysis, let me define the terms related to the BOLD data. Putting a subject into the MRI and running a single recording of 5 min, for instance, will result in an acquisition. This acquisition is composed of voxels from a single slice of the brain, for simplicity here I only consider a single slice, but multiple sections can also be acquired with some eventual delay. These voxels are identical in size, sharing the same width, height and depth. Along the 5 min of the acquisition, the BOLD signal is recorded within each voxel. Overall, the raw BOLD data of a single brain slice, with a thickness equal to the voxel's depth, can be represented by a 3D matrix of size $m \times n \times t$, m being the number of voxels in the vertical axis, n the number of voxels in the horizontal axis, and t the number of samples acquired over time. Many acquisitions can be done sequentially, resulting in a session.

4.2.2 Analysis process

Quite obviously, the interpretation of BOLD data supposes a thorough understanding of functional hyperemia spatial and temporal dynamics, which we do not yet have at this time in humans [Iadecola 2017, Kaplan *et al.* 2020]. Moreover, we are aware that hemodynamic changes are not solely consequences of neural activation, as explained in the previous chapter. These caveats are known limitations for the interpretation of BOLD functional imaging. The following section will quickly describe the most used way of analyzing BOLD data to extract neurally activated areas: the General Linear Model (GLM). It relies on a holistic model of neurovascular coupling, and the following sections will underline the impact of the studies I conducted during this PhD. Of course, there are multiple ways to analyze BOLD-fMRI data, with the main ones being described in [Soares *et al.* 2016]. Regarding GLM, a critical review of the method is found in [Monti 2011].

The point of any type of BOLD acquisition analysis is to output which voxels are active, i.e. contains neuronal activation, and what the temporal dynamic of the activation is. Conventionally, activation is determined by a statistically significant correlation between a pattern of stimulation and a post-processed BOLD signal. This definition raises two questions: why do we need to do a correlation analysis, instead of just looking at the actual signal? Why does the correlation have to be computed with a post-processed BOLD signal, rather than the raw one²?

Both these questions find their answer in the signal-to-noise ratio of the BOLD-fMRI. Figure 4.2 shows some BOLD-fMRI time series where we can hardly distinguish between noise and actual signal. GLM allows for compensating for various noise sources, notable confounding factors such as motion or heart rate [Soares *et al.* 2016]. Then, as described above, the absolute BOLD signal is only proportional to the $\frac{Hb}{dHb}$ ratio but does not inform on physiological values. Moreover, it has multiple variation sources and needs to be normalized across acquisitions, sessions and subjects [Poldrack *et al.* 2009]. It also needs temporal and spatial smoothing [Jezzard *et al.* 2001]. All in all, the raw BOLD signal cannot be used as it is, and requires pre-treatment before analysis. Then, this analysis is a statistical correlation to efficiently extract responses from the noise and have an objective threshold to distinguish whether a voxel is activated or not.

The GLM point is to explain the variations in the BOLD signal by fitting it with a linear sum of time-dependent regressors (Figure 4.3). The model is a sum of N_R " $X\beta$ " terms, with N_R being

²As a friend pointed out, the reasoning below is more "this because that" rather than "that therefore this", which can be tricky to follow. This is the way I found out about how it is done, and thus how I chose to write it down.

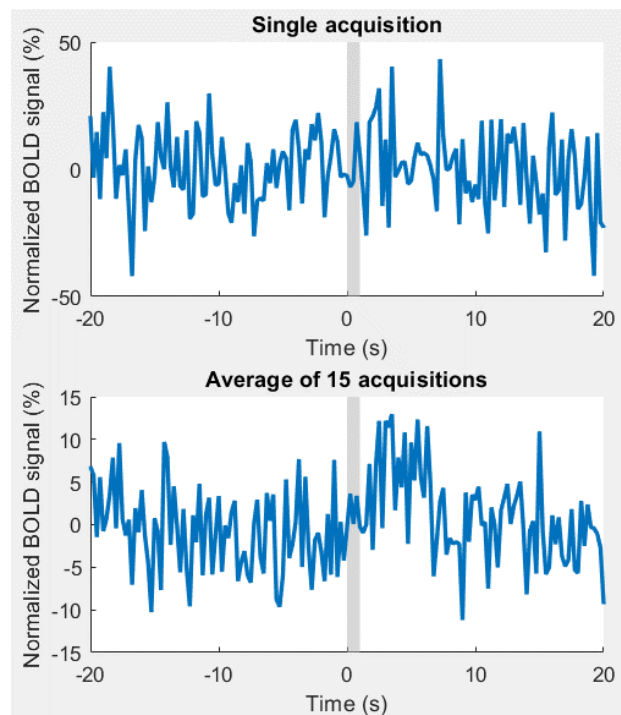


Figure 4.2: The BOLD has a very poor SNR.

The mouse received ET 6% for 1 s at $t = 0$ s while a BOLD acquisition was performed on the olfactory bulb. (top) Signal from a single voxel and a single acquisition that is above the significance threshold ($p < 0.05$). (bottom) Signal from the same voxel as above but averaged over 15 acquisitions. The response is barely visible.

the number of regressors, X being a vector of size $1 \times t$ representing one of the regressor and β the scaling factor of this regressor acting on the BOLD signal. Summed with an error term ε , the point is to fit the β factor of each regressor, for each voxel. The bigger the amplitude factor β of a given regressor, the bigger the influence this regressor supposedly have on the BOLD signal of the voxel. Thus, the GLM fits for each voxel a vector of size $1 \times N_R$ containing the β values of each regressor and a vector of size $1 \times t$ representing the error term ε over time. A review of the fitting methods can be found in [Waldorp 2009].

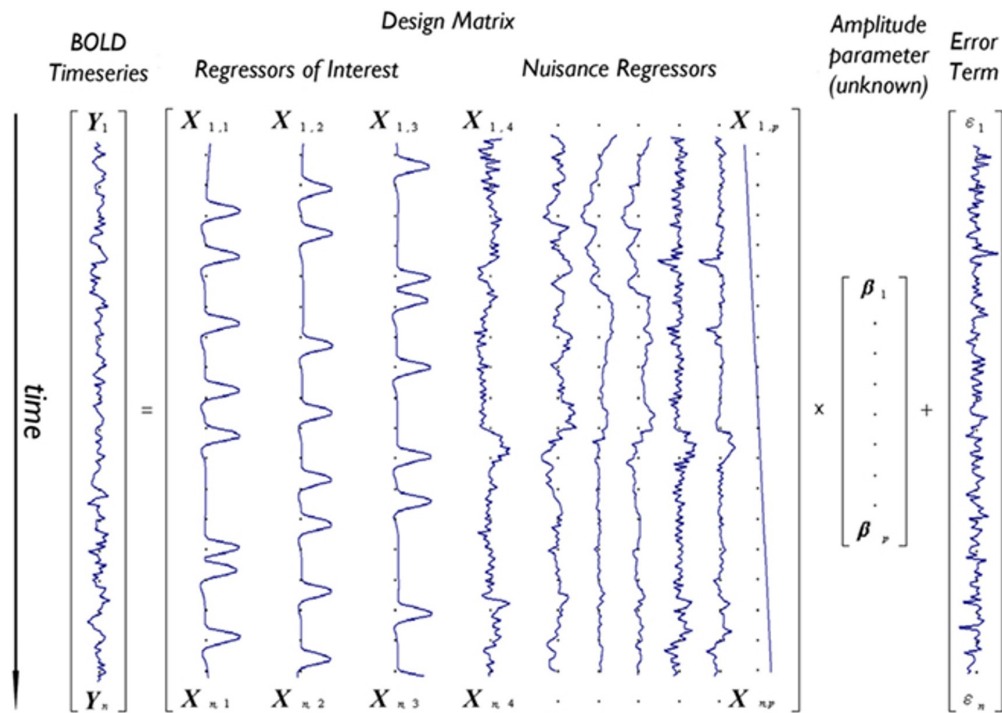


Figure 4.3: The GLM approach for BOLD analysis.

The BOLD signal from a single voxel (Y) is modeled as the sum of known regressors (X), among which regressors of interest such as the ones representing the stimuli (X_1 to X_3) and regressors of noise (X_1 to X_p), scaled with an unknown amplitude factor, and an error term. Fitting the amplitude factors for each regressor informs on the relative impact of the regressors on the BOLD signal. From [Monti 2011].

Whether a voxel is activated under a stimulus, i.e. a regressor of the fitting model, is then determined by the value of the β factor of this regressor. But how is the regressor defined at first, before even wondering about its β value? Here is where we get back to the holistic approach of neurovascular coupling modeling.

4.2.3 The hemodynamic response function

As explained above, the regressors represent external or internal factors, supposedly influencing the BOLD signal. The shape of regressor is user-defined and will obviously have an impact on the fitting of the β value. Consider we apply a visual stimulus to a subject and want to extract which voxels of the visual cortex are activated. We define two regressors, one for the visual stimulus and

another encompassing the artifacts we have been able to measure, e.g. the movements in different directions or the drift of the signal. To make sure that the β value of the visual regression is statistically significant and report the correct activation, one must have the correct regressor shape for this visual stimulus. This shape is the shape of the theoretical BOLD response to a visual stimulus in a voxel.

Somehow paradoxical or circular, detecting neuronal activity in the BOLD signal requires to know the shape of the neuronal activity eliciting the BOLD signal. One of the keys to get out of the circle is assuming that the neuronal BOLD signal is buried in the noise, and thus accepting that the only way to analyze is by having some idea of the shape of the response. One of the locks on the way out is that it is quite difficult to know exactly what shape it should have, I will get back to this later.

The regressor is computed as follows. The stimulus generates a neuronal activity, and by means of the neurovascular coupling, neuronal activation generates changes in blood flow which in turns changes the ratio $\frac{Hb}{dHb}$ and the BOLD signal. Since there is no way to precisely know the shape of the neuronal activation, the whole point of fMRI-BOLD being its non-invasiveness, one can only rely on the shape of the stimulus: canonically a square function (Figure 4.4). To improve the regressor shape, one still has to get from this square function to the expected BOLD response. This is done thanks to the hemodynamic response function (HRF) that I mentioned in the Chapter 2 (see section 3.3.3). Theoretically, it corresponds to the BOLD signal generated by a Dirac-shaped stimulus, i.e. an infinitely short in time stimulus. Convoluting this HRF with any kind of stimulus shape outputs the theoretical BOLD response.

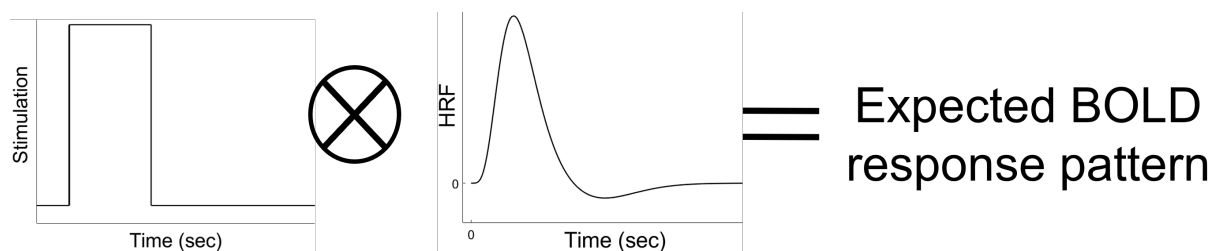


Figure 4.4: Schematic representation of the HRF use.

A square function goes up when the stimulus starts and down when it stops. When convoluted with the hemodynamic response function (HRF) it supposedly outputs the BOLD response measured in the activated voxels, allowing for a statistical comparison between the actual response and this expected response.

Many caveats underlie this reasoning. First and foremost, there is no linear relationship between the stimulus and the neuronal activation it generates, as shown by the habituation mechanisms. Since the HRF has a strict assumption of linearity, as any transfer function (TF), this non-linearity between stimulus and neuronal activation undermines the use of the HRF. Although very early studies in the BOLD history provided evidence that there is a linearity between stimulus characteristics, e.g. visual stimulus contrast, and the BOLD response [Boynton *et al.* 1996, Cohen 1997], we know that this assumption is wrong: neurons do not behave linearly and neither do vessels, as a modelization of their elastic characteristics showed [Buxton *et al.* 1998]. Monti clearly wrote in his review “it has now been extensively shown that there are at least two sources of non-linearities in the BOLD signal”, neurons and vessels. He

goes on by writing that these non-linearities are ignored by both the neurobiological and psychological BOLD literature [Wager *et al.* 2005, Monti 2011]. A few explanations may be given to this seemingly illogical behavior. A study showed that nonlinearities arise in the BOLD signal below a threshold of 4 seconds of stimulation [Robson *et al.* 1998, Vazquez & Noll 1998], but then again, the nonlinearities were only evaluated based on the BOLD signal without insights on neuronal activity. To avoid these non-linearity problems, a few methods were proposed [Friston *et al.* 1998, Friston *et al.* 2000, Calvisi *et al.* 2004, Monti 2011] but, as Monti puts it again, “most proposed solutions [...] require fitting of a large number of parameters which may cause severe degradation of power”.

The nonlinearities aside, the HRF raises questions too. Studies have shown that the HRF varies across individuals, brain regions and even days [Aguirre *et al.* 1998, H *et al.* 2004]. Using the same HRF makes the analyses prone to creating false positives or false negatives voxels [Lindquist *et al.* 2009].

Among the other caveats, which I do not describe in detail here, are the auto-correlation, which can affect the statistical significance of the activation tests [Friston *et al.* 1994, Boynton *et al.* 1996, Purdon & Weisskoff 1998]. Solutions have also been proposed as detailed in [Monti 2011].

The analysis pipeline I described here is limited to a single-subject analysis. To assess the robustness observed effects, group analysis is required. These analyses have requirements, such as the alignment of the anatomical structure. I do not go into these details here as they are not of significance for my studies.

4.2.4 The initial dip: improving the spatial specificity of the vascular responses

As I mentioned, functional hyperemia involves a larger brain volume than the neuronal activation that triggered it, due to dilation of the penetrating arteriole which irrigates tissue up to a 500 μm cylinder around the PA [Shih *et al.* 2015]. This problem has been known for quite some time, as D. Malonek & A. Grinvald wrote in 1996, “the vascular response is less localized [than the individual cortical columns], spreading over distances of 5 to 3 millimeters” upon sensory stimulus and intrinsic optical imaging of dHb and Hb [Malonek & Grinvald 1996]. Earlier, an IOS study reported what may be a solution to this problem and what eventually became an important controversy in the domain: the initial dip (ID) (Figure 4.5). Two extensive reviews interrogate the origin and existence of the initial dip [Hu & Yacoub 2012, Hong & Zafar 2018].

4.2.4.1 What is the initial dip?

The ID is a transient decrease in signal reported by several vascular-based techniques following a neuronal activation and preceding functional hyperemia. It has been first reported using intrinsic optical imaging [Frostig *et al.* 1990] and later BOLD-fMRI [Ernst & Hennig 1994]. The hypothesis was that this “signal drop during the early phase can be attributed to a temporary decrease in oxygenated hemoglobin concentration due to increased oxygen consumption”. In other words, neurons burn oxygen before functional hyperemia can compensate for it, and the ID is the burning that is measured. Malonek & Grinvald in their study [Malonek & Grinvald 1996] showed that an

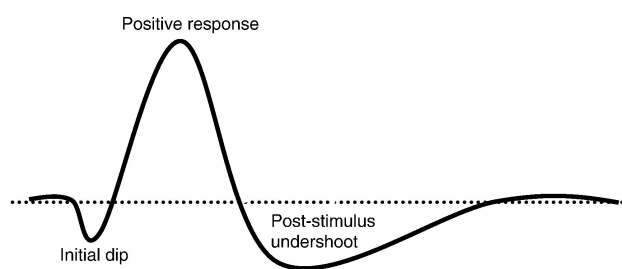


Figure 4.5: The initial dip in the HRF.

This curve is a version of the Hemodynamic Response Function, i.e. the BOLD response for a Dirac-like stimulus. The first part of the response is the initial dip, the transient decrease of signal supposedly originating from local oxygen consumption before functional hyperemia hits. I do not describe the post-stimulus undershoot here. From [Hu & Yacoub 2012].

increase of dHb occurs before the increase in Hb due to functional hyperemia, which confirmed the hypothesis from Ernst & Henig. Most importantly, they observed that the ID is spatially limited to the cortical columns, while functional hyperemia goes beyond it. This result was elegantly confirmed by Thompson and colleagues later on, using a Clark electrode in the visual cortex of a cat [Thompson *et al.* 2003]. They showed that the initial dip colocalizes with neuronal activation, in response to gratings with various angles. The ID appears when the angle activates the neurons and is not there otherwise. Functional hyperemia however is always measured, confirming its spatial non-specificity (Figure 4.6). It was further confirmed by other studies from the same team in the same structure [Thompson *et al.* 2004, Thompson *et al.* 2005].

The spatial specificity of the ID was assessed with intrinsic imaging or electrodes, but also with the BOLD signal. Menon and colleagues showed that voxels with an ID localize more in grey matter areas than the voxels showing a positive response, which were everywhere [Menon *et al.* 1995], however there was not any neuronal activity control and there is none to this day, showing a colocalization of neuronal activation and the ID in BOLD imaging, to my knowledge. Coherent with what we know of functional hyperemia, the dynamic of the ID is limited in time independently from stimulus duration [Hu *et al.* 1997]. Indeed, neurons can only activate and consume so much while functional hyperemia is less easily saturated and always occurs within the first seconds post-stimulus, making the ID necessarily short in time.

Our team performed a very elegant description of the initial dip in the olfactory bulb, thanks to the many advantages of this model regarding the study of neurovascular coupling (see section 5.4). In [Lecoq *et al.* 2009], we show that the ID is present in the glomeruli of the rat olfactory bulb. Moreover, we applied NBQX and D-AP5 and showed that the ID disappears in the neuropil upon inhibiting neuronal activation. This effect was reversible in under 10 min of washout. Later, we measured the ID in the olfactory bulb of the mouse with PtP-C343, the phosphorescent probe I described earlier (see section 3.4.2). We measured the transient decrease in oxygenation both in the tissue and in the capillaries (Figure 4.7) [Parpaleix *et al.* 2013]. This is an important difference to keep in mind: tissular oxygenation comes from the vessels, but tissue and vessels are not identical, in terms of oxygenation, as we measure a delay between the onset of the dip in the tissue and in the capillary. Indeed, the presence of the ID in the capillaries has never been shown before our

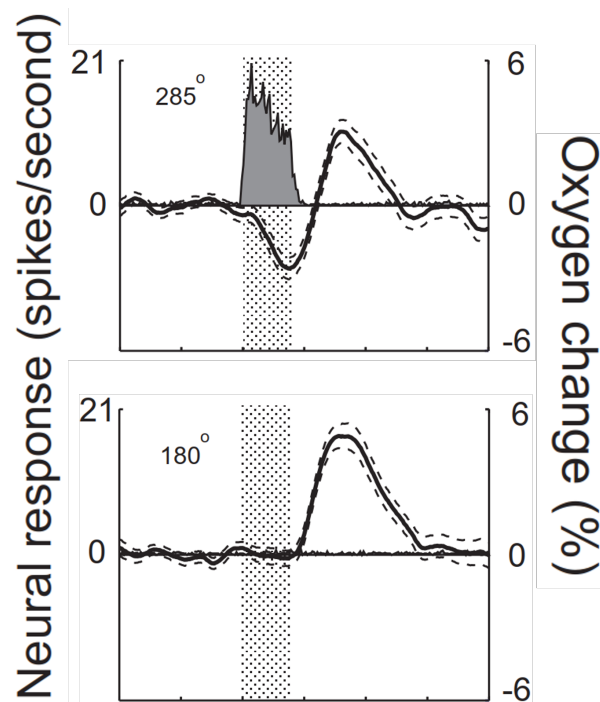


Figure 4.6: Measure of the initial dip in the visual cortex by Thompson and colleagues. An electrode is implanted in the visual cortex of a cat while it is imaged with intrinsic optical imaging. Neuronal response is shown as spike-time histograms by the grey solid area and oxygen changes is the full line, with 1 SE represented as dashed lines. Gray dotted regions is the stimulus time, which a sinusoidal gratings with various degrees of orientation. When the recorded area neurally activates, (top) an intitial dip is visible, (bottom) while functional hyperemia is present whatever the neuronal response. From [Thompson *et al.* 2003].

study in 2013.

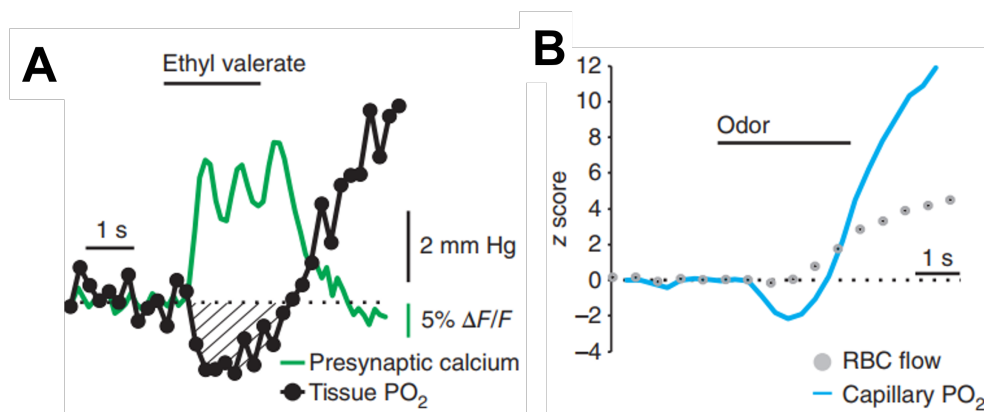


Figure 4.7: Measure of the initial dip in the olfactory bulb of the mouse.

A. Application of an odor activates the olfactory bulb of anesthetized mice, as measured by the GCaMP signal with two-photon microscopy. Using a pipette, PTP-C343 was expelled in the tissue, reporting a dip in oxygenation starting exactly when neurons activate.

B. Measuring oxygenation in the capillaries shows that the initial dip is delayed there compared to the tissular dip. Oxygenation increases as soon as the flow increase.

From [Parpaleix *et al.* 2013].

4.2.4.2 Does it really exist?

There are multiple results contradicting the existence of the ID in BOLD-fMRI imaging. In the visual cortex of the cat, it was not reported [Jezzard *et al.* 1997] where Thompson actually saw in 2003 and where other studies reported it [Duong *et al.* 2000, Kim *et al.* 2000]. Identically in the somatosensory cortex of the rat, a study showed the presence of the ID [Tian *et al.* 2010] when others did not [Mandeville *et al.* 1999, Mandeville *et al.* 1999, Yu *et al.* 2014].

Based on these contradictory results in BOLD and in other modalities, multiple hypotheses were formulated. Funnily enough, one of these could be that the ID is team specific [Hu & Yacoub 2012], as it was regularly the same research teams looking at the visual cortex and primarily in the humans that reported it. One study extended experimental data from anesthetized rats into a mathematical model and deduced that reduced basal oxygen level could induce an ID [Mayhew *et al.* 2001]. The use of different anesthetics was also pointed out as an important factor. Isoflurane dilates vessels and thus reduces vessels capacity for functional hyperemia, potentially increasing the initial dip size [Logothetis *et al.* 1999, Duong *et al.* 2000, Kim *et al.* 2000]. α -chloralose reduces blood flow, thus potentially increasing the effect of functional hyperemia, and studies using it do not report the ID [Silva *et al.* 1999, Marota *et al.* 1999, Mandeville *et al.* 1999].

A very interesting study showed a dependence of the measure of the ID to the lateness of the functional hyperemia [Watanabe *et al.* 2013]. By looking at the jitter of the positive peak at a single acquisition scale, they reported that the BOLD responses having late positive responses show an initial dip, as opposed to the responses having an early positive response (Figure 4.8). This is in line with the hypothesis that we most believe in: whether the initial dip can be measured depends

on the dynamic of the subsequent functional hyperemia. we also agree with the results about the anesthetics, as lower functional hyperemia with isoflurane seems like a factor increasing the ID. Very recently, a study using chronic awake animals [Şencan *et al.* 2020] and measuring oxygenation in nearly all vessel types but capillaries in the somatosensory cortex did not report the ID. As we know that acute experiments and anesthesia are impairing functional hyperemia, potentially increasing the ID size, this result raises the question of the existence of the ID in physiological conditions and whether what was seen before is an artifact of the experimental design.

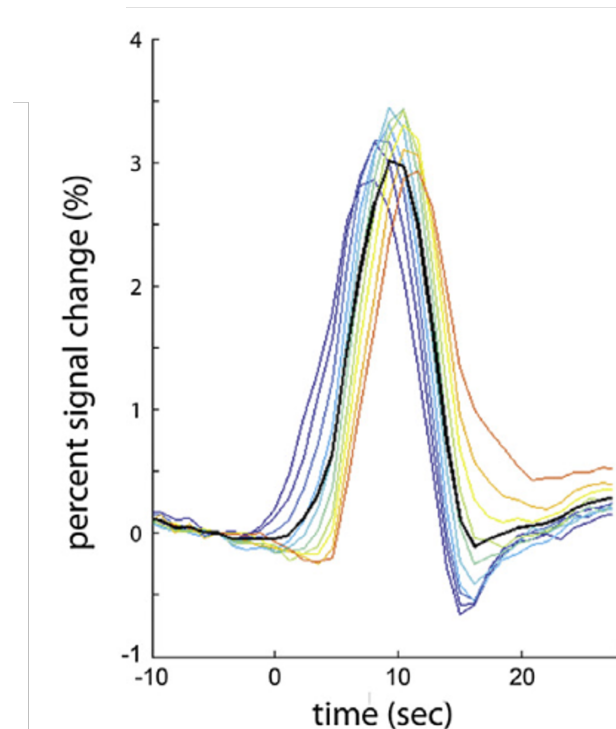


Figure 4.8: The BOLD initial dip depends on the lateness of the positive response.

Colored line are single-trials while the average response is in black. The yellow and orange trials shows a delayed peak compared to the blue trials but also display the initial dip. While it is seen at a single trial level, averaging the responses hide the dip. From [Watanabe *et al.* 2013].

4.2.5 Conclusion

BOLD-fMRI is to this day the most used functional imaging of the brain technique. It allows for brain wide measurements of oxygenation changes, related to neuronal activation, noninvasively for the human subject. However it has drawbacks: it requires the subject to stay still, making the study of young children or long sessions quite difficult³, it has a bad signal-to-noise ratio, forcing the use of analyses techniques with assumptions that may not be met by data, etc. It also relies on functional hyperemia to infer the location of neuronal activation, a phenomenon we know to be

³As for myself, I tend to fall asleep very fast there, much faster than in my own bed. Maybe I should install one in my studio.

spatially non-specific. Although many important discoveries about cognition and physiopathology have been made with fMRI, this pushes researchers to try and improve fMRI. One lead is the initial dip, whose mechanism is not fully understood to this day and existence is regularly questioned. This is why we designed and did a study to answer the question of the ID, at a microscopic level and in a neurovascular model that is reliable and easily controlled.

4.3 Functional Ultrafast Ultrasound

As opposed to the last part, the first project of this PhD contains experiments performed with Functional ultrasound (fUS). It was first presented in 2011 and since then, has been used in many neuroscience studies, from the first proof of concepts to new results regarding functional connectivity or information treatment in the brain. Although it has some caveats to overcome, odds are it will be an invaluable tool both for researchers and clinicians in the years to come. As before, I will present the physical principle underlying the fUS signal and the canonical ways to analyze it. I will go over some experimental considerations before quickly presenting some interesting results fUS yielded in the last years regarding brain physiopathology. More thoughts regarding the challenges fUS still has to overcome will be found in the discussion regarding my first paper.

Great reviews on fUS are [Deffieux *et al.* 2018, Rabut *et al.* 2020b, Edelman & Macé 2021]. I did not explore the many applications of functional ultrasound, apart from neuroimaging, which are well-described in [Rabut *et al.* 2020b].

4.3.1 Physical principle

As its name suggests, fUS physical basis is sending out ultrasound (US) pulses from a probe in an environment and measuring the echoes from those US which bounced back on scatter objects. The core principle allowing this is the Doppler effect, which I will describe before going into how it is applied in fUS.

4.3.1.1 The Doppler effect

Let us consider an object emitting sounds at a defined wavelength in a uniform and homogeneous medium: the speed of sound in this medium is constant. With the object standing still, the sound coming out of the object speakers will keep a constant wavelength, i.e. the distance between the crests of the wavelength is the same. The Doppler effect gets into the game when the object starts moving. Consider that the object starts moving to the left⁴, and that we observe the exact moment when the next crest comes out of the speaker, right after the object moved. The distance between the crest which came out right before the movement and the one coming out right after will be slightly shorter than the actual wavelength of the sound due to the object moving toward the first crest. That is, when an object emits a sound and moves in your direction at the same time, you will hear a sound with a shorter wavelength than what comes out from the speaker. Conversely, if

⁴Yup, this is a political stance. Although a bit misquoted here, science is deeply political, as much in its “affairs of the [people of the] city” original sense as in the ideological sense [Wellerstein 2018].

you are on the opposite side, the crests will get farther away from each other, and the wavelength will be longer (Figure 4.9).

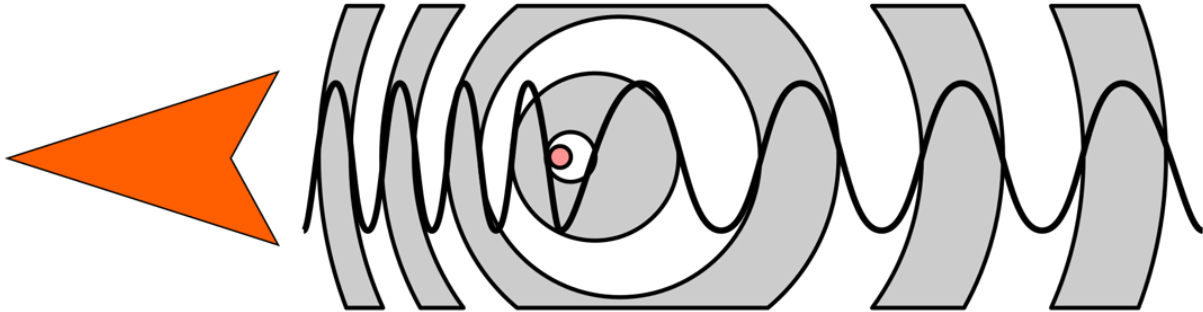


Figure 4.9: The Doppler effect. Image from [Wikipedia](#), CC BY-SA 3.0 [Tkarcher](#).

Intuitively, one can get that the faster the object goes, the greater the difference between the actual wavelength and the one picked up by the observer. This difference allows for measuring the speed of the object, based on the actual wavelength and the observed one:

$$\Delta v = \frac{cf}{2f_0} \quad (4.1)$$

with Δv being the speed of the object relative to the observer, c the speed of sound in the medium, f_0 the original frequency, i.e. the inverse of the wavelength, and f the observed frequency.

The Doppler effect, since its discovery in 1842 [[Doppler 1842](#)], has had great applications and simply revolutionized many fields of science and everyday life. One of these, maybe my favorite, is in astronomy where researchers use it to determine whether stars are moving toward or away from us and even to detect exoplanets, based on the radial changes of their velocity around their star, the so-called: "red shift".

4.3.1.2 What if the object is a red blood cell?

Now, imagine the object is a red blood cell. "What kind of sound would a RBC emit?", you may rightfully ask yourself. The RBC in itself does not emit any sound, as far as I know, but we can make it sound by sending soundwaves onto it. The wave will echo back to us, which is quite equivalent to emitting the soundwave by itself. If we send a wave with a given frequency, the faster the RBC approaches us, the higher the frequency of the echo will be, compared to the original frequency. The difference can be directly related to the speed of the RBC with the formula written above. Here we have a way to measure the speed of the RBCs in the brain.

Now imagine we have two RBCs next to each other, going in the same direction at the same speed. We will not pick up "a single" echo, but "twice" as much since two RBCs are echoing at the same time. Thus, we also have simultaneously a measure of the quantity of RBCs, i.e. the "blood volume" if we assume a constant hematocrit, along with their speed.

Note that, if the RBC is moving in a plane perpendicular to us, i.e. does not have any component of its speed that is going toward or away from us, the echo will have an identical frequency and the measured speed will be null. The Doppler effect can only measure axial speed, if the axial component is zero, the observed speed will be zero.

4.3.1.3 The fUS setup

The Doppler effect in ultrasound imaging has been used for a long time now, Doppler echocardiography for instance is a technique used by clinicians to examine the heart by measuring the speed and direction of blood flow. However, the canonical echography works like a standard two-photon microscope: beams focused on a single line in the axial direction are sequentially produced and their echoes are used to construct the image (Figure 4.10). First, this sequential procedure necessarily reduces the framerate, as each line is scanned after the other. Then, it also reduces the signal-to-noise ratio since achieving a reasonable frame rate limits the averaging over time.

Functional Ultrafast Ultrasound brought two main improvements to the canonical ultrasound. It overcame the problem of the focused beam by using a planar wave, scanning all axial lines at once [Fink & Tanter 2010]. This increased the framerate to more than a kilohertz. Then, to achieve a high signal-to-noise ratio and increase the sensitivity to image smaller vessels, fUS implements a sequential emission of tilted planar waves to generate a single image from multiple waves, usually from -8 to $+8$ degrees from the vertical axis [Bercoff *et al.* 2011]. This creates a compound image, with one image of the brain every millisecond. Moreover, having the whole brain acquired at once is paramount to study functional events in different areas and be able to correlate changes at a small time scale. These improvements and their application to brain imaging are described in [Macé *et al.* 2011, Mace *et al.* 2013].

The last point I want to emphasize is the frequency at which the ultrasounds should be emitted from the US probe. The classical US frequency, distinct from the frequency of emission, is 15 MHz. RBC velocity in the rodent brain ranges from below 1 mm.s^{-1} for capillaries up to two dozens of mm.s^{-1} . Note that the axial velocity is necessarily lower, since the biggest vessels in the brain are at the surface, and thus nearly parallel to the probe. Applying the Doppler formula (Equation 4.1), the probe will pick up doppler echoes with a frequency up to 250 Hz, for a velocity of 12.5 mm.s^{-1} . In order to measure an echo with such a frequency, the probe should at least emit the double according to the Nyquist theorem, although it may not strictly apply in the case of Power doppler (PD), a point which is made in [Mace *et al.* 2013], thus 500 Hz. That is, 500 US waves must be sent each second, with an intrinsic frequency of 15 MHz, to create a single image able to represent the full range of RBC speed in the brain. Lastly, note that increasing the frequency of the US, to 30 or 40 MHz, could improve the spatial resolution [Koekkoek *et al.* 2018] while reducing it can improve the penetration and the imaging of deeper structures [Deffieux *et al.* 2018].

4.3.2 Analysis process: extracting a map from the echoes

Once we put the probe over the mouse olfactory bulb, send our tilted US through the craniotomy and get back the echoes, how do we end up with an understandable acquisition over time?

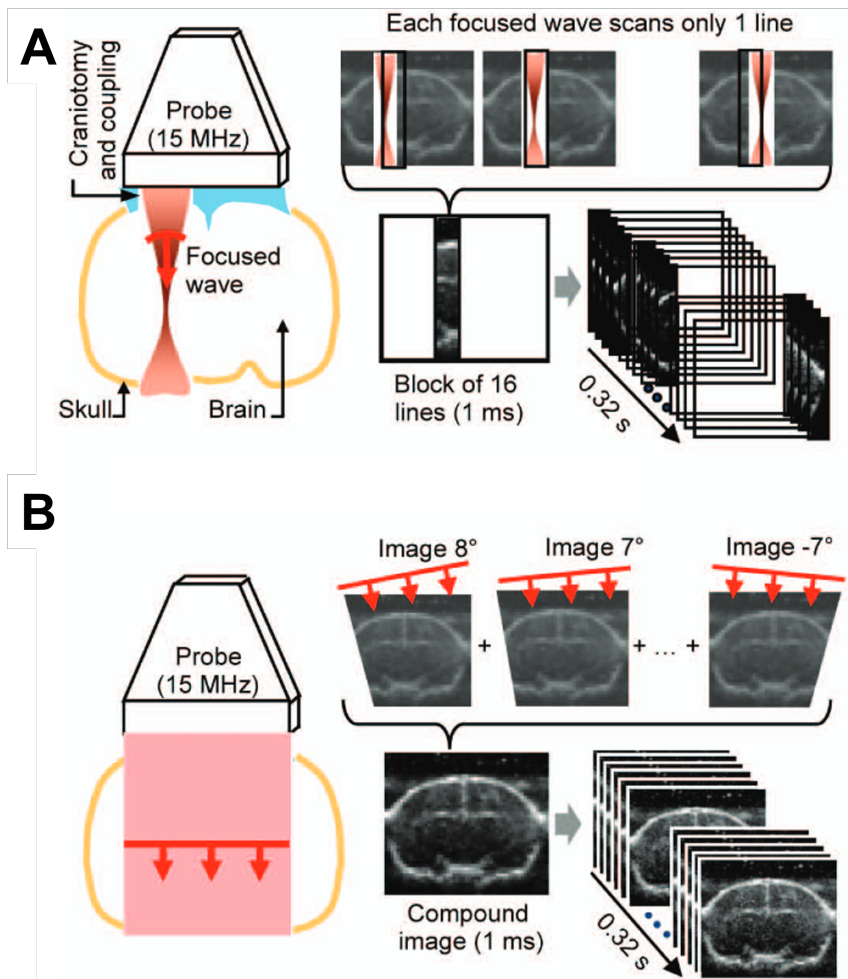


Figure 4.10: Functional Ultrafast Ultrasound.
A. Representation of a canonical US acquisition
B. Representation of a fUS acquisition;
 From [Mace *et al.* 2013].

Each final image of the acquisition is composed of all the tilted echoes. In order to merge them, the first step is to perform a beamforming, i.e. to coherently sum the image produced by each of the tilted waves [Bercoff *et al.* 2011]. Note that, due to the tilted nature of the waves, the signal echoed by a given RBC will be different for each tilt since the axial velocity of the RBC changes with the angle of the wave.

We now have a series of images each representing the state of the olfactory bulb (OB) at a specific time point. If we take a single voxel and look at its signal over time, the Power Doppler signal, we should be able to measure the changes in RBC number in this voxel over time, since more RBCs mean more echoes picked up by the probe. But is all the signal related to RBCs? Actually, if we look at the raw Power Doppler signal, we will see low frequency changes that are not related to RBCs but rather tissue motion (Figure 4.11). In the seminal paper, a high pass filter was applied to get rid of those [Macé *et al.* 2011] but since then a more efficient technique has been developed based on single value decomposition (SVD) [Demené *et al.* 2015]. Grossly, the principle is to compute eigenvalues representing coherent movement across the slice and across time. By removing the biggest eigenvalues, that is the coherent movements that are the larger, we can remove the tissue motion and focus on the RBCs.

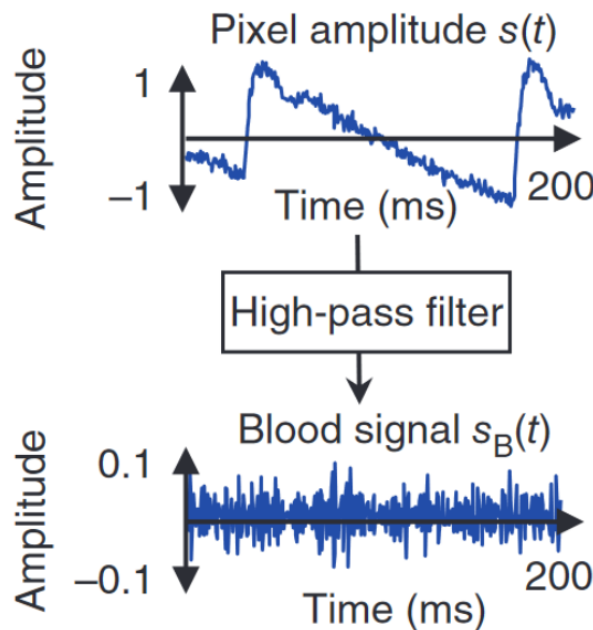


Figure 4.11: The fUS signal comprises both RBCs and tissue motions.

Looking at the raw signal from a single voxel, low frequency variations have to be filtered to focus on the blood signal rather than the tissue movement. From [Macé *et al.* 2011].

The last part of the pre-treatment process takes advantage of the Doppler effect. RBCs with different axial velocities echo different frequencies to the probe, frequencies which can be found back in the Power Doppler signal. By filtering the PD signal, we can measure the signal coming from RBCs with specific speeds (Figure 4.12). Note that we are forced to at least apply a high pass at around 10 Hz to get rid of the noise that the SVD treatment could not remove. This imposes a limit below which RBCs aren't detectable, $0.5 \text{ mm}\cdot\text{s}^{-1}$ for 10 Hz, meaning some capillaries are

hardly measurable with fUS even assuming they are wholly perpendicular to the probe.

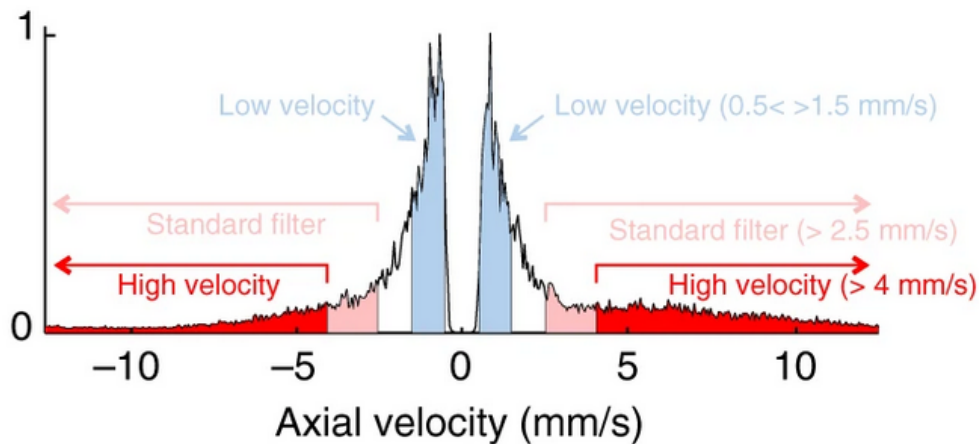


Figure 4.12: Filtering the fUS signal allows for focusing on specific RBC velocities.

The horizontal axis can either be the speed (as here) or the frequency of the echo emitted by the RBCs. Filtering some frequencies selects specific axial velocities, while taking the whole integral of the signal is proportional to the total RBCs quantity, without the central frequencies around 0 which are suppressed due to the SVD filtering. From [Boido *et al.* 2019].

Once these steps are performed, the experimenter has for each voxel of the slice a timeserie representing for the chosen speed range the variations of the blood volume, assuming a constant hematocrit.

4.3.3 Experimental considerations

Experimenting with fUS requires one to keep a few things in mind, in order to correctly interpret acquisitions and benefit from all the available information.

4.3.3.1 Voxel size and spatial specificity

Depending on the probe and on the intrinsic frequency of the emitted US, the size of the voxel may be different. The seminal paper presented a probe using 15 MHz US, a frequency we kept in our experiments, and stated that their “Point-Spread Function” was around $100 \times 100 \times 200 \mu\text{m}$ (height \times length \times width). In my first study, we did an experimental verification of this measurement using a glass bead and found similar results. However, this is only available for a bead placed at the focal distance, which depends on the probe characteristics. Going above or below from this focal height (when the probe is above the sample), the signal registered to a voxel will originate from a larger volume than expected. The voxel size being defined, is this enough to discriminate between functionally different voxels? In the auditory cortex of awake ferrets, functional resolution has been determined for voxels separated by $300 \mu\text{m}$ [Bimbard *et al.* 2018]. Note that in that case, the “resolution” was determined on the basis of differential responses to different sounds on the neighboring voxels. More recently, ocular dominance has been shown in non-human primates, with

ocular columns having a radius of around 250 μm [Blaize *et al.* 2020]. Of course, this functional resolution depends on the size of the functional unit in the brain. The rodent OB has glomeruli of around 60 μm in diameter, separating the activation of a single one would be impossible... and that is without taking into account the spatial non-specificity of functional hyperemia. Note that an important increase in sensitivity and spatial resolution is possible by using microbubbles injected intravenously [Errico *et al.* 2015, Couture *et al.* 2018, Sloun *et al.* 2021], a technique available in the human subject which achieved down to 25 μm in resolution [Demené *et al.* 2021]. Microbubbles replace RBCs as echo-emitters in that case.

4.3.3.2 Heating the tissue

One concern regarding the use of ultrasounds in the brain is that like lasers, US may heat the tissue it goes through. Our team previously showed that changing the brain temperature impacts the RBC flow and can thus have an impact of the PD signal [Roche *et al.* 2019]. No experimental results have been published regarding this point, as far as I know, but the use of fUS in neonates [Demene *et al.* 2017] implies that this verification has been made, at least theoretically, to be in accordance with the safety rules. Further description of the heating in the brain, which may be approximated as a water volume due to its composition, and how it varies with the intrinsic frequency and the power of the probe is required, to better calibrate the preclinical studies. Indeed, ultrasounds can have deleterious impact on brain physiology if applied for too long or without care for the power [Ang *et al.* 2006, Maršál 2010, Lalmaz *et al.* 2017].

4.3.3.3 Vessel orientation

I previously mentioned that only the axial velocity of the RBCs is taken into account by the fUS. This can make some vessels invisible if they are exactly parallel to the probe. Moreover, it creates an assumption of similarity between the vascular organization of different areas when comparing their responses. Consider we filter fUS data between 10 and 30 Hz, thus focusing on RBCs with axial velocities ranging from 0.5 to 1.5 $\text{mm}\cdot\text{s}^{-1}$. Such axial velocities can be found in strictly axial arterioles but also in large vessels that are slightly non-parallel to the probe, giving them a small axial velocity compared to their velocity in the parallel plane. Both types of vessels react differently to neuronal activation. Comparing two areas, one with arterioles and the other one with the large vessels, without considering this difference in vascular organization can easily lead to misinterpreting the fUS results. This issue is probably more applicable to the rodent than to the human subject, since voxel size may allow to determine vessel orientation in the human and thus to compensate for the axial velocity dependency.

One should also keep in mind that the acquisition is composed of voxels, and that the signal measured in each one of them is actually the sum of all the RBCs inside.

4.3.3.4 Impact of the surgical preparation

When the fUS probe sends an US wave into the sample and receives an echo, how can it know where the emitting RBC is? This issue is intuitively resolved by thinking about the physics of the

mechanism: the wave has a given speed, the speed of sound in the sample, and it travels twice the distance probe-RBC, once as the emission and again as the echo. Knowing the speed and the time, the distance is easily calculated. An important assumption here is that the speed of sound is constant all over the distance probe-emitter. As the brain is mostly water and the gel placed below the probe is similar, we can assume that the speed of sound in there is the same as the speed of sound in the water, around $1500 \text{ m}\cdot\text{s}^{-1}$. However, if we keep the skull in the rodent preparation, it will necessarily create artifacts if not taken into account. Indeed, the speed of sound in bones is higher than in water, above $2000 \text{ m}\cdot\text{s}^{-1}$ with the precise value depending on the composition [Pichardo *et al.* 2010]. The thickness of the bone also plays a role, although given the small variations around the skull of a given species, much precision may not be necessary.

An evaluation of the impact of our preparation is done in the discussion of the first study.

4.3.4 Results

Functional ultrafast ultrasound is a technique with a much better spatial and temporal resolution than BOLD-fMRI. The last decade has been full of studies, showing proof of works for fUS or new results taking advantage of fUS ease-of-use.

In the seminal paper, the authors showed that fUS could be used to measure the activation of the barrel cortex upon whisker stimulation of a rat [Macé *et al.* 2011]. Bimbard and colleagues recreated a tonotopic map of the auditory cortex of awake ferrets [Bimbard *et al.* 2018]. Later, the ocular dominance was assessed in the non-human primates [Blaize *et al.* 2020]. Combined with a NeuroPixel probe, the mesoscopic neural basis of fUS signal was studied in the visual cortex of awake mice [Nunez-Elizalde *et al.* 2021].

Our team used fUS to show that using blue light to optogenetically control neuronal activation had an effect on vascular activity [Rungta *et al.* 2017]. Later, we compared fUS and BOLD-fMRI in the same mice and under the same conditions, showing the better spatial and temporal resolution of fUS [Boido *et al.* 2019]. Osmanski and colleagues also used the olfactory stimuli to image the piriform cortex, a region which is near air-filled cavities and therefore tricky to image with BOLD-fMRI [Osmanski *et al.* 2014]. Based on their fUS data, and previous literature [Stettler & Axel 2009], they show that the piriform cortex does not map input data into the cortex volume as opposed to the other cortical regions. Very recently, fUS was used to study the neurovascular coupling in the white matter by exciting afferent fibers of the spinal cord and measuring the fUS response, in both physio- and pathological situations [Claron *et al.* 2020]. A first iteration of brain-machine interface was achieved with fUS in the motor context, to plan and control movement [Norman *et al.* 2021]. Imaging in freely-behaving mice with fUS has also been described [Sieu *et al.* 2015, Urban *et al.* 2015]. Whole-brain fUS imaging in the awake mouse showed its ability to uncover functional characteristics in the thalamus, a deep-seated region of the brain which is not easy to image, before confirming the results with electrophysiology [Macé *et al.* 2018].

A very important milestone was passed with a study done in neonates, where the authors measured sleep state and seizure activity, something nearly impossible with BOLD-fMRI [Demene *et al.* 2017]. Connectivity of brain areas was also assessed in neonates, making fUS a very interesting clinical tool to diagnose and evaluate neonates' brains [Baranger *et al.* 2021].

Functional ultrafast ultrasound still has some challenges to overcome. In young animals, transcranial imaging can be achieved [Tiran *et al.* 2017, Rabut *et al.* 2020a] but thin-skulled preparation is still mandatory in adult rodents while craniotomy is needed for thicker skulls, as for primates. Presence of the skull above the recorded brain volumes creates aberrations, which has to be corrected. Spatial and temporal resolution can still be improved [Ianni & Airan 2021], while actual quantitative measurements of blood flow are studied by some teams [Tang *et al.* 2020].

CHAPTER 5

THE OLFACTORY BULB, A NEUROVASCULAR MODEL

*Odors have a power of persuasion stronger
than that of words, appearances, emotions,
or will.*

Patrick Süskind in Perfume, 1985

Contents

5.1	Introduction	61
5.2	Neuronal organization	62
5.2.1	General organization	62
5.2.2	The glomerular layer	64
5.3	Vascular organization	64
5.4	A neurovascular coupling model	65

5.1 Introduction

The human olfactory sense has long been overseen, mainly due to the comparison to the vision or the audition, considered more important. As Sela and Sobel argue, the human olfactory sense is neither continuous, as we sniff as we breath, nor spatially informative [Sela & Sobel 2010]. Nonetheless, we are able to discriminate between up to a trillion olfactory stimuli [Bushdid *et al.* 2014]. In this

section, I will not focus on the human olfaction but rather on the rodent olfactory bulb (OB): the model we chose to study neurovascular coupling. I will mainly describe the outer part of the OB, the olfactory nerve layer and the glomerular layer as I mainly worked there¹. I will first describe the neuronal organization and then the vascular one. Finally, I will describe how the glomeruli are a suited model of NVC.

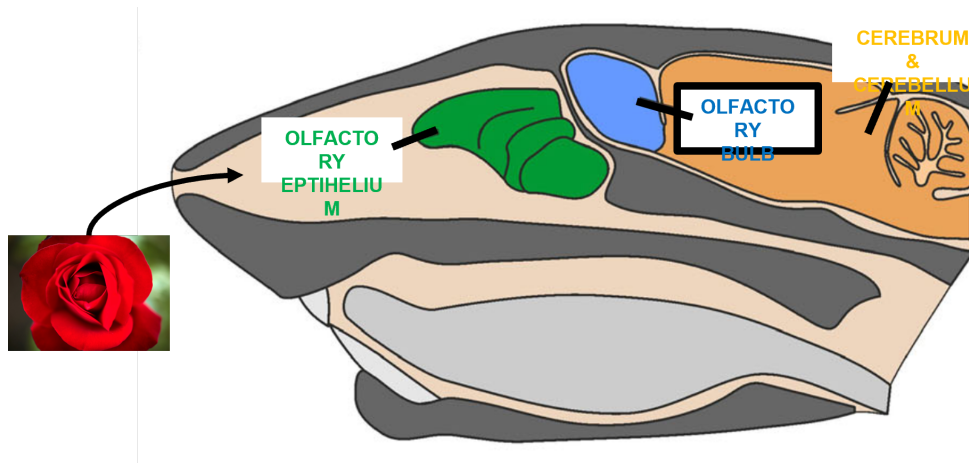


Figure 5.1: Schematic coronal slice of a mouse head.

Adapted from [Lohr *et al.* 2014]. Rose image from Patrick Fore on Unsplash.

5.2 Neuronal organization

5.2.1 General organization

The olfactory bulb is the first relay of olfaction in which axons of olfactory sensory neurons (OSN) converge (Figure 5.2). Each OSN expresses a single odorant receptor (OR) type on its membrane, and upon binding of an odorant molecule sends action potentials to the OB. Notably, an OR is specific to a given odorant molecule at low concentration. However, it loses its specificity and binds to other related odorant molecules at high concentration [Nara *et al.* 2011]. This peripheral part of the olfactory pathway is subject to adaptation and habituation [Lecoq *et al.* 2009]. Once in the bulb, OSN axons expressing the same OR transit in the olfactory nerve layer (ONL) and synapse in a single glomerulus onto mitral cells (MC) and other cell types that I will quickly mention below. MCs send their apical dendrite that form tufts into the glomerulus. Axons from the MCs are the main output of the OB to the piriform cortex and other subcortical structures. To be noted is the presence of a feedback loop, from the piriform cortex to the OB, regulating the activity of the mitral cells [Boyd *et al.* 2012].

The main advantages of the glomeruli, for experimental approaches, is their location in the mouse: less than a 100 μm from the OB surface, making *in vivo* access through microscopy quite easy. Then, as a first relay, we can precisely control the neuronal activation even with natural stimuli. I will get back to it below.

¹And because of a lack of time before handing back this manuscript. Oopsy.

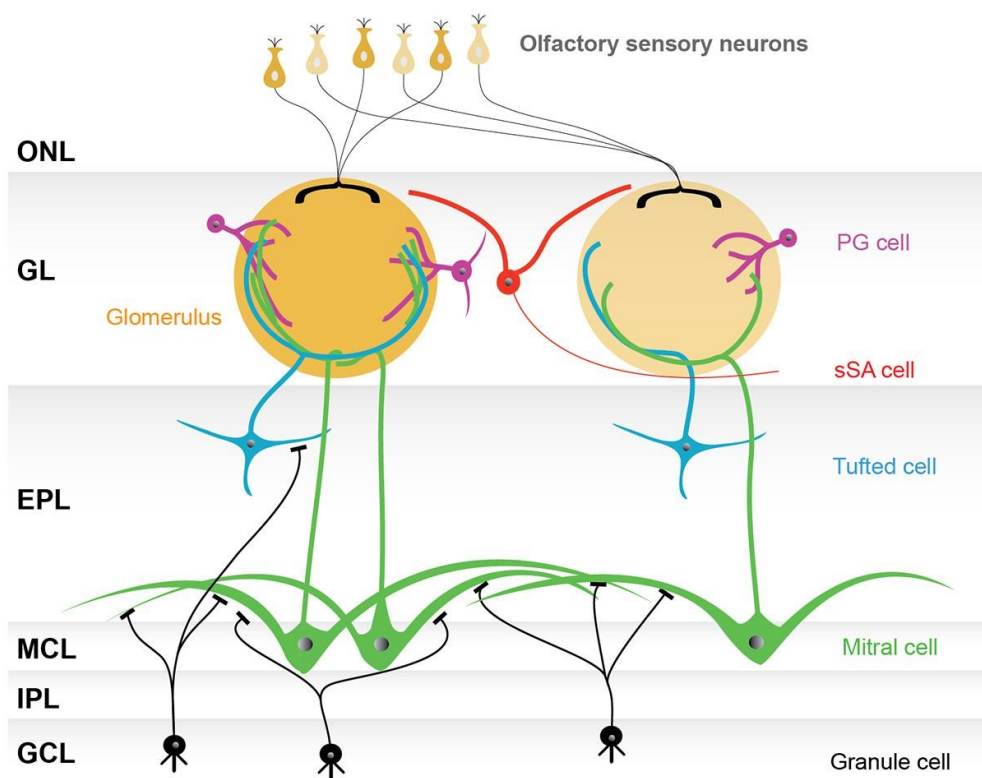


Figure 5.2: Schematic laminar organization of the OB.

ONL = Olfactory Nerve Layer ; GL = Glomerular Layer ; EPL = External Plexiform Layer ; MCL = Mitral Cell Layer ; IPL = Internal Plexiform Layer ; GCL = Granule Cell Layer.

From [Nagayama *et al.* 2014].

5.2.2 The glomerular layer

The ONL is composed of fascicles of axons from OSNs. OSNs expressing the same OR converge into two glomeruli per bulb, a dorsal and a ventral one. Thus, each glomerulus receives about 5000 OSNs expressing the same OR, with about 15 terminals per axon (i.e. 75000 OSN release sites). In the mouse OB, there are around 4000 glomeruli which are around 60 μm in diameter [Richard *et al.* 2010]. As opposed to the rat OB, the mouse glomeruli are not organized on a single layer, but are rather superimposed on each other across the glomerular layer (GL). A glomerulus has been defined as a spherical shaped neuropil by Sheperd and Greer, meaning that it lacks somata. Indeed, a glomerulus is composed of three elements: the axons of OSNs, the dendrites of principal and juxtglomerular neurons and astrocyte processes [Mombaerts 2006]. The somata of the astrocytes and juxtglomerular neurons are located in the periglomerular region.

Principal neurons are mainly mitral cells and tufted cells (TC), whose somata are all located below the GL. They both make synapses with the OSN axons in glomeruli but also make dendro-dendritic synapses with juxtglomerular neurons. These cells are either interneurons, external tufted cells or short-axon cells. They all form a complex microcircuitry, reviewed in [Wachowiak & Shipley 2006, Nagayama *et al.* 2014], which I will simplify in the following paragraph.

Odorant molecules enter the nasal cavity and go through the mucus to bind to the OR of OSNs for which they have enough affinity. OSNs fire and presynaptic glutamate is released in the glomerulus onto MC, TC and other relevant cellular actors. Juxtglomerular cells provide inhibition and modulation of the MC and TC activation. Finally, MCs send axons to cerebral structures such as the piriform cortex, where the olfactory input is integrated with other sensory information and further processed.

Regarding my work, I focused on postsynaptic activation of MCs expressing GCaMP6f [Dana *et al.* 2014]. This activation mainly depends on the signal from the OSNs, although it is modulated by other mechanisms. We showed that there is an exponential relationship between the odor concentration and the postsynaptic activation of the glomerulus that is the most sensitive to the odor, i.e. the one getting input from the OSNs expressing the OR with the highest affinity [Boïdo *et al.* 2019].

5.3 Vascular organization

OB vascular supply originates from branches of the ACA, either the olfactofrontal artery or the ventral frontal artery [Coyle 1975]. The dorsal part of the OB shows multiple pial vessels, arteries or veins, which penetrate/come out perpendicularly as penetrating arterioles/venules. Then, they irrigate the parenchyma by dividing into smaller and smaller vessels to form the capillary network.

A thorough description of the mouse vascular organization in the bulb was lacking until recent studies which systematically registered vessels down to the capillaries (see section 2.2.2.3). For simplicity, I will only give a few figures here. In the rat, we observed a very low density of capillaries in the ONL, around 45 $\text{mm} \cdot \text{mm}^{-3}$ while it is very high in the GL, around 1000 $\text{mm} \cdot \text{mm}^{-3}$ [Lecoq *et al.* 2009]. This corroborates the idea that vascular density follows metabolic needs, which

is higher around synapses (see section 2.2.2.3).

In the GL, vessels and capillaries do not show any preference for intra- or inter-glomerular space [Chaigneau *et al.* 2003]. We have recently shown that the average distance between the PA at the bulb surface and the capillary inside the glomeruli is around 700 to 800 μm , as the branch coming off the PA and going to the glomerulus is below the GL [Rungta *et al.* 2018]. Following a capillary up to its feeding pial, to study the Po_2 variations for instance, is quite difficult as we have to go deeper not to lose it.

5.4 A neurovascular coupling model

The olfactory bulb glomerulus is a good neurovascular model, as I describe below.

The GL is in the outer part of the OB, which is relatively easy to access optically, either through a chronic cranial window or through the bone thanks to the development of three-photon imaging and fUS.

In terms of neuronal activation, the glomerulus activation shows a very high degree of reproducibility together with a high spatial specificity when going down to low concentration of odor [Chaigneau *et al.* 2007, Boido *et al.* 2019]. There is a precise exponential relationship between odor concentration and MC activation, measured as the evoked-calcium response. This is important as my first study showed that the neurovascular relationship may change depending on the neuronal activation: we must be careful about how we stimulate the brain.

Vascularly speaking, we also found that RBC velocity and flow increases are highly reproducible [Chaigneau *et al.* 2007, Boido *et al.* 2019]. The high capillary density in the GL provides us with a wide choice of capillaries to measure, and the stereotypical organization is important to assess the accuracy of our results.

Overall, I think that the OB is a great tool to precisely characterize neurovascular coupling. The main difference with the cortex is that the cortex gets activated in a wide and synchronous manner, thus preventing any precise local measurement. This might also explain the differences we see, along with subtle changes in the cellular organization. This is discussed in the annexed paper, which focused on the timing of the vascular activation in the somatosensory cortex.

CHAPTER 6

SUMMARY

Too long, didn't read

Most people before this manuscript

Contents

6.1	Linking microscopic neuronal activation to mesoscopic fUS response . . .	67
6.2	Iliski	68
6.3	The initial dip: solving a controversy	68

In these chapters I tried to introduce the necessary knowledge to thoroughly discuss the results of this thesis, along with less necessary although interesting information. Below, I will detail what pushed us to pursue the studies I did in my PhD.

6.1 Linking microscopic neuronal activation to mesoscopic fUS response

Since my arrival in the lab, the use of fUS in fundamental and preclinical studies exploded due to the recent commercialization of the machine. Proof of concepts had been done showing the correlation between the fUS Power Doppler signal and the neuronal activity. Nonetheless, as I mentioned previously, a direct relationship between local vascular activity and local neuronal activity is far from evident, mainly due to the backpropagation of the vascular dilation. A thorough evaluation of whether fUS can accurately report local activation, in time and space, was missing.

Then fUS reports a signal that is proportional to a meaningful physiological feature: RBC quantity. Yet, no one had assessed this proportionality in a living animal at a microscopic level.

Finally, functional vascular imaging of the brain benefits from a complete understanding of the NVC dynamic. Our two-photon setup allowed us to simultaneously measure neuronal and vascular activation in a simple model of NVC, and thus bring more insights to the NVC dynamic.

6.2 Iliski

I programmed for the first study scripts to easily compute the numerous TFs we used to assess NVC dynamic. First as a moral obligation¹ and then as a way to make our work recognized, we decided to put these scripts together into a user-friendly interface and publish the software, Iliski, as a peer-reviewed publication.

6.3 The initial dip: solving a controversy

BOLD-fMRI has some downsides which hardens the interpretation of its signal. Among them, as for other vascular based imaging techniques, the backpropagation of the vascular signal makes functional hyperemia less spatially localized than the original neuronal activation. The initial dip, supposedly reporting local oxygen consumption, could have been the miracle solution. However, its existence is very controversial as I explained previously. A few years ago, we were able to measure it at a microscopic level in our model, the OB, and thus we decided to further study its characteristics: is it present everywhere in the bulb? Is there a neuronal activation threshold to its measure? Where in the capillary are we able to measure it, near RBCs or in-between them? How does it vary when measured in a chronic preparation, whether anesthetized or awake, rather than in an acute preparation?

As the last part of the results will show, our findings are not exactly what we expected. The study is yet to be finished, but I put together a preprint reporting every result we have to date.

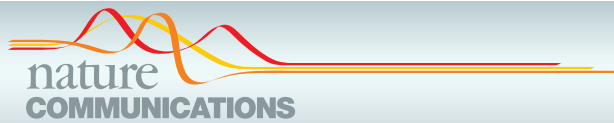
¹Read “because I insisted for many weeks”.

Part II

Results

CHAPTER 7

TRANSFER FUNCTIONS LINKING
NEURAL CALCIUM TO SINGLE
VOXEL FUNCTIONAL ULTRASOUND
SIGNAL



ARTICLE

<https://doi.org/10.1038/s41467-020-16774-9>

OPEN

Transfer functions linking neural calcium to single voxel functional ultrasound signal

Ali-Kemal Aydin^{1,2}, William D. Haselden³, Yannick Goulam Houssen¹, Christophe Pouzat⁴, Ravi L. Rungta^{1,2}, Charlie Demené⁵, Mickael Tanter⁵, Patrick J. Drew⁶, Serge Charpak^{1,2,8} & Davide Boido^{1,7,8}

Functional ultrasound imaging (fUS) is an emerging technique that detects changes of cerebral blood volume triggered by brain activation. Here, we investigate the extent to which fUS faithfully reports local neuronal activation by combining fUS and two-photon microscopy (2PM) in a co-registered single voxel brain volume. Using a machine-learning approach, we compute and validate transfer functions between dendritic calcium signals of specific neurons and vascular signals measured at both microscopic (2PM) and mesoscopic (fUS) levels. We find that transfer functions are robust across a wide range of stimulation paradigms and animals, and reveal a second vascular component of neurovascular coupling upon very strong stimulation. We propose that transfer functions can be considered as reliable quantitative reporters to follow neurovascular coupling dynamics.

¹INSERM U1128, Laboratory of Neurophysiology and New Microscopy, Université de Paris, Paris, France. ²INSERM, CNRS, Institut de la Vision, Sorbonne Université, Paris, France. ³Medical Scientist Training Program and Neuroscience Graduate Program, The Pennsylvania State University, University Park, PA, USA. ⁴MAP5, Mathématiques Appliquées Paris 5, CNRS UMR 8145, Paris, France. ⁵Physics for Medicine, ESPCI, INSERM, CNRS, PSL Research University, Paris, France. ⁶Department of Engineering Science and Mechanics, The Pennsylvania State University, University Park, PA, USA. ⁷NeuroSpin, Bât 145, Commissariat à l'Energie Atomique-Saclay Center, 91191 Gif-sur-Yvette, France. ⁸These authors contributed equally: Serge Charpak, Davide Boido. ✉email: serge.charpak@inserm.fr; davide.boido@cea.fr

Functional imaging techniques based on blood flow dynamics are extensively used to investigate normal and pathological brain function in humans. However, these techniques do not directly measure neuronal activation, reporting instead functional hyperemia, a delayed increase of blood flow resulting from neurovascular coupling (NVC). The signaling pathways by which NVC occurs are known to involve the cooperation of numerous cell types (neurons, astrocytes, smooth muscle cells, pericytes, endothelial cells) forming the neurovascular unit. However, the precise mechanisms by which these cell types interact and contribute to the coupling are highly debated¹. In addition, several studies have shown that local activation of neurons generates a back-propagating signal along vessels^{2–6}, dilating upstream large capillaries and arterioles, and increasing the brain volume irrigated by functional hyperemia^{7,8}. This raises the question of how functional imaging techniques based on blood dynamics and used to map brain activity with a mesoscopic spatial resolution report local cellular and vascular responses measured with microscopic resolution, i.e., with two-photon microscopy (2PM).

Functional ultrasound (fUS) has recently emerged as an efficient alternative to BOLD fMRI for functional brain mapping, with millisecond time and mesoscopic ($\sim 100 \times 100 \times 200 \mu\text{m}$) spatial resolution^{9,10}. It has been used to investigate olfactory^{5,11,12}, visual^{13,14}, and somatosensory^{9,15,16} responses in anesthetized and awake rodents, and applied to ferrets¹⁷, pigeons¹⁸, monkeys¹⁹ and humans^{20,21}. In the mouse olfactory bulb (OB), we have recently shown that global fUS sensory responses are tightly correlated to odor²². However, a major question remains: to what extent does the fUS signal report local brain activation? What Doppler signal change (which reflects the increase in cerebral blood volume) can be expected from cellular or vascular responses and reciprocally, what cellular or vascular responses can be deduced from fUS signals? Understanding these relationships is essential to interpreting fUS measurements.

Here, we develop a theoretical approach for transfer function computation and test its validity in establishing TFs between (i) microscopic neuronal and vascular signals and (ii) microscopic neuronal and mesoscopic fUS signals. In the OB of GCaMP6f expressing mice, we first use two-photon imaging to collect neuronal Ca^{2+} signals to odor, simultaneously with RBC velocity changes from capillaries located in the most responsive glomerulus. We then establish the TFs between the two microscopic signals and demonstrate their robustness and limitations. In a second step, we measure the fUS signal from the single fUS voxel containing the responsive glomerulus, i.e., precisely co-registered in the same animal. Finally, we quantify the extent to which mesoscopic TFs (mTFs) can be used to predict neuronal activation.

Results

The TF between neuronal and vascular responses within a single glomerulus. Using two-photon laser scanning microscopy, we imaged neuronal activity and capillary blood flow in the dorsal OB of mice expressing YFP and GCaMP6f under the control of the M72 and Thy1 promoters, respectively. The animals were chronically implanted with a polymethylpentene (PMP) window, allowing 2PM and fUS imaging sessions with reproducible responses over weeks²². In these animals, the M72 glomerulus (with terminals converging from olfactory sensory neurons expressing the M72 odorant receptor) was easily distinguishable (Fig. 1a) under a stereomicroscope or using 2PM. Vessels were labeled with Texas Red and linescan acquisitions were used to simultaneously monitor capillary RBC velocity and neuronal Ca^{2+} upon odor stimulation. While stimulation with 1–6% ethyl tiglate (ET) during 5 s activated several glomeruli in the close

vicinity of the M72 glomerulus, lowering the odor concentration in the range of 0.1% enabled us to isolate the most sensitive glomerulus, which was then selected for the rest of the study. Figure 1b illustrates a typical neurovascular response to the stimulation protocol (1% ET, 5 s) used to build a database from 15 mice, and compute a microscopic transfer function (μTF) between neuronal Ca^{2+} and capillary vascular responses. Deconvolution approaches based on Fourier transformation or Toeplitz matrix were too sensitive to the noise of Ca^{2+} and RBC velocity traces to compute a reproducible μTF . We thus chose to optimize a transfer function based on the gamma-distribution function, which is commonly used as a basis for the hemodynamic response function (HRF) in BOLD fMRI. We did not need a second, negative gamma-component as there was no post-stimulus undershoot. We also added a time-shift parameter (p_3), to better match the data (accounting for a vascular delay ≥ 1 ms, $H(t)$ is the heaviside unit step function).

$$\text{TF}(t) = H(t - p_3) p_4 \left(\frac{(t - p_3)^{p_1 - 1} p_2^{p_1} e^{-p_2(t - p_3)}}{\Gamma(p_1)} \right).$$

The μTF optimization was performed using a nondeterministic, machine-learning approach based on the simulated annealing algorithm (see Supplementary Fig. 1 and Methods for details). One μTF was optimized for each mouse, under the same stimulation protocol (1% ET, 5 s) (Fig. 1c, top). Using this approach, vascular response predictions were excellent (Fig. 1c, bottom, Pearson coefficient: 0.93 ± 0.03 , mean \pm SD). They remained robust using either the μTF optimized with each mouse own Ca^{2+} and RBC velocity data (self-validation), or the μTF optimized with data from other mice (leave-one-out cross-validation) (Fig. 1d). One μTF , peaking at 0.9 s and providing the best robustness (self and cross performance, for more details, see Methods), was then selected as the standard μTF to predict vascular responses from Ca^{2+} responses (Fig. 1e). The robustness of this μTF suggests that the ensemble of cellular mechanisms underlying NVC is tightly and similarly controlled across animals. However, whether this holds true across different stimulation durations or intensities remains unknown.

Testing TF robustness through various stimulation conditions.

We first decreased the odor delivery from 5 s, the duration at which the standard μTF was initially optimized, to 2 s, 1 s, and 120 ms, the latter duration corresponding to a single sniff stimulation. For such brief stimulation, which suffices for perception and odor discrimination^{23–25}, the olfactometer was locked to the respiration by means of a thermocouple placed close to the mouse nostril. Figure 2a shows that Ca^{2+} and RBC velocity responses increased according to the odor duration. Vascular responses predictions remained robust with all durations (Pearson coefficients for 120 ms, 1 s, 2 s, 5 s, respectively: 0.74 ± 0.15 , 0.79 ± 0.16 , 0.89 ± 0.07 to 0.89 ± 0.08 , mean \pm SD, $n = 5$ mice). This indicates that microscopic functional hyperemia is a robust reporter of neuronal activation duration. As stimulus intensity was the second stimulation parameter across which the μTF needed to be validated, we compared Ca^{2+} and RBC velocity responses at 1% ET (the concentration used to compute the standard μTF) and 6% ET (a strong concentration) in five other mice. As expected, at 1% ET the change in RBC velocity prediction was excellent. However, at 6% ET a secondary delayed phase of the RBC velocity response appeared and was poorly predicted (Fig. 2b). This secondary phase, peaking around 30 s is reminiscent of the delayed and astrocyte-mediated BOLD fMRI signal reported under strong stimulation in the neocortex²⁶. It could be isolated by subtracting prediction values from the

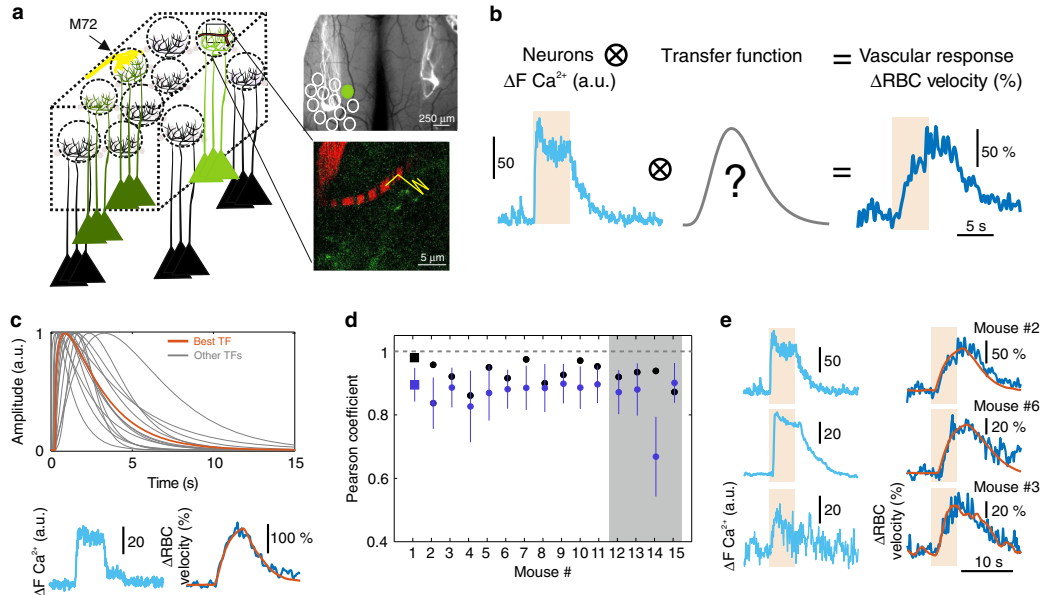


Fig. 1 The transfer function between neuronal and vascular responses within a single glomerulus: computation and robustness across mice. **a** Left, schematics of the dorsal olfactory bulb (OB) of a mouse expressing YFP and GCaMP6f under the control of M72 and Thy1 promoters, respectively. Depending on the odor concentration, ethyl tiglate (ET) activates several glomeruli or only the most responsive one, which is in close vicinity to the M72 glomerulus. Right top, axons converging in the two M72 glomeruli are imaged with a stereoscope through a chronically implanted PMP window (photographs were taken for all mice). Right bottom, an image showing a capillary labeled with Texas red. A broken line is used in the linescan acquisition mode to monitor Ca^{2+} in the neuropil (dendritic GCaMP6f) and RBC velocity in the capillary. **b** For each mouse, a microscopic transfer function (μTF) is convolved with Ca^{2+} signals, the μTF being optimized to predict RBC velocity changes in response to odor 1% ET (5 s). **c** Top, μTF s optimized for each mouse ($n=15$). The orange curve is the μTF optimized from Ca^{2+} and RBC velocity responses illustrated in bottom, which gives the prediction curve overlaid in orange on the RBC response. **d** Quantification (mean \pm SD, $n=15$ mice) of prediction robustness for each μTF s optimized using either the TF derived from the same mouse (black symbols, single self prediction) or data from other mice (blue symbols, mean cross-validation). The μTF from mouse #1 (square symbols) gives the best 'self' vascular prediction (see **c**) and good predictions across mice. It was selected as the standard μTF to predict vascular responses from Ca^{2+} responses. Gray shadow (#12-15) for Pearson coefficients obtained with data acquired in mice from Boido et al, 2019²². **e** Examples of vascular response predictions from three mice using the standard macroscopic TF and optimized for the amplitude (see Methods). Source data are provided as a Source Data file.

experimental data (Fig. 2c, black trace) and was observed in all mice, starting at ~ 15 s and peaking at ~ 25 –30 s (gray traces). To improve the standard μTF prediction and account for this secondary vascular phase, we first optimized a new set of μTF s for each mouse, linking Ca^{2+} responses and the subtracted secondary vascular component (Fig. 2d, left). These secondary μTF s displayed a strong peak jitter and shape heterogeneity. They could be combined with the standard μTF , taking into consideration the responses' amplitude ratio, to predict the vascular response over its full duration (Fig. 2d, inset). We then investigated whether the standard μTF could predict responses elicited by a second odor, isoamyl acetate (1%, 5 s). This odor very poorly activates the glomerulus most sensitive to ET. Supplementary Figure 2 shows that despite the very modest Ca^{2+} and RBC velocity responses, the μTF vascular response prediction remained robust ($n=4$ mice). Finally, we challenged the μTF robustness in predicting vascular responses with our data collected and used in previous publications: (1) In similarly sedated mice²², the prediction quality of the vascular response initial component remained robust at increasing odor concentrations of 0.4%, 1%, and 6% ET (Pearson coefficient: 0.83 ± 0.08 , 0.89 ± 0.06 , 0.89 ± 0.07 , respectively, mean \pm SD, $n=6$ mice); (2) In awake trained mice⁵, although vascular responses were briefer and occasionally

showing a delayed undershoot (Supplementary Fig. 4a), a phenomenon never observed during anesthesia, vascular responses were predicted with Pearson coefficients of 0.91, 0.84, 0.77, 0.92 ($n=4$ OBs, 3 mice). Altogether, these results indicate that the μTF can be efficiently used to predict vascular responses from neuronal Ca^{2+} signals, across mice, stimulation parameters and brain states. We next asked whether this quantitative approach of linking neuronal and local vascular responses with the μTF could be extended to mesoscopic imaging techniques. To establish μTF s, we measured fUS CBV responses from the single voxel ($\sim 100 \times 100 \times 200 \mu\text{m}$) comprising the most responsive glomerulus imaged with 2PM.

Single voxel fUS responses faithfully report microscopic responses. To co-register the 2PM and fUS imaging systems, the ultrasonic probe was attached to the microscope objective by means of a 3D-printed holding piece. A 50- μm glass bead, embedded in agar, was first localized with 2P imaging at given coordinates in 3D. The ultrasonic probe was then precisely translated over the bead and moved back and forth in the x , y , and z directions (Fig. 3a). This allowed to collect the Gaussian fUS intensity profiles in 3D for a selected voxel, which center was then fixed at the profile maxima, allowing the back and forth

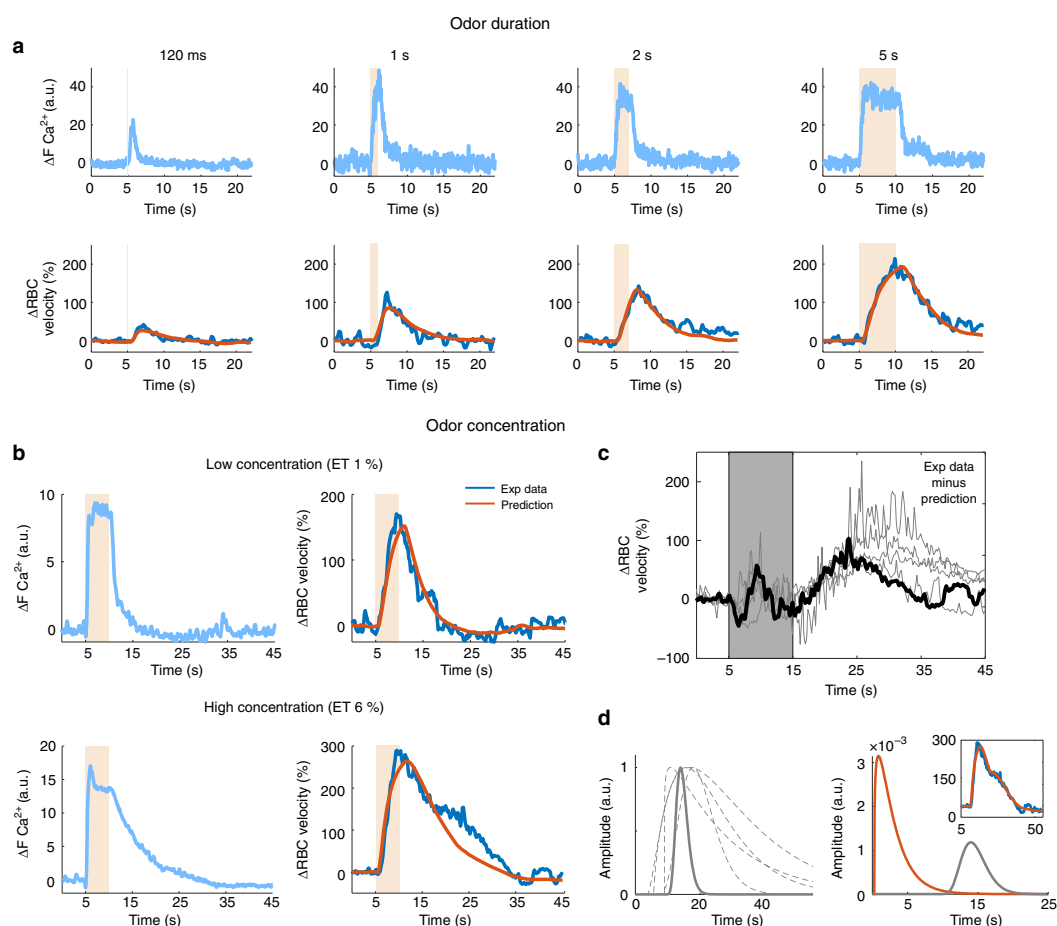


Fig. 2 Robustness of TFs with respect to stimulation duration and intensity. **a** Ca^{2+} (top) and RBC velocity (bottom) responses to single sniff (120 ms), 1 s, 2 s, and 5 s odor stimulations. Using the standard μTF (optimized with ET 1%, 5 s), vascular response predictions (orange traces) are robust for all durations. **b** Increasing the odor concentration from 1% (top traces, average of two trials) to 6% ET (bottom traces, average of three trials) reveals a delayed secondary vascular response, which is not correctly predicted (orange trace) with the standard TF (1% ET, 5 s). **c** Vascular responses after subtraction of their prediction using the standard TF ($n = 5$ mice, data from **b** in black). Note that trace fluctuations between 5 and 15 s (gray background) result from slight differences of onset, slope, and response peak between real and predicted responses. The second vascular component is clearly delayed by ~ 10 s. **d** Left, novel TFs optimized on vascular responses after subtraction (the thick trace is the TF from the data in **b** and **c**). Note the heterogeneity in peak jitter and shape. Right, combination of the two μTF s (standard μTF in orange, second component μTF in gray) can predict correctly the entire vascular response (see inset, same trace as in **b**) after adjustment of their corresponding amplitude.

displacement of the two imaging systems at the same co-registered location with a micrometric resolution (Fig. 3b), as well as the collection of micro/mesoscopic functional dataset. We first acquired 2PM neuronal and vascular data from the most responsive glomerulus upon 1% ET (5 s). fUS power Doppler signals were then collected from (1) the single voxel centered on the most responsive glomerulus, and (2) from a small voxel group (the specific voxel plus its five nearest neighbors) to account for the vascular backpropagation (Fig. 3c, d). Figure 4a shows that the time course of 2PM Ca^{2+} , RBC velocity and mesoscopic fUS $\Delta\text{PD}/\text{PD}$ responses acquired at two odor concentrations (1 and 6% ET) and two stimulation durations (120 ms and 5 s). The responses increased with either odor duration or concentration ($n = 5$ mice). Vascular responses (microscopic and mesoscopic)

were remarkably similar (Pearson coefficients between RBC velocity and fUS data (single voxel): 0.52 ± 0.21 (1%, 120 ms ET), 0.73 ± 0.05 (6%, 120 ms ET), and 0.67 ± 0.13 (1%, 5 s ET), 0.70 ± 0.05 (6%, 5 s ET) mean \pm SD). Using our previous TF optimization approach (single gamma-component), we obtained an MTF between neuronal Ca^{2+} and the co-registered single fUS voxel signal. In comparison with the μTF , this neuron-derived MTF had a slower decay (Fig. 4b). The prediction quality of single voxel fUS responses were low for brief stimulations, in particular at 1% ET (with the μTF : 0.33 ± 0.13 ; with the MTF: 0.35 ± 0.16 , mean \pm SD) (Fig. 4c). However, all predictions improved when considering fUS responses from the six voxels, i.e., with a better signal-to-noise ratio and a dynamic similar to that of the co-registered voxel. Note that upon high odor concentration (6% ET,

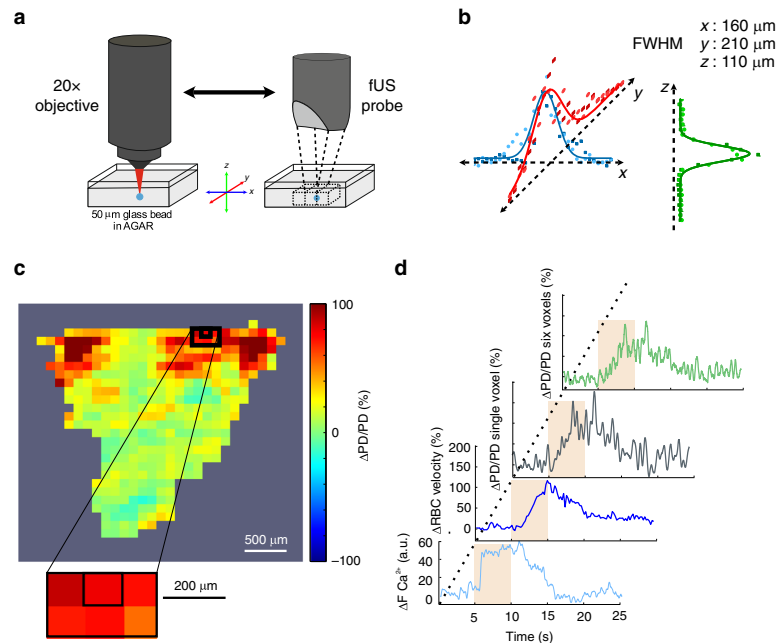


Fig. 3 Co-registration of fUS (single voxel) and two-photon imaging. **a** Schematics of the two imaging systems. The ultrasonic probe is attached to the $\times 20$ microscope objective by means of a 3D-printed holding system. A 50- μm glass bead, embedded in agar, is first localized with 2P imaging. The ultrasonic probe is then translated over the bead and placed at a position where the fUS signal maxima in x , y , and z are centered in a given voxel. The fUS and 2P imaging systems can then be displaced back and forth to the same co-registered location with a micrometric resolution. **b** Intensity profiles of fUS signals in x , y , z . FWHM for full width at half maxima. Square and circle points were acquired during back and forth acquisitions. **c** $\Delta\text{PD}/\text{PD}$ fUS activation map of an olfactory bulb coronal section in response to 1%, 5 s ET. The enlarged area shows the voxel centered on the most responsive glomerulus (first imaged with 2P) plus its five neighboring voxels. **d** From bottom to top, Ca^{2+} and RBC velocity glomerular responses (2P imaging), $\Delta\text{PD}/\text{PD}$ fUS responses from the co-registered voxel and the six voxels.

5 s), fUS responses showed a delayed secondary component (Supplementary Fig. 3), similar to RBC velocity responses at this concentration (Fig. 2b, c). Can the MTF be used with techniques reporting other types mesoscopic signal? We analyzed the freely available data from Winder et al.²⁷, collected in the somatosensory cortex of awake mice, and in which neuronal activity was monitored with electrophysiology and mesoscopic CBV responses with intrinsic optical recordings (IOS). Whisker stimulations evoked brief changes in the local field potential (LFP) gamma-band power and in light reflectance. Even though neuronal (Ca^{2+} versus gamma-band power in the LFP) and vascular (RBC velocity versus IOS reflectance) are different proxies signals, the MTF was still robust in predicting mesoscopic CBV changes (Supplementary Fig. 4b, d). Nonetheless, an ad hoc TF could be further optimized using our computing approach (Supplementary Fig. 4b–e, brown versus orange predictions), yielding a significant improvement to the prediction quality. In total, the MTF computed in the OB remains surprisingly robust in predicting vascular responses in the neocortex, even though it improves with optimization based on the dataset.

Statistical analysis of single versus six voxels fUS responses. We have recently shown that due to the poor specificity of odorant receptors and the vascular backpropagation, ET 1 and 6% activate numerous voxels in the OB²². The co-registration enabled us to test whether at such concentrations, blood flow responses and statistical analysis enable to extract the voxel containing the most

sensitive glomerulus from its five neighboring voxels. We first quantitatively compared fUS responses (areas under curves of $\Delta\text{PD}/\text{PD}$ responses) in the six voxels at 1% ET (5 s) (Fig. 5a). The fUS response from the voxel containing the most sensitive glomerulus was the largest in only one out of five mice. Statistical analysis, using statistical parametric mapping, the general linear model, RBC velocity responses as regressors and a statistical threshold ($p < 0.01 \pm \text{FWE}$), revealed that, as for the fUS signal (AUC), the t value of the voxel containing the most sensitive glomerulus was not systematically the highest (Fig. 5b). These findings remained valid at all four stimulation paradigms (Fig. 5c, d). Altogether these results point to the fact that at 1 and 6% ET, activation maps cannot sort out the voxel containing the most sensitive glomerulus.

Discussion

The OB glomerulus is an efficient biological model to compute TFs between neuronal activation and microscopic/mesoscopic vascular responses and test their use as surrogates of NVC, providing that the model strengths and weaknesses are recognized: as the first olfaction relay, odor processing by centrifugal inputs is moderate in contrast to sensory cortex models, and odor triggers local blood flow responses that are odorant-specific, concentration-dependent and correlated to local presynaptic and postsynaptic responses^{7,28–30}. However, odorant receptor specificity is odor concentration-dependent and additionally, vascular responses are not entirely specific as synaptic activation triggers a

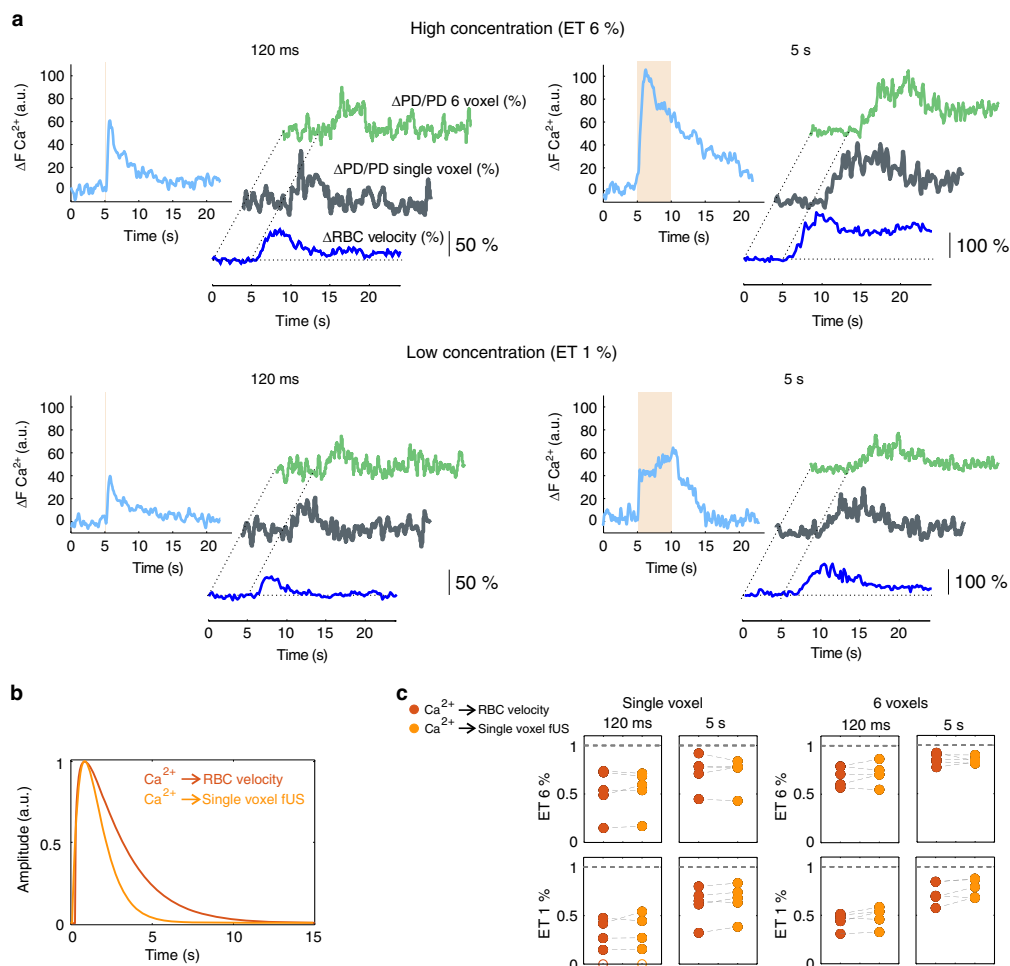


Fig. 4 Co-registration of microscopic and mesoscopic vascular responses to odor. **a** Microscopic responses were acquired in a glomerulus located in the center of a fUS voxel. The four panels illustrate Ca^{2+} , RBC velocity, and the three types of fUS responses (from the specific co-registered single voxel and the group of six voxels) to four odor stimulation protocols (120 ms and 5 s stimulations at two concentrations). All responses increased with time and odor concentration. The $\Delta PD/PD$ fUS traces from single voxels are in bold. **b** Comparison of the μTF and the mesoscopic mTF optimized between ΔCa^{2+} (ET 1%, 5 s) and the co-registered single fUS voxel signal. **c** Prediction quality (Pearson coefficients) of single and six voxels fUS responses using either the μTF (red), the neuron-derived mTF (orange) ($n = 5$ mice). Note that in one mouse (bottom left plot), the single voxel signal ~ 0 (open circles). Source data are provided as a Source Data file.

vascular signal that propagates retrogradely along the vascular arbour, causing a dilation of upstream arterioles⁵. Consequently, even when targeting the glomerulus most sensitive to a given odorant, in our case ET, odor stimulation will always cause an increase of blood flow over a brain volume larger than that of activated neurons. The use of TFs is thus limited by the spatial and temporal resolution of NVC. Ideally, modeling of NVC should give a better read out to predict functional hyperemia, as well as allowing better inference about neuronal activation from functional hyperemia. Unfortunately, there is a general agreement that transmitter release triggers a complex feed-forward cascade, and the differential weight of all the cellular partners involved in NVC remains unclear. The timing of Ca^{2+} signaling in astrocyte processes, endothelial cells, or contractile cells (enwrapping

pericytes and smooth muscle cells) is compatible with a role of these cells in NVC but without testing the functional consequences of silencing specific mechanisms, NVC modeling remains premature. By bypassing the NVC cellular cascade, TFs thus appear as efficient surrogates linking local neuronal activation to vascular responses.

TFs have been used to predict CBV and BOLD responses to spontaneous and evoked neuronal activation in numerous studies^{27,31–37}. The novelty of our approach relies on several technical advances: (i) we measured neuronal responses from a given compartment (the apical dendritic tuft) of specific cells (OB principal cells); (ii) we characterized the μTF at the site of synaptic activation; (iii) we used a machine-learning non-deterministic approach, based on the simulated annealing

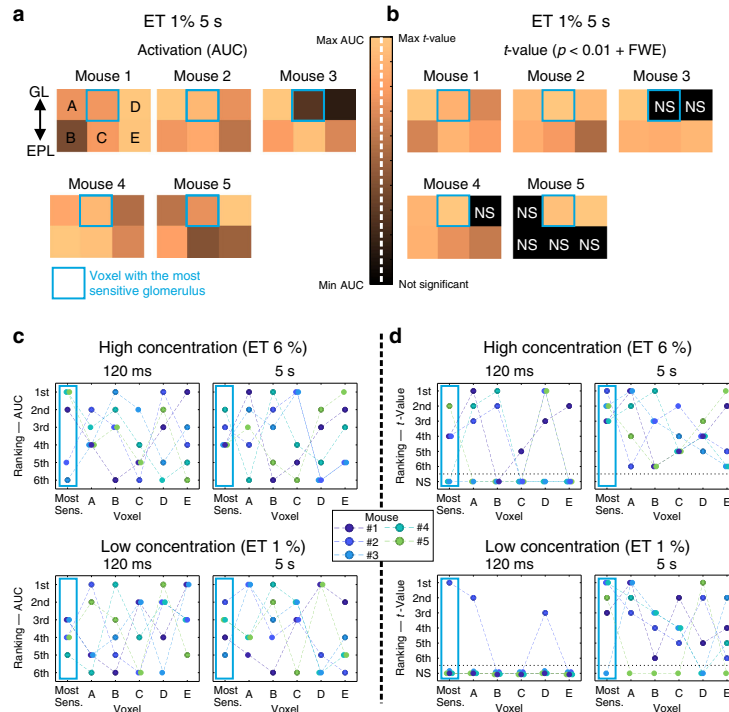


Fig. 5 Spatial resolution of fUS responses. **a** Quantification of fUS responses (area under the curve, ET 1%, 5 s) in the voxel containing the most sensitive glomerulus (outlined with a blue frame) and the five neighboring voxels (A–E, $n = 5$ mice, GL glomerular layer, EPL external plexiform layer). The color map shows that only in one case, the largest response was located in the blue voxel. The color bar was scaled with respect to the highest AUC value across the six voxels. **b** Statistical analysis (GLM) of fUS responses in the corresponding voxels using the RBC velocity response (CBV flowing at $0.5\text{--}1.5\text{ mm s}^{-1}$) as a regressor. The t value for the voxel containing the most sensitive glomerulus was not systematically the highest one. The applied statistical threshold was $p < 0.01 + \text{FWE}$ correction. NS for not significant. **c** Quantification of fUS responses (AUC) for four stimulation conditions. For the five mice, the voxel containing the most sensitive glomerulus and the other five voxels were ranked with the 1st place assigned to the voxel with the highest AUC value. **d** Statistical quantification of fUS responses with ranking based on t values. The 1st place was assigned to the highest t value. Source data are provided as a Source Data file.

algorithm, to optimize our TFs; (iv) we validated the robustness and reliability of the μ TF across mice and stimulation parameters; (v) we co-registered micro and mesoscopic vascular signals with the best spatial and temporal resolution so far and could compare fUS responses of the voxel comprising the activated synapses to neighboring voxel responses. Note that the comparisons were specifically limited to CBV changes in vessels with slow velocities, i.e., in capillaries^{16,22,38}. These advances allowed us to uncover several aspects of NVC. The μ TF had fast dynamics compatible with the previous finding⁵ that Ca^{2+} drops within ~ 300 ms in mural cells along the upstream arteriolar compartment, triggering vessel dilations. The μ TF was robust across mice and a wide range of stimulation duration and intensities. It is important to stress that between different animals, the μ TF robustness concerned the dynamics of NVC but not its amplitude. Interestingly, upon very strong stimulation, the μ TF and its vascular response prediction revealed a secondary and delayed CBV response. Note that ET at high odor concentration did not cause any respiration change, suggesting that there was no irritation from the stimulus. Bimodal vascular responses have previously been reported^{39,40}, Schulz et al.²⁶ suggesting that it results from the activation of astrocytes. Whatever mechanisms are responsible of the deviation from the standard μ TF, our observations imply that NVC, even in a small

and well characterized neuronal network, is robust, but only within a given activation range, since responses become bimodal with strong odor stimulation. This observation is essential to correctly process brain activation maps with blood-flow-based imaging techniques and interpret the linearity of signal processing upon strong stimulation.

In the second part of our study, we investigated the extent to which functional hyperemia measured at the site of synaptic activation is translated at the mesoscopic level, using CBV measurements with functional ultrasound imaging. fUS is now used to image functional neural circuits in the entire brain, yet, the biological nature of the fUS signal needs further characterization with simultaneous recording/imaging of neuronal activity. We find that fUS responses within the single voxel comprising the most sensitive glomerulus share the general shape and timing of RBC velocity responses. Note that they were so similar in time that they could be linked by a simple Dirac Delta function. As the μ TF tightly couples neural and RBC responses and strongly resembles the single voxel neuron-derived m TF, the fUS signal can be considered as a good reporter of local neuronal activity.

Both μ TF and m TF were obtained from data collected in sedated mice. Surprisingly, they still predicted correctly vascular response dynamics in the OB and the neocortex of awake

animals, even when collecting different types of neuronal and vascular markers. In awake animals, vascular responses are briefer, and in some cases, followed by a delayed negativity/undershoot of unknown cellular mechanism and which was never observed in anesthetized mice. As a result, predictions could be improved with further optimization using the same computing approach.

At 1 and 6%, ET strongly activated the OB, and due to vascular backpropagation^{4,5} and nonselective activation of several glomeruli, generated a widespread fUS signal in the entire coronal section (see Fig. 3c). This is in line with what we have previously reported (see Fig. 5 in Bojdo et al.²²). Consequently, the fUS response from the voxel containing the most sensitive glomerulus could not be discriminated with respect to the five surrounding voxels, whether assessed on the Power Doppler signal (AUC) or its correlation with RBC velocity responses (GLM analysis). This biological limit points to the risk of inferring with certainty the location of neuronal activation from single fUS voxels, in the OB.

Overall, TFs are efficient tools to report NVC, their robustness revealing a quantitative link between postsynaptic Ca^{2+} signal dynamics and both local microscopic vascular responses and mesoscopic CBV fUS responses.

Methods

Animal preparation. All animal care and experimentations were performed in accordance with the INSERM Animal Care and Use Committee guidelines (protocol numbers CEEA34.SC.122.12 and CEEA34.SC.123.12). Adult mice ($n = 15$, 3–12 months old, 20–35 g, both males and females, housed in 12 h light–dark cycle at 24 °C and 50% humidity, fed ad libitum) were used in this study. *Thy1-GCaMP6f* (GP5.11)⁴¹ mice were obtained from Jackson laboratory and crossed with *M72- > S50-IRES-hChR2-Venus* mice⁴² kindly provided by Thomas Bozza (Department of Neurobiology, Northwestern University, USA). Surgery, anesthesia and the experimental sedation protocol were performed as previously²². For craniotomies, mice were initially anesthetized with an intraperitoneal bolus of ketamine–medetomidine (100 and 10 mg kg⁻¹ body mass, respectively). Anesthesia lasted about 2 h, enough to perform the whole surgery. During surgery, mice freely breathed air supplemented with oxygen (final concentration of 40%) and body temperature was maintained at 36 ± 0.5 °C using a rectal probe and a heating pad. The bone over the OBs was carefully drilled while taking care of not applying pressure and avoiding heat with repetitive applications of a cool ACSF solution⁴³. A sheet of PMP, either 80 or 125 μm thick) was precisely cut to fit the cranium opening and sealed in place with Tetric Evoflow dental cement (Ivoclar Vivadent AG, Schaan, Liechtenstein). The same dental cement was also used to form a head-cap in which a titanium head-bar was embedded after the bone was treated with a primer, Optibond FL (Kerr Italia S.R.L., Salerno, Italia). Antibiotics and anti-inflammatory were administered as in⁴⁵ using Baytril 10% (Bayer, Germany) and Dexazone (Virbac, France) respectively. Buprecaire (Axience, France) was used to relieve pain. Mice were permitted to recover for at least 2 weeks before the experimental sessions began.

Experiments were performed under light sedation: mice were anesthetized for 2 min with 3% isoflurane and then head-fixed while isoflurane was lowered to 2%. A subcutaneous catheter was placed dorsally and medetomidine injected first as a bolus (0.05 mg kg⁻¹) and then immediately at a rate of 0.15 mg kg⁻¹ h⁻¹, which was maintained during the whole experiment. Isoflurane was progressively removed within 40 min. An additional 20 min delay was kept prior to recording. Note that sedation was stable and reliable after 2–3 priming sessions during which the exact same protocol was applied but without recording. During the experiments, breathing was monitored with an 80-μm-tip thermocouple (Omega 5TC-TT-KI-40-1M) connected to a N9212 amplifier (National Instruments, USA) and digitized with a cDAQ-9171 (National Instruments, USA). The thermocouple was placed in front of one of the mouse nostrils and the body temperature was maintained at 36.5 ± 0.5 °C using a rectal probe + heating pad (FHC, Bowdoin, ME). Mice were supplemented with 40% O₂ throughout all experiments.

Odor stimulation. All the experiments were conducted following the same stimulation protocol and materials, so no blinding was performed. Odors were delivered through a home built olfactometer. Odor and exhaust lines were equilibrated for pressure at the start of each experiment and the odor concentration and temporal profile was calibrated at the tubing end before every experiment, using a photo-ionization detector (miniPID 200B, Aurora Scientific, Aurora, Canada). The concentration reached 90% of steady state within ~50 ms and returned to baseline within the same range. The final odor concentration values were calculated after considering the dilution from the supplemental O₂ line that did not pass through the olfactometer. To compare the responses to different odor durations or concentrations, the stimulations were randomly interleaved, discarding anesthesia-

related changes. All microscopic (2PM) and mesoscopic (fUS) acquisitions lasted 30 s, with the exception of strong stimulations (6% ET, 5 s), for which 60 s acquisitions were used to allow complete recovery to baseline. All the traces reported in the figures represent the average of at least three odor applications, with the exception of Fig. 3a, top panel (two traces). Single sniff (120 ms) were usually averaged over 8–12 applications because of the low signal-to-noise ratio, in particular at 1% ET. The odor delivery was finely time-locked with the inhalation period, detected with the nasal thermocouple.

fUS data acquisition and post processing. fUS imaging was performed as follows²². In brief, a linear ultrasound probe (128 elements, 15 MHz central frequency, Vermon, Tours, France), connected to the ultrasound scanner (AixplorerTM, Supersonic Imagine, Aix-en-Provence, France), was placed 3 mm above the window. Custom transmit/receive ultrasound sequences were written in Matlab (Mathworks, USA). The backscattered echoes of ultrasound plane waves were collected and beam formed to produce OB echographic images, in the coronal plane. To increase the SNR of each echographic image taken at 500 Hz, the echographic images were compounded by transmitting several tilted plane waves and adding their backscattered echoes. The compounded sequence resulted in enhanced echographic images, thereby increasing the sensitivity of the Doppler measurement without aliasing in the mouse brain. In this study, the ultrasound sequence consisted of transmitting eleven different tilted plane waves (from -10° to 10° in 2° increments) with a 5500 Hz pulse repetition frequency (500 Hz final frame rate). Tissue signals were removed from backscattered waves using singular value decomposition and elimination of the largest eigenvalues. The Power Doppler was further filtered with a Butterworth filter (fifth order, 10–30 Hz band-pass). Each voxel signal was obtained by the incoherent temporal average of the blood signal. Voxel size at the focal plane was: 100 × 110 μm (x and z direction) and 200 μm (y direction, i.e., slice thickness).

fUS analysis. All analyses were performed with custom made software developed in Matlab 2018a (Mathworks, USA). Beam-formed data resulted in 500 Hz frame rate time series. GLM analysis of fUS data was performed with SPM12. fUS recordings were single voxel under-sampled at 20 Hz using a cubic interpolation ('interp' function, 'pchip' option, Matlab). Each frame was then converted to a NIFTI file. The absence of movement was previously assessed using a custom made Matlab script. No realignment or spatial smoothing was performed with SPM. Regressors used in GLM analyses were the RBC velocities recorded in the same mice. We applied a statistical threshold of $p < 0.01 + \text{FEW}$ correction, in response to each stimulation condition.

2PM acquisition and data analysis. 2PM imaging was performed using an ultra-flexible microscope⁴⁴ and data were collected and analyzed using a custom software. Eighty femtoseconds laser pulses were delivered by a Ti:Sapphire laser at 80 MHz (MaiTai HP DeepSee, MKS-Spectra Physics, Santa Clara, California). An acousto optic modulator (MT110B50-A1.5-IR-HK, AA Optoelectronic, Orsay, France) was used to modulate the laser power. Laser pulses were scanned on the sample with galvanometric mirrors (6215H Cambridge Technology, Bedford, Massachusetts). The excitation light was forwarded through a dichroic mirror (cut-off wavelength, 775 nm FF775-DiO1 Semrock) and focused on the sample with a 20 × 1.0 NA objective (XLUMPLFLN20XW Olympus, Tokyo, Japan). GCaMP6f and Texas Red were excited at 920 nm. The collected emission was separated in two channels with a dichroic mirror (cut-off wavelength, 560 nm FF560-DiO1 Semrock). The signal was filtered with a 525 nm band pass filter (FF03-525/50 Semrock) in the « green channel » and a 620 nm band pass filter (620 nm FF01-624/40 Semrock) in « the red channel ». In both channels, GaAsP PMTs (H10770PA-40; Hamamatsu Photonics, Japan) were used to collect light, and laser reflections were blocked with short pass filters (FF01-750/SP-25 Semrock). PMT signals were amplified, integrated with a custom-built electronic circuit and sampled with a National Instruments acquisition card (PCI 6115). Vessels were labeled with Texas Red dextran (70 kDa, Molecular Probes, ThermoFisher, Waltham, Massachusetts), administered intravenously by retro-orbital injections. Following mapping of the ET activated region in frame scan mode and selection of the most sensitive glomerulus to the odor, broken linescan recordings were performed to record both RBC velocity and Ca^{2+} signals in the neuropil, as previously described⁷. Linescan acquisitions (1.5–3 ms per line) were repeated during the different stimulation protocols, with 3 min between each trial. Ca^{2+} data were interpolated (10 ms cubic interpolation, 'interp' function, 'pchip' option, Matlab), turned into ΔCa^{2+} traces by subtracting the average value of the last 5 s of baseline. RBC velocities were extracted and analyzed using a custom software²². RBC velocity data were interpolated (200 ms, cubic interpolation, 'interp' function, 'pchip' option, Matlab), turned into $\Delta\text{RBC}/\text{RBC}$ traces by subtracting the average value of the last 5 s of baseline and then dividing by it. A median filter of three time points was applied to some traces to attenuate overestimated RBC velocity values.

Co-registration of fUS and two-photon imaging. To ensure that we image the same brain volume with fUS and 2PM, we attached the ultrasonic probe to microscope objective with a custom printed ABS holder (Makerbot 2x, USA). A 50-μm glass bead (Marteau & Lemarié, Sorbiers, France), embedded in 2.5% agar,

Table 1 Parameters of the different TFs computed in this study.

From > To	p_1	p_2	p_3	p_4 (amplitude)
Single-gamma HRF	6	1	0	1
Ca ²⁺ to RBC velocity (ET 1%, 5 s)	1.3	0.5	0.27	0.19
Ca ²⁺ to Single voxel fUS* (ET 1%, 5 s)	1.99	1.27	0.11	0.045

Source data are provided as a Source Data file.
*0 < Time shift (P3) < 0.5.

was first localized with 2PM and then detected with the ultrasonic probe, translated to a position such that the bead fUS signal maxima in x , y , and z were centered in a given voxel (Fig. 4a). The fUS and 2PM imaging systems could then be displaced back and forth to the same co-registered location with a micrometric resolution. Note that in our experimental conditions, two factors may have influenced the speed of sound and thus cause approximation along the z axis: the temperature of the media (brain tissue) and the thickness of the PMP cranial window, both of them creating a Δz approximation $\leq 25 \mu\text{m}$, for a mean speed of sound of $\sim 1500 \text{ m s}^{-1}$.

TF computation. The transfer function captures the dynamic link between neuronal responses and micro/mesoscopic vascular responses. Using Ca²⁺ and RBC velocity data collected with 2PM and fUS CBV data within the co-registered brain volume, we built TFs across the different imaging modalities. We used a fitting approach with a single-gamma distribution function, as there was no undershoot in flow in our data. We added a time-shift parameter with the heaviside unit step function, resulting in a total of four parameters for the optimization problem. These parameters capture the slope, the decay, the amplitude and time-shift, respectively, but they are not independent from each other: the optimization problem presents multiple minima configurations, a condition that is not favorable for quasi-Newtonian optimization algorithms.

All analyses were performed with a custom-written software in Matlab 2018a.

The four-parameters function, $\text{TF}(t) = H(t - p_3)p_4 \left(\frac{(t - p_3)^{p_1 - 1} p_2^{p_1} e^{-p_2(t - p_3)}}{\Gamma(p_1)} \right)$, was optimized by minimizing the sum of the square residuals, using simulated annealing, a machine-learning algorithm (*simulannealbnd* function, Matlab). Note that this is a nondeterministic algorithm: the same set of initial values can bring to different sets of optimized values for the parameters, unless the initial set represent a stable minimum for the optimization function. Note that it was not necessary to modify the Matlab default initial temperature (100) and temperature function (*temperatureexp* function, Matlab). Lower and upper boundaries were set to 10^{-3} and 10, respectively, for all parameters. Upper bounds were occasionally increased up to 20 during some optimizations. For Ca²⁺ to RBC velocity optimization the presence of the time shift granted a better fit of the onset phase of the responses. For Ca²⁺ to fUS optimization, we used a 0–0.5 s time shift.

Transfer functions were computed between two time series (*From* and *To*). Both were cut between 5 and 27 s (for 30 s acquisitions) and between 5 and 59 s (for 60 s acquisitions). *From* signals were Ca²⁺ responses and were interpolated at 50 ms (cubic interpolation, *interp1* function, *pchip* option, Matlab), as Ca²⁺ data can be noisy. *To* signals were either RBC velocity responses, or 1 and 6 voxels Power Doppler responses. The residual sum was computed as the difference between the *To* signal and the convolution of the *From* signal and the TF, down sampled to match *To*.

Simulated annealing being a nondeterministic algorithm, the initial values of the parameters are crucial for the outcome and the same set of initial values can bring to different outcomes at each optimization run. We used an iterative process for which we started with an initial set of values (the ones of the first gamma-component of the standard HRF (6; 1; 0.001; 1) with the time-shift initially set to zero (0.001 for computational requirements), and run the optimization process multiple times (50–100 times). We then scored the final sets of values based on the prediction quality and we took the set with the best prediction, provided its corresponding function started at the origin of the axes and was derivable at least twice (after the time-shift time). This set was then used as an initial set for another batch of multiple runs, and so on, until the algorithm did not improve anymore the prediction made by the set of initial values in a significant manner. Usually this took no more than three iterations (see Supplementary Fig. 1).

The best set of parameter values determined the TF optimized for a given mouse in response to 1% ET, 5 s. We computed the best parameters set for all the 15 recorded mice and checked each TF to find the best one across all mice by means of a leave-one-out cross-validation. In detail, each TF, optimized in a given mouse dataset, was then used to predict the vascular responses of the rest of dataset made other mice recordings. The best TFs, finally called μTF or $m\text{TF}$, were chosen being the best performing on its dataset and on dataset from other mice, on the basis of the highest average Pearson coefficient and smallest coefficient of

variability, the first preferred when the two conditions were not met by any mouse. Numerical values of the optimized TF parameters are provided in Table 1.

Analysis of data from Rungta et al. Vascular responses are those described as juxta-synaptic capillary in Fig. 7 of the original paper⁵. TF was computed as before, except for the fact that time series were only 15 s long. Data were collected in four OB glomeruli from three different mice⁵.

Analysis of data from Winder et al. Data from the original paper²⁷ are available on the following link: <https://psu.app.box.com/v/Winder2017-Code-Data>. We used the data (gamma-band LFP and IOS reflection changes in response to contralateral whisker stimulations) from the 12 mice (*_EVENTDATA_ files). We averaged every trace for both gamma-band LFP and IOS reflection changes. Data were changed into relative values and then averaged for each mouse. TF was computed as before²⁷.

Prediction computation. Micro and mesoscopic vascular predictions were computed by convoluting the Ca²⁺ responses or the step functions with the correspondent TFs. An optimization of the amplitude of the responses was performed to best match predictions over experimental data. We optimized a scaling factor with a classical derivative-free method (*fminsearch* function, Matlab) using the residuals between the prediction and vascular responses from 2 to 8 s after the odor application onset as a cost function. The final prediction was then multiplied by the optimized scaling factor. Note, this post processing does not affect the Pearson coefficient we used for all the quantifications of the study.

Custom made scripts to compute the TFs. A simple graphical user interface version of our scripts is available on GitLab (https://gitlab.com/AlIK_A/buildtf), as well as some data examples in order to give the opportunity to the reader to compute the TFs.

Statistical tests. All statistical analyses are reported in the manuscript, with p values. A confidence level of 5% was chosen, a priori, as threshold for significant difference between samples, however higher confidence levels are reported in some figures, with graphical indicators of p values.

Reporting summary. Further information on research design is available in the Nature Research Reporting Summary linked to this article.

Data availability

The datasets generated and analyzed during the current study are available from the corresponding authors on reasonable request. A subset of our data is available on Zenodo (<https://doi.org/10.5281/zenodo.3773863>) to test our software. Source data are provided with this paper.

Code availability

The whole code used to analyze the datasets and get the results and figures is available from the corresponding authors on reasonable request. As described in the "Methods" section, a simple version of our scripts, with a graphical user interface, and a subset of our data is available on GitLab (https://gitlab.com/AlIK_A/buildtf) and on Zenodo (<https://doi.org/10.5281/zenodo.3773863>).

Received: 29 November 2019; Accepted: 11 May 2020;

Published online: 11 June 2020

References

- Iadecola, C. The neurovascular unit coming of age: a journey through neurovascular coupling in health and disease. *Neuron* **96**, 17–42 (2017).
- Iadecola, C., Yang, G., Ebner, T. J. & Chen, G. Local and propagated vascular responses evoked by focal synaptic activity in cerebellar cortex. *J. Neurophysiol.* **78**, 651–659 (1997).
- Chen, B. R., Kozberg, M. G., Bouchard, M. B., Shaik, M. A. & Hillman, E. M. A critical role for the vascular endothelium in functional neurovascular coupling in the brain. *J. Am. Heart Assoc.* **3**, e000787 (2014).
- Longden, T. A. et al. Capillary K⁺-sensing initiates retrograde hyperpolarization to increase local cerebral blood flow. *Nat. Neurosci.* **20**, 717–726 (2017).
- Rungta, R. L., Chaigneau, E., Osmanski, B. F. & Charpak, S. Vascular compartmentalization of functional hyperemia from the synapse to the pia. *Neuron* **99**, 362–375 (2018).
- Cai, C. et al. Stimulation-induced increases in cerebral blood flow and local capillary vasoconstriction depend on conducted vascular responses. *Proc. Natl Acad. Sci. USA* **115**, E5796–E5804 (2018).

7. Jukovskaya, N., Tiret, P., Lecoq, J. & Charpak, S. What does local functional hyperemia tell about local neuronal activation? *J. Neurosci.* **31**, 1579–1582 (2011).
8. O'Herron, P. et al. Neural correlates of single-vessel haemodynamic responses in vivo. *Nature* **534**, 378–382 (2016).
9. Mace, E. et al. Functional ultrasound imaging of the brain. *Nat. Methods* **8**, 662–664 (2011).
10. Tanter, M. & Fink, M. Ultrafast imaging in biomedical ultrasound. *IEEE Trans. Ultrason. Ferroelectr. Freq. Control* **61**, 102–119 (2014).
11. Osmanski, B. F. et al. Functional ultrasound imaging reveals different odor-evoked patterns of vascular activity in the main olfactory bulb and the anterior piriform cortex. *Neuroimage* **95**, 176–184 (2014).
12. Rungta, R. L., Osmanski, B. F., Boido, D., Tanter, M. & Charpak, S. Light controls cerebral blood flow in naive animals. *Nat. Commun.* **8**, 14191 (2017).
13. Gesnik, M. et al. 3D functional ultrasound imaging of the cerebral visual system in rodents. *Neuroimage* **149**, 267–274 (2017).
14. Mace, E. et al. Whole-brain functional ultrasound imaging reveals brain modules for visuomotor integration. *Neuron* **100**, 1241–1251 (2018).
15. Urban, A. et al. Real-time imaging of brain activity in freely moving rats using functional ultrasound. *Nat. Methods* **12**, 873–878 (2015).
16. Urban, A. et al. Chronic assessment of cerebral hemodynamics during rat forepaw electrical stimulation using functional ultrasound imaging. *Neuroimage* **101**, 138–149 (2014).
17. Bimbar, C. et al. Multi-scale mapping along the auditory hierarchy using high-resolution functional ultrasound in the awake ferret. *Elife* **7**, e35028 (2018).
18. Rau, R. et al. 3D functional ultrasound imaging of pigeons. *Neuroimage* **183**, 469–477 (2018).
19. Dizeux, A. et al. Functional ultrasound imaging of the brain reveals propagation of task-related brain activity in behaving primates. *Nat. Commun.* **10**, 1400 (2019).
20. Demene, C. et al. Functional ultrasound imaging of brain activity in human newborns. *Sci. Transl. Med.* **9**, eaah6756 (2017).
21. Imbault, M., Chauvet, D., Gennisson, J. L., Capelle, L. & Tanter, M. Intraoperative functional ultrasound imaging of human brain activity. *Sci. Rep.* **7**, 7304 (2017).
22. Boido, D. et al. Mesoscopic and microscopic imaging of sensory responses in the same animal. *Nat. Commun.* **10**, 1110 (2019).
23. Uchida, N. & Mainen, Z. F. Speed and accuracy of olfactory discrimination in the rat. *Nat. Neurosci.* **6**, 1224–1229 (2003).
24. Abraham, N. M. et al. Maintaining accuracy at the expense of speed: stimulus similarity defines odor discrimination time in mice. *Neuron* **44**, 865–876 (2004).
25. Rinberg, D., Koulikov, A. & Gelperin, A. Sparse odor coding in awake behaving mice. *J. Neurosci.* **26**, 8857–8865 (2006).
26. Schulz, K. et al. Simultaneous BOLD fMRI and fiber-optic calcium recording in rat neocortex. *Nat. Methods* **6**, 597–602 (2012).
27. Winder, A. T., Echagarra, C., Zhang, Q. & Drew, P. J. Weak correlations between hemodynamic signals and ongoing neural activity during the resting state. *Nat. Neurosci.* **20**, 1761–1769 (2017).
28. Chaigneau, E., Oheim, M., Audinat, E. & Charpak, S. Two-photon imaging of capillary blood flow in olfactory bulb glomeruli. *Proc. Natl Acad. Sci. USA* **100**, 13081–13086 (2003).
29. Chaigneau, E. et al. The relationship between blood flow and neuronal activity in the rodent olfactory bulb. *J. Neurosci.* **27**, 6452–6460 (2007).
30. Storage, D. A., Cohen, L. B. & Choi, Y. Using genetically encoded voltage indicators (GEVIs) to study the input-output transformation of the mammalian olfactory bulb. *Front Cell Neurosci.* **13**, 342 (2019).
31. Silva, A. C. & Koretsky, A. P. Laminar specificity of functional MRI onset times during somatosensory stimulation in rat. *Proc. Natl Acad. Sci. USA* **99**, 15182–15187 (2002).
32. Buxton, R. B., Uludag, K., Dubowitz, D. J. & Liu, T. T. Modeling the hemodynamic response to brain activation. *Neuroimage* **23**, S220–S233 (2004).
33. Sirotni, Y. B. & Das, A. Anticipatory haemodynamic signals in sensory cortex not predicted by local neuronal activity. *Nature* **457**, 475–479 (2009).
34. Aquino, K. M., Robinson, P. A. & Drysdale, P. M. Spatiotemporal hemodynamic response functions derived from physiology. *J. Theor. Biol.* **347**, 118–136 (2014).
35. Gao, Y. R. & Drew, P. J. Effects of voluntary locomotion and calcitonin gene-related peptide on the dynamics of single dural vessels in awake mice. *J. Neurosci.* **36**, 2503–2516 (2016).
36. Uludag, K. & Blinder, P. Linking brain vascular physiology to hemodynamic response in ultra-high field MRI. *Neuroimage* **168**, 279–295 (2018).
37. Lambers, H. et al. A cortical rat hemodynamic response function for improved detection of BOLD activation under common experimental conditions. *Neuroimage* **208**, 116446 (2020).
38. Demene, C. et al. Spatiotemporal clutter filtering of ultrafast ultrasound data highly increases Doppler and fulltrasound sensitivity. *IEEE Trans. Med. Imaging* **34**, 2271–2285 (2015).
39. Silva, A. C., Koretsky, A. P. & Duyn, J. H. Functional MRI impulse response for BOLD and CBV contrast in rat somatosensory cortex. *Magn. Reson. Med.* **57**, 1110–1118 (2007).
40. Hirano, Y., Stefanovic, B. & Silva, A. C. Spatiotemporal evolution of the functional magnetic resonance imaging response to ultrashort stimuli. *J. Neurosci.* **31**, 1440–1447 (2011).
41. Dana, H. et al. Thy1-GCaMP6 transgenic mice for neuronal population imaging in vivo. *PLoS. ONE* **9**, e108697 (2014).
42. Smear, M., Resulaj, A., Zhang, J., Bozza, T. & Rinberg, D. Multiple perceptible signals from a single olfactory glomerulus. *Nat. Neurosci.* **16**, 1687–1691 (2013).
43. Holtmaat, A. et al. Long-term, high-resolution imaging in the mouse neocortex through a chronic cranial window. *Nat. Protoc.* **4**, 1128–1144 (2009).
44. Mayrhofer, J. M. et al. Design and performance of an ultra-flexible two-photon microscope for in vivo research. *Biomed. Opt. Express* **6**, 4228–4237 (2015).

Acknowledgements

Financial support was provided by the Institut National de la Santé et de la Recherche Médicale (INSERM), the European Research Council (ERC-2013-AD6; 339513), the Agence Nationale de la Recherche (ANR/NSF 15-NEUC-0003-02 and NR-16-RHUS-0004 [RHU TRT_cVD]), the Fondation Leducq Transatlantic Networks of Excellence program (16CVD05, Understanding the role of the perivascular space in cerebral small vessel disease) and the IHU FOReSIGHT [ANR-18-LAHU-0001] supported by French state funds managed by the Agence Nationale de la Recherche within the Investissements d'Avenir program. R.L.R. had a postdoctoral fellowship award from EMBO (ALTF 384-2015). We thank Manon Omnes for mice surgeries and Christophe Tourain for technical help.

Author contributions

A.-K.A., P.J.D., S.C., and D.B. designed the experiments. A.-K.A., W.D.H., C.P., P.J.D., S.C., and D.B. designed the analyses. C.D. and M.T. participated to the analysis of the fUS experiments. R.L.R. and P.J.D. provided the data from awake mice. A.-K.A. and D.B. wrote the customized Matlab and LabView scripts for the analyses. A.-K.A. and D.B. conducted the animal experiments and analyzed the data. Y.G.H. designed and built the co-registration setup. A.-K.A., Y.G.H., S.C., and D.B. wrote the original drafts and all authors edited the paper. S.C. and D.B. conceived the project.

Competing Interests

M.T. is co-founder and shareholder in the ICONEUS company. The remaining authors declare no competing interests.

Additional information


Supplementary information is available for this paper at <https://doi.org/10.1038/s41467-020-16774-9>.

Correspondence and requests for materials should be addressed to S.C. or D.B.

Peer review information *Nature Communications* thanks Patrick Hoford and the other, anonymous, reviewer(s) for their contribution to the peer review of this work. Peer reviewer reports are available.

Reprints and permission information is available at <http://www.nature.com/reprints>

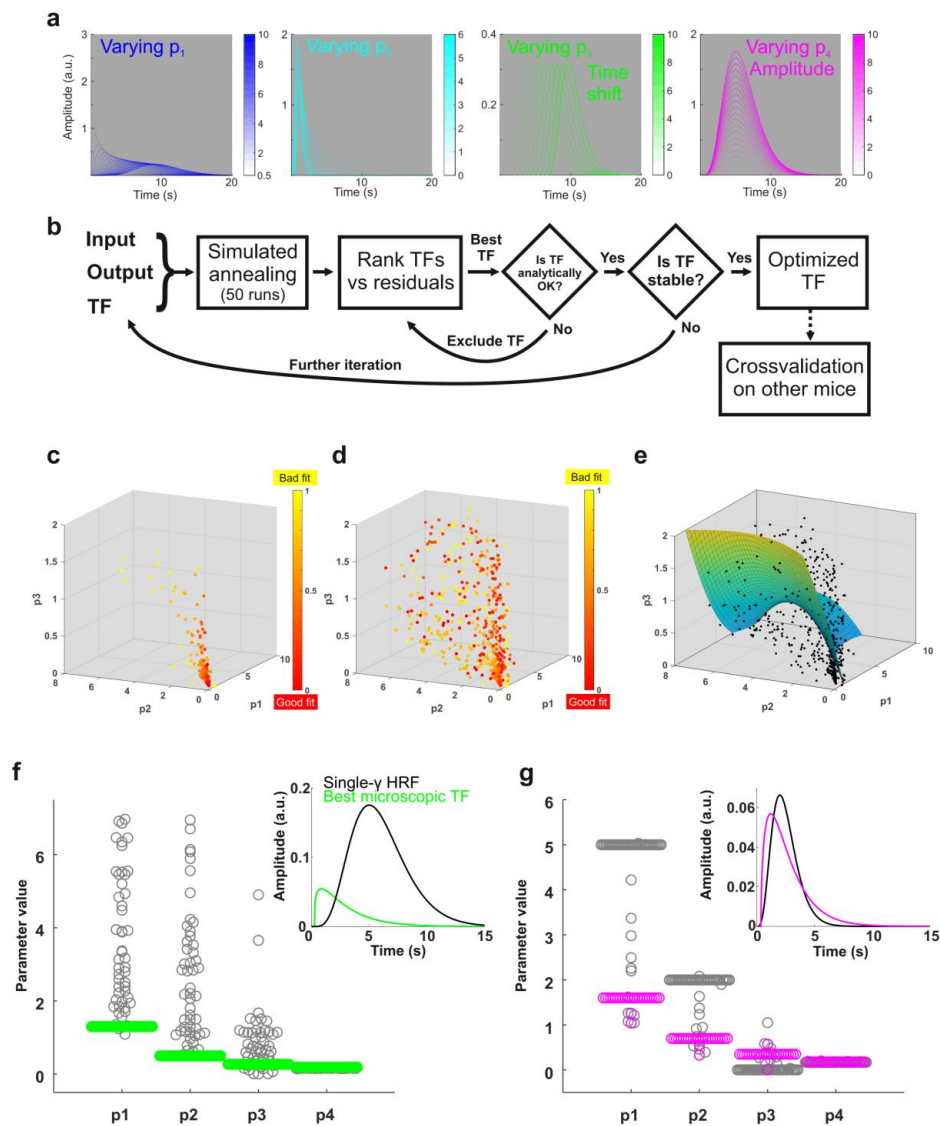
Publisher's note Springer Nature remains neutral with regard to jurisdictional claims in published maps and institutional affiliations.

 **Open Access** This article is licensed under a Creative Commons Attribution 4.0 International License, which permits use, sharing, adaptation, distribution and reproduction in any medium or format, as long as you give appropriate credit to the original author(s) and the source, provide a link to the Creative Commons license, and indicate if changes were made. The images or other third party material in this article are included in the article's Creative Commons license, unless indicated otherwise in a credit line to the material. If material is not included in the article's Creative Commons license and your intended use is not permitted by statutory regulation or exceeds the permitted use, you will need to obtain permission directly from the copyright holder. To view a copy of this license, visit <http://creativecommons.org/licenses/by/4.0/>.

© The Author(s) 2020

Supplementary Informations

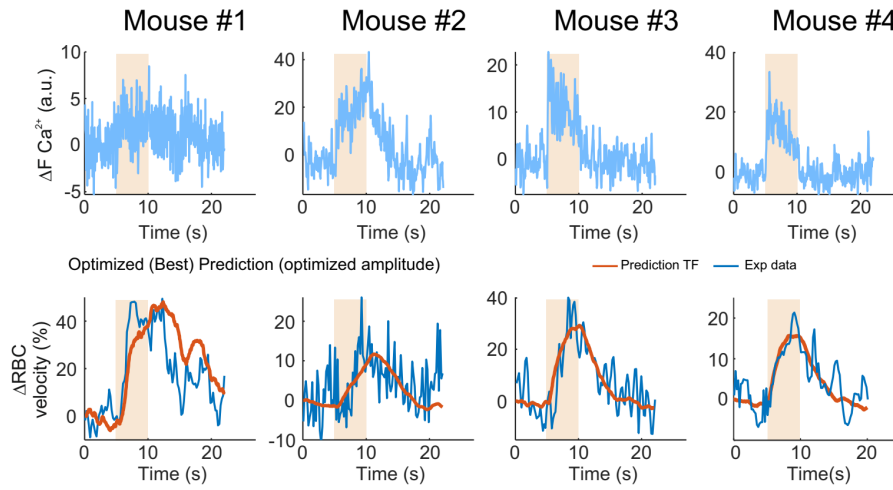
Transfer functions linking neural calcium to single voxel functional ultrasound signal,
Aydin et al., Nat Commun, 2020



Supplementary Fig.1 Legend on the next page

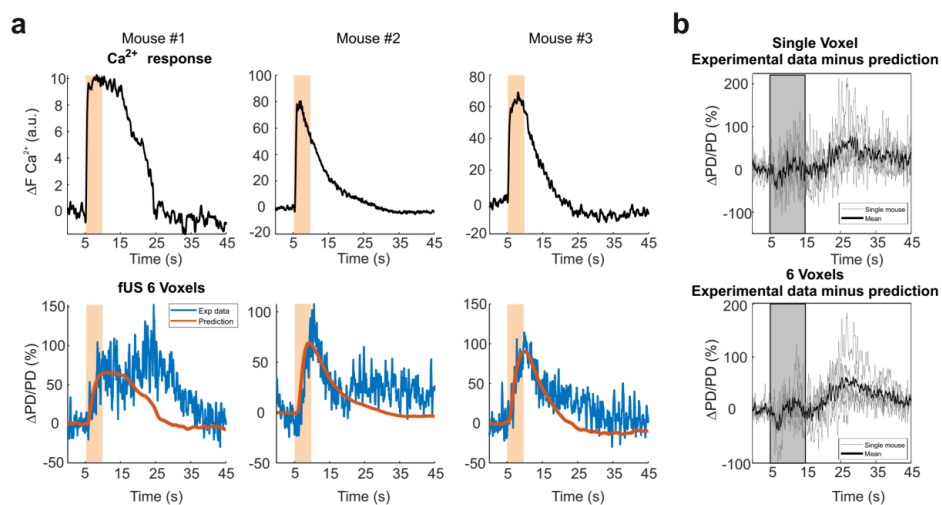
Supplementary Fig. 1 Optimization of the microscopic transfer function (μ TF)

(a) The initial single gamma TF was taken from SPM12, removing the second component (undershoot) and adding a time-shift parameter, thus making a total of 4 free parameters. Each parameter modifies the TF shape as shown in the panels. The color scale (Z axis) is the increasing value of the parameter. Y axis is the amplitude of the TFs generated while increasing the value of the parameter. Note that p_4 (scaling factor) has a major effect on amplitude, p_3 on the onset, p_1 and p_2 affecting the whole dynamics of the TF. (b) The algorithm used in the optimization process: with a machine learning optimization (simulated annealing), the same set of initial values (cost function fixed) result in many optimized TFs, then ranked with respect to their prediction quality. The best TF of the iteration is checked to be analytically acceptable (test on shape, see Methods) or discarded and the next TF in the rank is analyzed and so on. When a TF passes this first check, it is then tested for its stability over a high number of optimization runs (> 40). If the check on the shape eliminates too many TFs or if the TF is not stable over most of the optimization runs, its p_1 - p_4 parameters are passed to another iteration process. (c) The optimized TFs found with simulated annealing can be represented in terms of their first 3 parameters, (p_4 is a scaling factor) and the quality of the fit can be expressed as the inverse of the normalized residuals, color coded. The plot shows 200 optimization runs for a single mouse. Good fit parameters tend to accumulate close to the origin of the p_1 - p_2 axes. (d) Merging the same data with those from 5 mice. (e) 3D fit of order 2 approximates well the residual distribution (fit weighted by the inverse of the residuals). It makes further optimization faster to calculate by restricting the 3D space to a portion mapped by the hyper-plane. (f) Iteration optimization process for the microscopic TF: dispersion of the final value parameters set after optimization starting from the initial parameters of the single gamma-component HRF (gray curve in inset) is represented by grey circles (same p_1 - p_3 values as in (c)). Each optimization run produces a final set, corresponding to a local minimum, usually different from the initial one. In case the local minimum is very stable, the initial and final sets are identical. A second optimization iteration consists in 50 other runs, using the best fit from the previous iteration as the starting value set (green circles). The best fit (green curve in inset) is the one with the lowest residual and analytically acceptable (see Methods). All the green circles are stable, i.e., they do not vary after a new optimization process. Parameter stability over many optimization runs is a mandatory requirement to define a TF as optimal for a given dataset. In the inset, the gray curve represents the single gamma HRF while the green one is the best microscopic TF. (g) The choice of the initial value for the first iteration is important: starting from a function with parameters distant from those of the best TF, as in panel (f), results in heterogeneous fits, some bad and some possibly good. Choosing, instead, a starting TF 'close' to the best one (gray curve in inset) does not provide much heterogeneity in the fits and limits the improvement obtained with a second iteration (pink curve in the inset, similar to the best microscopic TF, but with a worse prediction performance). Source data are provided as a Source Data file.



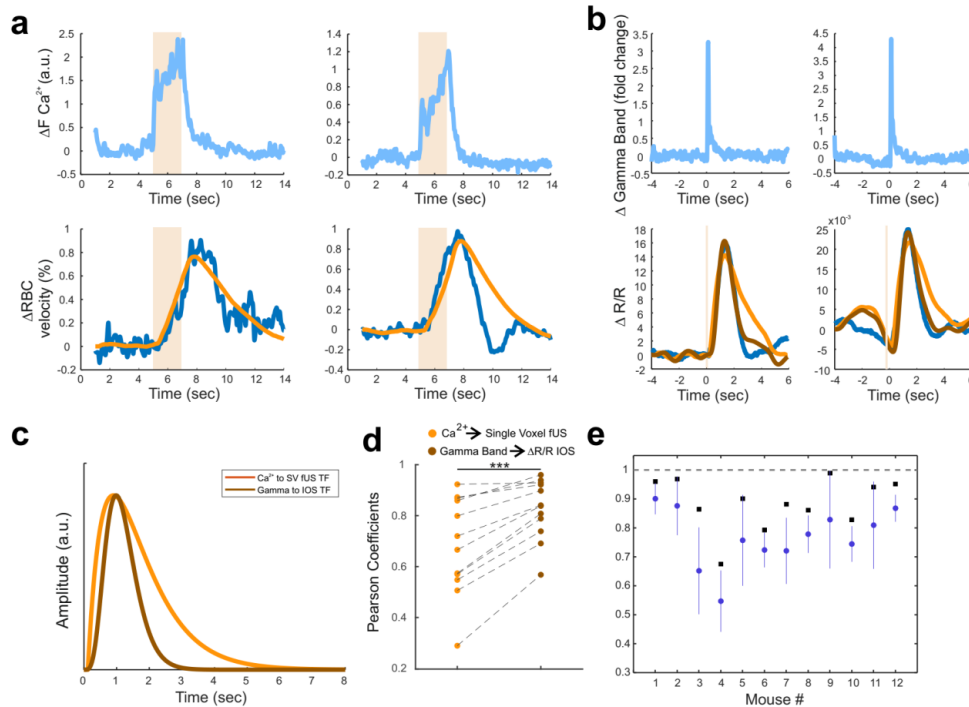
Supplementary Fig. 2 Vascular response predictions to isoamyl acetate (AA), using the ET-based μ TF

Ca^{2+} and RBC velocity responses to AA (1 %, 5 s). Although the μ TF was optimized on responses to ET, it provided good predictions across animals (Pearson coefficient in 4 mice: 0.77, 0.59, 0.86, 0.82).



Supplementary Fig. 3 At high odor concentration, the mTF reveals a delayed secondary component at a mesoscopic scale

(a) Ca^{2+} (top) and fUS (bottom) responses to 6 % ET (5 s) for 3 mice. Vascular responses are not correctly (orange traces) predicted with the mTF. (b) fUS vascular responses (single and 6 voxels) after subtraction of their prediction using the mTF. As at the microscopic level, traces fluctuate between 5 and 15 s (gray background) result from slight difference of onset, slope, and response peak between real and predicted responses. The fUS secondary component is delayed by ~10-15 s.



Supplementary Fig. 4 Application of the TFs to the OB and the somatosensory cortex of awake mice

(a) Ca^{2+} (top) and RBC velocity (bottom) responses to mild odor concentration (orange background) in the OB of awake mice. Data from Rungta et al., 2018¹. (b) Gamma-band LFP (top) and IOS reflection changes (bottom) from the somatosensory of awake mice. Data from Winder et al., 2017². Orange traces are the prediction made by our mTF, brown traces are the predictions made by a new TF optimized on these data (see below). (c) Comparison between the two TFs. (d) Prediction quality of both TFs ($n=12$ mice). Note the improvement with the new TF (paired two-sided t-test, $p=8.10^{-5}$). (e) As in Fig.1d, quantification of the prediction robustness (mean \pm SD, $n=12$ mice) for each TF, either on the data used to compute it (same mouse, self-validation, black square) or on other mice's data (cross-validation, blue symbols). Source data are provided as a Source Data file.

References

1. Rungta, R.L., Chaigneau, E., Osmanski, B.F., & Charpak, S. Vascular Compartmentalization of Functional Hyperemia from the Synapse to the Pia. *Neuron* **99**, 362-375 (2018).
2. Winder, A.T., Echagarruga, C., Zhang, Q., & Drew, P.J. Weak correlations between hemodynamic signals and ongoing neural activity during the resting state. *Nat. Neurosci* **20**, 1761-1769 (2017).

CHAPTER 8

ILISKI, A SOFTWARE FOR ROBUST
CALCULATION OF
TRANSFER FUNCTIONS

PLOS COMPUTATIONAL BIOLOGY

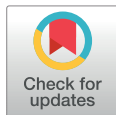
RESEARCH ARTICLE

Iliski, a software for robust calculation of transfer functions

Ali-Kemal Aydin^{1,2}, William D. Haselden³, Julie Dang², Patrick J. Drew⁴, Serge Charpak^{1,2}*, Davide Boido^{1,5,6}*

1 INSERM U1128, Laboratory of Neurophysiology and New Microscopy, Université de Paris, Paris, France, **2** INSERM, CNRS, Institut de la Vision, Sorbonne Université, Paris, France, **3** Medical Scientist Training Program and Neuroscience Graduate Program, The Pennsylvania State University, University Park, Pennsylvania, United States of America, **4** Departments of Engineering Science and Mechanics, Biomedical Engineering, and Neurosurgery, The Pennsylvania State University, University Park, Pennsylvania, United States of America, **5** NeuroSpin, UMR Baobab CEA CNRS, Commissariat à l'Energie Atomique—Saclay Center, Gif-sur-Yvette, France, **6** Université Paris Saclay, Gif-sur-Yvette, France

* These authors contributed equally to this work.

* davide.boido@cea.fr (DB); serge.charpak@inserm.fr (SC)

OPEN ACCESS

Citation: Aydin A-K, Haselden WD, Dang J, Drew PJ, Charpak S, Boido D (2021) Iliski, a software for robust calculation of transfer functions. *PLoS Comput Biol* 17(6): e1008614. <https://doi.org/10.1371/journal.pcbi.1008614>

Editor: Dina Schneidman-Duhovny, Hebrew University of Jerusalem, ISRAEL

Received: December 16, 2020

Accepted: May 18, 2021

Published: June 14, 2021

Peer Review History: PLOS recognizes the benefits of transparency in the peer review process; therefore, we enable the publication of all of the content of peer review and author responses alongside final, published articles. The editorial history of this article is available here: <https://doi.org/10.1371/journal.pcbi.1008614>

Copyright: © 2021 Aydin et al. This is an open access article distributed under the terms of the [Creative Commons Attribution License](https://creativecommons.org/licenses/by/4.0/), which permits unrestricted use, distribution, and reproduction in any medium, provided the original author and source are credited.

Data Availability Statement: Iliski is available on a GitHub repository at <https://github.com/alike-aydin/iliski>, along with more example data on Zenodo (<https://doi.org/10.5281/zenodo.3773863>). The raw data shown in the Figures and used for the

Abstract

Understanding the relationships between biological processes is paramount to unravel pathophysiological mechanisms. These relationships can be modeled with Transfer Functions (TFs), with no need of *a priori* hypotheses as to the shape of the transfer function. Here we present Iliski, a software dedicated to TFs computation between two signals. It includes different pre-treatment routines and TF computation processes: deconvolution, deterministic and non-deterministic optimization algorithms that are adapted to disparate datasets. We apply Iliski to data on neurovascular coupling, an ensemble of cellular mechanisms that link neuronal activity to local changes of blood flow, highlighting the software benefits and caveats in the computation and evaluation of TFs. We also propose a workflow that will help users to choose the best computation according to the dataset. Iliski is available under the open-source license CC BY 4.0 on GitHub (<https://github.com/alike-aydin/iliski>) and can be used on the most common operating systems, either within the MATLAB environment, or as a standalone application.

Author summary

Iliski is a software helping the user to find the relationship between two sets of data, namely transfer functions. Although transfer functions are widely used in many scientific fields to link two signals, their computation can be tricky due to data features such as multi-source noise, or to specific shape requirements imposed by the nature of the signals, e.g. in biological data. Iliski offers a user-friendly graphical interface to ease the computation of transfer functions for both experienced and users with no coding skills. It proposes several signal pre-processing methods and allows rapid testing of different computing approaches, either based on deconvolution or on optimization of multi-parametric functions. This article, combined with a User Manual, provides a detailed description of Iliski

Transfer Functions computations is available in the [Supporting Information](#) files as an HDF5 file.

Funding: Financial support was provided by the Institut National de la Santé et de la Recherche Médicale (INSERM), the Fondation pour la Recherche Médicale (<https://www.frm.org/>, EQU201903007811) to SC, the Agence Nationale de la Recherche (<https://anr.fr/>, ANR/NSF 15-NEUC-0003-02, ANR/TF-IUS-CADASIL and NR-16-RHUS-0004 [RHU TRT_cSVD]) to SC, the Fondation Leducq Transatlantic Networks of Excellence program (<https://www.fondationleducq.org/>, 16CVD05, Understanding the role of the perivascular space in cerebral small vessel disease) to SC, the IHU FOReSIGHT [ANR-18-IAHU-0001] supported by French state funds managed by the Agence Nationale de la Recherche within the Investissements d'Avenir program to SC and the NIH (<https://www.nih.gov/>, R01NS078168) to PJD. The funders had no role in study design, data collection and analysis, decision to publish, or preparation of the manuscript.

Competing interests: The authors have declared that no competing interests exist.

functionalities and a thorough description of the advantages and drawbacks of each computing method using experimental biological data. In the era of Big Data, scientists strive to find new models for patho-physiological mechanisms, and Iliski fulfils the requirements of rigorous, flexible, and fast data driven hypothesis testing.

This is a *PLOS Computational Biology* Software paper.

Introduction

Modelling and understanding of the relationship between complex and intermingled biological signals is often difficult, particularly when the drivers of the signals are unknown. The problem of the relationship between two time series can be addressed using deconvolution, which provides Transfer Functions (TFs) representative of the system processing on the input signal to generate the output signal [1]. Extracting the transfer function linking neuronal activity and imaging data is widely used in functional brain imaging [2–9], but TFs can also solve general problems in signal analysis, such as predicting the output of complex electrical circuits [10] or other industrial systems, for which a proper model is overly complex due to multiple processes working in parallel [11]. In brain imaging based on blood flow dynamics, transfer functions are classically used to lump the multitude of cellular and molecular processes linking neural activation to changes in blood flow. This coupling between neural activity and hemodynamics is known as neurovascular coupling (NVC) [12]. While there are many successful phenomenological models of NVC [3,13–17], most physiology-based models of neurovascular coupling [18–21] focus on a single cellular mechanism. As NVC is mediated through multiple processes (several molecular cascades, each mediated by different cell types), a more integrated approach is necessary. NVC has often been assessed with deconvolution [8,22], either in the frequency domain or with matrix-based approaches, like Toeplitz matrices [23]. While these approaches allow the unbiased extraction of the TF, these deconvolution methods suffer from sensitivity to noise, affecting the quality of the computed TFs. Reducing the noise (or bandwidth) of the signals improves the estimate of the TF. Alternatively, one can opt for optimization of known functions or a kernel of functions [7,9]. The first option may lead to information loss, e.g., in cases where the noise is not well characterized. Sophisticated smoothing methods partially prevent this loss, like Savitzky-Golay filter, or noise modelling as proposed by Seghouane and colleagues [24]. The second option relies on parametric functions to find the TF best linking the input to the output signals. The transfer function for neural activity to hemodynamic signals has been canonically modeled using a gamma-distribution function [3,14–16]. While making assumptions as to the shape of the TF has some drawbacks, it is robust in the face of noise and generates parametric representations of intrinsically smooth TFs. These approaches still can suffer from under/overfitting and the search for the minimum of the cost function for ill-posed problems may represent a challenging exercise. A valuable help comes from non-deterministic optimizations like simulated annealing or genetic algorithms, which despite their computational expense have potential advantages in extracting TFs from time series.

Recently, our group has been extensively involved in TF computation of neurovascular coupling in a study based on multi-modal recordings, namely two-photon microscopy and ultrafast functional ultrasound [25]. For the required task, we comprehensively tested many

deconvolution and optimization algorithms to choose the best-suited approach. We noticed that there is no standard software package providing all these different TF extraction tools, nor a program where all these approaches are available in a comfortable signal pre-treatment and I/O workflow. Here, we present Iliski ([Ilɪski]), meaning “relationship” in Turkish), a software which contains all the functionalities that we previously used (Aydin et al.) and which, being open source, can be further improved by the users. Although Iliski was initially thought to help data analysis in Biology, its features make it suitable for diverse applications [26,27].

Design and implementation

Iliski can compute TFs between an input and an output time series, regardless of their nature. The originality of Iliski resides in its multiple options to process and analyze input signals. Iliski provides users with efficient pre-treatment and several deconvolution or optimization algorithms, through a clear graphic interface. It is meant to be easy-to-use for anyone, even with basic digital signal processing skills. The experienced users, instead, will find both convolution and function optimization approaches—two classes of problems usually comprised in different toolboxes—in a single data analysis environment.

Iliski can be used either as a suite of functions or through a Graphical User Interface (Fig 1A). Functions are grouped according to the analysis workflow to keep the interface simple. Fig 1B shows the general purpose of Iliski.

Data loading and pre-treatment

We propose two input files format: either plain text files or HDF5 data, the latter being an open-source file format with advanced database features. As experimental acquisitions are prone to multiple component noise, we provided, as an option to the analysis workflow, smoothing (Savitzky-Golay method) and median filter functions, to exclude outliers. The input and output signals are interpolated to a chosen time interval (Δt). Both signals can be cut between two given time points to study continuous recordings while computing TFs on chunks of signal (Fig 1C). As an option, boxcar function of variable duration can be used in place of the input signal. Note that Iliski was not coded to handle complex-valued signals.

TF computation options

Two main types of TF computation are proposed: deconvolution or function optimization. The former is straightforward, either Toeplitz or Fourier deconvolution, and does not require any specific settings. The latter is the optimization of a parametric function, which requires further settings depending on the chosen algorithm. Beside the proposed fitting functions, the users can input their own function in the graphical interface or add it to the default ones by modifying a text file (the procedure is described in the Iliski Manual). The TF dimension is user-defined, with setting of the TF duration and ‘Sampling Time’ parameters that match the original data or can be augmented by non-linear interpolation. Optimization of parameters can be done with various Matlab algorithms, each coming with pros and cons (see Results section) (Fig 1C, middle).

Evaluation of the TF accuracy

A TF is evaluated comparing its prediction—the convolution of the input signal and the TF—to the expected output. Two metrics are used in Iliski: the Pearson coefficient (*corrcoef* function, Matlab, Fig 1C, right) and the residual sum of squares. The former was chosen to have a metric solely focusing on the dynamic, allowing for inter-subject comparisons, while the latter

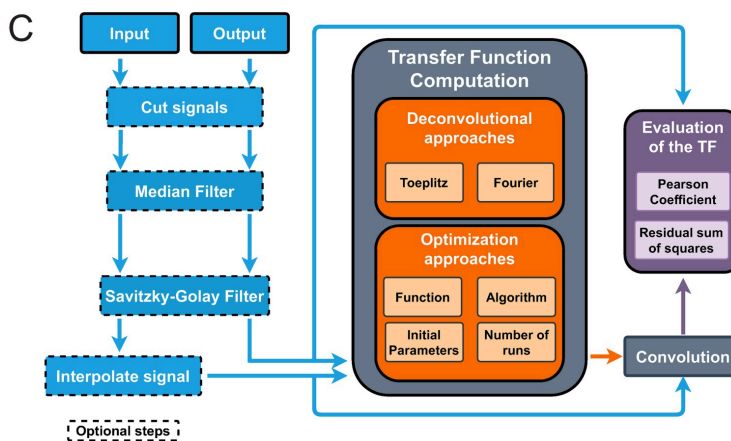
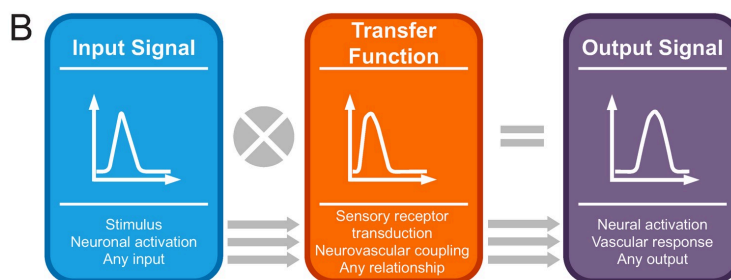
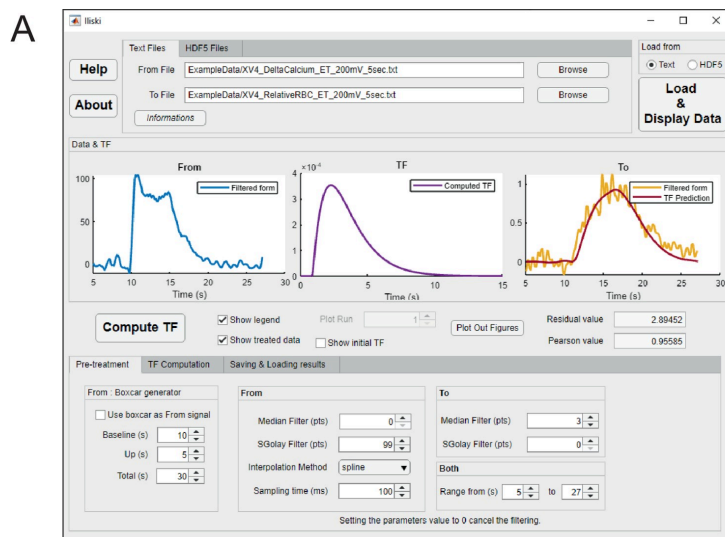


Fig 1. Overview of Iliski. (A) Iliski has a clear interface with tabs bringing through the analysis steps. (B) The usage of Iliski are many; although it has been conceived for biological data, there is no limitation to load any discretized signal. Iliski can easily be used as a tool for fast testing different approaches for TFs computation. (C) Iliski workflow is modular so that signal pre-processing is optional and functions to compute TFs can be modified by the user preserving the I/O modules.

<https://doi.org/10.1371/journal.pcbi.1008614.g001>

evaluates the overall fit, considering the amplitude of the prediction. The cost function of all the optimization algorithms tested in this article is the residual sum of squares (**hereinafter referred to as "residuals"**).

Post-computation

The results structure is arranged to be as informative as possible while avoiding useless repetition of data. Iliski allows for loading previously computed results structures to check them again. After TF computation, results structure can be saved either as XLS file, readable by any Excel-like software, or as a MAT-file (MATLAB formatted binary file format), but it is also available in Matlab workspace to be exported in various data formats by the user.

Implementation

Iliski is accessible both as a GUI and as a set of functions to be used in scripts. It has been developed using Matlab R2018a, with the following dependencies: Optimization Toolbox, Signal Processing Toolbox and Global Optimization Toolbox.

Common user errors are thoroughly prevented by various messages and fail safes. In parallel, all errors are treated and saved in a log file, to allow for efficient bug-fixing by any developer. We purposely kept just a few parameters to modify through the GUI, with the goal of providing an easy-to-use tool for people not used to these functions. In most cases, Matlab default parameters of each deconvolution/optimization function worked well with our data, and we believe that it can be extended to many biological datasets. However, a user skilled with Matlab and optimization algorithms can easily modify the parameters of each function used.

Animal research

This study uses already published data of animal experimentation (Aydin et al.). All animal care and experimentations were performed in accordance with the INSERM Animal Care and Use Committee guidelines (protocol numbers CEEA34.SC.122.12 and CEEA34.SC.123.12).

Results

Here we present the use of Iliski to find the best mathematical representation of neurovascular coupling, an ensemble of cellular mechanisms that links brain activation to local increases of blood flow. Neural activity is reported by GCaMP6f [28], a calcium-sensitive protein expressed in specific neurons. Blood flow is quantified by measuring red blood cells velocity changes in capillaries [29].

Several deconvolution and function optimization algorithms are provided. Choosing the algorithm(s) and settings to compute a TF that gives faithful and robust predictions is not always a straightforward task. It must be done according to the data features. Here we use some data from our published study on neurovascular coupling [25] to point out how TFs change with different algorithms and settings, and we show the critical points in the usage of non-deterministic methods. Finally, we propose a step-by-step guide to optimize the best TF on practical situations.

Choosing the best TF computation approach

Fig 2 shows TF computation with different settings over the same couple of signals: neuronal (Ca^{2+}) activations and vascular (red blood cells velocity) flow increases recorded in a mouse upon odor application. Our example data display unavoidable and complex noise coming from many sources: the biological system, the optical setup, the electronics, etc. Deconvolution with Fourier or Toeplitz approaches predicts the vascular responses very well for a given data set. However, the high-frequency noise is amplified by deconvolution [24] and transmitted to the TF, the predictions are not robust across data sets and the actual dynamics of neurovascular coupling is completely hidden in the TF noise (Fig 2). In this example, we show what we regard as a typical case of overfitting. The TF is capturing the high frequency noise of the system because it does not have any previous expectations for the shape of the relationship between the input and the output signals. This contrasts to the optimization of a parametric function approach which, although it imposes constraints on the shape of the TF, gives meaningful neurovascular relationship and does not need noise clearing. In blood flow-based neuroimaging, the standard function used to represent neurovascular coupling is composed of one or two Γ functions, depending on the nature of the signals, i.e. purely vascular or based on oxygen level[30].

Below is the one Γ -driven function we used with our data.

$$\text{TF}(t; p_1, p_2, p_3, p_4) = H(t - p_3) \cdot p_4 \cdot \frac{(t - p_3)^{p_1 - 1} \cdot p_2^{p_1} \cdot e^{-p_2 \cdot (t - p_3)}}{\Gamma(p_1)}$$

Where p_1, \dots, p_4 are the parameters to optimize, and H is the Heaviside function that includes a time-shift parameter (p_3). In some cases, the time shift significantly improved the prediction and is a known biological phenomenon to consider[31]. Its four parameters are not all independent from one another, e.g., p_1, p_2 and p_4 all impact the TF amplitude. This inter-dependency between the parameters brings an ill-posed optimization problem with multiple local minima of the cost function, the sum of the residual squares, in the 4D space of the parameters. To tackle the function optimization problem, we chose standard algorithms (all implemented in the Optimization Toolbox of Matlab) to encompass the main available options.

A derivative-free optimization method [6] is provided by the *fminsearch* function in Matlab, which uses the Nelder-Mead simplex algorithm. This approach on our data produced a TF with more than one underivable point that is not representative of the smooth dynamic of neurovascular coupling.

Another common option is provided by Quasi-Newton optimization algorithms, which uses an approximation of the Jacobian: for this approach too, we tested an unconstrained built-in method (*fminunc* function, Matlab). This prediction is, overall, as good as with *fminsearch* (Fig 2, Pearson coefficients, *fminunc* vs. *fminsearch*: 0.95 vs. 0.96), but the onset phase is not properly fit. Moreover, although not evident from the plot, the optimized time shift was negative (-120 ms), implying that the onset of the vascular response precedes the neuronal activation.

All the optimization methods tested above are deterministic, meaning that repeating them with the same initial parameters will bring the same result. The pitfall of these methods when applied to ill-posed problem is that optimization process will get attracted to the nearest local minimum, regardless of the many other deeper minima, which may be far away in the parameters space. In other words, deterministic algorithms are sensitive to the initial parameters set before starting the optimization.

Non-deterministic algorithms exist to overcome the local minimum issue, adding some level of randomness in the optimization process, and for this purpose Iliski uses the Simulated

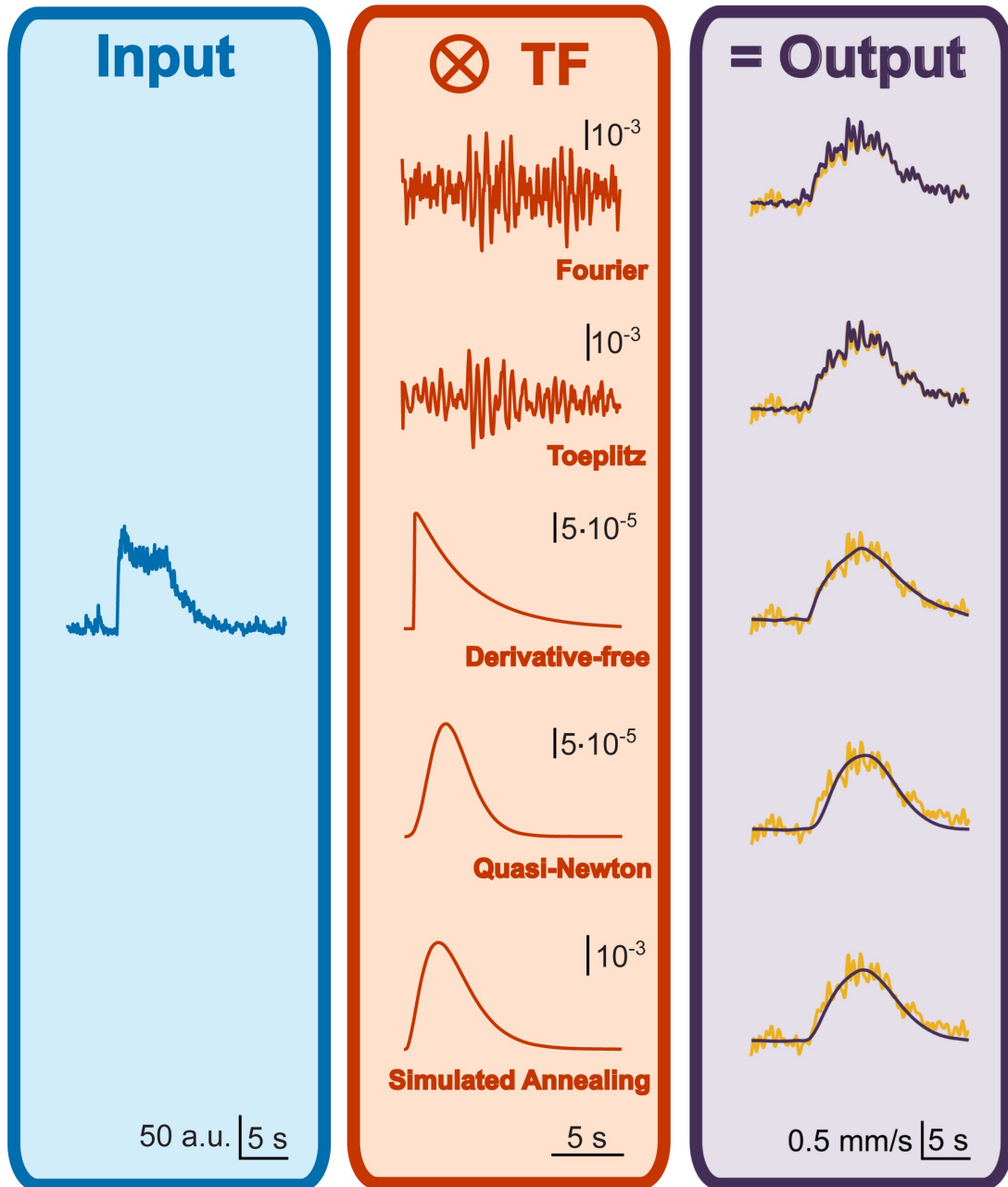


Fig 2. Comparison of deconvolution and optimization algorithms on a batch of data. Odor stimulation elicited a neuronal response in the Olfactory Bulb of a mouse, reported by a calcium-dependent fluorescent signal (in blue, left panel), providing the input of TF computation. Output is given by the vascular response, measured as the change in speed of red blood cells flowing inside a capillary proximal to the recorded neuronal activation (in yellow, right panel). Both experimental data have been resampled at 50ms and used to compute a set of TFs (in orange) either with direct deconvolution approaches (Fourier or Toeplitz methods, middle-upper panel TFs) or with 1- Γ function optimization performed by 3 different algorithms (middle-lower panel TFs). Complex TFs bring accurate prediction but amplify the noise of the data used to deconvolve them, with a consequent loss of robustness on other datasets. Smoother TFs are less accurate on the training dataset, but much robust when applied to test datasets.

<https://doi.org/10.1371/journal.pcbi.1008614.g002>

Annealing algorithm. Each optimization run can yield a different result, reaching possibly a different cost function's minimum each time. We define as 'run' a single application of the optimization with a given set of initial values, and 'iteration' the ensemble of runs sharing the same initial values. By running the algorithm multiple times, one can choose the result with the lowest residual, while avoiding TFs which shape are biologically not acceptable. In fact, to represent the NVC, a TF cannot start at 0 sec, because of the delay due to the cellular cascades triggering the vascular response, and it must be smooth to comply with the progression of biological processes. In Aydin et al. (2020), we described a workflow of runs and iterations to get to biologically consistent TFs (see Supplementary Fig 1 in Aydin et al. [25]). To speed up computation, we imposed bounds over the parameters. Note that such bounds can be set through the Ilski GUI for any constrainable algorithm.

Using our data, Simulated Annealing gave a smooth TF and a prediction as good as *fmin-search* for the onset phase of the vascular response. The data shown in Fig 2 is representative of the rest of the data. In fact, optimization of TFs using neural and vascular recordings from other mice, tested with the same odor stimulation, produced similar residual values of the cost function across the 3 optimization algorithms presented above (1-way ANOVA, $F(2, 17) = 0.035$, $p = 0.97$, Fig 3A). However, as in the example of Fig 2, deterministic algorithms are prone to biologically inconsistent TFs (Fig 3B). The non-deterministic, Simulated Annealing algorithm with subsequent iterations method allows to efficiently exclude these TFs and obtain the best trade-off between prediction performance and biological consistency at the cost of a longer computation time. Direct deconvolution is a good option when the goal is the prediction quality within the training database. Deterministic optimization algorithms are fast but yield to TFs that may have biologically inconsistent dynamics. Note that for all the computations we used a short Δt (50 ms) for interpolation to preserve most of the information.

Evaluating the number of runs in a non-deterministic case

As already mentioned, the Simulated Annealing algorithm requires several runs and iterations to obtain a good TF, where 'run' means a single optimization and 'iteration' an ensemble of runs sharing the same initial values of the fitting function. In our experience, starting the optimization with a 'bad' TF—whose shape is different from what is expected for the processed dataset—helps to collect more local minima in a pool of optimization runs. For example, in our previous study [25], we proposed iterations of 50 runs and started with the initial values of the standard TF (one Γ HRF) which, peaking at 5 seconds, turned to be much slower than any of the optimized TFs. The sequence of 50-runs iterations stopped when, within an iteration, no clear improvement was found in the optimized TF [25]. On average, 2 iterations were sufficient to get a stable TF with Pearson coefficient above 0.9. Here, we investigated if a higher number of runs is beneficial to the detection of the minimum of the cost function and if it prevents the need for further iterations. We compared 50 and 200 runs with single and double iterations, in cascade (Fig 4A). In a mouse dataset, we observed a non-significant trend towards more scattered TFs shapes for computation using 50 runs versus 200 runs (1-way ANOVA, $F(3, 16) = 2.086$, $p = 0.14$, Fig 4B). Similarly, the quality of the TFs did not

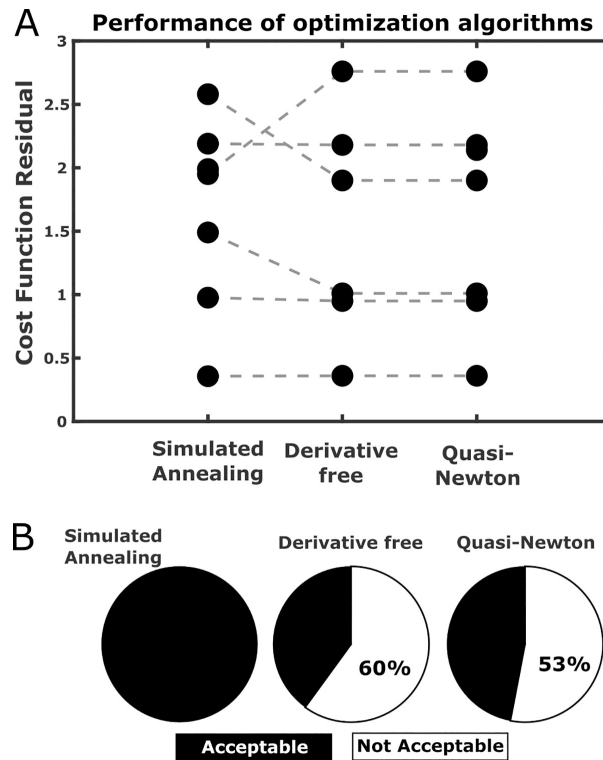


Fig 3. Prediction performance of different optimization algorithms. (A) 3 algorithms were compared in terms of the residuals of the cost function of the optimized TF on 7 mice datasets (Derivative free algorithm failed in optimizing a TF in a mouse). No significant difference was found across the 3 methods. (B) However, simulated annealing was the only approach to provide TFs consistent with the nature of biological data (TF with no more than 1 non-derivable point), while both the other deterministic methods run into inconsistent TFs in roughly 60% of the cases.

<https://doi.org/10.1371/journal.pcbi.1008614.g003>

significantly improve with increasing runs (1-way ANOVA, $F(3, 16) = 2.299$, $p = 0.12$). As a result, TFs with fast dynamics (peaking within 1 and 2 sec), was a common feature independently of the adopted protocol (Fig 4C). In a dataset from another mouse (Fig 4D and 4E), TFs with sparse time to peak values after 200 runs improved after a second iteration, with the same number of runs (2.3 ± 0.3 s VS 1.5 ± 0.1 s (mean \pm SEM), two-tailed T-test, unpaired, $p = 0.02 < 0.05$). Note that this compression of TF dynamics was not accompanied by a significant improvement of the TF quality (residuals: 10.1 ± 2.1 vs. 6.9 ± 0.8 (mean \pm SEM) for 200 and 200 + 200 runs respectively, two-tailed T-test, unpaired, $p = 0.19$). To conclude, depending on the input/output signals, non-deterministic algorithms can produce TFs with different dynamics but close performances in the prediction. The choice of a specific optimization process, with more or less iterations and runs, becomes crucial when the interest is not limited to the prediction quality, but extends to the temporal dynamics of the TF. Because of the noise, TFs with distinct shapes can yield very close residual values.

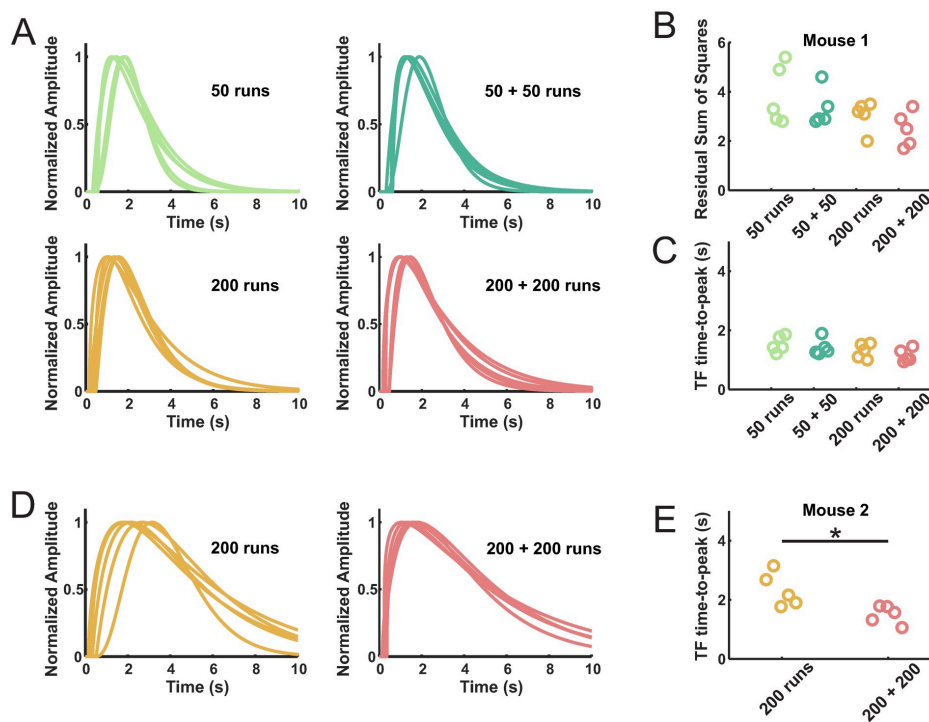


Fig 4. Influence of the number of runs and iterations on the TF shape and quality. (A) Using the Simulated Annealing algorithm, we tested 4 protocols of 50 or 200 optimization runs, either done a single time or repeated (5 TFs computed for each protocol). (B) Residuals of the cost function do not significantly differ across the protocols, although the protocols with the highest number or runs show a trend of smaller residuals. (C) Similarly, there was no significant difference for TFs time-to-peak values. (D, left) Same protocols comparison on a dataset from a different mouse revealed a sparse dynamic of optimized TFs, even if the best TFs were selected on a pool of many TFs (200 runs). (D, right) A second iteration of 200 runs gave more homogeneous TFs dynamics. (E) Quantification of the dynamic heterogeneity was made by measuring the time-to-peak which resulted in a scattered distribution for the 200 runs protocol, packed up repeating the same iteration a second time. Residual values, not reported in this figure, were not significantly different for mouse 1 and 2.

<https://doi.org/10.1371/journal.pcbi.1008614.g004>

Guide to choose the algorithm best fitting your needs

We provide a decision diagram to choose the best approach to compute a TF based on the features of the user's dataset (Fig 5). Nonetheless, we believe it is always a good choice to test different approaches before making the final choice.

Discussion

Iliski provides a user friendly, interactive, and rich in options software for quickly testing different methods and settings to compute TFs between biological processes. In addition to its standard integrated functions, it also allows for user-defined functions of any number of parameters and the possibility of replacing an input signal with a boxcar function, enlarges its usage. Using data from the NVC field, we demonstrate how critical is the choice of the method for computing TFs and the caveats of parameters such as the number

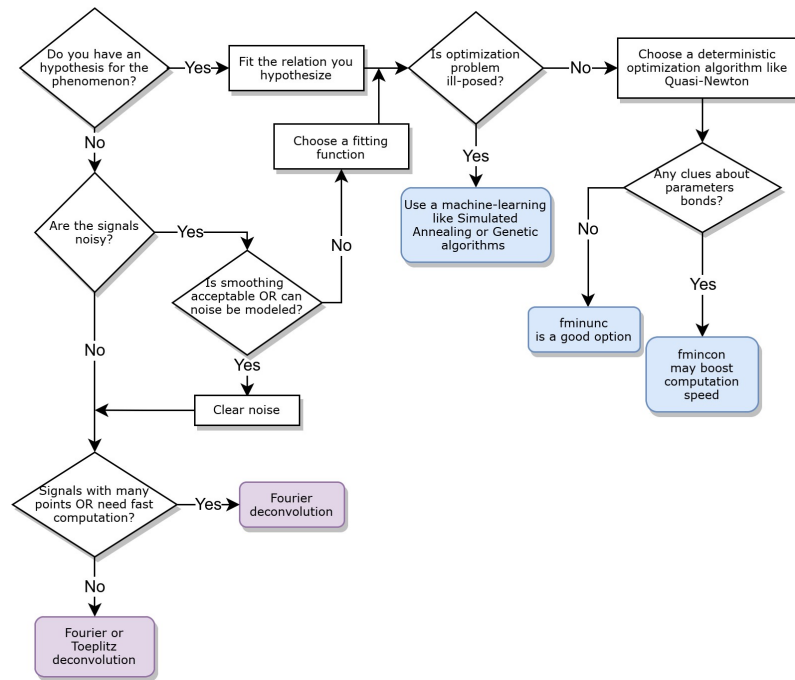


Fig 5. Decision tree to help choosing the most efficient method to compute a TF with Iliski, based on the data features.

<https://doi.org/10.1371/journal.pcbi.1008614.g005>

of iterations necessary to non-deterministic algorithms. Note that we did not report the influence of smoothing, interpolation, fitting and cost functions choice that are also known to affect the result. The use of multimodal datasets, i.e., neuronal calcium signal, measurements of vascular responses at both the microscopic and mesoscopic scales enabled us to demonstrate that NVC is represented by a similar TF which is much faster than the classical HRF, a finding which is getting accepted in the field of brain imaging based on blood flow [5,25,32,33].

Availability and future directions

Iliski is open-source and freely available under the Creative Commons Attribution 4.0 International (CC BY 4.0) license. Iliski is maintained on GitLab, enabling user-friendly bug report and community work to make the tool fit the users' need. It can be found here: <https://github.com/alike-aydin/Iliski>.

In the neurovascular imaging field, computing the hemodynamic response function is paramount to interpreting vascular activation in terms of neural activation. In any other field, computing TFs may be of help to go deeper in the interpretation of the results. For these reasons, we think it is extremely helpful to have a data analysis tool which lets fast testing of different algorithms with a user-friendly interface.

Supporting information

S1 Data. Raw Data: This HDF5 files contains both the raw numerical data shown in the figures and the experimental biological data used to compute them with Iliski.

(H5)

S2 Data. GitHub Repository Clone: This ZIP file contains a clone of the GitHub repository at the time of the publication (also available at <https://doi.org/10.5281/zenodo.4765555>).

Current version is available at <https://github.com/alike-aydin/Iliski>.

(ZIP)

S3 Data. Example Data: This ZIP file contains example data for testing purposes. A detailed description of the data is available on Zenodo at <http://doi.org/10.5281/zenodo.3773863>.

(ZIP)

S1 Text. User Manual: This is Iliski's User Manual at the time of the publication. Current version is available in the GitHub repository at <https://github.com/alike-aydin/Iliski>.

(PDF)

Acknowledgments

We thank Yannick Goulam Houssen for his insights during the development process.

Author Contributions

Conceptualization: Ali-Kemal Aydin, Serge Charpak, Davide Boido.

Data curation: Ali-Kemal Aydin.

Formal analysis: Ali-Kemal Aydin, Julie Dang, Davide Boido.

Funding acquisition: Serge Charpak.

Investigation: Ali-Kemal Aydin, Davide Boido.

Methodology: Ali-Kemal Aydin, William D. Haselden, Davide Boido.

Software: Ali-Kemal Aydin, Julie Dang, Davide Boido.

Supervision: Serge Charpak, Davide Boido.

Validation: Ali-Kemal Aydin.

Visualization: Ali-Kemal Aydin.

Writing – original draft: Ali-Kemal Aydin, Davide Boido.

Writing – review & editing: Ali-Kemal Aydin, William D. Haselden, Patrick J. Drew, Serge Charpak, Davide Boido.

References

1. Dijk G van. Distribution Theory Convolution, Fourier Transform, and Laplace Transform, 2013.pdf. Gruyter de, editor. 2013.
2. Marmarelis PZ, Naka K-I. White-Noise Analysis of a Neuron Chain: An Application of the Wiener Theory. *Science*. 1972; 175: 1276–1278. <https://doi.org/10.1126/science.175.4027.1276> PMID: 5061252
3. Silva AC, Koretsky AP, Duyn JH. Functional MRI impulse response for BOLD and CBV contrast in rat somatosensory cortex. *Magnet Reson Med*. 2007; 57: 1110–1118. <https://doi.org/10.1002/mrm.21246> PMID: 17534912

4. Theunissen FE, David SV, Singh NC, Hsu A, Vinje WE, Gallant JL. Estimating spatio-temporal receptive fields of auditory and visual neurons from their responses to natural stimuli. *Netw Comput Neural Syst.* 2009; 12: 289–316. <https://doi.org/10.1080/net.12.3.289.316>
5. Lambers H, Segeroth M, Albers F, Wachsmuth L, Alst T van, Faber C. A cortical rat hemodynamic response function for improved detection of BOLD activation under common experimental conditions. *NeuroImage.* 2019; 116446. <https://doi.org/10.1016/j.neuroimage.2019.116446> PMID: 31846759
6. Sirotin YB, Das A. Anticipatory haemodynamic signals in sensory cortex not predicted by local neuronal activity. *Nature.* 2009; 457: 475. <https://doi.org/10.1038/nature07664> PMID: 19158795
7. Cardoso M, Lima B, Sirotin YB, Das A. Task-related hemodynamic responses are modulated by reward and task engagement. *PLOS Biology.* 2019; 17: e3000080. <https://doi.org/10.1371/journal.pbio.3000080> PMID: 31002659
8. Winder AT, Echagarruga C, Zhang Q, Drew PJ. Weak correlations between hemodynamic signals and ongoing neural activity during the resting state. *Nat Neurosci.* 2017; 20: 1761–1769. <https://doi.org/10.1038/s41593-017-0007-y> PMID: 29184204
9. Herman M, Cardoso M, Lima B, Sirotin YB, Das A. Simultaneously estimating the task-related and stimulus-evoked components of hemodynamic imaging measurements. *Neurophotonics.* 2017; 4. <https://doi.org/10.1117/1.NPh.4.3.031223> PMID: 28721355
10. Basso CP. Linear Circuit Transfer Functions. n.d. <https://doi.org/10.1002/9781119236344>
11. Sayyafzadeh M, Pourafshary P, Haghghi M, Rashidi F. Application of transfer functions to model water injection in hydrocarbon reservoir. *J Petrol Sci Eng.* 2011; 78: 139–148. <https://doi.org/10.1016/j.petrol.2011.05.009>
12. Iadecola C. The Neurovascular Unit Coming of Age: A Journey through Neurovascular Coupling in Health and Disease. *Neuron.* 2017; 96: 17–42. <https://doi.org/10.1016/j.neuron.2017.07.030> PMID: 28957666
13. Nishimoto S, Vu AT, Naselaris T, Benjamini Y, Yu B, Gallant JL. Reconstructing Visual Experiences from Brain Activity Evoked by Natural Movies. *Curr Biol.* 2011; 21: 1641–1646. <https://doi.org/10.1016/j.cub.2011.08.031> PMID: 21945275
14. Goense JBM, Logothetis NK. Neurophysiology of the BOLD fMRI Signal in Awake Monkeys. *Current Biology.* 2008; 18: 631–640. <https://doi.org/10.1016/j.cub.2008.03.054> PMID: 18439825
15. Boynton GM, Engel SA, Heeger DJ. Linear systems analysis of the fMRI signal. *NeuroImage.* 2012; 62: 975–984. <https://doi.org/10.1016/j.neuroimage.2012.01.082> PMID: 22289807
16. Boynton GM, Engel SA, Glover GH, Heeger DJ. Linear Systems Analysis of Functional Magnetic Resonance Imaging in Human V1. *J Neurosci.* 1996; 16: 4207–4221. <https://doi.org/10.1523/JNEUROSCI.16-13-04207.1996> PMID: 8753882
17. Huo B-X, Gao Y-R, Drew PJ. Quantitative separation of arterial and venous cerebral blood volume increases during voluntary locomotion. *NeuroImage.* 2014; 105: 369–79. <https://doi.org/10.1016/j.neuroimage.2014.10.030> PMID: 25467301
18. Buxton RB, Wong EC, Frank LR. Dynamics of blood flow and oxygenation changes during brain activation: The balloon model. *Magnet Reson Med.* 1998; 39: 855–864. <https://doi.org/10.1002/mrm.1910390602> PMID: 9621908
19. Haselden WD, Kedarasetti RT, Drew PJ. Spatial and temporal patterns of nitric oxide diffusion and degradation drive emergent cerebrovascular dynamics. *Plos Comput Biol.* 2020; 16: e1008069. <https://doi.org/10.1371/journal.pcbi.1008069> PMID: 32716940
20. Withoft A, Filosa JA, Karniadakis G. Potassium Buffering in the Neurovascular Unit: Models and Sensitivity Analysis. *Biophysical Journal.* 2013; 105: 2046–2054. <https://doi.org/10.1016/j.bpj.2013.09.012> PMID: 24209849
21. Moshkforoush A, Ashenagar B, Harraz OF, Dabertrand F, Longden TA, Nelson MT, et al. The capillary Kir channel as sensor and amplifier of neuronal signals: Modeling insights on K⁺-mediated neurovascular communication. *Proc National Acad Sci.* 2020; 117: 16626–16637. <https://doi.org/10.1073/pnas.2000151117> PMID: 32601236
22. Huo B-X, Greene SE, Drew PJ. Venous cerebral blood volume increase during voluntary locomotion reflects cardiovascular changes. *NeuroImage.* 2015; 118: 301312. <https://doi.org/10.1016/j.neuroimage.2015.06.011> PMID: 26057593
23. Hansen PC. Deconvolution and Regularization with Toeplitz Matrices. *Numer Algorithms.* 2002; 29: 323–378. <https://doi.org/10.1023/a:1015222829062>
24. Seghouane A-K, Shah A, Ting C-M. fMRI hemodynamic response function estimation in autoregressive noise by avoiding the drift. *Digital Signal Processing.* 2017; 66: 29–41. <https://doi.org/10.1016/j.dsp.2017.04.006>

25. Aydin A-K, Haselden WD, Houssen YG, Pouzat C, Rungta RL, Demené C, et al. Transfer functions linking neural calcium to single voxel functional ultrasound signal. *Nat Commun.* 2020; 11: 2954. <https://doi.org/10.1038/s41467-020-16774-9> PMID: 32528069
26. Zimolong A, Rau G, Gaelings E, Rutten W. DETERMINATION OF THE OPTICAL IMPULS RESPONSE FUNCTION OF BIOLOGICAL TISSUE AND TECHNICAL CONSTRAINTS. *IEEE Eng Med Biol.* 1996.
27. Egi H. On Identification of Biological Systems. Universitet U, editor. 2014.
28. Chen T-W, Wardill TJ, Sun Y, Pulver SR, Renninger SL, Baohan A, et al. Ultrasensitive fluorescent proteins for imaging neuronal activity. *Nature.* 2013; 499: 295–300. <https://doi.org/10.1038/nature12354> PMID: 23868258
29. Chaigneau E, Oheim M, Audinat E, Charpak S. Two-photon imaging of capillary blood flow in olfactory bulb glomeruli. *Proceedings of the National Academy of Sciences of the United States of America.* 2003; 100: 13081–6. <https://doi.org/10.1073/pnas.2133652100> PMID: 14569029
30. Friston KJ, Josephs O, Rees G, Turner R. Nonlinear event-related responses in fMRI. *Magnetic Resonance in Medicine.* 1998; 39: 41–52. <https://doi.org/10.1002/mrm.1910390109> PMID: 9438436
31. Rungta RL, Chaigneau E, Osmanski B-F, Charpak S. Vascular Compartmentalization of Functional Hyperemia from the Synapse to the Pia. *Neuron.* 2018; 99: 362–375.e4. <https://doi.org/10.1016/j.neuron.2018.06.012> PMID: 29937277
32. Gao Y-R, Greene SE, Drew PJ. Mechanical restriction of intracortical vessel dilation by brain tissue sculpts the hemodynamic response. *NeuroImage.* 2015; 115: 162–176. <https://doi.org/10.1016/j.neuroimage.2015.04.054> PMID: 25953632
33. Drew PJ. Vascular and neural basis of the BOLD signal. *Current Opinion in Neurobiology.* 2019; 58: 61–69. <https://doi.org/10.1016/j.conb.2019.06.004> PMID: 31336326

CHAPTER 9

CHARACTERIZATION OF THE OXYGEN
INITIAL DIP
IN CAPILLARIES OF CHRONICALLY
PREPARED MICE

1 Characterization of the oxygen initial dip in 2 capillaries of chronically prepared mice

3

4 **Abstract**

5 Functional brain imaging techniques such as BOLD-fMRI rely on functional hyperemia, a local increase of
6 blood flow to map brain activated areas. However, functional hyperemia extends over a brain volume
7 larger than the original neuronal activation. This discrepancy has pushed the fMRI community to look for
8 a biological marker with a better spatial specificity, such as the BOLD initial dip, a transient decrease in
9 oxygenation due to local neuronal consumption. The existence of the initial dip and its characteristics
10 have remained controversial. Here, we used two-photon life time microscopy and precise PO_2
11 measurements to investigate the initial dip characteristics in olfactory bulb capillaries of anesthetized
12 mice, chronically prepared. Targeting the glomerulus most sensitive to a specific odor, we show that the
13 dip is detectable, but of very low amplitude and its amplitude is much smaller than in acutely prepared
14 mice. The dip is exclusively present in the most highly responding and when functional hyperemia is
15 delayed. Our results suggest that if the initial dip is an elusive signal to enhance BOLD fMRI spatial
16 resolution, it could be used as biological marker of delayed functional hyperemia.

17 **Introduction**

18 Functional hyperemia is the increase of blood flow that follows neuronal activation, and
19 which is used by functional imaging techniques to map brain activation. The signaling pathways
20 by which neurovascular coupling generates functional hyperemia are known to involve the
21 interactions of several cell types but their respective contribution to the coupling is not fully
22 established (Iadecola, 2017; Kaplan et al., 2020). In addition, the local activation of neurons
23 generates a back-propagating signal along upstream vessels, generating a dilation of large
24 arterioles and the irrigation of a brain volume exceeding that of the activated neurons (Rungta et
25 al., 2018, 2021). Overall, the spatiotemporal dynamic of functional hyperemia is still poorly

26 understood. This raises the question of how functional imaging techniques based on blood
27 dynamics faithfully report local neuronal activity.

28 BOLD fMRI remains the most used functional imaging technique to map brain activity in
29 human. The classical positive BOLD signal depends in a complex manner on changes of blood flow,
30 blood volume, oxygen consumption and mostly reports signal changes from the venous side of
31 the vascular arbor, i.e. not necessarily close to the neuronally activated area. The origin of the
32 BOLD signal has been widely discussed (Drew, 2019; Fukuda et al., 2021; Howarth et al., 2021;
33 Logothetis and Wandell, 2004). The spatial limitation in the mapping of neural activation was
34 acknowledged early and incited several groups to investigate if the initial dip, an early negativity
35 preceding the positive BOLD signal, could be used to improve BOLD spatial resolution (Hong and
36 Zafar, 2018; Hu and Yacoub, 2012). The nature of the initial dip was initially considered to reflect
37 a rapid and local increase in deoxyhemoglobin resulting from neuronal oxygen consumption, as
38 first reported with intrinsic optical signal imaging (IOS) (Frostig et al., 1990). The dip was later
39 supported by local oxygen measurements directly in the visual cortex of the cat (Thompson et al.,
40 2005, 2004, 2003). Still several studies raised concerns regarding the existence of the BOLD initial
41 dip, creating an important controversy extensively discussed in (Hu and Yacoub, 2012).

42 We previously studied the initial dip in our neurovascular model, the glomerular layer of
43 the rodent olfactory bulb. Using Clark electrodes and two-photon laser scanning microscopy
44 (TPLSM), we investigated the correlation between firing, synaptic transmission, and oxygen
45 consumption during sensory stimulation (Lecoq et al., 2011). We found that odor triggers an initial
46 dip in the glomerular neuropil oxygenation, characteristic of an immediate consumption, and a
47 delayed Po_2 increase resulting from local functional hyperemia. The oxygen dip started within 100
48 ms of neuronal activation and was blocked by focal application of glutamate receptor antagonists
49 in the activated glomerulus i.e., the oxygen dip resulted from postsynaptic activation. We then
50 used two-photon phosphorescence lifetime microscopy (2PLM) to monitor Po_2 changes in both
51 the vascular and tissue compartments of rat and mouse glomeruli (Parpaleix et al., 2013).
52 Although we systematically observed the Po_2 initial dip in the tissue, it was barely detectable in
53 individual capillaries. However, averaging the responses from numerous capillaries and thus

54 improving the response SNR revealed for the first time a small (≈ 1 mmHg) Po_2 vascular dip in
55 capillaries.

56 Several limitations may have impaired our previous studies of the oxygen dip. The experiments
57 were performed in animals that underwent acute neurosurgery and during anesthesia, both
58 experimental conditions affecting resting homeostasis (Kaplan et al., 2020) and increasing the
59 delay between neural activation and functional hyperemia (Gao et al., 2017; Rungta et al., 2021).
60 In addition, in the OB the initial dip was investigated in responsive glomeruli but not in the most
61 sensitive (MSG) one to a given odor, which can be expected to show a higher oxygen
62 consumption. Finally, we used PtP-C343, an oxygen sensor that has a two-photon cross section
63 lower than the recent Oxyphor 2P (Esipova et al., 2019).

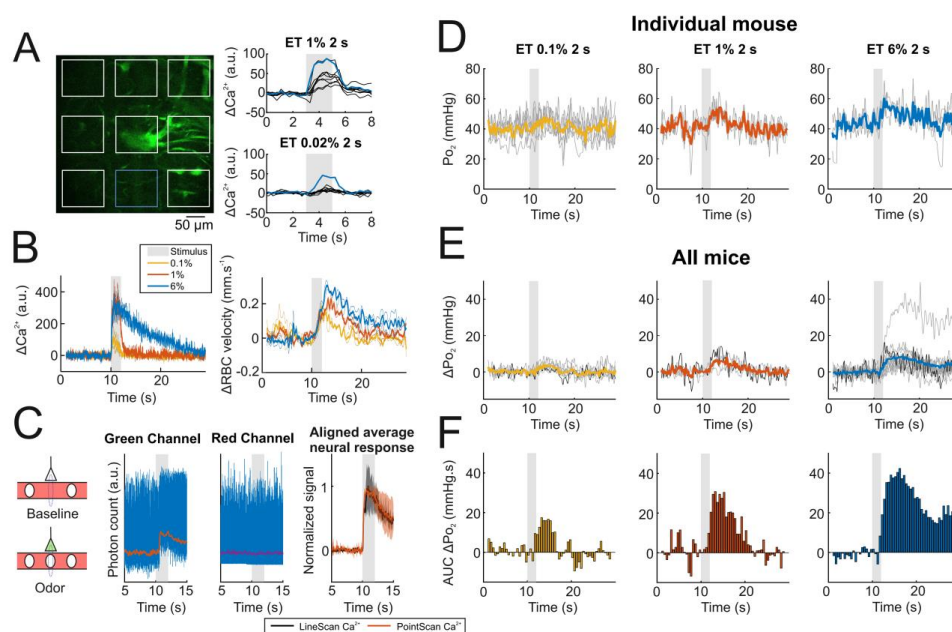
64 Here, we reinvestigate the issue in mice chronically implanted with a glass window, and which
65 express post-synaptic GCaMP6f in the glomerular layer. We measured changes of neural Ca^{2+} and
66 capillary velocity with TPLSM and monitored Po_2 in the glomerular capillaries and neuropil with
67 2PLM and Oxyphor 2P. Our results show a very small initial dip in $\approx 60\%$ mice and only in the most
68 sensitive glomerulus to our odor, where activation is theoretically higher. This further indicates
69 that the use of the initial dip is not a viable option for improving BOLD-fMRI.

70 **Results**

71 Po₂ responses in anesthetized mice supplemented with oxygen.

72 We focused our work on the MSG to Ethyl tiglate (ET), as in our previous work (Aydin et
73 al., 2020). Mice were anesthetized (see Methods) and the most sensitive glomerulus was found
74 in the vicinity of the glomerulus labelled with YFP under the M72 promoter, by lowering the ET
75 concentration to the range of 0.4% where only a single glomerulus shows high and fast Ca^{2+}
76 response in its postsynaptic dendrites (**Fig 1A**). Intravenous injection of Texas Red coupled with
77 linescan acquisitions further confirmed that the activation of the MSG is concentration-
78 dependent both for Ca^{2+} and RBC velocity responses (**Fig 1B**). To account for the jitter related to
79 the mouse breathing, we aligned every response so that the onset of the neuronal response starts
80 at 10 s. Linescan acquisitions were easily timeshifted since neuronal activation was measured

81 simultaneously to RBC velocity. However, oxygen measurements are done with a pointscan
 82 acquisition in the capillaries, with theoretically no excitation in the tissue. Nonetheless, we took
 83 advantage of the point-spread function (PSF) of our setup which is slightly larger than the capillary
 84 to measure simultaneously the neuronal response and the Po_2 one (Fig 1C). Measuring the
 85 functional hyperemia in the same capillary as in Fig 1B, we see concentration dependent Po_2
 86 increases, even at low ET concentration. However, no initial dip was detectable prior to the Po_2
 87 increases, even when averaging the responses from all mice (Fig 1D) or when comparing Po_2
 88 values immediately after neuronal activation (see the first 3 bins preceding the Po_2 increase) (Fig
 89 1E). It is worth stressing that as mice were anesthetized, the dip was not masked by a change of
 90 breathing frequency, which increases vascular Po_2 in awake mice (Zhang et al., 2019).



91

92 **Fig 1. The initial dip cannot be measured in the most sensitive glomerulus to Ethyl tiglate.**

93 A. The most sensitive glomerulus (MSG) to Ethyl tiglate (ET) is determined by lowering ET concentration in the vicinity
 94 of the YFP-expressing M72 glomerulus. MSG (blue square and trace) shows fast and high neuronal (Ca^{2+}) responses
 95 to very low concentration of ET. Traces are single acquisitions spatially averaged over the squares shown on the left,
 96 for a single mouse.

97 B. Single (thin) and average (thick) responses to increasing odor concentrations in the MSG for a single mouse.
 98 Neuronal (Ca^{2+}) and vascular (RBC velocity) responses are acquired simultaneously with a linescan in two-photon

99 microscopy. Each acquisition is aligned on the onset of the Ca^{2+} response. $n = [2, 2, 2]$ single acquisitions, respectively
100 for ET 0.1%, 1% and 6%.

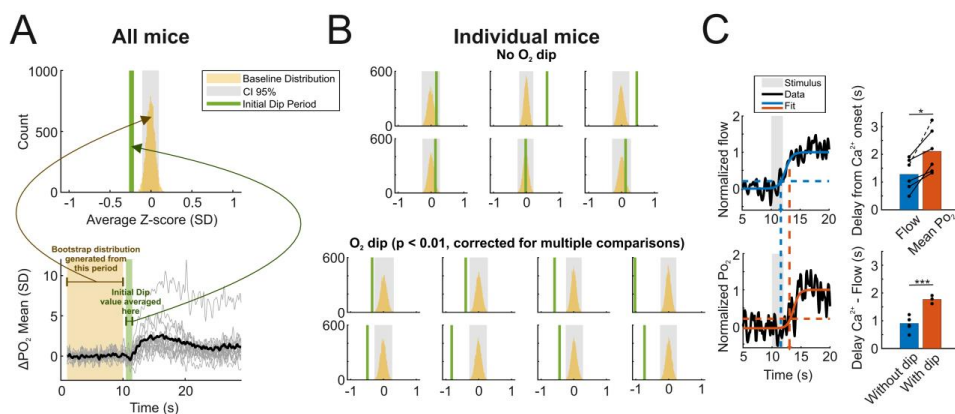
101 C. Alignment for pointscan acquisitions is done thanks to the PSF of our system being slightly larger than the capillary
102 radius (left). This allows to extract from the ON period of the pointscan (see Figure 2A and Methods) the Ca^{2+} shape
103 in the green channel, while the red channel stays flat (middle) Normalized average responses from the pointscan
104 (orange) and the linescan (black) are superimposable ($R^2 = 0.97$), shade is ± 1 SD (right).

105 D. Single (thin grey) and average (thick colored) Po_2 responses to increasing odor concentrations in a capillary of the
106 MSG for the same mouse as in panel B. $n = [5, 3, 3]$ single acquisitions, respectively for ET 0.1%, 1% and 6%.

107 E. Average for a single mouse (thin grey) and average over all mice (thick colored) Po_2 responses to increasing odor
108 concentrations in a capillary of the MSG. Thin black curves correspond to the average response of the mouse shown
109 in panel B and C. $n = [6, 4, 14]$ mice, respectively for ET 0.1%, 1% and 6%.

110 F. Area under the curve (AUC) histogram (binned over 0.5 s) of the Po_2 responses over all mice.

111 To maximize our chance of detecting the initial dip, we normalized our timeseries by the
112 noise in the baseline and plotted Z-scores (**Fig2A bottom**). To detect whether the dip was present
113 in average, we bootstrapped the baseline values and computed a 95% confidence interval (see
114 Methods). The initial dip location was chosen as the period between 0.5 and 1.5 s after the
115 stimulus, as we previously determined (Parpaleix et al., 2013). In the response averaged over all
116 mice at a rather high concentration (ET 6%), we found that there is an initial dip with a mean value
117 of 0.3 SD (**Fig 2A**). By focusing on individual mice, we found that 8 of the 14 mice exhibited the
118 initial dip (**Fig 2B**). We have been able to measure the flow of RBCs for only a subset of these mice
119 and we report that there is a delay of 0.7 s between Po_2 onset and flow onset (**Fig 2C**).
120 Interestingly, we found that the mice with an initial dip all have a longer delay for their flow
121 response compared to the mice without an initial dip with an apparent threshold between 1.2-
122 1.6 s.



123

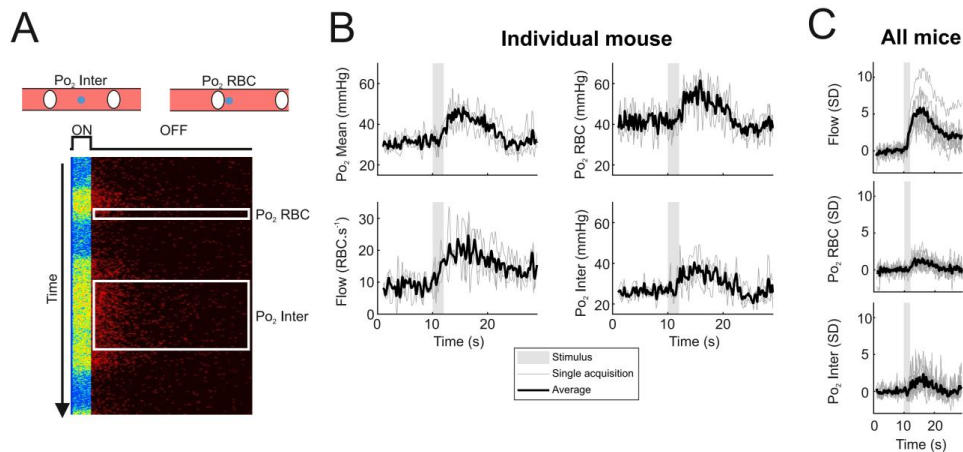
124 **Fig 2. A small initial dip is visible in the Z-score response to high ET concentration and is correlated with a longer**
 125 **delay of flow response onset.**

126 A. Generating a distribution (top) of the baseline values in Z-score (bottom) shows that the initial dip, calculated as
 127 the average value of the signal between 10.5 and 11.5 s, is out of the 95% confidence interval of the baseline
 128 distribution (see Methods). The average initial dip has a value of 0.26 SD. $n = 14$ mice, $p = 0$.

129 B. 8 out of the 14 mice show an initial dip in their responses to ET 6%. $p = [0.96, 1, 1, 0.92, 0.99, 0.89]$ for the top
 130 part, from left to right and up to bottom. $p = [0.0023, 0, 0, 0, 0, 0, 0, 0]$ for the bottom part, from left to right and up
 131 to bottom.

132 C. There is a delay between the flow and the Po_2 onset, as measured by fitting single mouse responses with a
 133 sigmoidal curve (colored full line) and taking the 20% mark as onset (colored dotted line) (left). Mean flow delay is
 134 1.3 s while mean Po_2 delay is 2 s (top right). Dispersion is represented by the single measures (black dot). $p = 0.0156$,
 135 one-sided Wilcoxon signed rank test. The delay between Ca^{2+} is significantly higher between mice showing a dip ($n =$
 136 3) and those without ($n = 6$) (bottom right). $p = 5.4 \cdot 10^{-4}$, one-sided two-sampled t-test.

137 We previously demonstrated that 2PLM measurements have the necessary spatial
 138 resolution to measure the Po_2 fluctuations associated with the passage of individual erythrocytes
 139 over the scanned point, i.e. erythrocyte-associated transients (EAT) capillaries (Lyons et al., 2016;
 140 Parpaleix et al., 2013; Roche et al., 2019). **Fig 3A** illustrates this concept. Separating the Po_2 RBC,
 141 i.e. measured the RBCs border, and the Po_2 InterRBC, i.e. measured at mid-distance of flowing
 142 RBCs, we report that the increase in Po_2 Mean, i.e. measured at all time, is due to both an increase
 143 in RBC oxygenation and in plasmatic oxygenation (**Fig 3B**). By averaging all mice, we see that the
 144 previously reported initial dip in Po_2 Mean is observed in the Po_2 InterRBC traces rather than Po_2
 145 RBC traces (**Fig 3C**).



146

147 **Fig 3. Separating RBC and plasmatic oxygenation shows that the initial dip is seen in the plasma.**

148 A. Averaging Oxyphor 2P decays in-between RBCs allows for measuring the plasmatic Po₂, called Po₂ Inter. The decays
 149 next to RBCs approaches the Po₂ in the RBCs, namely Po₂ RBC. Upper panel is a schematic of the point scanned (blue
 150 dot) with RBCs flowing, allowing to measure either Po₂ Inter or Po₂ RBC. Po₂ Mean is measured by averaging every
 151 decay. Lower panel shows an acquisition where the ON period separates RBC (blue part) from the plasma (yellow
 152 part), and the OFF period contains the decays where Po₂ is measured.

153 B. Single (thin grey) and average (thick black) reponses acquired with pointscans to ET 6% in the MSG for an individual
 154 mouse. Po₂ Mean is separated into Po₂ Inter and Po₂ RBC.

155 C. Single mouse response (thin grey) and average over all mice (thick black, n = 9) in Z-score, with the SD determined
 156 as the average SD over the baseline. Po₂ Mean is already shown in Figure 2A. Average Po₂ Inter shows the initial dip
 157 while we do not see it in Po₂ RBC.

158 Notably, we solely worked in the most sensitive neuronal network to our odor in these
 159 experiments, which hypothetically increases the size of the initial dip due to higher neuronal
 160 activation. Taken together, these data suggests that the capillary initial dip is smaller in chronically
 161 implanted mice, 0.3 SD, than in the acute mice where we previously reported an initial dip of over
 162 2 SD of amplitude with PtP-C343 (Parpaleix et al., 2013), which is noisier than the Oxyphor 2P
 163 used in this study (Esipova et al., 2019).

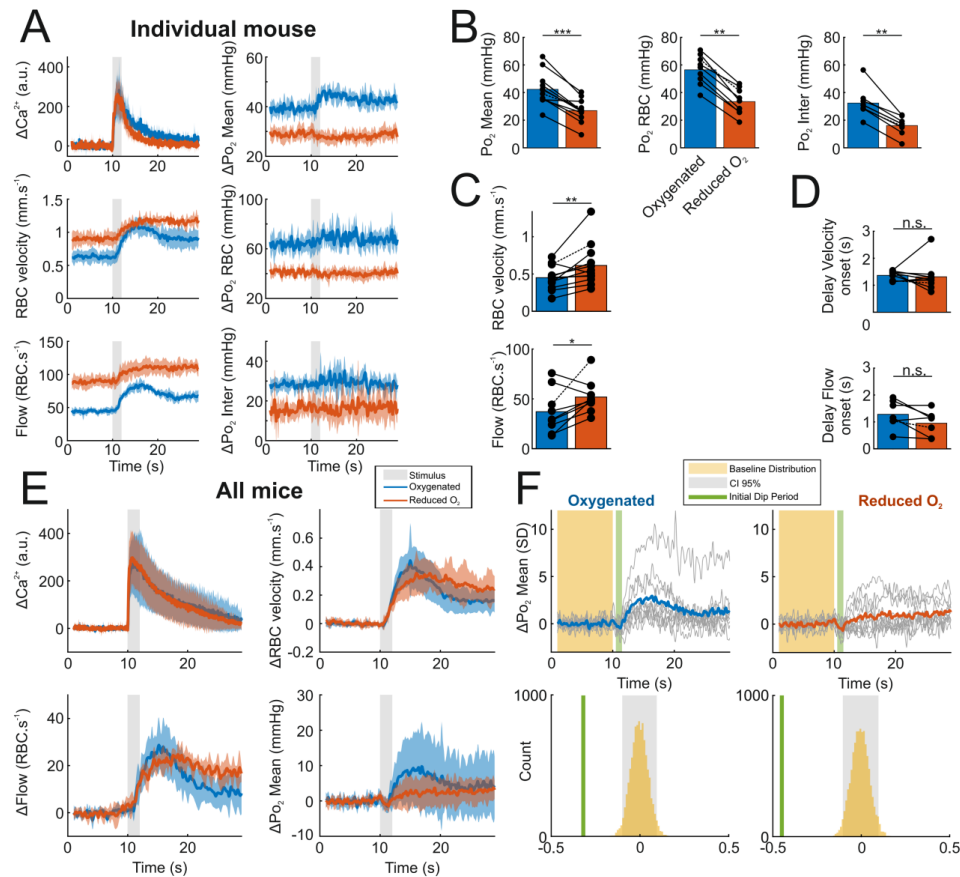
164 Effects of oxygen supplementation suppression

165 One study hypothesized that inhaled oxygen level can impact the presence of the initial
 166 dip (Mayhew et al., 2001). As its current amplitude in the MSG is of no use to BOLD-fMRI, we
 167 wondered if reducing inhaled oxygen was able to enhance it and whether it would be sufficiently

168 high to be useful in vascular functional imaging. Thus, we performed experiments where we
169 sequentially measured the neuronal and vascular responses to ET 6% with and without oxygen
170 supplementation (30% vs. 21% in the inhaled air) in anesthetized chronic mice breathing freely.
171 **Fig 4A** illustrates a typical case where removing the supplementation changed all resting vascular
172 parameters: Po_2 Mean, Po_2 RBC and Po_2 Inter decreased, whereas RBC velocity and flow
173 increased. In response to odor, neuronal calcium increased similarly, whereas functional
174 hyperemia was reduced and the evoked-increase of Po_2 suppressed. These consequences of O_2
175 removal were robust (**Fig 4B-D**) while the timing of Calcium, RBC velocity and flux responses
176 remained stable. Note that as resting Po_2 Inter reports Po_2 in the juxta-capillary tissue (Parpaleix
177 et al., 2013), one can expect a drop of tissue by at least 50%. Given that Po_2 RBC is in equilibrium
178 with the oxygen inside RBCs and using previously published values of the Hill coefficient and P50
179 for C57BL6/J mouse hemoglobin (Uchida et al., 1998), resting hemoglobin saturation dropped
180 from 70%, in accordance with previously reported measures (Lyons et al., 2016; Roche et al.,
181 2019), to 37.5%.

182 Averaging the responses from all mice (**Fig 4E**) shows (**Fig 4E**) that whereas neuronal
183 response dynamics was not sensitive to the drop of resting Po_2 , RBC velocity and flux responses
184 slowed down. Applying the same procedure as in **Fig 2** revealed that there was a significant initial
185 dip in both oxygenation conditions and that dip amplitude increases from 0.33 SD to 0.47 SD upon
186 removing O_2 supplementation.

187 Overall, these data shows that i) neuronal responses are insensitive at a small time scale
188 to the drop of resting Po_2 Mean and ii) removing oxygen supplementation effectively increase the
189 amplitude of the initial dip when normalized by the noise however, iii) the initial dip is still small
190 and hidden in the noise.



191

192 **Fig 4. Reducing the oxygen supply to the anesthetized mouse does not reveal a large initial dip in the MSG.**

193 A. Comparison of the responses to ET 6% 2 s in an individual mouse, either oxygenated or with reduced oxygen
 194 supply. Ca²⁺ response remains constant (top left), while both baseline values and overall dynamics of vascular
 195 responses changes (middle and bottom left). Po₂ response totally disappears with reduced O₂ supply, with even a
 196 tendency to a decrease of Po₂ in this mouse (right panels). Traces are shown as average \pm 1 SD (shaded area). Upper
 197 and middle left panels are linescans (n = [4, 4] for oxygenated or reduced O₂ respectively). Bottom right and left
 198 panels are pointscans (n = [8, 8] for oxygenated or reduced O₂ respectively).

199 B. Reducing the oxygen supply significantly alters the capillary Po₂. p = [2.4·10⁻⁴, 0.02, 0.02] respectively from left to
 200 right, one-sided Wilcoxon signed rank test.

201 C. Reducing the oxygen supply significantly increases the baseline values of RBC velocity and flow. p = [0.0046, 0.0195]
 202 respectively for top and bottom panels, one-sided Wilcoxon signed rank test.

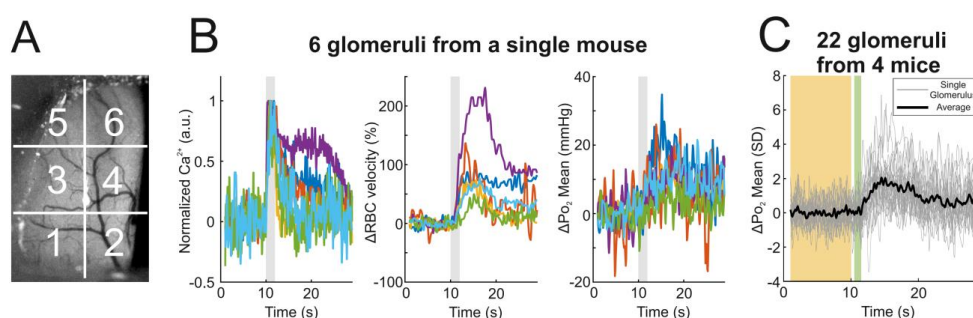
203 D. Reducing the oxygen supply does not change the onset delay for RBC velocity and flow responses. p = [0.36, 0.11]
 204 respectively for top and bottom panel.

205 E. Comparison of the average paired responses to ET 6% 2 s in all mice, either oxygenated or with reduced oxygen
 206 supply. Traces are shown as average \pm 1 SD (shaded area). $n = [9, 6, 10]$ mice, respectively for the upper panels, the
 207 bottom left and the bottom right one.

208 F. As in Figure 2A. In both conditions, the initial dip is significantly different from the baseline distribution. The initial
 209 dip value is slightly enhanced upon O_2 reduction.

210 Po₂ responses in other glomeruli than the most sensitive one

211 Is this observation a general rule that can be extended to glomeruli, non-specific to ET? At
 212 high odor concentration, odorant receptors lose their specificity (Wachowiak and Cohen, 2001).
 213 Thus, we randomly looked for responsive glomeruli in 4 mice. Each dorsal olfactory bulb was
 214 divided into 6 areas and recording responses from one glomerulus per area (Fig 5A, B). In average,
 215 we did not measure any initial dip in the 22 glomeruli tested (Fig 5C, $p = 0.89$).



216

217 **Fig 5. Non-specific glomeruli do not show any initial dip.**

218 A. Image acquired with a stereoscope through the chronically implanted window. Each olfactory bulb was divided
 219 into 6 different regions. A glomerulus responding to ET 6 % was selected in each region.

220 B. Neural and vascular responses to ET 6 % for an individual mouse.

221 C. As in Fig. 2A. Here the bootstrap confidence interval contains the initial dip period. $p = 0.89$.

222 Discussion

223 Using the the olfactory bulb glomerulus, a suited model for neurovascular coupling study,
 224 we investigated the existence and characteristics of the oxygen initial dip in capillaries. Previous
 225 studies raised the controversy regarding whether the initial dip was a regular phenomenon and
 226 thus could be used to improve the spatial specificity of BOLD-fMRI. Here we report that the initial
 227 dip can be detected in the capillaries of the most sensitive glomerulus in response to ET (6%, 2 s)
 228 when responses are normalized by the noise. The amplitude of the initial dip is then only about
 229 0.3 SD in average. Interestingly, the initial dip is present in mice having a larger flow delay and is

230 carried mostly by plasmatic Po_2 (Po_2 Inter). Decreasing resting Po_2 modestly increases the dip
231 amplitude from 0.34 SD to 0.47 SD, the dip remaining below the noise level. Finally, the dip is
232 specific to the glomerulus best activated by its specific odor.

233 These results are in line with the presence of the initial dip being dependent on the
234 impairment of NVC dynamics. Previous results from our group (Parpaleix et al., 2013) reported an
235 initial dip ~ 2 SD of amplitude. However, the experiments were performed in acute mice,
236 anesthetized and under condition of neurosurgery, i.e. with a long delay between neuronal and
237 vascular responses. In chronically implanted mice, i.e. with > 1 week of recovery post-surgery,
238 functional hyperemia is faster and the amplitude of the initial dip is smaller. We expect that in
239 awake mice the capillary initial dip may not be measurable anymore, even in the MSG.

240 One limit of our study is that it focuses on the vascular initial dip, rather than on tissue
241 Po_2 . We hypothesize that the decrease measured in Po_2 Inter faithfully reports the juxtacapillary
242 tissue change as we previously showed in resting state. The remaining question is to determine
243 the actual amplitude of the tissue dip in chronic awake mice, as it was only ~ 2 mmHg in the acute
244 anesthetized rat (Parpaleix et al., 2013). A recent study reported that no initial dip is measurable
245 with IOS in the cortex of awake animals (Şencan et al., 2020) but this technique lacks the spatial
246 resolution of 2PLM measurements and was in a model with a much more difficult neuronal
247 activation control.

248 How should we interpret BOLD-fMRI studies that reported the existence of an initial dip
249 in awake humans? BOLD fMRI voxels are large and may sum better the small signal. However,
250 the BOLD SNR is bad in comparison to 2PLM. Functional hyperemia in human could be slower,
251 revealing better the local oxygen consumption. The study from Watanabe and colleagues
252 supports this hypothesis (Watanabe et al., 2013). However, in regards with our results which bring
253 precise insights into the physiology of the initial dip, using it for a better interpretation of the
254 BOLD-fMRI remains poorly plausible, unless we find a pharmacological trick to remove functional
255 hyperemia safely and transiently.

256

257 **Methods**

258 Animal preparation

259 All animal care and experimentations were performed in accordance with the INSERM Animal
260 Care and Use Committee guidelines (protocol numbers CEEA34.SC.122.12 and
261 CEEA34.SC.123.12). Adult mice (n=XX, 3–12 months old, 20–35 g, both males and females,
262 housed in 12 h light-dark cycle at 24 °C and 50 % humidity, fed ad libitum) were used in this
263 study. Thy1-GCaMP6f (GP5.11) mice (Dana et al., 2014), from Jackson Laboratory, were crossed
264 with M72->S50-IRES-hChrVenus mice (Smear et al.) kindly provided by Thomas Bozza
265 (Department of Neurobiology, Northwestern University, USA). All mice underwent a surgery
266 composed of the placement of a headbar on the bone behind the craniotomy, above the
267 olfactory bulbs. Anesthesia was performed as before (Roche et al., 2019), thanks to an intra-
268 peritoneal bolus of ketamine (100 mg.kg⁻¹ body mass) and medetomidine (0.5 mg.kg⁻¹ body
269 mass). To prevent inflammatory reaction and avoid infections, Enrofloxacin (Baytril 10%, Bayer,
270 Germany) and Dexamethasone (Dexazone, Virbac, France) were administered 1 hour before the
271 surgical procedure, respectively at 5 mg.kg⁻¹ and 6 mg.kg⁻¹ body mass. For the time of the
272 surgery, mice breathed oxygen-supplemented air ([O₂]_{final} = 40%) while their body temperature
273 maintained at 36 ± 0.5 °C using a rectal probe and a heating pad. The headbar is first placed
274 with Tetric Evoflow dental cement (Ivoclar Vivadent AG, Schaan, Liechtenstein) after treating
275 the bone with a primer, Optibond FL (Kerr Italia S.R.L., Salerno, Italia). The bone above the
276 olfactory bulbs was carefully drilled and removed, while making sure no pressure is applied on
277 the brain tissue and heat is regularly dispersed by means of a cool aCSF solution (Holtmaat et
278 al., 2009). A cranial window cut out of glass was placed over the bare olfactory bulbs and sealed
279 in place with the same dental cement as the headbar. Buprenorphine (Buprecare, Axience,
280 France) was injected to relieve pain at 0.05 mg.kg⁻¹ body mass. 3 days of post-surgery follow-up
281 was systematically performed to make sure mice were safe. They recovered for more than a
282 week before starting experimental procedures.

283

284 Experimental procedure under anesthesia

285 Mice were injected with the same mix as for the surgery, ketamine-medetomidine at 100 and
286 0.4 mg.kg⁻¹ body mass respectively. Dextran Fluorescein (MW = 70kDa, D1823, ThermoFisher,

287 Waltham, Massachusetts) mixed with Oxyphor 2P (Esipova et al., 2019) (5 μ M in the mouse
288 blood) was injected intra-venously by retro-orbital injection right after the induction. Mouse
289 temperature was monitored as during the surgery, and unless it is otherwise stated
290 supplemented with oxygen to attain 30% of O₂ in the breathed air. Notably, in the **Fig 4**, oxygen
291 supplementation was removed to evaluate the effect of the oxygenation level on the initial dip.
292 In that case, O₂ concentration in the air was 21% as no supplementation was provided.
293 Experiments were stopped as soon as the mouse showed signs of awakening.

294

295 Odor stimulation

296 All experiments from a given figure were performed with the same stimulation protocol, so no
297 blinding was involved. Odor delivery follows similar procedure as previous studies (Aydin et al.,
298 2020; Boido et al., 2019). Odors were delivered thanks to a home built olfactometer, based on
299 the one from the Ringer Lab (<https://www.janelia.org/open-science/olfactometer>), and
300 controlled by a custom LabView software. Odor and exhaust lines were systematically
301 equilibrated before each day of experiment, to avoid neuronal activation to pressure changes.
302 Odor concentration and stability over the stimulus were assessed and calibrated using a photo-
303 ionization detector (miniPID 200B, Aurora Scientific, Aurora, Canada). To check for anesthesia-
304 related variations, the different stimulus conditions were randomly interleaved by the
305 experimenter. Except for the **Fig 5**, where linescans were performed once to allow for a high
306 number of glomeruli, all traces are the average of at least 2 responses. See the figure legends
307 for details regarding the acquisition number for each mouse. Odor applications were separated
308 by 3 min period, to allow neuronal and vascular activity along with the neurovascular coupling
309 to return to baseline.

310

311 TPLSM acquisition

312 TPLSM imaging was performed with a custom-built microscope, previously described (Lyons et
313 al., 2016; Roche et al., 2019) and data collected with a custom LabVIEW software (National

314 Instruments). 120 femtoseconds laser pulses were delivered by a Ti:Sapphire laser (Mira by
315 Coherent, Santa Clara, California, 76 MHz). Laser power was modulated with an acousto-optic
316 modulator (AA Optoelectronic, Orsay, France, MT110B50-A1.5-IR-Hk). Galvanometric mirrors
317 (Cambridge technology, Bedford, Massachusetts) were used to focus to target the sample at the
318 desired points. Light was focused onto the sample through either a 40XW 0.8NA or a 60XW
319 1.1NA objective (Olympus, Tokyo, Japan). GCaMP6f, Fluorescein and Oxyphor 2P were excited
320 at 920 nm, and their emission was separated from excitation light with a dichroic mirror (DXCR
321 875, Chroma, Bellows Falls, Vermont). Red light from Oxyphor 2P was filtered through a E800
322 (Chroma) and a FF01 794/160 (Semrock), while GCaMP6f and Fluorescein emissions passed
323 through a E800SP2 and a HQ525/50 nm (Chroma). The “red channel” photomultiplier, placed
324 after the filters, is a R6357 photomultiplier tube (Hamamatsu, Naka-ku, Japan), while the “green
325 channel” one is a GaAsP photomultiplier tube (Hamamatsu). Output of the photomultipliers was
326 amplified by custom-built electronics and sampled at 1.25 MHz.

327 Linescan acquisitions were performed by scanning with a broken line (1 to 2.5 ms per line) for
328 30 seconds. Part of the line was in a capillary, allowing for velocity measurements in the green
329 channel thanks to the intravenous fluorescein as previously described (Aydin et al., 2020;
330 Chaigneau et al., 2003; Jukovskaya et al., 2011; Roche et al., 2019). The rest of the line scanned
331 the parenchyma, allowing for GCaMP6f measurements.

332 Pointscan acquisitions were performed by scanning over a single point, either in a capillary or in
333 the tissue. In the capillary, it allowed us to measure simultaneously the RBC flow and the Po_2 .
334 Each scan is composed of an ON period, lasting for 25 μ s, where the point is excited by light at
335 920 nm, and an OFF period, lasting for 225 μ s. RBC flow is extracted from the ON period in the
336 green channel, thanks to fluorescence variations related to the RBCs flowing. Po_2 is extracted
337 from the OFF period, by estimating the decay of phosphorescence in the red channel and
338 converting the half-life of the decay to an absolute value of partial pressure of oxygen in mmHg
339 (Esipova et al., 2019). Note that our experiments were done at a brain temperature of 35.7 °C,
340 as measured in Roche et al. (2019) and that the corresponding calibration curve between half-
341 life and Po_2 was used. A single point of Po_2 in our timeseries is the result of the average decay
342 over 250 ms i.e., 1000 decays for Po_2 Mean. Po_2 RBC and Po_2 Inter are extracted on the same

343 timescale, but by averaging only the decays around RBCs or in-between RBCs, respectively. Note
344 that the number of averaged decays for a single Inter RBC P_{O_2} point is thus lower than P_{O_2}
345 Mean. Decays regarding P_{O_2} Inter were discarded if they were too close to the RBCs, to measure
346 the bottom part of the erythrocyte-associated transients and report the real plasmatic P_{O_2} (see
347 Parpaleix et al., Roche et al. and Figure 2). Due to this lower number of decays, the signal-to-
348 noise ratio is higher and some obviously out-of-range points (> 100 mmHg change for a single
349 point) were removed, for a maximum of 6 points over all the entirety of the acquisitions.

350

351 Linescan data analysis

352 Raw calcium timeseries were downsampled to $\Delta t = 50$ ms (*interp1* function, 'pchip' option,
353 MATLAB 2018a) and aligned so that their onset is at 10 s. Response onset was determined by
354 the experimenter by looking at each single trace in its raw form. After alignment, single
355 acquisitions were normalized by subtracting the mean baseline value of the last 5 seconds
356 before stimulus onset. Traces were then averaged per stimulus condition and mouse.

357 RBC velocity extraction from the linescan acquisition is done with a custom LabVIEW software,
358 with a point every 300 ms. RBC velocity is also aligned with the same timeshift as the
359 simultaneously acquired calcium trace. Timeserie is then upsampled at $\Delta t = 100$ ms.

360 Normalization is done by subtracting the mean baseline value of the last 5 seconds before
361 stimulus onset, to get the Δ RBC velocity timeseries in mm.s⁻¹. **Fig 5** shows Δ RBC velocity
362 timeseries in % of changes, where the previous timeseries is divided by the same baseline value.
363 Traces were then averaged per stimulus condition and mouse.

364 Baseline values shown in **Fig 3** are computed as the average value before the stimulus onset of
365 the average non-normalized timeseries per stimulus condition and mouse.

366

367 Pointscan data analysis

368 Timeseries from the pointscan is aligned on the Calcium onset, simultaneously acquired, as
369 described in **Figure 1** and the next section. Each trace is aligned so that the neuronal response
370 starts at 10 s.

371 Raw RBC flow, PO_2 , Mean, RBC or Inter, is first aligned and then upsampled to $\Delta t = 100$ ms.
372 Average baseline value of the last 5 seconds before the stimulus onset is subtracted to
373 normalize the timeseries, before averaging per stimulus condition and mouse. Z-score traces are
374 computed by using the normalized acquisition and dividing the trace by the average standard
375 deviation (*std* function, MATLAB 2018a) over the last 5 seconds of the baseline. Single
376 acquisitions are then averaged per stimulus condition and mouse.

377 Baseline values shown in **Figure 3** are computed as the average value before the stimulus onset
378 of the average non-normalized timeseries per stimulus condition and mouse.

379

380 Alignment of Pointscan data

381 Linescan data are easily aligned on the calcium response onset, since the calcium is
382 simultaneously acquired in the parenchymal part of the linescan. To do the same with the
383 pointscan data, only acquiring in theory vascular activity, we took advantage of the radius of the
384 capillaries, which is slightly smaller than the PSF in its z axis. Thus, GCaMP6f changes in the
385 parenchyma can be recorded in the green channel (**Fig 1C**). To extract the most faithfully
386 possible the calcium response, we only extracted the response when RBC were passing below
387 the point to avoid pollution from plasmatic fluorescein. Focus on RBC was done by using the
388 points that are in the first 30% amplitude part of the green channel signal. Full amplitude was
389 computed as the difference between the minimum and the maximum signal in 30 ms windows,
390 to make sure that RBCs pass in this time window. **Fig 1C** shows that we can faithfully recover the
391 calcium response dynamic, and we keep a steady trace in the red channel. Time shift for the
392 alignment is defined for each acquisition by the experimenter, as for the linescans.

393

394 Vascular onset computation

395 As shown in **Fig 3**, vascular onsets were determined by fitting RBC velocity, RBC flow or Po_2
396 Mean traces with a sigmoidal function thanks to custom-made script (MATLAB 2018a). The
397 onset was determined as the 20% amplitude mark of the sigmoidal fit. Each fit was hand-
398 checked by the experimenter to make sure that the fits were faithful. Note that this way of
399 measuring onset supposes that the increase rate of the responses are similar for the first 20% of
400 the response, otherwise the 20% mark would be biased as it would not report onset differences
401 faithfully.

402 Statistical analysis

403 Comparison between paired onset delays (**Fig 3, 4**) was performed with a one-sided Wilcoxon
404 test (*signrank* function, MATLAB 2018a), as we do not have enough data to assume the normal
405 distribution and because we had hypotheses regarding the direction of the differences.

406 To determine whether there is a dip in each mouse or in average we performed a bootstrap test
407 (**Fig 2, 4, 5**), adapted to consider the noise of the responses. A bootstrap distribution of the
408 average value of the baseline was determined by the following procedure: 1/ get all the single
409 acquisition for a given mouse (or the average per mouse), 2/ generate 10,000 new baseline by
410 picking up, for each timepoint of the baseline, the corresponding timepoint from a random
411 acquisition (or mouse), 3/ compute the average baseline value for each of the 10,000 new
412 baselines, 4/ generate a 95% confidence interval based on the distribution of the baseline
413 values. A significant dip is defined by the average value of the dip, computed as the mean
414 response between 10.5 and 11.5 s (see Results), being smaller than the lower threshold of the
415 confidence interval. The p-value of the test is determined as the number of baseline values
416 smaller than the average dip value, divided by 10,000. Baseline distribution is generated by
417 considering the timepoints before the stimulus onset. All traces were Z-scores.

418

419

420 Aydin A-K, Haselden WD, Housen YG, Pouzat C, Rungta RL, Demené C, Tanter M, Drew PJ,
421 Charpak S, Boido D. 2020. Transfer functions linking neural calcium to single voxel functional
422 ultrasound signal. *Nat Commun* **11**:2954. doi:10.1038/s41467-020-16774-9

- 423 Boido D, Rungta RL, Osmanski B-F, Roche M, Tsurugizawa T, Bihan DL, Ciobanu L, Charpak S.
424 2019. Mesoscopic and microscopic imaging of sensory responses in the same animal. *Nat*
425 *Commun* **10**:1110. doi:10.1038/s41467-019-09082-4
- 426 Chaigneau E, Oheim M, Audinat E, Charpak and S. 2003. Two-photon imaging of capillary blood
427 flow in olfactory bulb glomeruli. *Proceedings of the National Academy of Sciences*.
428 doi:10.1073/pnas.2133652100
- 429 Dana H, Chen T-W, Hu A, Shields BC, Guo C, Looger LL, Kim DS, Svoboda K. 2014. Thy1-GCaMP6
430 Transgenic Mice for Neuronal Population Imaging In Vivo. *Plos One* **9**:e108697.
431 doi:10.1371/journal.pone.0108697
- 432 Drew PJ. 2019. Vascular and neural basis of the BOLD signal. *Curr Opin Neurobiol* **58**:61–69.
433 doi:10.1016/j.conb.2019.06.004
- 434 Esipova TV, Barrett MJP, Erlebach E, Masunov AE, Weber B, Vinogradov SA. 2019. Oxyphor 2P: A
435 High-Performance Probe for Deep-Tissue Longitudinal Oxygen Imaging. *Cell Metab* **29**:736-
436 744.e7. doi:10.1016/j.cmet.2018.12.022
- 437 Frostig RD, Lieke EE, Ts'o DY, Grinvald A. 1990. Cortical functional architecture and local
438 coupling between neuronal activity and the microcirculation revealed by in vivo high-
439 resolution optical imaging of intrinsic signals. *Proc National Acad Sci* **87**:6082–6086.
440 doi:10.1073/pnas.87.16.6082
- 441 Fukuda M, Poplawsky AJ, Kim S-G. 2021. Time-dependent spatial specificity of high-resolution
442 fMRI: insights into mesoscopic neurovascular coupling. *Philosophical Transactions Royal Soc*
443 *B* **376**:20190623. doi:10.1098/rstb.2019.0623
- 444 Gao Y-R, Ma Y, Zhang Q, Winder AT, Liang Z, Antinori L, Drew PJ, Zhang N. 2017. Time to wake
445 up: Studying neurovascular coupling and brain-wide circuit function in the un-anesthetized
446 animal. *Neuroimage* **153**:382–398. doi:10.1016/j.neuroimage.2016.11.069
- 447 Hong K-S, Zafar A. 2018. Existence of Initial Dip for BCI: An Illusion or Reality. *Front*
448 *Neurorobotics* **12**:69. doi:10.3389/fnbot.2018.00069
- 449 Howarth C, Mishra A, Hall CN. 2021. More than just summed neuronal activity: how multiple cell
450 types shape the BOLD response. *Philosophical Transactions Royal Soc B* **376**:20190630.
451 doi:10.1098/rstb.2019.0630
- 452 Hu X, Yacoub E. 2012. The story of the initial dip in fMRI. *Neuroimage* **62**:1103–1108.
453 doi:10.1016/j.neuroimage.2012.03.005
- 454 Iadecola C. 2017. The Neurovascular Unit Coming of Age: A Journey through Neurovascular
455 Coupling in Health and Disease. *Neuron* **96**:17--42. doi:10.1016/j.neuron.2017.07.030

- 456 Jukovskaya N, Tiret P, Lecoq J, Charpak S. 2011. What does local functional hyperemia tell about
457 local neuronal activation? *J Neurosci* **31**:1579–82. doi:10.1523/jneurosci.3146-10.2011
- 458 Kaplan L, Chow BW, Gu C. 2020. Neuronal regulation of the blood–brain barrier and
459 neurovascular coupling. *Nat Rev Neurosci* **21**:416–432. doi:10.1038/s41583-020-0322-2
- 460 Lecoq J, Parpaleix A, re, Roussakis E, Ducros M, Houssem YG, Vinogradov SA, Charpak S. 2011.
461 Simultaneous two-photon imaging of oxygen and blood flow in deep cerebral vessels. *Nat*
462 *Med* **17**:893–898. doi:10.1038/nm.2394
- 463 Logothetis NK, Wandell BA. 2004. Interpreting the BOLD Signal. *Annu Rev Physiol* **66**:735–769.
464 doi:10.1146/annurev.physiol.66.082602.092845
- 465 Lyons DG, Parpaleix A, Roche M, Charpak S. 2016. Mapping oxygen concentration in the awake
466 mouse brain. *Elife* **5**:e12024.
- 467 Mayhew J, Johnston D, Martindale J, Jones M, Berwick J, Zheng Y. 2001. Increased Oxygen
468 Consumption Following Activation of Brain: Theoretical Footnotes Using Spectroscopic Data
469 from Barrel Cortex. *Neuroimage* **13**:975–987. doi:10.1006/nimg.2001.0807
- 470 Parpaleix A, re, Houssem YG, Charpak S. 2013. Imaging local neuronal activity by monitoring PO₂
471 transients in capillaries. *Nat Med* **19**:241–6. doi:10.1038/nm.3059
- 472 Roche M, Chaigneau E, Rungta RL, Boido D, Weber B, Charpak S. 2019. In vivo imaging with a
473 water immersion objective affects brain temperature, blood flow and oxygenation. *eLife* **8**.
474 doi:10.7554/eLife.47324
- 475 Rungta R, Chaigneau E, Osmanski B, Neuron C-S. 2018. Vascular compartmentalization of
476 functional hyperemia from the synapse to the pia.
- 477 Rungta RL, Zuend M, Aydin A-K, Martineau É, Boido D, Weber B, Charpak S. 2021. Diversity of
478 neurovascular coupling dynamics along vascular arbors in layer II/III somatosensory cortex.
479 *Commun Biology* **4**:855. doi:10.1038/s42003-021-02382-w
- 480 Şencan İ, Esipova T, Kiliç K, Li B, Desjardins M, Yaseen MA, Wang H, Porter JE, Kura S, Fu B,
481 Secomb TW, Boas DA, Vinogradov SA, Devor A, Sakadžić S. 2020. Optical measurement of
482 microvascular oxygenation and blood flow responses in awake mouse cortex during
483 functional activation. *J Cereb Blood Flow Metabolism* 0271678X2092801.
484 doi:10.1177/0271678x20928011
- 485 Thompson JK, Peterson MR, Freeman RD. 2005. Separate Spatial Scales Determine Neural
486 Activity-Dependent Changes in Tissue Oxygen within Central Visual Pathways. *J Neurosci*
487 **25**:9046–9058. doi:10.1523/jneurosci.2127-05.2005

-
- 488 Thompson JK, Peterson MR, Freeman RD. 2004. High-resolution neurometabolic coupling
489 revealed by focal activation of visual neurons. *Nat Neurosci* **7**:919–920. doi:10.1038/nn1308
- 490 Thompson JK, Peterson MR, Freeman RD. 2003. Single-Neuron Activity and Tissue Oxygenation
491 in the Cerebral Cortex. *Science* **299**:1070–1072. doi:10.1126/science.1079220
- 492 Uchida K, Reilly MP, Asakura T. 1998. Molecular Stability and Function of Mouse Hemoglobins.
493 *Zool Sci* **15**:703–706. doi:10.2108/zsj.15.703
- 494 Wachowiak M, Cohen LB. 2001. Representation of Odorants by Receptor Neuron Input to the
495 Mouse Olfactory Bulb. *Neuron* **32**:723–735. doi:10.1016/s0896-6273(01)00506-2
- 496 Watanabe M, Bartels A, Macke JH, Murayama Y, Logothetis NK. 2013. Temporal Jitter of the
497 BOLD Signal Reveals a Reliable Initial Dip and Improved Spatial Resolution. *Curr Biol* **23**:2146–
498 2150. doi:10.1016/j.cub.2013.08.057
- 499 Zhang Q, Roche M, Gheres KW, Chaigneau E, Kedarasetti RT, Haselden WD, Charpak S, Drew PJ.
500 2019. Cerebral oxygenation during locomotion is modulated by respiration. *Nat Commun*
501 **10**:5515. doi:10.1038/s41467-019-13523-5

502

Part III

Discussions & Perspectives

CHAPTER 10

LINKING MICROSCOPIC NEURONAL ACTIVATION TO MESOSCOPIC FUS RESPONSE

Contents

10.1 Summary	127
10.2 Discussion	128
10.2.1 Transfer function computation	128
10.2.2 Co-registration	129
10.2.3 Functional ultrasound activation maps	129
10.3 Perspectives	130
10.3.1 Transfer function to dissect NVC	130

10.1 Summary

In this first study, we took advantage of the olfactory bulb model and its specific neuronal characteristics in the glomerular layer. We focused on the most sensitive glomerulus for the odor we use, Ethyl tiglate (ET). Thus, we could record the same functional area across mice. We measured simultaneously the neuronal activity using GCaMP6f fluorescence in MC dendrites and vascular activity via RBC velocity in a nearby capillary. Then, we computed a transfer function to quantify NVC. Remarkably this TF, computed over the data of a single mouse at a given odor concentration and duration, was able to reliably predict the vascular response shape of all the other mice at

an identical stimulus. This shows that for a given neuronal activation, NVC dynamic is reliably conserved across animals at a microscopic level. This TF peaks at ≈ 1 s and onsets at ≈ 250 ms.

By predicting the vascular responses over a wide range of durations and concentrations we experimentally acquired, we showed that the single TF is still reliable. Notably, we wondered whether NVC changes at very weak or very strong stimuli. We went down in duration to a single sniff, the smallest natural stimulus, by optimizing our delivery process to match the breathing frequency of the mouse, and we could still confirm the validity of the TF. However, at high odor concentration, nonlinearities appear and the TF is unable to predict an additional late response that we named “the 2nd vascular component”. Thus, NVC dynamic is highly conserved across neuronal activation characteristics, apart from very strong neuronal activations where another mechanism emerges.

Going from microscopic to mesoscopic with fUS, we wanted to make sure that we were measuring the fUS signal from the same location as with the microscope. We developed a 3D-printed module physically securing the objective of the microscope to the fUS probe. We precisely evaluated the displacement of the 3D-printed module to focus at the same place between both modalities by means of a 50 μm glass bead. This allowed us to measure the “Point-Spread Function” of the fUS, which were similar to a previously one (160 \times 110 \times 210 μm). We show that the microscopic shape of the functional hyperemia closely relates with the fUS response shape. We compared the voxel containing the most sensitive glomerulus in the fUS slice to the 5 around it and found that their shape was reliably similar. This is discussed below.

Despite this resemblance, we reported that the TF computed between local neuronal activation and the co-registered fUS response is slightly different than the microscopic TF. Nonetheless, they both peak at the same time.

Finally, we analyzed whether activation maps based on this vascular modality faithfully reported local neuronal activation. First, thanks to the good SNR of the fUS, we considered the integral of the fUS signal as a proxy for neuronal activation. Surprisingly, the voxel containing the most sensitive glomerulus was not reliably the most active one. We went further by using the canonical way to analyze BOLD-fMRI data, a General Linear Model approach, and again the single voxel never got to be the most active one. In one mouse, the co-registered voxel, did not even pass the threshold for significance. Both these issues are discussed below.

10.2 Discussion

I will only discuss the points that are not in the actual paper here.

10.2.1 Transfer function computation

The common way to test whether a TF based on actual data is relevant, is to do the computation on half of the data and test it on the other half. I performed the computation of the TF on each mouse and assessed whether a single one was relevant for the whole batch of mice, a technique named “*leave-p-out*” with $p = n - 1$. To our surprise it did, and that is why I did not go further

by doing it the canonical way. For the sake of the demonstration, I will present this canonical way of computing at the thesis defense¹.

During the analysis, we computed a single TF per mouse, all slightly different from one another. One can wonder why it was not the same each time, and deduce that NVC is not as constant as we say it is. I think these discrepancies are due to the unsteady SNR of the different mice. Brain movement due to vessels dilating can render the acquisitions noisy, and thus alter the TF computation. Indeed, the mouse in which we found the TF provided beautiful traces.

10.2.2 Co-registration

As I mentioned in the introduction (see section 4.3.3.4), the location of a given voxel is calculated based on the speed of sound in water. However, the skull or the PMP window we used changes the speed of sound. This changes the relative location of the voxels. Usually, this does not cause any problem because every voxel of the slice is located under the same thickness of skull/PMP: the artifact is the same everywhere and can be ignored. However, the co-registration is based on a bead placed in a petri box without skull/PMP above it. Thus, the localization of the right voxel is different between the calibration and the actual experiment.

Let us calculate the amount of displacement. The speed of sound in the PMP is around 1900 m.s⁻¹, and it is 100 μm thick. Going back and forth through the PMP, the US wave takes around 53 ns, while it would take 67 ns in water. This 14 ns difference translates into an error of 21 μm , which is > 5 times smaller than the actual height of a voxel. Thus, we did not compensate for this systematic error.

10.2.3 Functional ultrasound activation maps

Our results showed that the voxel containing the most sensitive glomerulus is almost never the most activated one in the vicinity of the co-registered voxel. It can seem like a major downside to using vascular based imaging for inferring neuronal activation. Here I provide some hypotheses on this uncertainty on the localization of the highest neuronal activation using blood flow based imaging. First, due to the odor concentrations we used in order to get a good signal, there was a wide activation of the olfactory bulb. It may be that due to adaptation of the most sensitive glomerulus, which then was not actually the most active [Lecoq *et al.* 2009]. Second, the vascularization pattern may change between voxels: if a voxel has numerous vessels parallel to the fUS probe, its signals will be much lower than its actual blood volume. Third, we filtered the signal to get only the small axial speeds, between 0.5 and 1.5 mm.s⁻¹, which can also alter the inference. Lastly, the backpropagation of the signal dilates larger vessels upstream. If these vessels are close to the co-registered area, they can make a larger signal in fUS than the co-registered voxel. Nonetheless, the largest response is not where we expect it to be and further research is needed. I will come back to this in the next section.

¹And not here for two reasons: (i) to keep some surprises but mostly (ii) because I did not have the time yet.

10.3 Perspectives

To precisely evaluate whether fUS is able to reveal the most activated area, the OB is the perfect model. By going down to very low concentrations, we are able to activate a single glomerulus [Boido *et al.* 2019]. Thanks to the co-registration and by averaging enough acquisition, we can assess whether the low precision in localizing the most sensitive glomerulus with fUS is due to our experimental design or to the backpropagation of the vascular signal. If the last is true, an evaluation, at microscopic scale, of the vascular arbor of the brain and of the NVC dynamic would be required to evaluate the spatial specificity of the fUS. Moreover, using various speed filtrations, we could gather interesting information.

Another experiment would be to simultaneously record wide-field Ca^{2+} changes, together with IOS and fUS, via a 3D-printed holder. We would correlate neuronal activation with the fUS changes and the oxygen consumption at a very large scale. Expression of the GCaMP would have to be well known, as we know that postsynaptic activity is probably the best correlate of FH, rather than somatic or axonal activation.

Vessel anisotropy evaluates vessel orientations, i.e. how much they are parallel to the transversal plane. Recently, a study of vessel anisotropy came out down to the capillary level, together with their diameter [Ji *et al.* 2021]. In resting state, these numbers and the location of vessels can help correct the orientation-dependence of the fUS signal, by applying a factor to each voxel depending on the diameter and anisotropy of vessels inside. However, it is a huge work that is probably feasible in only a handful of mice. I would use it to check whether correcting for the orientation-dependence drastically changes in resting state the fUS signal across voxels. Doing it upon neuronal activation would be limited by the assumption that all vessels dilate identically, independently of their direction or their location. A full characterization of the flow changes in all vessels from a voxel is needed to interpret fUS upon stimulus.

10.3.1 Transfer function to dissect NVC

The main advantage of using a holistic approach to model NVC is that it comprises all of the mechanisms inside. By cancelling various known pathways of NVC and computing new TFs, we could precisely assess an eventual impairment of the NVC dynamic for a given phenotype. Note that this would have to be done on a small timescale to avoid any adaptation of the physiological mechanisms and be reversible to make sure that the silencing did not perturb the NVC irreversibly.

As a proof of concept, you can see that in the Figure 4 of the study in annex (see annex B) we measured the difference in NVC dynamic between anesthetized and awake mice by means of TFs. As expected, we show that anesthesia slows acrshortNVC and makes acrshortFH lasts longer.

CHAPTER 11

ILISKI

Contents

11.1 Summary	131
11.2 Discussion	132
11.3 Perspectives	133

11.1 Summary

Iliski is the software I developed to perform TF computation easily and I used in the previous project of my PhD period. To share it and make it user-friendly, I developed a graphical user interface allowing anyone to use it with or without the necessary computational background. One can still use it as MATLAB functions in its own scripts, as the code and every function is available on [GitHub](#). The current version of the user manual is in the appendices (see annex A).

The paper introducing Iliski presents all processes made available in Iliski to compute TFs, all of which are highly adaptable by the user. Then, we make use of the Results section to present how we computed the TFs of [Aydin *et al.* 2020](#). Biological data have specific characteristics that need to be taken into account to produce meaningful results, e.g. the noise of both biology and acquisition setup or inherent restrictions deriving from the physiological processes. Thus, we present several possible ways to compute TFs and how we chose non-deterministic algorithms with specific boundaries: for instance, functional hyperemia cannot start either before or right at the time of the neuronal activation. For this purpose, we set the time-shift parameter, which does not exist in the classical HRF, to be at least 1 ms. Using non-deterministic approaches, we have to repeat the computation process to find out a deep minimum of the cost function. We provide insights into

how increasing the repetitions impact the final result, based on our biological data.

Finally, we provide a decision tree to help anyone who might need it to choose the best computation approach.

11.2 Discussion

With Iliski we put a step into open science (OS) and the open software world, providing the scientific community with all we have used for the previous study. The OS framework comprises multiple domains (Figure 11.1). The main ones, or the most known, are Open Access and OpenData/Software. I will only focus on Open Data and Open Software below, as I found a lot of confusion about it in the last years. The interested reader can find more information on Open Access in [Fraser *et al.* 2020], which presents the impact of publishing preprints, in [Eve & Gray 2020], a book raising concerns about its possible consequences.

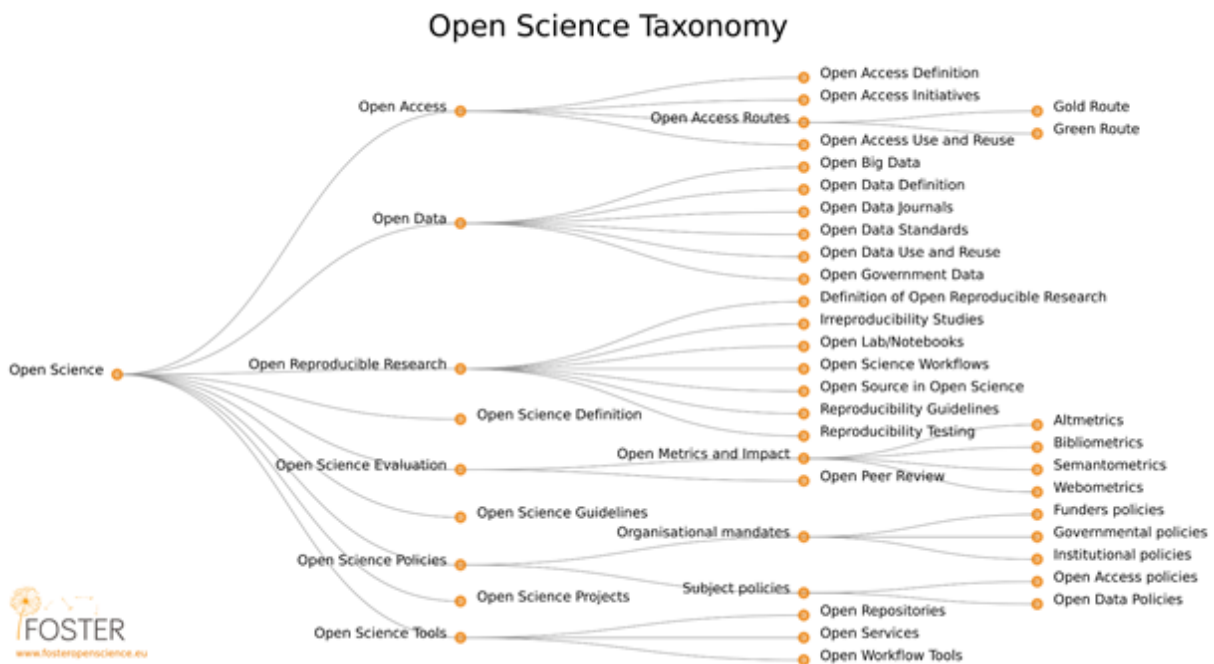


Figure 11.1: Open Science Taxonomy. From [Pontika *et al.* 2015].

Recently, many peer-reviewed analyses show how much of published scientific studies are ir-replicable, i.e. the overall finding of the study cannot be found by other laboratories, or irre-producible, i.e. using the same data the analysis output is different [Kerr 1998, Fanelli 2010, John *et al.* 2011, Munafò *et al.* 2017]. Of interest, researchers showed that only 11% of 53 pre-clinical research papers on cancer were found replicable while trying to develop the corresponding treatment [Begley & Ellis 2012]. 21 of those articles were published in journals with an impact factor > 20 , thus supposedly with higher expectations regarding their methods and results. Indeed, the majority of researchers themselves believe that there is a reproducibility crisis in our scientific results [Baker 2016].

Munafò and colleagues provide in their 2017 paper many explanations as to why and when problems can happen in the whole scientific process [Munafò *et al.* 2017]. Data analysis is one of them. Indeed, a recent study showed that only 26% of the results were replicable using the same software and the same data as the original authors, in a sample of 203 papers from Science after they updated their policy to force scientists to share more [Stodden *et al.* 2018].

Sharing our code forces us to have clean code, debugged and double checked by other users/developers. Sharing allows others to reuse our code and gain time to produce new results, while citing our own work. Overall, sharing is the best way to promote our own work. Recent events, the infamous COVID-19 pandemic, showed that sharing is an inestimable tool to evaluate and accelerate research results and help save lives. This specific issue is discussed in [Besançon *et al.* 2021].

11.3 Perspectives

Upcoming work on Iliski will mainly depend on whether users from other labs need anything, supposing they find it useful. On my side, I plan to develop two new features: allow for a customizable cost function and, as I described in the discussion of the first project (see section 10.2.1), allow the computation of TFs based on multiple traces rather than a single one.

CHAPTER 12

TO DIP OR NOT TO DIP

12.1 Summary

In this study, we wanted to gain insight into the physiological mechanisms underlying the initial dip (ID). The ID is elusive since its first description (REF SUBSECTION), yet it may be an important tool for the interpretation of BOLD-fMRI. We mainly focused on the most sensitive glomerulus to Ethyl tiglate, under the assumption that it activates and consume oxygen more than others and should thus create a bigger ID than elsewhere. We started by measuring neuronal and vascular responses at various concentrations in the most sensitive glomerulus (MSG). As expected, MC dendritic activation measured with GCaMP6f shows a concentration-dependent behavior, like the RBC velocity in a nearby capillary measured simultaneously. We showed that hyperemic responses are also concentration-dependent, as expected. Looking at the responses normalized by the baseline and averaged, we did not report the ID in any of the concentrations.

However, by turning the traces into Z-scores we revealed the presence of an initial dip at high concentration with an average amplitude of 0.3 SD, in 60% of the mice. Analysis of the delay between neuronal and RBC flow onset showed that the mice with ID all have a longer delay (> 1.6 s) than the other mice (< 1.2 s).

We went further in the analysis by separating the oxygenation of either the RBC (Po_2 RBC) or the plasma (Po_2 Inter). Doing so, we showed that while the ID is not seen in the average Z-score of the Po_2 RBC, we see a decrease in the Po_2 Inter.

As a previous study modeled the initial dip amplitude and showed that decreasing the oxygenation level could enhance it [Mayhew *et al.* 2001], we tested this hypothesis in our model. We reduced the oxygen level by removing the oxygen supplementation in the anesthetized mice. Comparing both conditions, we reported that neuronal activation stays stable while Po_2 resting values decrease, as could be expected. Both resting RBCs velocity and flow increase in response to hypoxia. We measured that the overall dynamic of the vascular response changes in response to

hypoxia: RBCs velocity and flow responses get back to baseline much slower, but their onsets did not change. Strikingly, the Po_2 response nearly disappears in this new condition. We reported that this hypoxic state slightly increased the amplitude of the initial dip, from 0.33 to 0.47 SD, while still being below noise level.

Then, we wondered what would be measured in other glomeruli. Hypothetically, the initial dip would be smaller as neuronal activation is lower than in the MSG. Indeed, we did not report any initial dip in the 22 glomeruli measured.

Taken together, these results undermine the usefulness of the initial dip in BOLD-fMRI interpretation. The only way to detect it is by turning traces into Z-scores and, even in that case its amplitude is ridiculously small. Given the signal-to-noise ratio of BOLD, we do not believe that it is a suitable solution. However, these results bring insights into why it has been measured many times in the last decades: both anesthesia and acute preparations are known to impair NVC. This is in line with the fact that the ID is seen in mice having a longer delay for the RBC flow onset upon neuronal activation.

12.2 Discussion

I will go over some of the points that are not discussed in the preprint. The main question, whether the ID exists and upon which conditions, is already extensively discussed in the paper.

12.2.1 Delay between RBCs flow and hyperemic responses

In Figure 2C we show that there is a delay of around 0.7 s between the onsets of the RBCs flow and the Po_2 increases. At first, I was surprised about this difference: the increase in flow is what brings more oxygen in the capillaries and by diffusion into the tissue. However, this difference can be due to which RBC brings more oxygen. If we imagine that the hyperoxygenated RBCs are quite upstream of the capillary, there should be a delay between the increase in flow, which is nearly instantaneous upon vessel dilation [Rungta *et al.* 2018], and the subsequent increase in Po_2 which depends on the hyperoxygenated RBCs reaching the capillary.

Nonetheless I measured a delay of around 0.7 s, and we previously measured the distance from the arteriole, being the primary dilating compartment, to the capillary in the OB to be 700-800 μm . With a very conservative RBC velocity of 1 $\text{mm}\cdot\text{s}^{-1}$ in upstream vessels, as it is the speed in capillaries, the hyperoxygenated RBCs should get to the capillary in 700-800 ms. Given that the actual speed is much higher, we previously reported 5 $\text{mm}\cdot\text{s}^{-1}$ in the large dilating capillaries in resting state, this delay should be smaller. We do not know to what extent. It was part of the initial project to determine the rate of single RBC deoxygenation along its path, but the results regarding the dip changed these plans.

12.2.2 Changes in vessel dynamic upon hypoxia

While comparing oxygen supplemented and not supplemented responses, we saw that the response shapes are quite different for the RBCs velocity and flow. Obviously, the output of neurovascular coupling changes, as neuronal activation is stable while the vascular one is different. What can explain this difference? My main hypothesis would be that vessels dilate due to the hypoxic state, which is corroborated by the increase in resting RBCs velocity and flow, and that this dilation changes the subsequent vascular reaction to NVC. In other words, the cellular and molecular mechanisms of NVC makes the vessels act differently depending on their initial dilation. Another plausible explanation would be that NVC itself changes, i.e. the cellular and molecular mechanisms are different depending on the oxygen levels. The adaptation is quick, we waited 15 min between removing oxygen supplementation and the first acquisitions in the hypoxic state. I doubt that there are changes in the proteome changing NVC, but several enzymes have KDs depending on oxygen and thus, NVC could slightly differ with P_{O_2} . This is clearly supported by the fact that hyperemia nearly disappears in the hypoxic state. This at odd with previous papers stating that FH is independent of oxygenation [Lindauer *et al.* 2009].

I intentionally left out some considerations on the experimental and analytical process, especially regarding the difficulty to get accurate P_{O_2} RBC and P_{O_2} Inter measurements . Both related to physiological parameters of the vasculature, notably velocity and flow, and to having animals that keep a clean window over the weeks and the experiments, it explains why the measures of P_{O_2} RBC and P_{O_2} Inter are scarcer than P_{O_2} Mean.

12.3 Perspectives

This work is not yet finished, some experiments are going on and the final version of the article should have a few figures more which will be presented at the defense. Some of them are quickly described below, among other considerations.

Three main experiments should be performed to better understand the physiological mechanisms behind the ID. First, our experiments should be reproduced in the awake animals. With a faster functional hyperemia, we could check the hypothesis that the ID is due to NVC impairment. Given our current data, we would have to focus on the MSG since this is the only location where we measure it in the anesthetized mice.

Second, as mentioned in the discussion of the paper, tissular P_{O_2} measures are important as they are different from the capillary ones.

Last, we could co-register two-photon microscopy and BOLD-fMRI, like we did in the first study. Given that the BOLD signal originates not only from local P_{O_2} , it would be a very elegant way to further link microscopic and mesoscopic measures.

Part IV

Appendices

APPENDIX A

ILISKI: USER MANUAL

Iliski: User Manual

Ali-Kemal Aydin

INSERM, CNRS, Institut de la Vision, Sorbonne Université, Paris, France

Davide Boido

NeuroSpin, Bât 145, Commissariat à l'Energie Atomique-Saclay Center, 91191, Gif-sur-Yvette, France

Iliski is a software developed in the Charpak Team. It aims to compute **Transfer functions** between any two timeseries, to represent their dynamic relationship. *Iliski* is further described in the following pre-print available on [BioRxiv](#).

Contents

<i>Iliski</i>: User Manual		
	Ali-Kemal Aydin & Davide Boido	1
1	Overview of <i>Iliski</i>	4
	1.1 Where to find <i>Iliski</i> ?	4
	1.2 Overview of the workflow	5
	1.3 How to use <i>Iliski</i> ?	5
2	Input data	5
	2.1 Input files	5
	2.2 Use a boxcar function as From signal	9
3	TF computation process	10
	3.1 Data pre-treatment	10
	3.2 Transfer Function computation	12
	3.3 Evaluation of the TF	17
	3.4 Available options	18
4	Saving a computation and accessing a previous one	19
	4.1 Saving as a MAT-File	19
	4.2 Saving as Excel file	20
5	<i>Iliski</i> as a suite of scripts	20
6	Specifications	20
7	Contact	20
	Glossary	20
	Acronyms	21
	Bibliography	21

Ali-Kemal Aydin & Davide Boido

1 Overview of *Iliski*

Iliski ([ɪlɪʃki]) means *relationship* in turkish. It computes relationships between timeseries¹ of any type. Figure 1 shows the software's **Graphical User Interface (GUI)**. The user can also use the scripts independently of the **GUI**. *Iliski* is written with MATLAB.

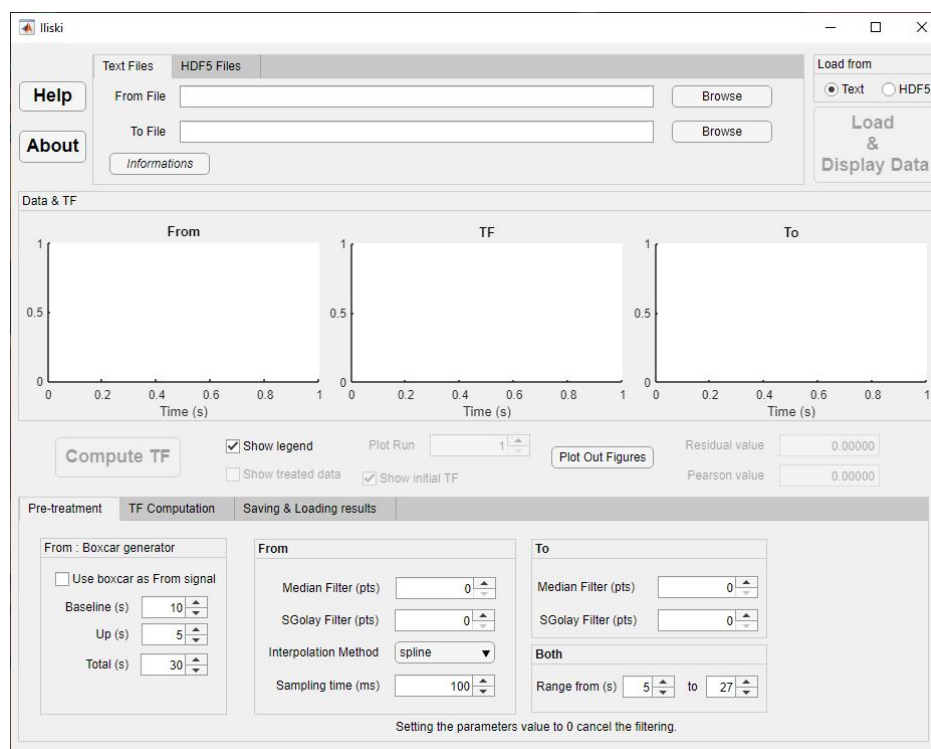


Figure 1: View of *Iliski* right after it being launched.

1.1 Where to find *Iliski*?

Iliski can be downloaded on GitHub at the following link: <https://github.com/alike-aydin/Iliski>. Refer to the ReadMe part of the repository for more details on what version to download depending on your system and MATLAB installation.

¹Although we state here and in *Iliski* that data are time-dependent, there are no such requirement. One can use any type of x coordinates, but will have to be careful with the options regarding the time to keep the resulting TFs reliable.

Iliski: User Manual

Some example datasets are available on Zenodo: <https://doi.org/10.5281/zenodo.3773863> and some are already in the ExampleData folder.

1.2 Overview of the workflow

Iliski gets two different signals as inputs: the 'From' signal, herein after referred as **From**, and the 'To' signal, similarly referred as **To**, both functions of time¹. *Iliski* will compute **Transfer function** (TF) to accurately solve (1.1). The * operator denotes the convolution operation.

$$From(t) * TF(t) = To(t) \quad (1.1)$$

Each option of *Iliski* aims at modifying the way the TF will be computed, either directly with the computation options or indirectly with the signal pre-processing options. There are three main parts to the computation process, illustrated in Figure 2:

1. Data pre-treatment: **From** and **To** data are modified to allow for a better TF computation.
2. **Transfer function** computation: there are several ways to compute a TF.
3. TF evaluation: a TF computed from a parametric function optimization algorithm never perfectly predicts the test dataset. It has to be evaluated.

Every option of each part is described in the section 3.2 (page 12).

1.3 How to use *Iliski*?

As written above, *Iliski* can be used in two different ways: through its GUI, or by directly calling its functions in one's own scripts. Note that everything has been written in MATLAB 2018a (see section 6, page 20). The GUI version can be used as a MATLAB file, thus needing an operational MATLAB installation, or as a standalone application. Refer to the section 5 (page 20) for more details on the various functions at the user's disposal for using *Iliski* as a suite of scripts.

2 Input data

2.1 Input files

Iliski can treat various file formats as input data. The simpler one is text-based, e.g. .txt, numerical data-file. *Iliski* also allows for HDF5 files but it will need

Ali-Kemal Aydin & Davide Boido

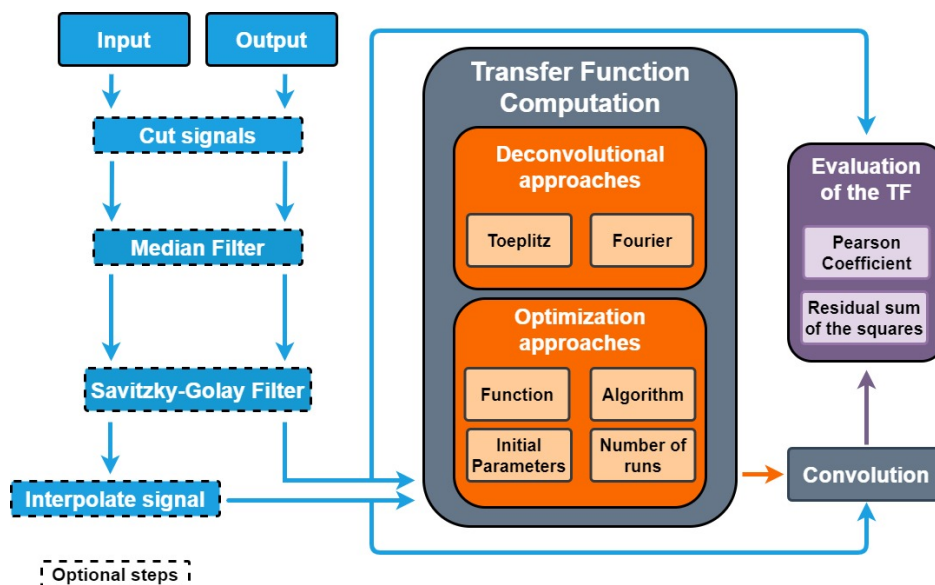


Figure 2: *Iliski*'s workflow is separated in three main parts, from left to right: pre-treatment of the input data, computation of the **TF** and evaluation of the computed **TF**.

a more restrictive format, as described in section 2.1.2.1 (page 7). There are two tabs, depending on the file format. The user must also specify the format correspondant to the input data above the **Load and Display** button (see Figure 3 and Figure 4). Note that *Iliski* was not coded to handle complex-valued signals.

Iliski supposes **From** and **To** data are timeseries. For this reason, we will call 'time' the vector of x coordinates of **From** and **To**. As such, it needs to have a time vector matching the data vector for both. Note that the sampling does not need to be identical between both signals: *Iliski* provides interpolation to account for that (for more details see section 3, page 10).

2.1.1 Text-based files

Both **From** and **To** must have their own file (see Figure 3). Data inside a text-based file should be in a column form, separated either by tabulations or spaces. Depending on the number of columns, *Iliski* will interpret the files differently:

- Two-columns file: the first column is the time vector, while the second one is the data vector.

Iliski: User Manual

- One-column file: the only column will be used as the data vector. The x vector will be artificially created as a vector starting from 0 up to the number of points, with a step of 1.
*Make sure that this interpretation will not create discrepancies between the **From** and **To** signals.*
- More than two columns file: only the first two columns will be accounted for, respectively as time and data vectors.

Figure 3: Paths to the **From** and **To** text data files should be put in the left red box. The right red box specifies what format is to be loaded.

2.1.2 HDF5 files

Iliski accesses data stored inside HDF5 file (Hierarchical Data Format)². Paths to the HDF5 files containing the **From** and **To** data must be written in the boxes circled in Figure 4. Note that if the HDF5 file containing the **From** and **To** data are the same, a checkbox is placed on the right to avoid typing twice the same path. Figure 5 shows *Iliski* after loading data from an HDF5 file (VT31.h5, available on the GitLab repository).

Figure 4: Paths to the **From** and **To** HDF5 data files should be put in the left red box. The right red box specifies what format is to be loaded.

2.1.2.1 HDF5 files requirements for *Iliski*

HDF5 files contains data organized in groups, i.e. folders and subfolders. To access the data to compute a **TF** on, *Iliski* has two separate text boxes for the

² [HDF official website](#) & [HDF Wikipedia page](#)

Ali-Kemal Aydin & Davide Boido

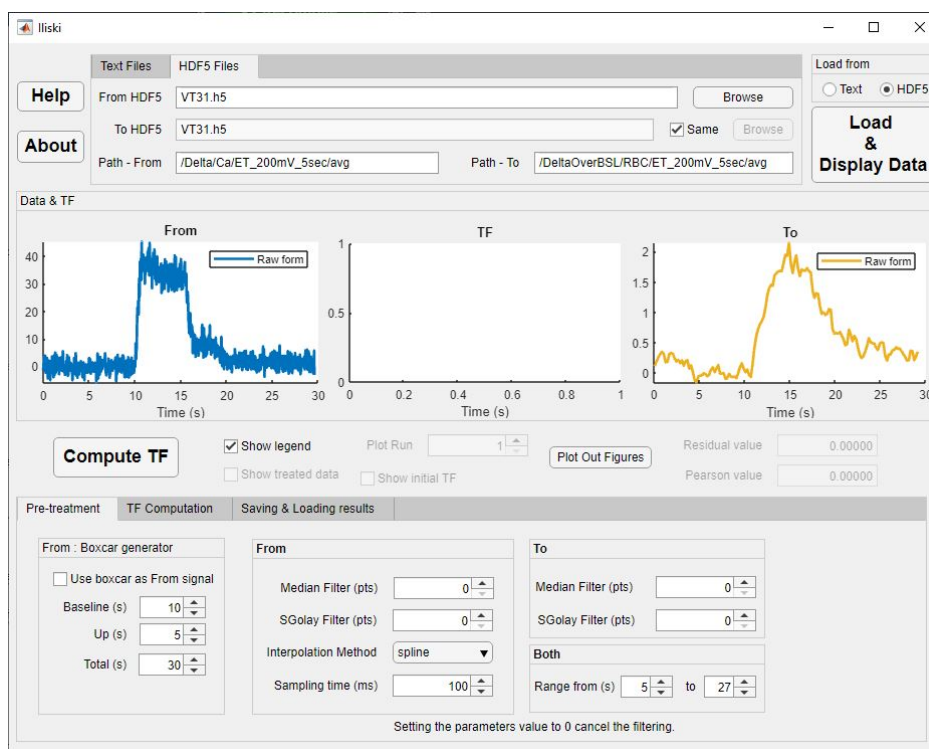


Figure 5: **From** and **To** data are loaded from an HDF5 file.

From and **To** data files. Figure 6 shows where they are.



Figure 6: Paths to the **From** and **To** data, inside the HDF5 files, should be put in the boxes circled in red.

For *Iliski* to retrieve the corresponding time vector inside the HDF5 arborescence, it follows two rules (see Figure 7):

- The time vector is supposed to have the same dimensions as the data vector, since every datapoint has its corresponding time point.

Iliski: User Manual

- The time vector is placed in the same group as the data vector and is named 'time'.

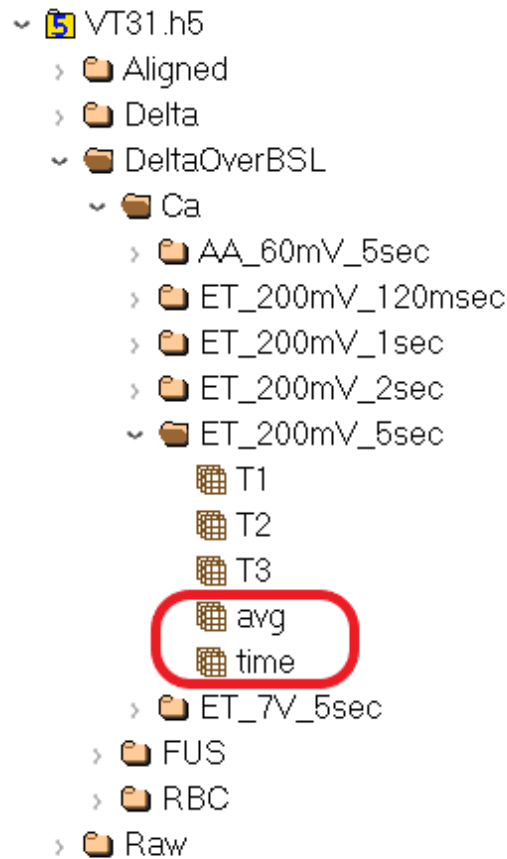


Figure 7: The x coordinates vector must be named 'time' and be in the same HDF5 group as the y coordinates vector, here 'avg' for instance. Screenshot from the HDFView software.

2.2 Use a boxcar function as **From** signal

We developed *Iliski* to study the neurovascular coupling. One main application is a better understanding of the **Blood Oxygen Dependent Level based Functional Magnetic Resonance Imaging (BOLD-fMRI)**. Extracting activated brain ar-

Ali-Kemal Aydin & Davide Boido

as from **BOLD-fMRI** requires to somehow represent the neural activation. If no information is available on the neuronal activity, a conservative approach consists in using the temporal representation of the stimulus application with the shape of a **boxcar function** (see Figure 8) going from 0 to 1 when the subject under the **BOLD-fMRI** is stimulated³.

Iliski lets the user use a **boxcar function** as the **From** signal if needed. Figure 8 shows where the parameters are placed in the **GUI**:

- **Baseline**: Duration, in second, of the pre-stimulus 0 period.
- **Up**: Duration, in second, of the stimulus 1 period.
- **Total**: Duration, in second, of the total timeserie (baseline + stimulus + post-stimulus periods).
- **Sampling time**: Time between points, in milliseconds.

Once the corresponding boxes are filled with the paths to the input files, a click on **Load and Display Data** makes *Iliski* load them. If you want to use a boxcar function, fill the **To** path(s) before checking the checkbox among the boxcar parameters.

3 TF computation process

Figure 2 outlines the main parts of the computation process.

Once *Iliski* loads your data, as described in section 2 (page 5), the computation process can start. After clicking on the **Compute TF** button in the **GUI**, *Iliski* will first treat your data.

3.1 Data pre-treatment

Iliski allows for **cutting signals to a given time range**, specified by two parameters: start and end timepoints. Both of them are in the same unity as your time vector, which is displayed as "seconds" in the **GUI**.

Your input data, either **From** or **To**, may be noisy. To get a meaningful **TF**, i.e. a meaningful relationship between your input data, removing part of the noise can be useful while paying attention to keep as much information as necessary in your timeseries. *Iliski* offers two methods you may combine:

1. **Median Filter**⁴: to remove outliers from your timeseries. The parameters

³ Dear **BOLD-fMRI** people, apologies for the quick-and-dirty explanation.

⁴ [Moving median function *movmedian* MATLAB documentation](#)

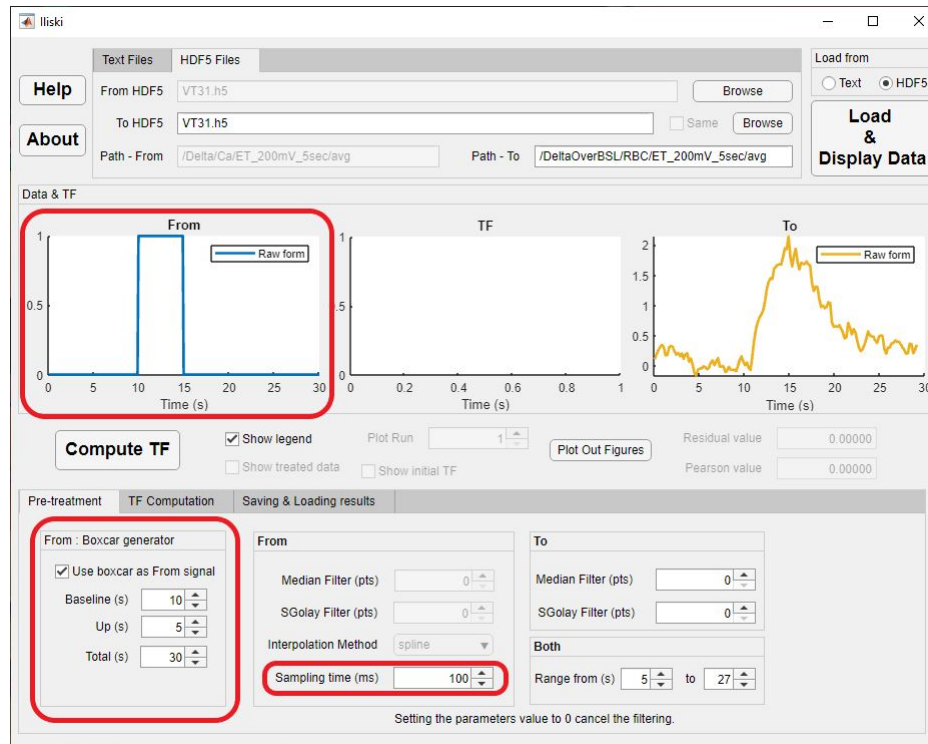
Iliski: User Manual

Figure 8: The lower red circle outlines the parameters placement for the boxcar function, while the upper red circle show the resulting signal.

value is the number of points to apply the median filter on. If selected, this filter is applied first.

2. **Savitzky-Golay Filter**⁵: to smooth your timeseries while avoiding the shift caused by a sliding average. In practice, the filter will go over each point of the timeserie and fit a 3rd degree polynomial. The current point will then be replaced by the time point corresponding in the fit. The parameter corresponds to the number of points to fit, note that it has to be an **odd number** so that the current point is the center of the fit.

Both these parameters are available for the **From** and **To** signals. Use 0 as parameter to specify not to use these filters.

The last step of the data pre-treatment is the **interpolation** of the input data.

⁵ [Savitzky-Golay filter function *sgolayfilt* MATLAB documentation](#)

Ali-Kemal Aydin & Davide Boido

Iliski has different behaviors depending on the **TF** computation you chose (see section 3.2, page 12):

- **Deconvolutional approaches:** either through **Fourier Transform** or **Toeplitz Matrix**. Both signals must share the same time vector, thus, both **From** and **To** have to be interpolated to the same sampling time.
- **Optimization algorithm:** either with a **deterministic** or **non-deterministic algorithm**. This **TF** computation process does not require the **To** to have the same sampling time as **From** (see section 3.3, page 17).
- Using a **boxcar function** as **From** signal: interpolation is not performed to avoid changing the shape of the boxcar function (note that in Figure 8, the pre-treatment parameters are grayed).

There are two parameters to set for the interpolation:

- **Interpolation method**⁶: *Iliski* uses the *interp1* MATLAB function. The drop-down list allows you to chose the interpolation method used by the *interp1* function.
- **Sampling time:** the new sampling time in milliseconds (namely one thousandth of the unity of your time vector⁷). Note that if your time vector is regularly spaced and you put the original sampling time, no interpolation will occur. Also, note that this parameter should be **equal to the sampling time of the boxcar function** if you use it as **From** timeserie, otherwise an error message will pop-up.

See Figure 9 to get the parameters placement on the **GUI**.

3.2 Transfer Function computation

Once the input data is pre-treated, the **TF** can be computed. *Iliski* offers several ways to do so. See the attached scientific paper for more details on the difference between them ([BioRxiv paper](#)). The parameters for each type are described in the subsection 3.2.3 (page, 16).

⁶ [Interpolation function *interp1* MATLAB documentation](#)

⁷ Well, not necessarily time as already stated page 4

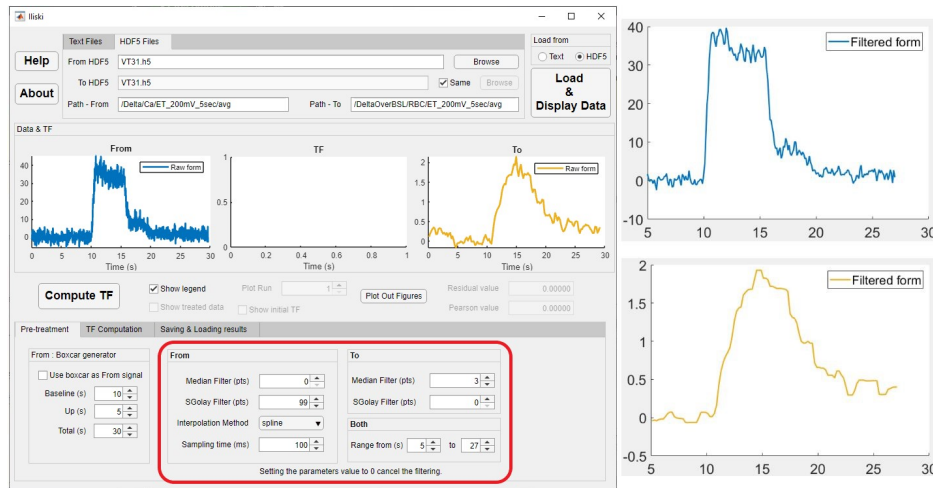
Iliski: User Manual

Figure 9: Circled in red are the parameters for the pre-treatment of the input data. On the right are the resulting data, treated according to the parameters on the left.

3.2.1 Deconvolutional methods

Deconvolutional methods are the canonical way to compute TFs. They avoid making any assumptions on the shape of the relationship. However, they are very sensitive to the noise of the signal: although there is a pre-treatment step, it may not be enough to get a clean enough signal while keeping all the relevant information.

Iliski proposes two deconvolutional methods:

- **Fourier Transform**
- **Toeplitz Matrix**

Most of the time, they will both give close results.

3.2.2 Optimization algorithms

Optimization algorithms require to define a function whose parameters are to be optimized to minimize a cost function value (see section 3.3, 17). *Iliski* has pre-registered functions, useful in the neurovascular coupling field, but one can use his own function too (see section 3.2.2.3, page 14). We propose two classes of optimization algorithms in our software: deterministic and non-deterministic algorithms.

Ali-Kemal Aydin & Davide Boido

3.2.2.1 Deterministic algorithms

3 different deterministic algorithms are proposed:

- **fminsearch**⁸: unconstrainable ;
- **fminunc**⁹: unconstrainable ;
- **fmincon**¹⁰: constrainable.

For **fmincon** and the non-deterministic algorithms, constraints can be applied to the optimization of the parameters. The user can define upper and lower bounds for each parameters in the GUI (see Figure 10).

3.2.2.2 Non-deterministic algorithms

Non-deterministic algorithms have a random component in their optimization process, to be able to jump from one cost-function minimum to another. Their purpose is to skip local minima and to reach the global minimum. In *Iliski*, we propose:

1. **Simulated Annealing**¹¹: constrainable ;
2. **Simulated Annealing** followed by **fminunc**: the point here is to try to get a deeper minimum by adding a layer of deterministic optimization over the non-deterministic one. The underlying hypothesis is that Simulated Annealing may not get to the absolute minimum but still be inside the well, in which case **fminunc** will go down to the minimum of that well.

3.2.2.3 Pre-registered and personalized functions

Iliski has two embedded functions, with t being the time and p the parameters to optimize:

- **1-Gamma Hemodynamic Response Function**: with H being the Heaviside function and Γ the Gamma function.

$$H(t - p_3) \times p_4 \times \left(\frac{(t - p_3)^{p_1 - 1} \times p_2^{p_1} \times e^{-p_2 \times (t - p_3)}}{\Gamma(p_1)} \right) \quad (1.2)$$

⁸ **fminsearch** function MATLAB documentation

⁹ **fminunc** function MATLAB documentation

¹⁰ **fmincon** function MATLAB documentation

¹¹ **Simulated Annealing** function *simulannealbnd* MATLAB documentation

Iliski: User Manual

- **2-Inverse Logit**

$$p_5 \times \frac{1}{1 + e^{-\frac{t-p_1}{p_3}}} - p_6 \times \frac{1}{1 + e^{-\frac{t-p_2}{p_4}}} \quad (1.3)$$

The user can optimize its own function either by typing directly in the right box (see Figure 10, choose **Personalized Function** in the **Function** dropdown list) or by making it a pre-registered function, as described below. Either way, the function has to follow some ground rules to be interpreted by *Iliski*:

- The function follows MATLAB writing rules and calls MATLAB functions when needed (e.g. the exponential function `exp`). Note that the function can call any function recognized by MATLAB.
- The function is written as an anonymous function, according to the pattern below. Note that `t` is necessarily the x vector and the last parameter.

`@(Par1, Par2, ..., t)FunctionHandle`

- As `t` is the x vector, the function handle has to be adapted to it. It may have to use element-wise operator like `./` instead of the classical `/`.

If you want to introduce your function as a pre-registered one, the following rules also apply:

- You have to add your function to the `DefaultParametricFunctions_Iliski.txt` file as a new line.
- The line is made of three parts, each separated by the `' : '` symbol:
 1. the function name, showed in the **GUI** ;
 2. the anonymous function handle, as described above ;
 3. the default parameters to be showed in the tab of the **GUI** (see Figure 10)

As an example, here are the lines for the two-pregistered functions (with `#` when there is a new line for reading purposes) in `DefaultParametricFunctions_Iliski.txt`:

```
1-Gamma: @(p1, p2, p3, p4, t)((t-p3)>=0).*p4.*(t-p3).^(p1-1).*(p2^p1).* #
exp(-p2.*(t-p3))./(gamma(p1)): [6 1 0 1]
2-Inverse Logit: @(p1, p2, p3, p4, p5, p6, t)p5*(1./(1+exp(-((t-p1)/p3)))) #
- p6*(1./(1+exp(-((t-p2)/p4)))): [2 2 2 2 2]
```

Ali-Kemal Aydin & Davide Boido

3.2.3 Parameters for TF computation

Parameters are outlined in Figure 10, although depending on the algorithm some parameters are not used.

First of all, the user can choose the function to use in the corresponding drop-down list. If the user chooses a deconvolutional approach, i.e. **Fourier** or **Toeplitz**, all other computation parameters will turn gray as they are useless. Otherwise, the following parameters are used:

- **Duration:** Duration, in seconds, of the parametric TF to optimize.
For every optimization algorithms, deterministic or or non-deterministic. The TF dimension is user-defined, with setting of the TF duration and ‘Sampling Time’ parameters that match the original data or can be augmented by non-linear interpolation.
- **Number of runs:** Number of subsequent runs of the *non-deterministic* algorithm with the same **starting parameters**. Note that a counter is available below the **TF** plot to go over all the optimized **TFs**, as many as the number of runs.
Only for non-deterministic algorithms.
- **Algorithm:** as described above. Check the corresponding checkbox to run **Simulated Annealing** before **fminunc**.
- **Parameters tab:** This tab contains 4 columns.
For every optimization algorithms, deterministic or or non-deterministic.
 1. Parameters name, as it appears in the default functions file or in the personalized function handle ;
 2. Starting value: the optimization algorithm will set the parameters to those values before working its way to better ones ;
 3. Lower and upper bounds: if the algorithm is *constrainable* (**fmincon**, **fminsearch**, **simulated annealing**), these values will restrain the parameters optimization. Otherwise, these parameters will do nothing.
- **GONG:** as the computation can take some time, checking this box will sonorize the end of the computation process.

A click on the **Compute TF** button starts the computation, once all settings are fine.

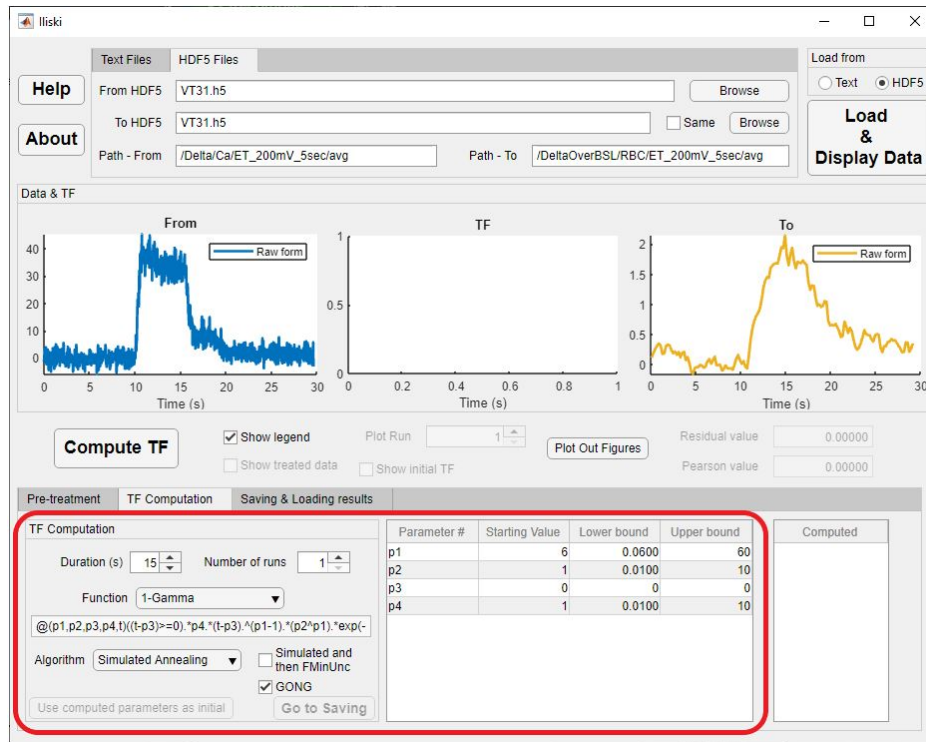


Figure 10: **TF** computation parameters are circled in red, in the second tab of the lower part of *Iliski*.

3.3 Evaluation of the TF

TFs are evaluated in two different ways, both of which quantify the correspondence between the actual **To** signal and the prediction made by the **TF**, i.e. the result of the convolution between **From** and the **TF**.

- **Residual sum of squares**: this is the absolute difference between the two timeseries. This metric is used as the cost function for the optimization algorithm. It varies from 0 to $+\infty$, 0 being a perfect overlap of the curves¹².
- **Pearson coefficient**: this metric measures how well two timeseries follow each other in their dynamics. It does not take into account the amplitude

¹² Note that this metric only makes sense for a given couple of **From** & **To** signals and their pre-processing parameters, since it has no normalization process.

Ali-Kemal Aydin & Davide Boido

but only the increases and decreases of the curves. It varies from 0 to 1, 1 being perfect correspondence.

When the user computes multiple runs with a non-deterministic optimization, the runs are ordered by **residual sum of squares** in the increasing order.

3.4 Available options

The table below lists and serves as a memorandum for all the parameters *Iliski* offers. They are divided according to their purposes.

Input data pre-treatment	
From	Median filter (number of points) Savitzky-Golay filter (number of points) Sampling time (ms)
To	Median filter (number of points) Savitzky-Golay filter (number of points)
Boxcar function generator	Baseline duration (s) Step duration (s) Total duration (s) Sampling time (s)
TF computation	
Function	Fourier deconvolution Toeplitz deconvolution 1-Gamma 2-Inverse Logit Personalized function
Algorithm ¹³	Non-deconvolutional approaches fminunc (D & U) fmincon (D & C) fminsearch (D & C) Simulated Annealing (ND & C) Simulated Annealing and fminunc (ND & U)
Optimization algorithm	TF duration (s, ND & D) Number of runs (#, ND) Starting parameters (a.u., ND & D) Lower and upper bounds (a.u., C)

¹³ D : Deterministic, ND : Non-Deterministic, U : Unconstrainable, C : Constrainable.

4 Saving a computation and accessing a previous one

Iliski's results can be saved in an Excel file or in MATLAB binary format: MAT-File. Once a computation is done, go to the corresponding tab to save it (see Figure 11). Note that you can only load back results into *Iliski* if they have been saved as MAT-File.

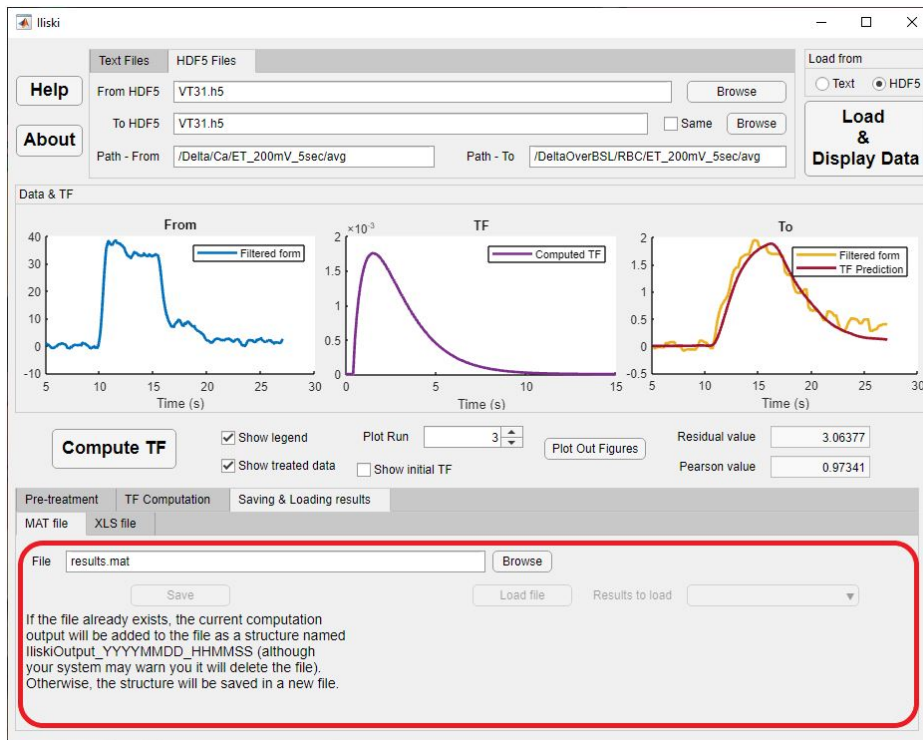


Figure 11: The user can save and load back his results in the third tab of the lower part of *Iliski*, either as a MAT-file or as an Excel Spreadsheet. Here, the displayed tab is for saving as a MAT-file.

4.1 Saving as a MAT-File

If the saving file already exists, it will add the current results to the one already registered inside. Else, it will create the file.

You can load an old result file by clicking on the appropriate button, and go through the results as if they were just computed. If multiple computations were

Ali-Kemal Aydin & Davide Boido

saved to the same MAT-file, the **Results to load** dropbox will let you choose the one to load.

4.2 Saving as Excel file

Likewise, you can save the results in an Excel file. The tabs in the resulting spreadsheet are quite self-explanatory. Note that if you used a non-deterministic algorithm and multiple runs, although every set of computed parameters will be saved, only the first **TF** and Prediction timeseries will be written in the corresponding tab (i.e. the one with the smaller residual sum of squares).

5 *Iliski* as a suite of scripts

As described in section 1.3 (page 5), *Iliski* can also be used as scripts. The main function to call is `Iliski_TF.m`, in the Functions folder. An example is available in the `test_Iliski.m` file, to explain how to use it.

6 Specifications

Iliski has been written with MATLAB 2018a, while the GUI was made with AppDesigner from the same MATLAB version. It has been tested on both Windows 10 and Mac OSX 10.14.3 (Mojave), and it should run on any computer running MATLAB 2018a and the following dependencies: Global Optimization Toolbox, Optimization Toolbox and Signal Processing Toolbox. Its standalone version does not need MATLAB to be installed.

7 Contact

In case of questions or bugs, do not hesitate to contact us at ali-kemal.aydin@inserm.fr and davide.boido@cea.fr. An `Errors.log` file inside the software folder is updated with every error *Iliski* encounters, please send the file alongside your bug description so that we can help you in the best way.

You can also open an issue directly on the GitLab repository, do not hesitate to do so and to thoroughly describe the problem you encounter: <https://github.com/alike-aydin/Iliski/issues>.

Iliski: User Manual

Glossary

from **From** is the input signal, to be convolved with the **Transfer function** to get **To**. 3, 5–12, 17, 18, 21

to **To** is the output signal, corresponding to the convolution of **From** and **Transfer function**. 5–8, 10–12, 17, 18, 21

transfer function Mathematical object representing the relationship between two signals. Hereafter, it is the function linking the input signal **From** and the output signal **To**. 1, 5, 21

Acronyms

BOLD-fMRI Blood Oxygen Dependent Level based Functional Magnetic Resonance Imaging. 9, 10

GUI Graphical User Interface. 4, 5, 10, 12, 15

TF **Transfer function**. 5–7, 10, 12, 16–18, 20, 21

TFs **Transfer functions**. 4, 13, 16, 17

APPENDIX B

DIVERSITY OF NEUROVASCULAR
COUPLING DYNAMICS ALONG
VASCULAR ARBORS IN LAYER II/III
SOMATOSENSORY CORTEX

communications biology

ARTICLE

<https://doi.org/10.1038/s42003-021-02382-w>

OPEN

Diversity of neurovascular coupling dynamics along vascular arbors in layer II/III somatosensory cortex

Ravi L. Rungta ^{1,2,3,4}✉, Marc Zuend ^{5,6}, Ali-Kemal Aydin ^{1,7}, Éric Martineau ^{2,3,4}, Davide Boido ^{1,8}, Bruno Weber ^{5,6} & Serge Charpak ^{1,7}✉

The spatial-temporal sequence of cerebral blood flow (CBF), cerebral blood volume (CBV) and blood velocity changes triggered by neuronal activation is critical for understanding functional brain imaging. This sequence follows a stereotypic pattern of changes across different zones of the vasculature in the olfactory bulb, the first relay of olfaction. However, in the cerebral cortex, where most human brain mapping studies are performed, the timing of activity evoked vascular events remains controversial. Here we utilized a single whisker stimulation model to map out functional hyperemia along vascular arbours from layer II/III to the surface of primary somatosensory cortex, in anesthetized and awake Thy1-GCaMP6 mice. We demonstrate that sensory stimulation triggers an increase in blood velocity within the mid-capillary bed and a dilation of upstream large capillaries, and the penetrating and pial arterioles. We report that under physiological stimulation, response onset times are highly variable across compartments of different vascular arbours. Furthermore, generating transfer functions (TFs) between neuronal Ca^{2+} and vascular dynamics across different brain states demonstrates that anesthesia decelerates neurovascular coupling (NVC). This spatial-temporal pattern of vascular events demonstrates functional diversity not only between different brain regions but also at the level of different vascular arbours within supragranular layers of the cerebral cortex.

¹INSERM U1128, Laboratory of Neurophysiology and New Microscopy, Université Paris Descartes, Paris, France. ²Faculté de Médecine Dentaire, Université de Montréal, Montréal, QC, Canada. ³Centre Interdisciplinaire de Recherche sur le Cerveau et l'Apprentissage, Université de Montréal, Montréal, QC, Canada. ⁴Groupe de Recherche sur le Système Nerveux Central, Université de Montréal, Montréal, QC, Canada. ⁵Institute of Pharmacology and Toxicology, University of Zurich, Zurich, Switzerland. ⁶Neuroscience Center Zurich, University of Zurich and ETH Zurich, Zurich, Switzerland. ⁷INSERM, CNRS, Institut de la Vision, Sorbonne Université, Paris, France. ⁸NeuroSpin, Bat. 145, Commissariat à l'Energie Atomique ' Saclay Center, Gif-sur-Yvette, France. ✉email: ravi.rungta@umontreal.ca; serge.charpak@inserm.fr

Hemodynamic-based imaging techniques such as BOLD and CBV fMRI are commonly used to infer neuronal activation patterns in humans and in animal models. They report dynamic parameters of functional hyperemia, i.e., changes of CBV, CBF, or their consequences on brain oxygenation. However, despite their importance for the interpretation of various functional imaging techniques, the spatial-temporal sequence of these vascular events remains unclear.

Across different brain regions, it has become common practice to name different vessel segments based on their branching order with respect to the upstream arteriole. In the specialized olfactory bulb (OB) glomerular model, synaptic activation is concentrated around the mid-capillary bed, constituted by an extremely dense network of capillaries outlined by long thin-strand pericytes. Upon activation, a vascular signal back propagates rapidly along the vasculature to activate sub-types of mural cells (ensheathing pericytes and smooth muscle cells) on dilating capillaries and arterioles, thereby increasing blood flow in a capillary bed volume larger than that of activated neurons¹. Importantly, the temporal pattern of diameter changes in OB is stereotypic; the onset of dilation occurs in the parenchymal arteriole and the proximal part of the 1st order emerging branch, and delayed dilation occurring in downstream 2nd to ~4th order capillary branches and upstream pial arteriole. In the rapidly dilating compartment, red blood cell (RBC) velocity can decrease, remain stable, or increase with a delay, and is a poor correlate of blood flow due to a local increase in blood volume¹. The retina is another region where the spatial-temporal sequence of vascular events has been quantitatively investigated. There, a global light flickering stimulus regulates the amplitude of vessel dilation differently in the superficial, intermediate and deep vascular layers, although, with no statistical difference in onset times between different vascular branch orders². However, whether such stereotyped patterns of activation across specific segments of the vascular arbor extend to higher-order cortical regions remains unclear.

In the cortex, past studies on the dynamics of diameter changes across different types of vessels have yielded inconsistent results^{3–7}, some reporting that vasodilation occurs earlier in penetrating arterioles and others in the proximal capillary branches (1st–4th order). One possible explanation underlying these differences is methodological differences between studies; (1) the location of neuronal activation was not systematically mapped out in relation to the vasculature, (2) electrical stimulations were used, (3) the use of acute surgical preparations or anesthetics, (4) the methods used to define the latency of dilation, of importance as baseline vasomotion may vary with the vessel type. In addition to methodological differences, it is important to note that the anatomical and functional properties of vascular compartments could vary beyond the simple distinction based on their vascular branch order. For example, increasing evidence suggests that the “transitional segment”, “pre-capillary arteriole” or “secondary functional unit” (as we named in the OB) must be considered a specific functional compartment, distinct from both the downstream capillary bed and the upstream arteriole. This compartmentalized distinction is highlighted by recent anatomical studies characterizing the presence and variability in the morphology of smooth-muscle cell and pericyte sub-types and their expression of the contractile protein α -SMA, exhibiting variable length and branch order coverage after the penetrating arteriole between different vascular arbors^{8–10}, thereby raising the question of whether similar branch order variability could exist in the onset timings of compartment specific vasodilation. Here, we utilized a single whisker deflection paradigm and neuronal Ca^{2+} signals in Thy1-GCaMP6 mice to reinvestigate the degree of stereotypy or diversity of the sequence of diameter and velocity dynamics along

layer 2/3 (L2/3) vascular arbors in relation to sensory-evoked neuronal activity.

Results

We first set out to examine the dynamics of functional hyperemia across the vascular arbor of ketamine–medetomidine anesthetized mice. Chronic glass windows were implanted over vibrissae somatosensory cortex (vS1) of mice expressing GCaMP6s under the Thy1 promoter¹¹. All but 1 whisker were trimmed (~0.5 cm) to ensure activation of a single “spared” whisker which was deflected at a rate of 5 Hz (Fig. 1a). In a first step, we used a stereoscope and widefield Ca^{2+} imaging to identify the area of neuronal activation evoked by deflecting the whisker. Consistent with previous studies using voltage indicators¹², we observed that although only a single whisker was stimulated, the neuronal Ca^{2+} signal spread over an area larger than the barrel column itself (Fig. 1b). Thresholding the signal (see methods) allowed sorting out the area with the largest increase in fluorescence (Fig. 1b) for subsequent 2-photon imaging sessions. Similar to our previous study in OB, we measured functional responses first in capillaries of the mid-capillary bed in relation to local neuronal activity, and then retrogradely traced the direction of blood flow to locate the upstream feeding vessels, i.e., “transitional dilating capillaries”, the 1st order branch, the penetrating arteriole, and the pial arteriole (Fig. 1c), then sequentially measuring the diameter and velocity changes in each compartment. In contrast to the OB, the single whisker stimulation systematically evoked widespread calcium signals in pyramidal cell somata and/or the neuropil, surrounding all types of vascular compartments (Fig. 1d, e), from the mid-capillary bed to the upstream penetrating arteriole. As expected, these calcium responses were followed by increases in red blood cell (RBC) velocity in capillaries and dilations of the upstream arteriole (Fig. 1f). However, in many experiments, the magnitude of the velocity or diameter changes were small compared to the “~0.1 Hz” baseline fluctuations^{13,14}. Therefore, to precisely determine and compare the onset time of vessel responses, we computed the z-score for each trial with a 9.5 s long baseline (see methods), prior to averaging the trials (Fig. 1g). The data was then fit with a sigmoid function. The time to 25% of the peak of the fit was used to calculate the onset of the diameter change or the RBC velocity change. This systematic approach minimized the contribution of the trials with the largest baseline fluctuations (see a case with particularly large fluctuations in Fig. 1g). Of note, trial-to-trial variability in the magnitude of evoked diameter increases was similar across different compartments with no pattern of adaptation across consecutive trials (Supplementary Fig. 1).

Averaged diameter increases across different compartments of 10 vascular networks from 6 mice show that all upstream compartments, from the transitional segment (3rd, 2nd order branches), to the pial arteriole, increase their diameter in response to sensory stimulation (Fig. 2a). However, across the analyzed compartments these dilations were much smaller in percentage change than those previously observed in the OB¹, (e.g., for penetrating arterioles 8% vs. 29%, for the transitional segment 6% vs. 13%, pial arteriole 6% vs. 27%), and the onset of the diameter increases overlapped from one compartment to another. Note that for higher-order capillaries (≥ 4 th order), diameter changes were minute, as was the case in the OB¹ and we did not further quantify their onset, although it appeared delayed compared to the local velocity increase in the average across mice. Using the z-score approach improved the analysis for individual vessels (Fig. 2b), however, it did not further reveal any statistical differences in timing onsets (Supplementary Data 16, time to 10, 25 and 50% of the peak). Figure 2c, displays the onset

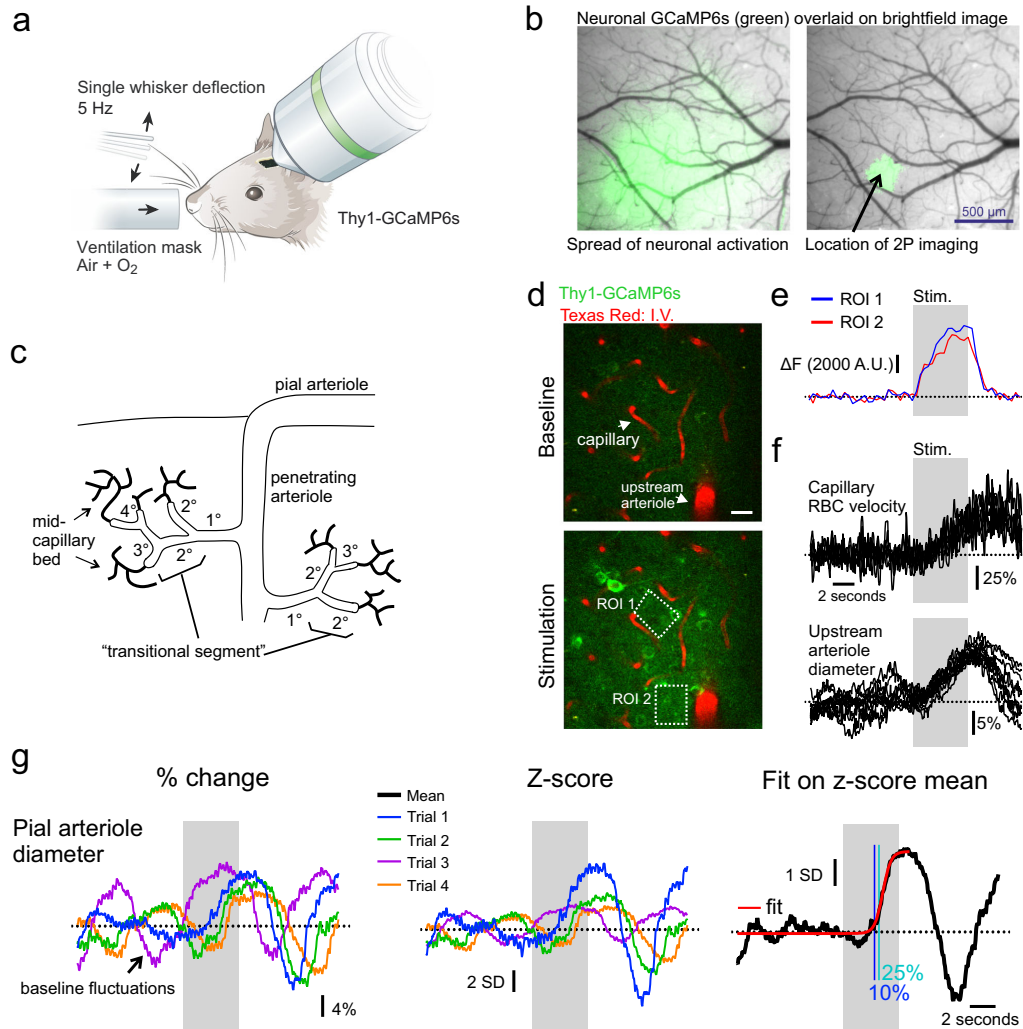


Fig. 1 Imaging neurovascular coupling in somatosensory cortex to single whisker stimulations. **a** Schematic of experimental preparation; single whisker of ketamine-medetomidine anesthetized mouse expressing GCaMP6s in pyramidal neurons is deflected at 5 Hz for 5 s. Modified from ref. ⁵¹. **b** Ca^{2+} signal acquired using epifluorescence and a stereoscope is used to locate area with the largest increase in activity (right). **c** Schematic of vasculature and sites of recordings in L2/3 of vS1. **d** Images showing baseline and stimulation induced increase in neuronal Ca^{2+} surrounding capillaries and upstream arteriole in L2/3. **e** Quantification of Ca^{2+} from 2 ROIs experiment shown in **d**. **f** Increases in capillary velocity (7 trials) and upstream arteriole diameter (11 trials), indicated with arrowheads in **d**. **g** Left, single-trial changes in the diameter of a pial arteriole measured as percentage change from baseline; middle, z-score calculation of single trials relative to baseline period; right, average z-score of the vessel (black) is fit with a sigmoid (red), the blue line indicates the time at which the fit crosses 10% of peak, and teal line 25% of peak. Gray bar indicates time of stimulation, dotted line indicates the mean baseline value.

times of each compartment across all the vascular networks imaged. Similarly, RBC velocity changes in vS1 were much smaller than those in the OB (Fig. 2a), measured in classical capillaries (≥ 4 th order, lumen diameter of $\sim 2\text{--}4\ \mu\text{m}$) and upstream vessels (vertical penetrating arterioles could not be correctly measured with line scans). This indistinguishable sequence of events in the cortex, contrasts to what was observed in the OB¹ and resulted from the fact that averaged responses masked a diversity of response onsets along the vascular arbors in

the cortex (Fig. 2c) and not in the OB (Fig. 2d). In the OB, the parenchymal arteriole and proximal portion of the 1st order branch dilated faster than downstream 2nd–3rd order vessels and upstream pial arteriole (Fig. 2d, Supplementary Data 16, z-score analysis of a data set that is primarily composed of experiments from Rungta et al.¹). Figure 2e shows examples of timing differences in individual vascular networks in the cortex. In some, the 2nd order vessel dilated fast, whereas in others it dilated with a delay. In others, the pial vessel dilated as fast as

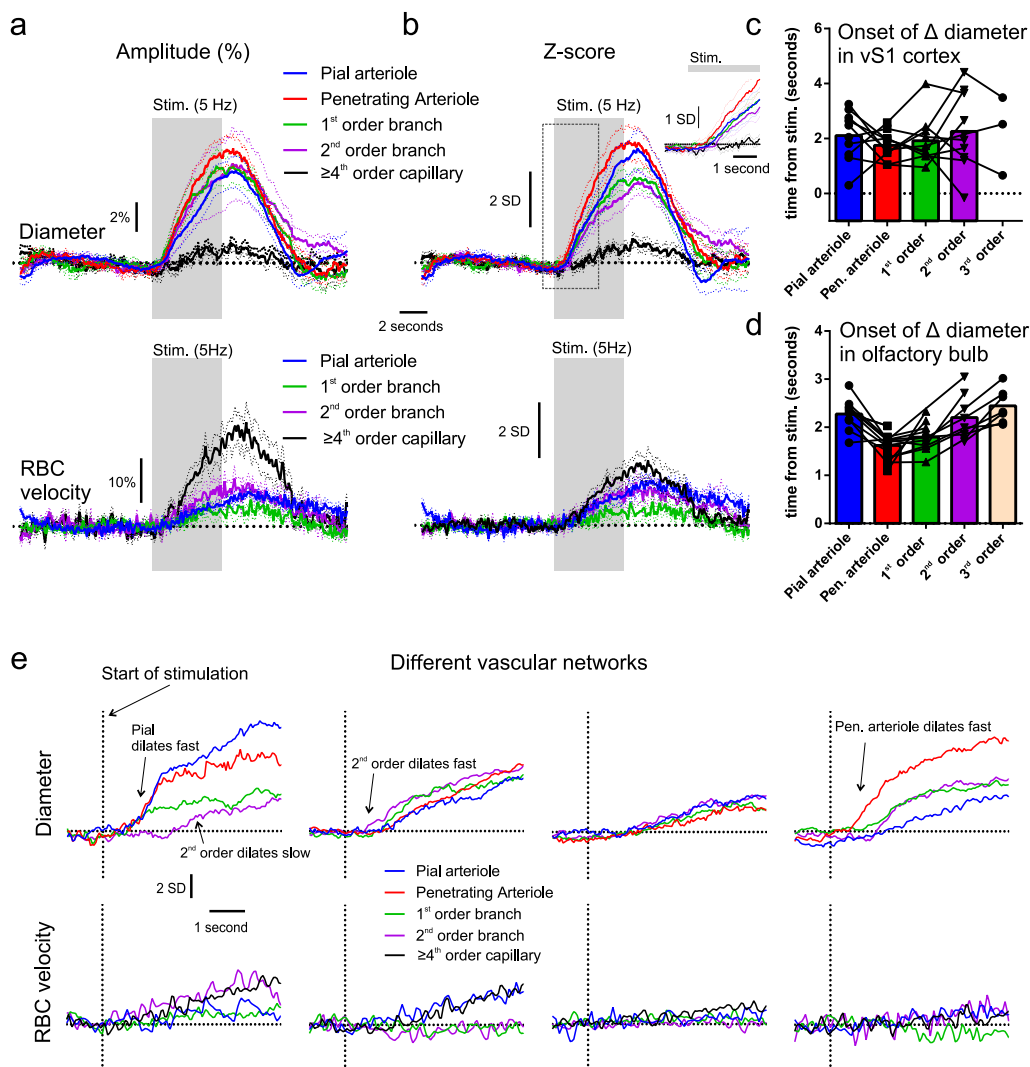


Fig. 2 Diversity of functional hyperemia onset times across the vascular arbor of vS1. **a** Average changes in diameter (top) and RBC velocity (bottom) of different vascular compartments in percent increase from baseline. **b** Average z-score changes in diameter (top) and RBC velocity (bottom) of different vascular compartments. Dotted lines in **a** and **b** represent SEM. Dotted line box outlines zoomed-in inset in the top right corner. **c** Histogram of onset times (25% of fit peak) across different compartments in vS1 cortex. Data in **a–c** represent 10 vascular networks from 6 mice. **d** Histogram of onset times (25% of fit peak) across different compartments in OB, made on a data set primarily formed from previously published experiments¹. Symbols in **c** and **d** represent data points from individual experiments. **e** Examples of the timing of diameter and velocity increases (z-score), from 4 different vascular networks.

the penetrating arteriole, whereas in the OB it was routinely delayed. Finally, velocity responses were also not consistent across cortical vascular arbors and did not always increase in the dilating transitional segment and pial arteriole. Note that the z-score responses of velocity were small (Fig. 2b, e), as single-trial responses were not much larger than the resting fluctuations. Overall, the dynamics of functional hyperemia in layer II/III reveal a diversity across vascular networks that contrasts to the OB stereotypy.

We further examined these responses to investigate potential sources of variability. In mouse vS1 the diameter of the first order offshoot from the penetrating arteriole is correlated with α -SMA expression further downstream⁹, raising the question of whether 1st order branch variability could account for some of the variability in onset timing. Consistent with this previously described anatomical correlation, we observed a trend towards faster onset times in second-order vessels originating from large first-order offshoots ($>8 \mu\text{m}$), compared to those from smaller

first-order offshoots ($<6\ \mu\text{m}$) (Supplementary Fig. 2a). We also assessed if baseline vasomotion affected the responses, vasomotion being an indicator of vessel contractility but also spontaneous neuronal oscillations^{13,14}. We analyzed the baseline vasomotion by calculating the power density of the low frequency band centered around 0.1 Hz (0.02–1 Hz) for single-trial diameter baselines, and did not detect any correlation between the power density of vasomotion and onset times in any compartments (Supplementary Fig. 2b). However, there was a positive correlation between baseline vasomotion and the amplitude of the diameter increases, which was removed or became slightly negative when plotted against the z -score amplitude, reinforcing the use of this approach to normalize responses across trials (Supplementary Fig. 2). Finally, we assessed if the phase of the low frequency vasomotion (~ 0.1 Hz) across single trials had an effect on the responses as it may be expected that those in a certain phase (i.e., increasing at stim onset), would show stronger responses. No effect of the vasomotion phase on response amplitude was observed across all compartments from the Pia to 2nd order vessels when the responses were normalized to the entire baseline period. However, if alternatively, an offset was applied to co-align the baselines of different phases at stimulation onset, the phase did appear to have an impact on the response as in this case the change from baseline incorporated additive effects of vasomotion and the stimulation evoked response (Supplementary Fig. 3).

Next, we aimed to compare these dynamics to the awake mouse ($n=6$ vascular networks, 4 mice). We used a single whisker stimulation protocol developed for minimizing movements of the mouse during stimulation and which does not evoke increased arousal¹⁵. The mice were trained to lick a water reward at the end of each trial for >3 weeks prior to recordings, resulting in them staying still during imaging trials. First, we tested whether the single whisker stimulation (90 Hz, 3 s, Fig. 3a), was capable of evoking functional hyperemia in awake mice. Indeed, increases in mid-capillary bed velocity changes were often observed adjacent to neuronal Ca^{2+} increases (Fig. 3b, c), however, both the evoked neuronal and vascular responses under these conditions were variable from one trial to the other, and blood velocity changes were small in amplitude (mean \pm SEM, $16.1 \pm 1.6\%$ for ≥ 4 th order capillaries in vS1 cortex, compared to $86.7 \pm 5.8\%$ increase in the OB¹). As in anesthetized mice, the upstream transitional segment, penetrating arteriole, and pial arteriole increased their diameter, however, with variability in diameter and velocity changes across different vascular networks (Fig. 3d, e). Small ≥ 4 th order capillaries remained the compartment of largest RBC velocity increases in percentage, as was observed during anesthesia. In 4 out of 6 vascular networks, we were able to find and image a segment of the penetrating arteriole, which was parallel to the imaging plane for a very brief length, and found that, as expected, RBC velocity did not increase (Fig. 3d), and even appeared to decrease in some cases (Fig. 3e, bottom left), similar to in the OB¹. Pial arteriole velocity changes also rarely increased under these conditions in awake mice (Fig. 3d, e), suggesting that the increase in flow in arterioles is primarily mediated by a change in blood volume.

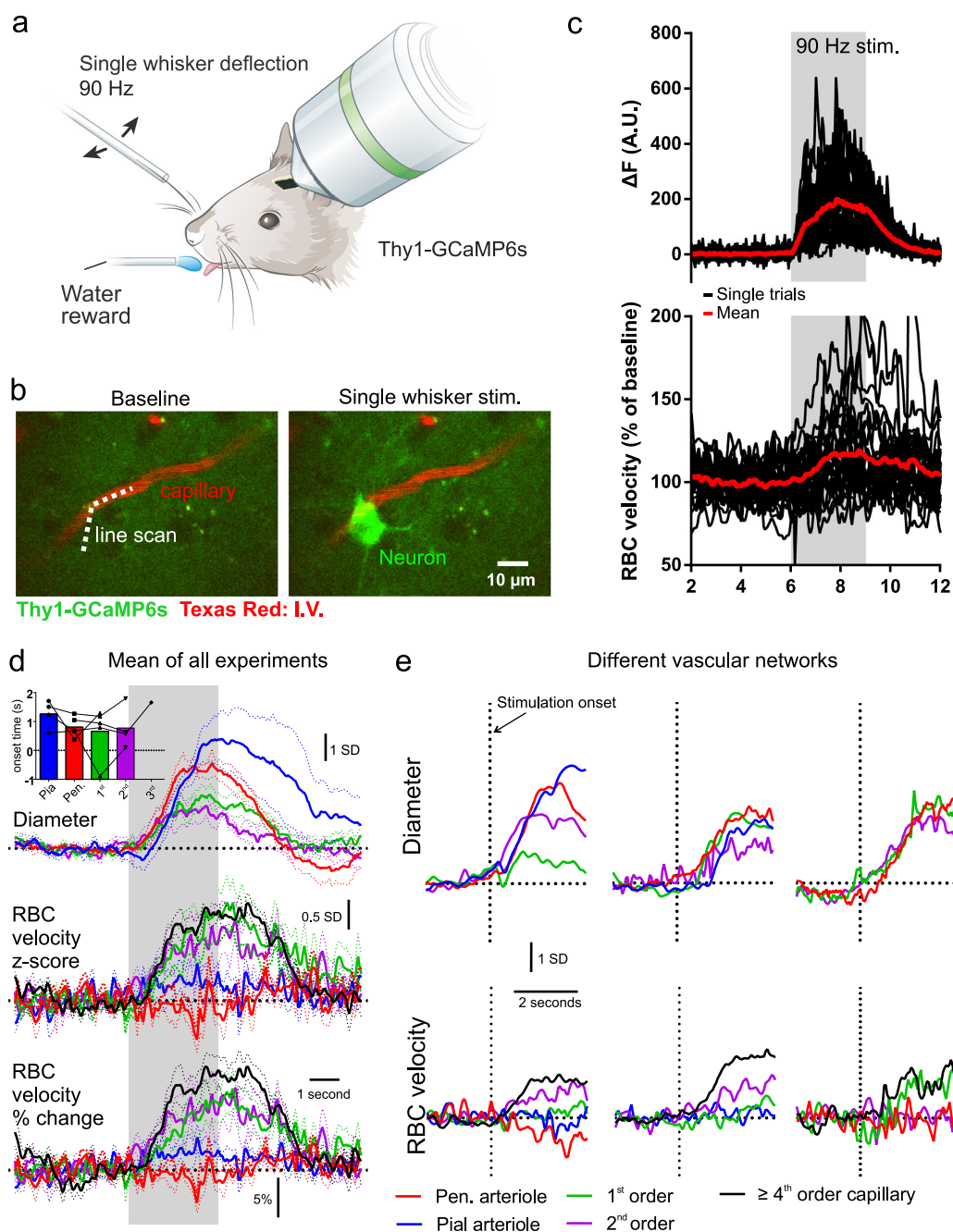
Finally, we examined the impact of anesthesia on neurovascular coupling (NVC) dynamics. We used transfer functions (TFs) to serve as a proxy for NVC¹⁶, TFs allowing us to directly compare the relationship between calcium and vascular dynamics, even though the stimulation paradigm differed during brain states (5 s for anesthesia, 3 s for awake). We first computed transfer functions (see ref. ¹⁶) using the response means across anesthetized mice between neuronal Ca^{2+} and either capillary RBC velocity (Ca^{2+} -RBC) or penetrating arteriole dilation (Ca^{2+} -dilation) (Fig. 4a–d). Both the Ca^{2+} -RBC and the Ca^{2+} -dilation TFs predicted their respective signals when tested on

experimental data from individual vascular networks of anesthetized mice (Fig. 4e, Pearson coefficient mean \pm SD, Ca^{2+} -dilation: 0.93 ± 0.04 , Ca^{2+} -RBC: 0.83 ± 0.11 , 10 vascular networks, 6 mice). However, when the same anesthetized TFs (TF_{AN}) were used to predict awake responses, they were much less accurate (Fig. 4g, h), with predictions evidently delayed compared to the data. Therefore, we generated new awake TFs (TF_{AW}) for both Ca^{2+} -dilation and Ca^{2+} -RBC, using mean responses of the awake data set (Fig. 4f). Indeed, the TF_{AW} was faster and significantly better than the TF_{AN} at predicting awake data across all networks for both Ca^{2+} -dilation and Ca^{2+} -RBC (Fig. 4g–i and Supplementary Data 16). These results demonstrate that NVC is faster in awake animals.

Discussion

Here we address the sequence of compartmentalized vascular changes that occur across vascular networks in L2/3 of primary whisker somatosensory cortex in response to physiological stimulation. Our work extends on previous studies which have examined the dynamics of diameter changes in different compartments in several ways: (1) we trace out and map the vascular network in relation to neuronal activity in transgenic mice, (2) we use a single whisker stimulation to better spatially control the stimulation, (3) our experiments are performed in chronic rather than acute preparations, and were extended to the awake state, (4) we record both diameter and velocity changes across several compartments of the same vascular network from the mid-capillary bed to the upstream pial arteriole, and (5) we investigate the impact of vasomotion on the stimulation driven vasodilation across compartments. Under these conditions, our results reveal that among dilating compartments, the location of onset varies across different vascular arbors. Averaging all responses per compartment masked this diversity and resulted in the inability to identify the fastest dilating compartment. This contrasts with our previous work in the OB, where we observed a more stereotyped pattern of activation. In OB, although intracellular Ca^{2+} dropped synchronously in pericytes of the transitional segment and the upstream arteriole, diameter changes occurred fastest in the parenchymal arteriole and proximal 1st branching vessel¹.

Although the functional diversity across compartments seems surprising, put in the context of the literature, it is similar to the anatomical diversity which has been described by other groups, in which branch order transition points in the expression of proteins such as smooth-muscle actin can vary across different vascular arbors^{8,9,17,18}. Here the purpose of our work was to examine the degree of stereotypy and/or diversity in the timing of compartmentalized functional responses across the vascular arbor, and not add to the controversy over whether capillaries actively dilate which is in part an issue of semantics. It is now evident that different microvascular zones exist¹⁹, defined by the molecular expression patterns of endothelial and mural cells as well as their morphology^{8,9}. Importantly, there exists a transitional segment between the arteriole and mid-capillary bed, in which the mural cells exhibit pericyte-like ovoid cell bodies, and express the contractile protein α -SMA. This transitional segment is analogous to what we called the secondary functional unit in the OB, which actively dilated with a delay. In barrel cortex, the expression of α -SMA is more likely to extend to 2nd and 3rd order branches when the 1st order offshoot of the arbor has a large diameter⁹. Consistent with this anatomical correlation, we observed a trend towards faster dilations of 2nd order vessels arising from larger diameter 1st order offshoots, suggesting that some of the observed functional diversity may be due to branch order variability in α -SMA expression levels. This adds to the emerging picture from several labs showing the importance of the transitional segment



in activity-dependent blood-flow regulation^{1–5,20–22}. It further highlights an increased level of complexity and the presence of functional diversity between branch orders of this transitional segment. In the mid-capillary bed, thin-strand pericytes do not express or express far lower levels of α -SMA actin^{8–10,21}.

Although, we remain cautious in interpreting the minute diameter changes observed in high-order capillaries, when averaged across all mice they appeared delayed. Even if passively driven by increased pressure, given their high resistance this would be expected to produce meaningful increases in blood flow^{1,23}.

Fig. 3 Single whisker evoked vascular dynamics in awake mice. **a** Schematic of experimental setup, single whisker threaded into a capillary tube and deflected at 90 Hz. Modified from ref. 51. **b** Example images showing increase in neuronal Ca^{2+} following stimulation adjacent to a capillary labeled with intravenous Texas Red-dextran. **c** Single trials (black) and mean (red) response of neuronal Ca^{2+} (top), and capillary RBC velocity (bottom) to single whisker stim. Data were acquired by scanning along the line path shown in **b** (dotted line) and the portion outside the vessel used to record the Ca^{2+} signal. **d** Average z-score changes in diameter (top), RBC velocity (middle) and average % changes in RBC velocity (bottom) across different compartments. Dotted lines represent SEM. Data from 6 whisker/vascular arbor pairs in 4 mice (not all compartments recorded in each network). Inset shows a histogram of onset times (25% of fit peak) across different compartments. **e** Examples of timing of diameter and velocity increases (z-score), from 3 different vascular networks.

A further complication in determining onset times arises from the spontaneous vasomotion of individual compartments. We found that vasomotion power was significantly correlated with the magnitude of the stimulation evoked diameter changes. Furthermore, at a single trial level, the phase of the low-frequency vasomotion ~ 0.1 Hz had an impact on the dynamics of the diameter change, indicating that the time-locked response represents a mixture of the stimulation evoked response superimposed upon the vasomotion. To minimize the effect of vasomotion on the onset time calculations we normalized each trial to the standard deviation of the baseline (z-score), and then averaged z-score trials obtained from each compartment of each arbor. This approach minimized the contribution of those trials with the largest vasomotor fluctuations. We implemented a sigmoid fitting approach and calculated onsets on % peak values of the fit. This removes variability caused by different “signal to noise” levels between different compartments of different arbors, which are subjective to error when using threshold values on the traces themselves (e.g., time to 2 standard deviations). Although we were not able to statistically separate onset times across compartments due to them being masked by variability in the sequence across different arbors, this does not exclude the possibility that differences in mean onset times would become apparent with much larger sample sizes.

The neural circuitry in L2/3 vS1 differs from that of the OB. In the OB, odors selectively activate few glomeruli at low concentration^{24,25}. In the mouse, these glomeruli represent individual functional units of ~ 50 – 100 μm diameter where an estimated 75,000–150,000 olfactory sensory neuron terminals converge^{26,27} and surround the mid-capillary bed contacted by thin-strand pericytes¹. In L2/3 of vS1, touch evoked spiking patterns are sparsely distributed^{28–31}. As a result, synaptic activity is less spatially concentrated than in OB and occurs more spread out across different compartments of the vascular arbor in vS1. This may contribute to the smaller magnitude vascular responses in vS1 compared to OB and potentially to the greater compartment specific heterogeneity we observed in vS1. vS1 has become the most utilized brain region for the study of neurovascular coupling due to its well-defined circuitry³² and vascular anatomy³³. Here we chose to study the dynamics in superficial L2/3 due to ease of optical access with 2P microscopy and for better comparison with previous studies. In vS1 first order thalamocortical input from VPM arrives predominantly in L4 (and L5b) whereas L2/3 receives second-order projections within a few ms (much faster than the hemodynamic responses that are evoked). To ensure stimulation of a single whisker we trimmed all but one whisker to ~ 0.5 cm in length, a commonly used protocol which is known to induce circuit remodeling, but importantly in this model, excitatory population responses retain the highest levels of activity within the whisker specific column (L2/3 neurons \sim twice as likely to respond to touch as those in neighboring columns³⁰). It is important to note that dilation onset times and fMRI responses have been reported to occur faster in deeper layers^{7,34}, which may add a further level of complexity to the

diversity we report within L2/3. Furthermore, as pial vessel dilation is mediated by the integration of retrograde signals from several penetrating arterioles^{35,36}, a possible source of onset variability in the pial arterioles could therefore arise from differences in the arteriole networks they perfuse.

One limitation of this study is that we limit our recordings of neuronal activity to Thy1 expressing excitatory pyramidal neurons. The purpose of recording neuronal activity in this study was to examine the location and timing of the neuronal response, and not intended to shed light on the specific cell types involved. Given the contribution of interneurons and astrocytes to neurovascular coupling³⁷, it would indeed be possible for mismatches between the level of local excitatory neuron activity and vascular dilation to occur. Optogenetic stimulation has become a popular tool for dissecting the contribution of specific cell types to increases in blood flow, however, this triggers robust and synchronous activation of populations of cells, which does not replicate their sequence of activation during natural stimulations. As we aim to understand the microvascular changes that contribute to hemodynamic based functional imaging signals, we believe it is important to understand the spatial-temporal pattern of vascular changes to natural stimulations.

It is widely acknowledged that anesthetics affect neurovascular coupling^{38–40}. In the OB glomerulus, these effects are likely less dramatic as it is a first synaptic relay and therefore, information is less susceptible to thalamic modulation by anesthesia, in contrast to the neocortex. Using simultaneous measurements of neuronal and vascular responses, we find that in L2/3 the temporal dynamics of functional hyperemia differed according to the brain state. As the onsets and overall dynamics of the neuronal calcium responses in anesthetized and awake animals overlapped, whereas the slope and peak of vascular responses (arteriole dilation and RBC velocity responses) were flatter and delayed during anesthesia, we demonstrate that NVC is faster in awake animals. By computing TFs between calcium and both types of vascular responses, we ensured that this difference was not due to a difference in stimulation duration. These differences in awake vs. anesthetized TFs have important implications for brain mapping studies (e.g., fMRI), which routinely employ hemodynamic response functions to map activity patterns. As the transfer function between neuronal activity and vasodilation is brain state-dependent, modifying the hemodynamic response function to account for differences in brain region and the state of the animal would be important for improving the accuracy of fMRI mapping and interpretation.

In summary, we report functional diversity of neurovascular coupling dynamics between different brain regions (OB vs. vS1 cortex) and between microvascular zones of different vascular arbors within L2/3. These results outline how these different microvascular zones cooperate to increase cerebral blood flow during functional hyperemia in response to a well-defined and physiological sensory stimulation. They also outline the spatial-temporal sequence of blood volume and velocity changes that underlie human brain mapping techniques.

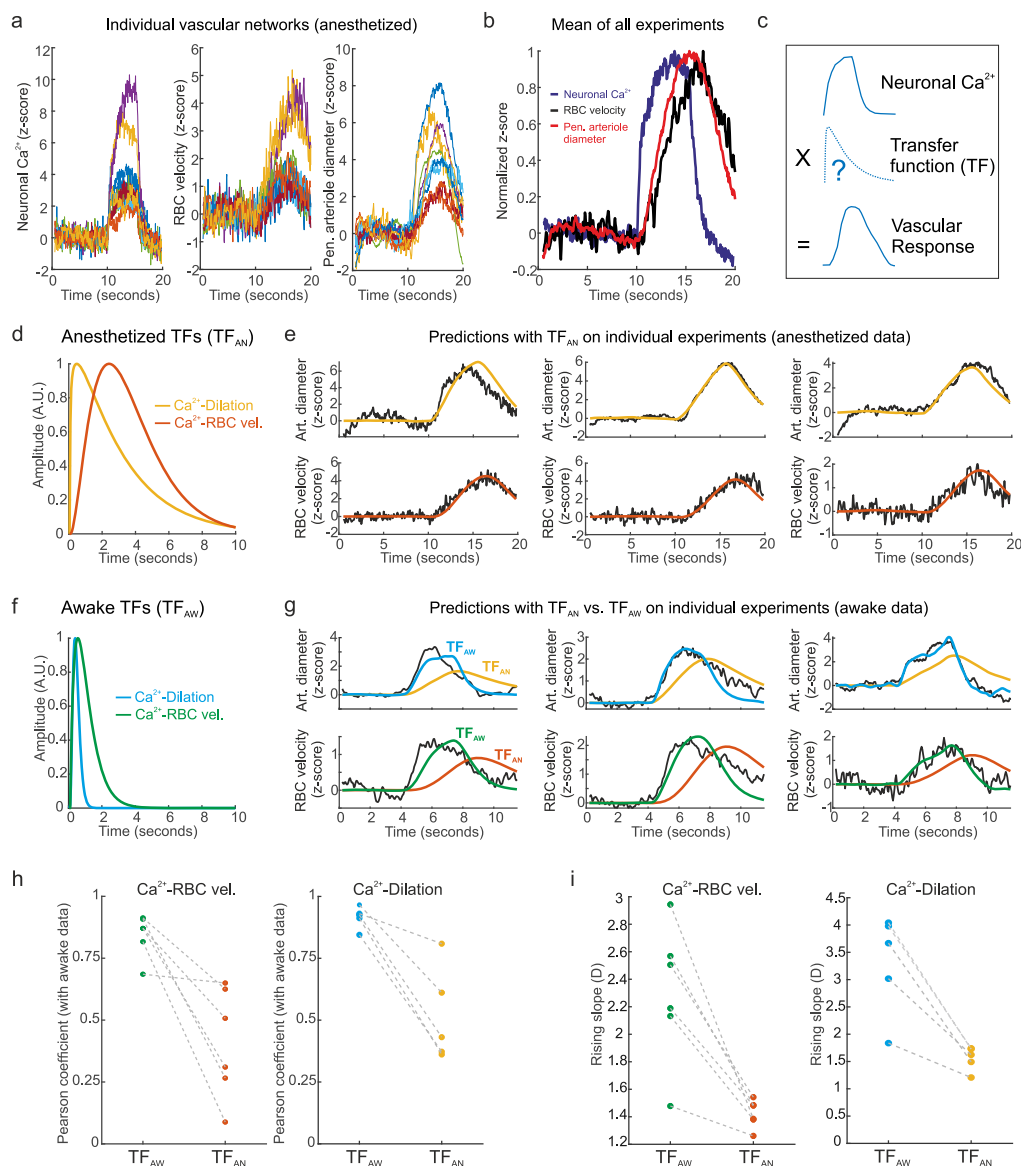


Fig. 4 Analysis of differential NVC dynamics in awake vs. anesthetized mice using TFs. **a** Overlaid dynamics of Neuronal Ca^{2+} (GCaMP6 signal), RBC velocity (≥ 4 th order capillaries), and penetrating arteriole diameter from all anesthetized experiments (10 vascular networks, 6 mice). **b** Mean traces of normalized data shown in **a**. **c** Transfer functions (TFs) are convolved with the average neuronal Ca^{2+} signal and optimized to predict the vascular response (RBC velocity or arteriole diameter). **d** TFs optimized to predict arteriole dilation (yellow) or RBC velocity (orange) dynamics computed with the mean anesthetized data. **e** TF predictions for arteriole diameter (top) and RBC velocity (bottom) from the experimental data from 3 different anesthetized experiments (TF_{AN}), top and bottom are paired experiments. **f** TFs optimized to predict arteriole dilation (blue) or RBC velocity (green) dynamics computed with the mean awake data (TF_{AW}). **g** Comparison of (TF_{AW}) and (TF_{AN}) prediction for arteriole diameter (top) and RBC velocity (bottom) from the experimental data from 3 different awake experiments, top and bottom are paired experiments. **h** Correlation of (TF_{AW}) and (TF_{AN}) with awake experimental data for RBC velocity (left) and arteriole diameter (right). **i** Comparison of rising slope for TF predictions made with (TF_{AW}) and (TF_{AN}) on awake data for RBC velocity (left) and arteriole diameter (right). The slope is defined as the D parameter of the 4-parameter sigmoidal fit formula: $A + B/(1 + \exp(-(-x - C) * D))$. Data here are also represented in Figs. 1–3.

Methods

Animals and chronic window implantation. All animal care and experimentation was performed in accordance with the INSERM Animal Care and Use Committee guidelines. Adult mice (2–6 months old, 20–35 g, both males and female, housed in 12-h light-dark cycle) were used in this study. *Thyl1-GCaMP6s (GPA3)* mice were purchased from Jackson laboratory. All mice were bred on a *C57BL/6* background. Chronic craniotomies were performed as previously described⁴¹. In brief, mice were initially anesthetized with an intraperitoneal (IP) bolus of ketamine–medetomidine (100 and 0.4 mg kg⁻¹ body mass, respectively). Further 10–20% of the same mixture was injected IP as necessary to maintain surgical plane anesthesia. During surgery, the mice breathed a mixture of air and supplementary oxygen and the body temperature was monitored with a rectal probe and maintained at ~36.5 °C by a feedback-controlled heating pad. A craniotomy (3.5 mm lateral and 1 mm posterior to bregma) was performed with a dental drill, care was taken not to apply pressure to the bone and the area was regularly flushed with cool aqueous buffer solution to avoid damage or heating of the underlying tissue. A cover glass (100 μm thick) was used for the window and sealed in place with photopolymerizable dental cement, which was also used to form a head-cap in which a head-bar was embedded. Mice were permitted to recover for at least 3 weeks before the imaging sessions began. For anesthetized experiments, mice were anesthetized with ketamine–medetomidine (100 and 0.4 mg kg⁻¹ body mass, respectively) injected IP. Experiments were routinely performed between 25 and 120 min after the first injection, and a second bolus IP was occasionally injected during the experiment if the animal's respiration rate started to increase. Breathing rate (2–3 Hz, regular and rhythmic) was monitored with a pneumogram transducer (Biopac Systems). Body temperature was maintained at ~36.5–37 °C using a heating pad. Blood pressure and heart rate were not measured. Mice breathed a mixture of air and supplementary oxygen (the final inhaled proportion of oxygen was ~30%). Under these same conditions, we have characterized brain temperature at the surface of the brain to be ~32 °C, with capillary PO₂ to be similar to in awake mice⁴². No post-mortem analysis was performed to access the integrity of the cortex.

Imaging. All but one spared whisker were trimmed down to ~0.5–1 cm to facilitate single whisker stimulations. Mapping of epifluorescence GCaMP6 signals was performed on a Zeiss stereomicroscope (Stereo Discovery V20, GFP band pass filter of 525/50). ~5–15 trials were averaged and images were displayed as the integral of the change in fluorescence during the stimulation period relative to the baseline. This mapping procedure was done >3 days before 2-photon imaging sessions began. Signals were thresholded to identify the region with the largest increase in fluorescence and guide subsequent 2-photon imaging experiments. 2-photon imaging was performed as previously described¹, using a femtosecond laser (Mai Tai eHP; SpectraPhysics) with a dispersion compensation module (Deepsee; SpectraPhysics) emitting ~70-fs pulses at 80 MHz. GCaMP6s and Texas Red were excited at 920 nm. Emitted light was collected with either a ×60/1.10NA (Olympus) or ×40/0.8NA (Leica) water immersion objective and was sent to a pair of lenses, coupled into a 2-mm diameter core polymethyl methacrylate optical fiber. Collected light was split using a dichroic mirror at 580 nm and the signals were each detected with a dedicated GaAsP photomultiplier tube (Hamamatsu) after passing through an appropriate emission filter (GCaMP6: 525 nm, 50 nm bp; Texas Red: 620 nm, 60 nm bp). Customized Labview software was used to control imaging parameters. Texas Red dextran (70 kDa, Molecular Probes) was administered intravenously by retro-orbital injection. For awake experiments, mice were briefly (<2 min) anesthetized with isoflurane in order to inject the Texas Red dextran and recovered for >1 h before the experimental session began. Recordings of diameter and velocity across different segments were made sequentially across different trials. In a subset of experiments in which two segments were visible in the same plane, the line scan was extended to capture both of their diameter changes in the same trial.

Stimulation setups. Awake mouse whisker stimulation was done as previously described¹⁵. A custom-made head-fixation box was built for chronic imaging and stimulation as previously described in detail⁴³. A click noise 1 ms duration with 2–18-kHz bandwidth and delivered by stereo speakers positioned 20 cm away from the animal's head was sounded to indicate the end of each trial upon which the animal could lick to receive a water reward. The drinking spout included a piezo sensor (LDT0-028K; Measurement Specialties) and was mounted in front of the animal. The spout was connected to a solenoid valve (Type 0330; Burkert) that controlled water delivery upon spout deflection. To stimulate a single whisker, it was threaded into a glass capillary affixed to a piezo element (T223-H4CL-303X; Piezo Systems) vibrated at 90 Hz. A custom-made piezo movement sensor for monitoring movement was positioned under the animal's body. A camera with an infrared light source was used for monitoring animals. We used the custom-written LabVIEW program (Version 2012; National Instruments) and multifunctional data acquisition cards to control and monitor all components of the behavioral apparatus⁴³. For anesthetized mice, the whisker was stimulated with metal rod attached to a mechanical shutter/chopper which deflected the whisker at a rate of 5 Hz.

Training. Animals were first handled and familiarized with the experimenter, 1 week after implantation at least 2 times a day (~15–20 min) and acclimated to the behavioral setup. They were gradually accustomed to tolerate brief periods of head fixation and to drink water from a pipette tip administered by the experimenter. Water-deprived mice (12 h before training sessions) were then accustomed to head fixation in the experimental setup and to drink water from a spout delivered at fixed intervals and preceded by a sound cue. Finally, mice were habituated to the stimulation of a random whisker and water delivered at the end of each trial. The total training procedure required a minimum of 3 weeks before data was acquired.

Transfer function computation. TFs were computed between an input (GCaMP6, Ca²⁺) and an output signal (RBC velocity or arteriolar dilation). Computation was done with a home-made software, based on the scripts from^{16,44,45}. The following function was optimized $TF(t) = H(t - p_3) p_4 \frac{(t - p_3)^{p_1 - 1} p_2^{p_1} e^{-p_2(t - p_3)}}{\Gamma(p_1)}$ using the simulated annealing algorithm ("simulannealbm" function, Matlab). Initial values for the parameters were (1.3; 0.5; 0.27; 0.19) as found previously for a TF representing the NVC¹⁶. Two rounds of 200 optimization runs were performed, the second run initial values being the parameters for the best TF found from the first run. The final TF was the one showing the smallest coefficient of determination between the output signal and the convolution of the TF and the input signal, while being physiologically plausible (i.e., TFs = 0 for time = 0 and none non-derivable point in the TF after the onset).

Prediction of the TFs computation. Predictions are the result of the convolution between the Ca²⁺ signal of the mouse with the corresponding TF. Amplitude was optimized to match the experimental data when TFs were applied on datasets different from the one on which they have been optimized. The scaling factors were found with the "fminsearch" function of Matlab by using the sum of the square residuals as the cost function. The final evaluation of the prediction quality, the Pearson coefficient, is not impacted by the amplitude but only by the dynamic which remains the same with the scale factor.

Quantification. Ca²⁺ signals were calculated as $\Delta F = (F - F_0)$ where F_0 represents baseline fluorescence and F the fluorescence at time t in arbitrary units. Vessel diameter and velocity measurements were made as previously described¹. Red blood cells were imaged as shadows within the fluorescent plasma and their velocity was calculated based on the distance traveled per unit of time. Lumen diameters were measured with line scans perpendicular to and crossing the vessel and calculated using the fluorescent boundaries of the Texas Red (70 kDa) fluorescence, which labels the blood plasma (excluding the glycocalyx). A 200 ms mean filter (preceding time, t) was used, and fluorescence was interpolated between pixels on the distance axis. A subset of the recordings was made in frame scanning mode. z-score traces were calculated on individual trials relative to baseline and then averaged across each vessel segment from each vascular network. These average z-score traces were fit with a sigmoid, using the method of least squares (Matlab fit function). Onset times were calculated as the time to reach 10, 25, and 50% of the peak on the fit.

Statistics and reproducibility. The anesthetized data set consisted of data from 10 vascular arbors of 6 mice. The awake data set consisted of 6 vascular arbors from 4 mice. Statistical analysis was conducted using R (version 3.6.2, R Core Team, 2019). Linear mixed-effects models⁴⁶ were used to analyze the differences between onset times of different compartments. The vascular compartment was specified as fixed effects, and intercepts for each mouse were specified as random effects. P-values for differences between groups were obtained post-hoc using the Tukey correction for multiple comparisons⁴⁷. All P-values are reported in Supplementary data 16. The data from the histograms show data per vascular network, not grouped by the animal. Average data throughout the paper is displayed as the mean ± SEM. No randomization or blinding was used. No statistical methods were used to pre-determine sample sizes. A subset of mice did not respond efficiently to the training protocol and were not used to collect data.

Inter-trial variability. Inter-trial variability was measured from z-score traces by calculating the standard deviation (STD) of the response amplitude across trials for each vascular segment from each vascular network. Trial-to-trial adaptation of the response was assessed by comparing the amplitude of the response between the first three trials for each vascular segment.

Vasomotion estimation. Baseline vasomotion was estimated by performing a power spectrum analysis in the 0.02 to 1 Hz frequency band, encompassing vasomotion oscillations as previously described^{48–50}. Average bandpower in the 0.02–1 Hz frequency band was extracted from the baseline of relative diameter change traces (% change) using the classical method (Matlab bandpower function). To analyze the contribution of the low frequency (~0.1 Hz) vasomotion cycle phase on measured dilations, single-trial traces were sorted based on the pattern of vasomotion oscillation before stimulation onset. First, diameter traces relative to

the baseline period (% change) were lowpass filtered with a 0.2 Hz threshold. Then, filtered traces were classified based on their oscillation pattern in a 2.5 s window before stimulation onset, corresponding to a quarter of an oscillation cycle at 0.1 Hz. Traces were classified as above baseline average and ascending (phase 1), above baseline average and descending (phase 2), below baseline average and descending (phase 3) or below baseline average and ascending (phase 4) as illustrated in Supplemental Fig. 3A.

Reporting summary. Further information on research design is available in the Nature Research Reporting Summary linked to this article.

Data availability

Data files associated with the manuscript are available as Supplementary Data 1–15.

Code availability

Code and software used to generate transfer functions are available online^{44,45} <https://doi.org/10.5281/zenodo.4765555>.

Received: 16 November 2020; Accepted: 10 June 2021;

Published online: 09 July 2021

References

- Rungta, R. L., Chaigneau, E., Osmanski, B.-F. & Charpak, S. Vascular compartmentalization of functional hyperemia from the synapse to the pia. *Neuron* **99**, 362–375.e4 (2018).
- Kornfield, T. E. & Newman, E. A. Regulation of blood flow in the retinal trilateral vascular network. *J. Neurosci.* **34**, 11504–11513 (2014).
- Hall, C. N. et al. Capillary pericytes regulate cerebral blood flow in health and disease. *Nature* **508**, 55–60 (2014).
- Cai, C. et al. Stimulation-induced increases in cerebral blood flow and local capillary vasoconstriction depend on conducted vascular responses. *Proc. Natl Acad. Sci. USA* **115**, E5796–E5804 (2018).
- Mishra, A. et al. Astrocytes mediate neurovascular signaling to capillary pericytes but not to arterioles. *Nat. Neurosci.* **19**, 1619–1627 (2016).
- Wei, H. et al. Erythrocytes are oxygen-sensing regulators of the cerebral microcirculation. *Neuron* **91**, 851–862 (2016).
- Tian, P. et al. Cortical depth-specific microvascular dilation underlies laminar differences in blood oxygenation level-dependent functional MRI signal. *Proc. Natl Acad. Sci. USA* **107**, 15246–15251 (2010).
- Ratelade, J. et al. Reducing hypermuscularization of the transitional segment between arterioles and capillaries protects against spontaneous intracerebral hemorrhage. *Circulation* **141**, 2078–2094 (2020).
- Grant, R. I. et al. Organizational hierarchy and structural diversity of microvascular pericytes in adult mouse cortex. *J. Cereb. Blood Flow Metab.* **39**, 411–425 (2017).
- Alarcon-Martinez, L. et al. Capillary pericytes express α -smooth muscle actin, which requires prevention of filamentous-actin depolymerization for detection. *Elife* **7**, e34861 (2018).
- Dana, H. et al. Thy1-GCaMP6 transgenic mice for neuronal population imaging in vivo. *PLoS ONE* **9**, e108697 (2014).
- Ferezou, I., Bolea, S. & Petersen, C. C. H. Visualizing the cortical representation of whisker touch: voltage-sensitive dye imaging in freely moving mice. *Neuron* **50**, 617–629 (2006).
- Mateo, C., Knutsen, P. M., Tsai, P. S., Shih, A. Y. & Kleinfeld, D. Entrainment of arteriole vasomotor fluctuations by neural activity is a basis of blood-oxygenation-level-dependent “resting-state” connectivity. *Neuron* **96**, 936–948.e3 (2017).
- Winder, A. T., Echagarruga, C., Zhang, Q. & Drew, P. J. Weak correlations between hemodynamic signals and ongoing neural activity during the resting state. *Nat. Neurosci.* **20**, 1761–1769 (2017).
- Zuend, M. et al. Arousal-induced cortical activity triggers lactate release from astrocytes. *Nat. Metab.* **2**, 179–191 (2020).
- Aydin, A.-K. et al. Transfer functions linking neural calcium to single voxel functional ultrasound signal. *Nat. Commun.* **11**, 2954 (2020).
- Damisah, E. C., Hill, R. A., Tong, L., Murray, K. N. & Grutzendler, J. A fluoro-Nissl dye identifies pericytes as distinct vascular mural cells during in vivo brain imaging. *Nat. Neurosci.* **20**, 1023–1032 (2017).
- Kureli, G. et al. F-actin polymerization contributes to pericyte contractility in retinal capillaries. *Exp. Neurol.* **332**, 113392 (2020).
- Vanlandewijck, M. et al. A molecular atlas of cell types and zonation in the brain vasculature. *Nature* **554**, 475 (2018).
- Biesecker, K. R. et al. Glial cell calcium signaling mediates capillary regulation of blood flow in the retina. *J. Neurosci.* **36**, 9435–9445 (2016).
- Hill, R. A. et al. Regional blood flow in the normal and ischemic brain is controlled by arteriolar smooth muscle cell contractility and not by capillary pericytes. *Neuron* **87**, 95–110 (2015).
- Gonzales, A. L. et al. Contractile pericytes determine the direction of blood flow at capillary junctions. *Proc. Natl Acad. Sci. USA* **117**, 27022–27033 (2020).
- Hartmann, D. A. et al. Brain capillary pericytes exert a substantial but slow influence on blood flow. *Nat. Neurosci.* **24**, 633–645 (2021).
- Boido, D. et al. Mesoscopic and microscopic imaging of sensory responses in the same animal. *Nat. Commun.* **10**, 1110 (2019).
- Lecoq, J., Tiret, P. & Charpak, S. Peripheral adaptation codes for high odor concentration in glomeruli. *J. Neurosci.* **29**, 3067–3072 (2009).
- Mobley, A. S., Rodriguez-Gil, D. J., Imamura, F. & Greer, C. A. Aging in the olfactory system. *Trends Neurosci.* **37**, 77–84 (2014).
- Bressel, O. C., Khan, M. & Mombaerts, P. Linear correlation between the number of olfactory sensory neurons expressing a given mouse odorant receptor gene and the total volume of the corresponding glomeruli in the olfactory bulb. *J. Comp. Neurol.* **524**, 199–209 (2016).
- Clancy, K. B., Schnepel, P., Rao, A. T. & Feldman, D. E. Structure of a single whisker representation in layer 2 of mouse somatosensory cortex. *J. Neurosci.* **35**, 3946–3958 (2015).
- Crochet, S., Poulet, J. F. A., Kremer, Y. & Petersen, C. C. H. Synaptic mechanisms underlying sparse coding of active touch. *Neuron* **69**, 1160–1175 (2011).
- Peron, S. P., Freeman, J., Iyer, V., Guo, C. & Svoboda, K. A cellular resolution map of barrel cortex activity during tactile behavior. *Neuron* **86**, 783–799 (2015).
- Mayrhofer, J. M., Haiss, F., Helmchen, F. & Weber, B. Sparse, reliable, and long-term stable representation of periodic whisker deflections in the mouse barrel cortex. *Neuroimage* **115**, 52–63 (2015).
- Staiger, J. F. & Petersen, C. C. H. Neuronal circuits in barrel cortex for whisker sensory perception. *Physiol. Rev.* **101**, 353–415 (2021).
- Blinder, P. et al. The cortical angioome: an interconnected vascular network with noncolumnar patterns of blood flow. *Nat. Neurosci.* **16**, 889–897 (2013).
- Silva, A. C. & Koretsky, A. P. Laminar specificity of functional MRI onset times during somatosensory stimulation in rat. *Proc. Natl Acad. Sci. USA* **99**, 15182–15187 (2002).
- Chen, B. R., Kozberg, M. G., Bouchard, M. B., Shaik, M. A. & Hillman, E. M. A critical role for the vascular endothelium in functional neurovascular coupling in the brain. *J. Am. Heart Assoc.* **3**, e000787 (2014).
- O’Herron, P. et al. Neural correlates of single-vessel haemodynamic responses in vivo. *Nature* **534**, 378–382 (2016).
- Iadecola, C. The neurovascular unit coming of age: a journey through neurovascular coupling in health and disease. *Neuron* **96**, 17–42 (2017).
- Pisauro, A. M., Dhruv, N. T., Carandini, M. & Benucci, A. Fast hemodynamic responses in the visual cortex of the awake mouse. *J. Neurosci.* **33**, 18343–18351 (2013).
- Masamoto, K. & Kanno, I. Anesthesia and the quantitative evaluation of neurovascular coupling. *J. Cereb. Blood Flow. Metab.* **32**, 1233–1247 (2012).
- Tran, C. H. T. & Gordon, G. R. Astrocyte and microvascular imaging in awake animals using two-photon microscopy. *Microcirculation* **22**, 219–227 (2015).
- Rungta, R. L., Osmanski, B.-F., Boido, D., Tanter, M. & Charpak, S. Light controls cerebral blood flow in naive animals. *Nat. Commun.* **8**, 14191 (2017).
- Roche, M. et al. In vivo imaging with a water immersion objective affects brain temperature, blood flow and oxygenation. *Elife* **8**, e47324 (2019).
- Mayrhofer, J. M. et al. Novel two-alternative forced choice paradigm for bilateral vibrotactile whisker frequency discrimination in head-fixed mice and rats. *J. Neurophysiol.* **109**, 273–284 (2013).
- Aydin, A.-K. et al. Iliiski, a software for robust calculation of transfer functions. *Plos Comput. Biol.* <https://journals.plos.org/ploscompbiol/article?id=10.1371/journal.pcbi.1008614> (2020).
- Aydin, A.-K. et al. Iliiski, a software for robust calculation of transfer functions (Version 1.0.0). *Zenodo* <https://doi.org/10.5281/zenodo.4765555> (2021).
- Bates, D., Mächler, M., Bolker, B. & Walker, S. Fitting linear mixed-effects models using lme4. *J. Stat. Softw.* **67**, 1–48 (2015).
- Hothorn, T., Bretz, F. & Westfall, P. Simultaneous inference in general parametric models. *Biometrical J.* **50**, 346–363 (2008).
- Drew, P. J. et al. Chronic optical access through a polished and reinforced thinned skull. *Nat. Methods* **7**, 981–984 (2010).
- Kleinfeld, D., Mitra, P. P., Helmchen, F. & Denk, W. Fluctuations and stimulus-induced changes in blood flow observed in individual capillaries in layers 2 through 4 of rat neocortex. *Proc. Natl Acad. Sci. USA* **95**, 15741–15746 (1998).
- Veluw, S. Jvan et al. Vasomotion as a driving force for paravascular clearance in the awake mouse brain. *Neuron* **105**, 549–561.e5 (2019).
- Mächler, P. et al. In vivo evidence for a lactate gradient from astrocytes to neurons. *Cell Metab.* **23**, 94–102 (2016).

Acknowledgements

Financial support to SC lab was provided by the Institut National de la Santé et de la Recherche Médicale (INSERM), the Fondation pour la Recherche Médicale (EQU201903007811), the Fondation Leducq Transatlantic Networks of Excellence program (16CVD05, Understanding the role of the perivascular space in cerebral small vessel disease) and by French state funds managed by the ANR within the Investissements d'Avenir program (IHU FOReSIGHT [ANR-18-IAHU-0001], NR-16-RHUS-0004 [RHU TRT_cSVD]). R.L.R. acknowledges support from a Canada Research Chair Tier 2 and the Natural Sciences and Engineering Research Council (NSERC), [RGPIN-2020-05276]. BW lab is supported by the Swiss National Science Foundation Grant 310030_182703.

Author contributions

R.L.R. and S.C. designed research, R.L.R. performed experiments, M.Z. and B.W. provided equipment and software, R.L.R., A.-K.A., E.M., M.Z. and D.B. analyzed data. All authors edited the manuscript.

Competing interests

The authors declare no competing interests.

Additional information

Supplementary information The online version contains supplementary material available at <https://doi.org/10.1038/s42003-021-02382-w>.

Correspondence and requests for materials should be addressed to R.L.R. or S.C.

Peer review information *Communications Biology* thanks the anonymous reviewers for their contribution to the peer review of this work. Primary Handling Editors: Karli Montague-Cardoso.

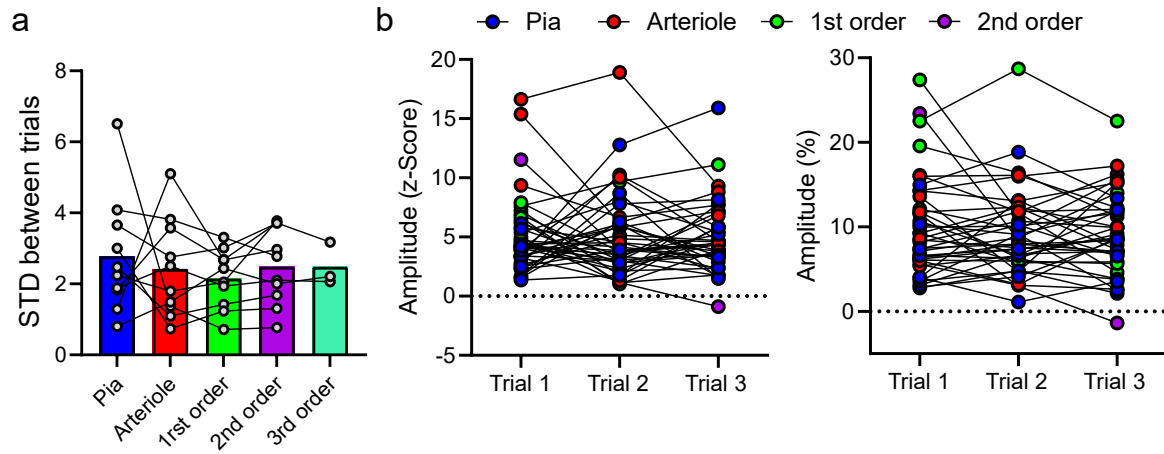
Reprints and permission information is available at <http://www.nature.com/reprints>

Publisher's note Springer Nature remains neutral with regard to jurisdictional claims in published maps and institutional affiliations.



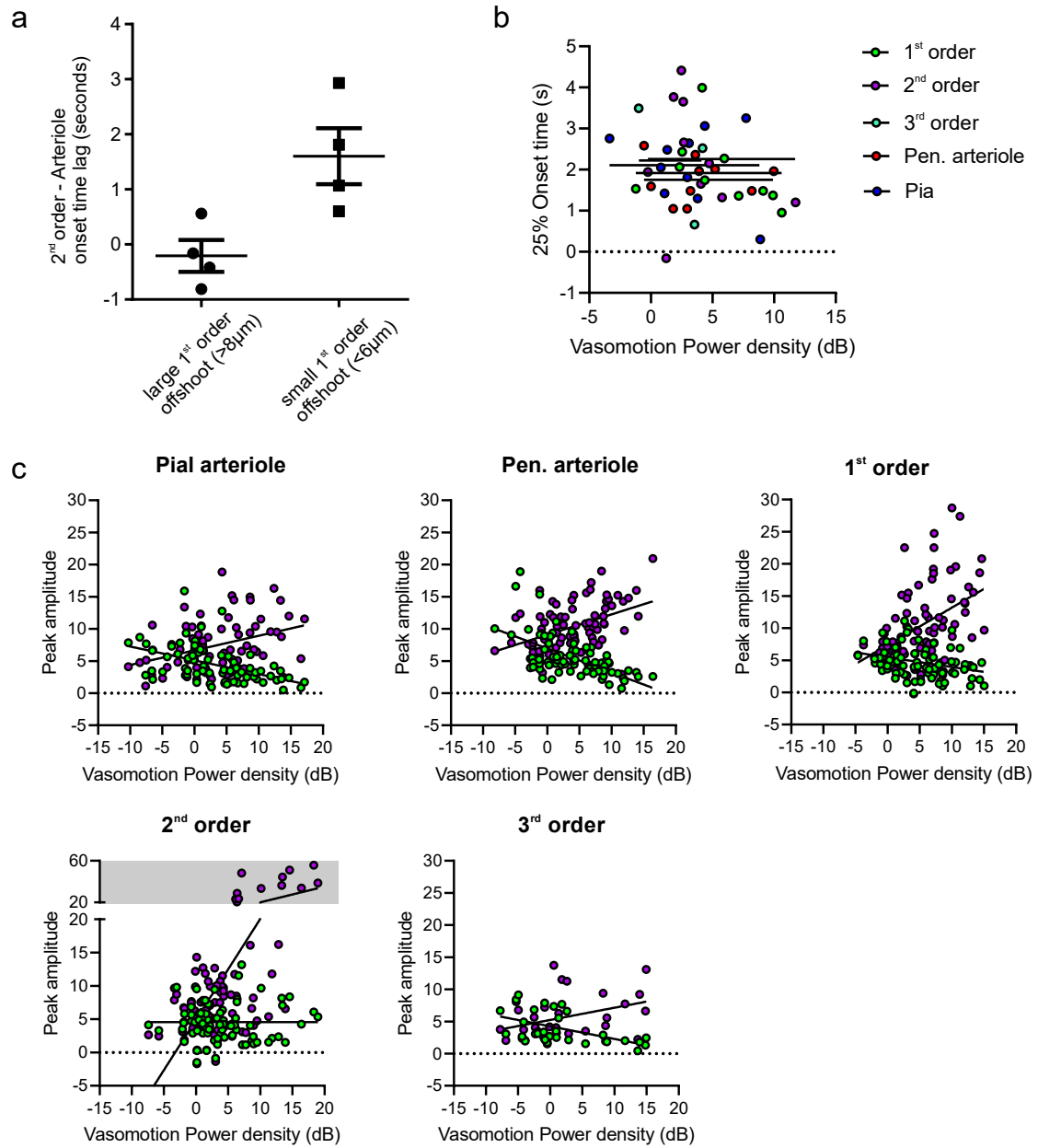
Open Access This article is licensed under a Creative Commons Attribution 4.0 International License, which permits use, sharing, adaptation, distribution and reproduction in any medium or format, as long as you give appropriate credit to the original author(s) and the source, provide a link to the Creative Commons license, and indicate if changes were made. The images or other third party material in this article are included in the article's Creative Commons license, unless indicated otherwise in a credit line to the material. If material is not included in the article's Creative Commons license and your intended use is not permitted by statutory regulation or exceeds the permitted use, you will need to obtain permission directly from the copyright holder. To view a copy of this license, visit <http://creativecommons.org/licenses/by/4.0/>.

© The Author(s) 2021



Supplementary Figure 1: Individual trial variability

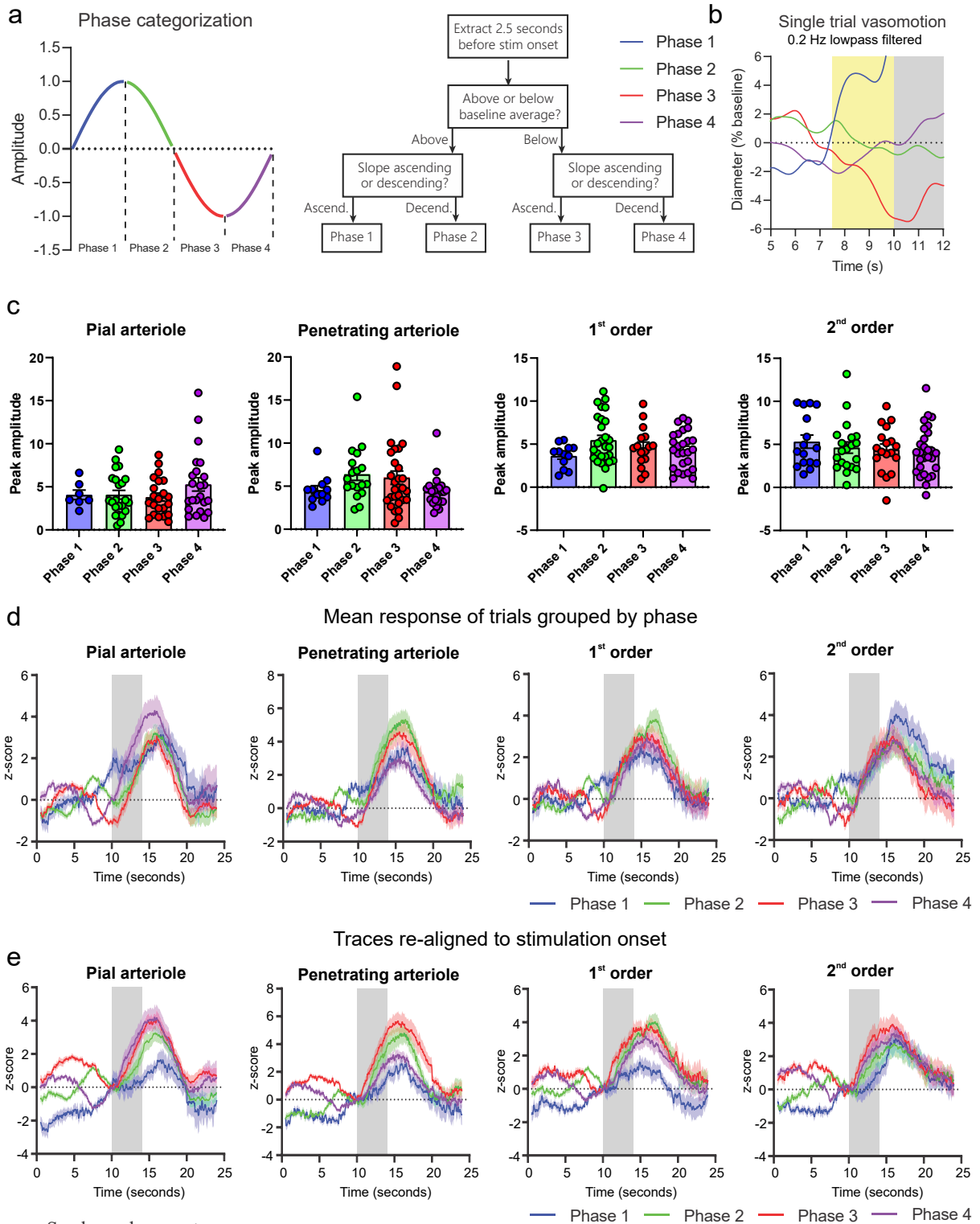
- STD of z-score peak amplitude between different trials of individual vascular networks (connected lines), sorted by compartment.
- No pattern of trial-to-trial adaptation was observed across consecutive trials. Left, z-score peak; Right, percent increase from baseline.



See legend on next page.

Supplementary Figure 2: Relationship between first order offshoot size and vasomotion with stimulation evoked diameter increases.

- a) Difference in onset times between connected arteriole – 2nd order branch pairs (lag), on vascular arbours with large vs. small 1st order branch offshoots. $p = 0.01$, paired t-test if different vascular networks from same mouse considered independent, $p = 0.06$ when grouped by animal (see methods), $n = 8$ vascular networks, 6 mice.
- b) Onset time is not correlated with vasomotion power, colour coded circles represent trial averaged data from individual vascular arbours. None of the fits significantly deviated from 0.
- c) The stimulation evoked diameter peak amplitude (% change, purple) and (z-score, green) vs. vasomotion power. Data points are single trial data across multiple vascular arbours. Shaded area on 2nd order plot represents a re-scaling of the y-axis. All fits of data in % change relative to baseline (purple) significantly deviated from 0 ($p < 0.05$).



Supplementary Figure 3: Relationship between low frequency vasomotion phase and stimulation evoked response.

- a) Flow chart describing single trial phase classification as “Phase 1-4”
- b) Four trials from a pial arteriole lowpass filtered and characterized as different phases by analyzing the polarity and direction in the yellow shaded area (2.5 seconds).
- c) Peak amplitude of each trial grouped by their phase classification for different vascular segments.
- d) Average traces obtained from trials grouped according to phase.
- e) Same as in (d), except the baseline was re-aligned to the time of stimulation onset (10 seconds). Shaded colours in (d and e) represents standard error of the mean (SEM). Grey bar indicates time of whisker stimulation.

BIBLIOGRAPHY

- [Aguirre *et al.* 1998] Geoffrey K. Aguirre, Eric Zarahn and Mark DEsposito. *A critique of the use of the Kolmogorov-Smirnov (KS) statistic for the analysis of BOLD fMRI data*. *Magnetic Resonance in Medicine*, vol. 39, no. 3, pages 500–505, 1998. (Cited on page 46.)
- [Alderton *et al.* 2001] Wendy K Alderton, Chris E Cooper and Richard G Knowles. *Nitric oxide synthases: structure, function and inhibition*. *Biochemical Journal*, vol. 357, no. 3, page 593, 2001. (Cited on page 29.)
- [Andreone *et al.* 2015] Benjamin J. Andreone, Baptiste Lacoste and Chenghua Gu. *Neuronal and Vascular Interactions*. *Annual Review of Neuroscience*, vol. 38, no. 1, pages 1–22, 2015. (Cited on page 26.)
- [Andresen *et al.* 2006] Jon Andresen, Nadeem I. Shafi and Robert M. Bryan. *Endothelial influences on cerebrovascular tone*. *Journal of Applied Physiology*, vol. 100, no. 1, pages 318–327, 2006. (Cited on page 23.)
- [Ang *et al.* 2006] Eugenius S. B. C. Ang, Vicko Gluncic, Alvaro Duque, Mark E. Schafer and Pasko Rakic. *Prenatal exposure to ultrasound waves impacts neuronal migration in mice*. *Proceedings of the National Academy of Sciences*, vol. 103, no. 34, pages 12903–12910, 2006. (Cited on page 57.)
- [Ashby & Mack 2021] Julianne W. Ashby and Julia J. Mack. *ENDOTHELIAL CONTROL OF CEREBRAL BLOOD FLOW*. *The American Journal of Pathology*, 2021. (Cited on page 23.)
- [Attwell & Laughlin 2001] David Attwell and Simon B. Laughlin. *An Energy Budget for Signaling in the Grey Matter of the Brain*. *Journal of Cerebral Blood Flow & Metabolism*, vol. 21, no. 10, pages 1133–1145, 2001. (Cited on page 8.)
- [Attwell *et al.* 2010] David Attwell, Alastair M. Buchan, Serge Charpak, Martin Lauritzen, Brian A. MacVicar and Eric A. Newman. *Glial and neuronal control of brain blood flow*. *Nature*, vol. 468, no. 7321, pages 232–243, 2010. (Cited on pages 22, 26 and 29.)

- [Aydin *et al.* 2020] Ali-Kemal Aydin, William D. Haselden, Yannick Goulam Houssen, Christophe Pouzat, Ravi L. Rungta, Charlie Demené, Mickael Tanter, Patrick J. Drew, Serge Charpak and Davide Boido. *Transfer functions linking neural calcium to single voxel functional ultrasound signal*. Nature Communications, vol. 11, no. 1, page 2954, 2020. (Cited on pages 30, 32 and 131.)
- [Baker 2016] Monya Baker. *1,500 scientists lift the lid on reproducibility*. Nature, vol. 533, no. 7604, pages 452–454, 2016. (Cited on page 132.)
- [Baranger *et al.* 2021] Jerome Baranger, Charlie Demene, Alice Frerot, Flora Faure, Catherine Delanoë, Hicham Serroune, Alexandre Houdouin, Jerome Mairesse, Valerie Biran, Olivier Baud and Mickael Tanter. *Beside functional monitoring of the dynamic brain connectivity in human neonates*. Nature Communications, vol. 12, no. 1, page 1080, 2021. (Cited on page 58.)
- [Begley & Ellis 2012] C. Glenn Begley and Lee M. Ellis. *Raise standards for preclinical cancer research*. Nature, vol. 483, no. 7391, pages 531–533, 2012. (Cited on page 132.)
- [Belliveau *et al.* 1991] JW Belliveau, DN Kennedy, RC McKinstry, BR Buchbinder, RM Weisskoff, MS Cohen, JM Vevea, TJ Brady and BR Rosen. *Functional mapping of the human visual cortex by magnetic resonance imaging*. Science, vol. 254, no. 5032, pages 716–719, 1991. (Cited on page 18.)
- [Bercoff *et al.* 2011] J Bercoff, G Montaldo, T Loupas, D Savery, Fabien Meunier, M Fink and M Tanter. *Ultrafast compound doppler imaging: providing full blood flow characterization*. IEEE Transactions on Ultrasonics, Ferroelectrics, and Frequency Control, vol. 58, no. 1, pages 134–147, 2011. (Cited on pages 53 and 55.)
- [Besançon *et al.* 2021] Lonni Besançon, Nathan Peiffer-Smadja, Corentin Segalas, Haiting Jiang, Paola Masuzzo, Cooper Smout, Eric Billy, Maxime Deforet and Clémence Leyrat. *Open science saves lives: lessons from the COVID-19 pandemic*. BMC Medical Research Methodology, vol. 21, no. 1, page 117, 2021. (Cited on page 133.)
- [Bimbard *et al.* 2018] Célian Bimbard, Charlie Demene, Constantin Girard, Susanne Radtke-Schuller, Shihab Shamma, Mickael Tanter and Yves Boubenec. *Multi-scale mapping along the auditory hierarchy using high-resolution functional UltraSound in the awake ferret*. eLife, vol. 7, page e35028, 2018. (Cited on pages 56 and 58.)
- [Blaize *et al.* 2020] Kévin Blaize, Fabrice Arcizet, Marc Gesnik, Harry Ahnine, Ulisse Ferrari, Thomas Deffieux, Pierre Pouget, Frédéric Chavane, Mathias Fink, José-Alain Sahel, Mickael Tanter and Serge Picaud. *Functional ultrasound imaging of deep visual cortex in awake nonhuman primates*. Proceedings of the National Academy of Sciences, vol. 117, no. 25, pages 14453–14463, 2020. (Cited on pages 57 and 58.)
- [Blinder *et al.* 2010] Pablo Blinder, Andy Y. Shih, Christopher Rafie and David Kleinfeld. *Topological basis for the robust distribution of blood to rodent neocortex*. Proceedings of the National Academy of Sciences, vol. 107, no. 28, pages 12670–12675, 2010. (Cited on pages 11 and 12.)
- [Blinder *et al.* 2013] Pablo Blinder, Philbert S Tsai, John P Kaufhold, Per M Knutsen, Harry Suhl and David Kleinfeld. *The cortical angiome: an interconnected vascular network with noncolumnar patterns of blood flow*. Nature Neuroscience, vol. 16, no. 7, pages 889–897, 2013. (Cited on pages 12, 13 and 27.)

- [Boido *et al.* 2019] Davide Boido, Ravi L. Rungta, Bruno-Félix Osmanski, Morgane Roche, Tomokazu Tsurugizawa, Denis Le Bihan, Luisa Ciobanu and Serge Charpak. *Mesosopic and microscopic imaging of sensory responses in the same animal*. Nature Communications, vol. 10, no. 1, page 1110, 2019. (Cited on pages 32, 56, 58, 64, 65 and 130.)
- [Borowsky & Collins 1989] Iris Wagman Borowsky and Robert C. Collins. *Metabolic anatomy of brain: A comparison of regional capillary density, glucose metabolism, and enzyme activities*. Journal of Comparative Neurology, vol. 288, no. 3, pages 401–413, 1989. (Cited on page 12.)
- [Boyd *et al.* 2012] Alison M Boyd, James F Sturgill, Cindy Poo and Jeffrey S Isaacson. *Cortical feedback control of olfactory bulb circuits*. Neuron, vol. 76, no. 6, pages 1161–1174, 2012. (Cited on page 62.)
- [Boynton *et al.* 1996] Geoffrey M. Boynton, Stephen A. Engel, Gary H. Glover and David J. Heeger. *Linear Systems Analysis of Functional Magnetic Resonance Imaging in Human V1*. Journal of Neuroscience, vol. 16, no. 13, pages 4207–4221, 1996. (Cited on pages 45 and 46.)
- [Brezzo *et al.* 2020] Gaia Brezzo, Julie Simpson, Kamar E. Ameen-Ali, Jason Berwick and Chris Martin. *Acute effects of systemic inflammation upon the neuro-glial-vascular unit and cerebrovascular function*. Brain, Behavior, & Immunity - Health, vol. 5, page 100074, 2020. (Cited on page 33.)
- [Bushdid *et al.* 2014] C. Bushdid, M. O. Magnasco, L. B. Vosshall and A. Keller. *Humans Can Discriminate More than 1 Trillion Olfactory Stimuli*. Science, vol. 343, no. 6177, pages 1370–1372, 2014. (Cited on page 61.)
- [Buxton *et al.* 1998] Richard B. Buxton, Eric C. Wong and Lawrence R. Frank. *Dynamics of blood flow and oxygenation changes during brain activation: The balloon model*. Magnetic Resonance in Medicine, vol. 39, no. 6, pages 855–864, 1998. (Cited on page 45.)
- [Calvisi *et al.* 2004] Michael L. Calvisi, Andrew J. Szeri, David T. J. Liley and Thomas C. Ferree. *Theoretical Study of Bold Response to Sinusoidal Input*. The 26th Annual International Conference of the IEEE Engineering in Medicine and Biology Society, vol. 1, pages 659–662, 2004. (Cited on page 46.)
- [Cauli & Hamel 2018] Bruno Cauli and Edith Hamel. *Brain Perfusion and Astrocytes*. Trends in Neurosciences, vol. 41, no. 7, pages 409–413, 2018. (Cited on page 23.)
- [Chaigneau *et al.* 2003] Emmanuelle Chaigneau, Martin Oheim, Etienne Audinat and Charpak, and Serge. *Two-photon imaging of capillary blood flow in olfactory bulb glomeruli*. Proceedings of the National Academy of Sciences, 2003. (Cited on pages 12, 25, 35 and 65.)
- [Chaigneau *et al.* 2007] Emmanuelle Chaigneau, Pascale Tiret, J'érLecoq, Mathieu Ducros, Thomas Kn"opfel and Serge Charpak. *The relationship between blood flow and neuronal activity in the rodent olfactory bulb*. The Journal of Neuroscience: The Official Journal of the Society for Neuroscience, vol. 27, no. 24, pages 6452–6460, 2007. (Cited on pages 33 and 65.)
- [Chen *et al.* 2013] Tsai-Wen Chen, Trevor J Wardill, Yi Sun, Stefan R Pulver, Sabine L Renninger, Amy Baohan, Eric R Schreiter, Rex A Kerr, Michael B Orger, Vivek Jayaraman, Loren L Looger, Karel Svoboda and Douglas S Kim. *Ultrasensitive fluorescent proteins for imaging neuronal activity*. Nature, vol. 499, no. 7458, page 295, 2013. (Cited on page 34.)

- [Cipolla *et al.* 2004] Marilyn J. Cipolla, Rui Li and Lisa Vitullo. *Perivascular Innervation of Penetrating Brain Parenchymal Arterioles*. *Journal of Cardiovascular Pharmacology*, vol. 44, no. 1, pages 1–8, 2004. (Cited on pages 11 and 12.)
- [Cipolla 2016] Marilyn J. Cipolla. *The Cerebral Circulation*, Second Edition, volume 8 of *Colloquium Series on Integrated Systems Physiology: From Molecule to Function*. 2016. (Cited on pages 7, 13, 15 and 16.)
- [Claron *et al.* 2020] Julien Claron, Vincent Hingot, Isabelle Rivals, Line Rahal, Olivier Couture, Thomas Deffieux, Mickael Tanter and Sophie Pezet. *Large-scale functional ultrasound imaging of the spinal cord reveals in-depth spatiotemporal responses of spinal nociceptive circuits in both normal and inflammatory states*. *Pain*, vol. 162, no. 4, pages 1047–1059, 2020. (Cited on page 58.)
- [Cohen 1997] Mark S. Cohen. *Parametric Analysis of fMRI Data Using Linear Systems Methods*. *NeuroImage*, vol. 6, no. 2, pages 93–103, 1997. (Cited on page 45.)
- [Couture *et al.* 2018] Olivier Couture, Vincent Hingot, Baptiste Heiles, Pauline Muleki-Seya and Mickael Tanter. *Ultrasound Localization Microscopy and Super-Resolution: A State of the Art*. *IEEE Transactions on Ultrasonics, Ferroelectrics, and Frequency Control*, vol. 65, no. 8, pages 1304–1320, 2018. (Cited on page 57.)
- [Coyle 1975] Peter Coyle. *Arterial patterns of the rat rhinencephalon and related structures*. *Experimental Neurology*, vol. 49, no. 3, pages 671–690, 1975. (Cited on page 64.)
- [Craigie 1945] E. Horne Craigie. *The architecture of the cerebral capillary bed*. *Biological Reviews*, vol. 20, no. 4, pages 133–146, 1945. (Cited on pages 12 and 18.)
- [Dahl 1973] Erik Dahl. *The fine structure of intracerebral vessels*. *Zeitschrift für Zellforschung und Mikroskopische Anatomie*, vol. 145, no. 4, pages 577–586, 1973. (Cited on page 14.)
- [Damisah *et al.* 2017] Eyiymisi C. Damisah, Robert A. Hill, Lei Tong, Katie N. Murray and Jaime Grutzendler. *A fluoro-Nissl dye identifies pericytes as distinct vascular mural cells during in vivo brain imaging*. *Nature Neuroscience*, vol. 20, no. 7, pages 1023–1032, 2017. (Cited on page 14.)
- [Dana *et al.* 2014] Hod Dana, Tsai-Wen Chen, Amy Hu, Brenda C. Shields, Caiying Guo, Loren L. Looger, Douglas S. Kim and Karel Svoboda. *Thy1-GCaMP6 Transgenic Mice for Neuronal Population Imaging In Vivo*. *PLoS ONE*, vol. 9, no. 9, page e108697, 2014. (Cited on pages 34 and 64.)
- [Deffieux *et al.* 2018] Thomas Deffieux, Charlie Demene, Mathieu Pernot and Mickael Tanter. *Functional ultrasound neuroimaging: a review of the preclinical and clinical state of the art*. *Current Opinion in Neurobiology*, vol. 50, pages 128–135, 2018. (Cited on pages 41, 51 and 53.)
- [Demene *et al.* 2017] Charlie Demene, Jérôme Baranger, Miguel Bernal, Catherine Delanoe, Stéphane Auvin, Valérie Biran, Marianne Alison, Jérôme Mairesse, Elisabeth Harribaud, Mathieu Pernot, Mickael Tanter and Olivier Baud. *Functional ultrasound imaging of brain activity in human newborns*. *Science Translational Medicine*, vol. 9, no. 411, page eaah6756, 2017. (Cited on pages 57 and 58.)

- [Demené *et al.* 2015] Charlie * Demené, Thomas Deffieux, Mathieu Pernot, Bruno-Félix Osmanski, Valérie Biran, Jean-Luc Gennisson, Lim-Anna Sieu, Antoine Bergel, Stéphanie Franqui, Jean-Michel Correas, Ivan Cohen, Olivier Baud and Mickael Tanter. *Spatiotemporal Clutter Filtering of Ultrafast Ultrasound Data Highly Increases Doppler and fUltrasound Sensitivity*. IEEE Transactions on Medical Imaging, vol. 34, no. 11, pages 2271–2285, 2015. (Cited on page 55.)
- [Demené *et al.* 2021] Charlie Demené, Justine Robin, Alexandre Dizeux, Baptiste Heiles, Mathieu Pernot, Mickael Tanter and Fabienne Perren. *Transcranial ultrafast ultrasound localization microscopy of brain vasculature in patients*. Nature Biomedical Engineering, vol. 5, no. 3, pages 219–228, 2021. (Cited on page 57.)
- [Dienel 2019] Gerald A. Dienel. *Brain Glucose Metabolism: Integration of Energetics with Function*. Physiological Reviews, vol. 99, no. 1, pages 949–1045, 2019. (Cited on page 8.)
- [Dijk 2013] Gerrit van Dijk. *Distribution Theory Convolution, Fourier Transform, and Laplace Transform*. De Gruyter, 2013. (Cited on page 29.)
- [Dirnagl *et al.* 1992] Ulrich Dirnagl, Arno Villringer and Karl Max Einhäupl. *In-vivo confocal scanning laser microscopy of the cerebral microcirculation*. Journal of Microscopy, vol. 165, no. 1, pages 147–157, 1992. (Cited on page 35.)
- [Dirnagl *et al.* 1993] Ulrich Dirnagl, Ute Lindauer and Arno Villringer. *Role of nitric oxide in the coupling of cerebral blood flow to neuronal activation in rats*. Neuroscience Letters, vol. 149, no. 1, pages 43–46, 1993. (Cited on page 29.)
- [Doppler 1842] Christian Doppler. *Über das farbige Licht der Doppelsterne und einige andere Gestirne des Himmels*. 1842. (Cited on page 52.)
- [Duong *et al.* 2000] Timothy Q. Duong, Dae-Shik Kim, Kâmil Uğurbil and Seong-Gi Kim. *Spatiotemporal dynamics of the BOLD fMRI signals: Toward mapping submillimeter cortical columns using the early negative response*. Magnetic Resonance in Medicine, vol. 44, no. 2, pages 231–242, 2000. (Cited on page 49.)
- [Edelman & Macé 2021] Bradley Jay Edelman and Emilie Macé. *Functional ultrasound brain imaging: bridging networks, neurons and behavior*. Current Opinion in Biomedical Engineering, vol. 18, page 100286, 2021. (Cited on page 51.)
- [Epp *et al.* 2020] Robert Epp, Franca Schmid, Bruno Weber and Patrick Jenny. *Predicting Vessel Diameter Changes to Up-Regulate Biphasic Blood Flow During Activation in Realistic Microvascular Networks*. Frontiers in Physiology, vol. 11, page 566303, 2020. (Cited on page 27.)
- [Ernst & Hennig 1994] Thomas Ernst and Jürgen Hennig. *Observation of a fast response in functional MR*. Magnetic Resonance in Medicine, vol. 32, no. 1, pages 146–149, 1994. (Cited on page 46.)
- [Errico *et al.* 2015] Claudia Errico, Juliette Pierre, Sophie Pezet, Yann Desailly, Zsolt Lenkei, Olivier Couture and Mickael Tanter. *Ultrafast ultrasound localization microscopy for deep super-resolution vascular imaging*. Nature, vol. 527, no. 7579, pages 499–502, 2015. (Cited on page 57.)

- [Erwin *et al.* 2001] Joseph M. Erwin, Esther A. Nimchinsky, Patrick J. Gannon, Daniel P. Perl and Patrick R. Hof. *Functional Neurobiology of Aging*. Section II: Memory: Neocortical and Hippocampal Functions, no. Z. Med. Wiss.191881, pages 447–455, 2001. Average brain weight: 1.3kg. (Cited on page 8.)
- [Esipova *et al.* 2019] Tatiana V. Esipova, Matthew J.P. Barrett, Eva Erlebach, Artëm E. Masunov, Bruno Weber and Sergei A. Vinogradov. *Oxyphor 2P: A High-Performance Probe for Deep-Tissue Longitudinal Oxygen Imaging*. *Cell Metabolism*, vol. 29, no. 3, pages 736–744.e7, 2019. (Cited on page 37.)
- [Estrada *et al.* 2008] Arnold D Estrada, Adrien Ponticorvo, Tim N Ford and Andrew K Dunn. *Microvascular oxygen quantification using two-photon microscopy*. *Optics Letters*, vol. 33, no. 10, page 1038, 2008. (Cited on page 37.)
- [Eve & Gray 2020] Martin Paul Eve and Jonathan Gray. *Reassembling Scholarly Communications: Histories, Infrastructures, and Global Politics of Open Access*. The MIT Press, 1 édition, 2020. (Cited on page 132.)
- [Fanelli 2010] Daniele Fanelli. *“Positive” Results Increase Down the Hierarchy of the Sciences*. *PLoS ONE*, vol. 5, no. 4, page e10068, 2010. (Cited on page 132.)
- [Faraci & Heistad 1990] F M Faraci and D D Heistad. *Regulation of large cerebral arteries and cerebral microvascular pressure*. *Circulation Research*, vol. 66, no. 1, pages 8–17, 1990. (Cited on page 15.)
- [Farkas & Luiten 2001] Eszter Farkas and Paul G.M Luiten. *Cerebral microvascular pathology in aging and Alzheimer’s disease*. *Progress in Neurobiology*, vol. 64, no. 6, pages 575–611, 2001. (Cited on page 25.)
- [Fern *et al.* 2010] Fern, F. ez Klett, Nikolas Offenhauser, Ulrich Dirnagl, Josef Priller and Ute Lindauer. *Pericytes in capillaries are contractile in vivo, but arterioles mediate functional hyperemia in the mouse brain*. *Proceedings of the National Academy of Sciences*, vol. 107, no. 51, pages 22290—22295, 2010. (Cited on page 23.)
- [Filosa *et al.* 2016] J.A. Filosa, H.W. Morrison, J.A. Iddings, W. Du and K.J. Kim. *Beyond neurovascular coupling, role of astrocytes in the regulation of vascular tone*. *Neuroscience*, vol. 323, pages 96–109, 2016. (Cited on pages 15, 20, 21 and 23.)
- [Fink & Tanter 2010] Mathias Fink and Mickael Tanter. *Multiwave imaging and super resolution*. *Physics Today*, vol. 63, no. 2, pages 28–33, 2010. (Cited on page 53.)
- [Forstermann & Munzel 2006] Ulrich Forstermann and Thomas Munzel. *Endothelial Nitric Oxide Synthase in Vascular Disease*. *Circulation*, vol. 113, no. 13, pages 1708–1714, 2006. (Cited on page 29.)
- [Fraser *et al.* 2020] Nicholas Fraser, Fakhri Momeni, Philipp Mayr and Isabella Peters. *The relationship between bioRxiv preprints, citations and altmetrics*. *Quantitative Science Studies*, vol. 1, no. 2, pages 618–638, 2020. (Cited on page 132.)
- [Freygang & Sokoloff 1959] W.H. Freygang and Louis Sokoloff. *Quantitative Measurement of Regional Circulation in the Central Nervous System by the use of Radioactive Inert Gas*. *Advances in Biological and Medical Physics*, vol. 6, pages 263–279, 1959. (Cited on page 18.)

- [Friedland & Iadecola 1991] R P Friedland and C Iadecola. *Roy and Sherrington (1890): A centennial reexamination of "On the Regulation of the Blood-Supply of the Brain"*. *Neurology*, vol. 41, no. 1, pages 10–10, 1991. (Cited on page 18.)
- [Friston *et al.* 1994] K J Friston, P Jezzard and R Turner. *Analysis of functional MRI time-series*. *Human Brain Mapping*, vol. 1, no. 2, pages 153–171, 1994. (Cited on page 46.)
- [Friston *et al.* 1998] Karl J. Friston, Oliver Josephs, Geraint Rees and Robert Turner. *Nonlinear event-related responses in fMRI*. *Magnetic Resonance in Medicine*, vol. 39, no. 1, pages 41–52, 1998. (Cited on page 46.)
- [Friston *et al.* 2000] K.J. Friston, A. Mechelli, R. Turner and C.J. Price. *Nonlinear Responses in fMRI: The Balloon Model, Volterra Kernels, and Other Hemodynamics*. *NeuroImage*, vol. 12, no. 4, pages 466–477, 2000. (Cited on page 46.)
- [Frostig *et al.* 1990] R D Frostig, E E Lieke, D Y Ts'o and A Grinvald. *Cortical functional architecture and local coupling between neuronal activity and the microcirculation revealed by in vivo high-resolution optical imaging of intrinsic signals*. *Proceedings of the National Academy of Sciences*, vol. 87, no. 16, pages 6082–6086, 1990. (Cited on page 46.)
- [Furchgott & Zawadzki 1980] Robert F. Furchgott and John V. Zawadzki. *The obligatory role of endothelial cells in the relaxation of arterial smooth muscle by acetylcholine*. *Nature*, vol. 288, no. 5789, pages 373–376, 1980. (Cited on page 29.)
- [Gao *et al.* 2017] Yu-Rong Gao, Yuncong Ma, Qingguang Zhang, Aaron T. Winder, Zhifeng Liang, Lilith Antinori, Patrick J. Drew and Nanyin Zhang. *Time to wake up: Studying neurovascular coupling and brain-wide circuit function in the un-anesthetized animal*. *NeuroImage*, vol. 153, pages 382–398, 2017. (Cited on page 32.)
- [Gardner 2010] Justin L. Gardner. *Is cortical vasculature functionally organized?* *NeuroImage*, vol. 49, no. 3, pages 1953–1956, 2010. (Cited on page 31.)
- [Girouard & Iadecola 2006] Helene Girouard and Costantino Iadecola. *Neurovascular coupling in the normal brain and in hypertension, stroke, and Alzheimer disease*. *Journal of Applied Physiology*, vol. 100, no. 1, pages 328–335, 2006. (Cited on page 25.)
- [Golub & Pittman 2005] Aleksander S. Golub and Roland N. Pittman. *Erythrocyte-associated transients in Po2 revealed in capillaries of rat mesentery*. *American Journal of Physiology-Heart and Circulatory Physiology*, vol. 288, no. 6, pages H2735–H2743, 2005. (Cited on page 38.)
- [Gould *et al.* 2016] Ian Gopal Gould, Philbert Tsai, David Kleinfeld and Andreas Linninger. *The capillary bed offers the largest hemodynamic resistance to the cortical blood supply*. *Journal of Cerebral Blood Flow & Metabolism*, vol. 37, no. 1, pages 52–68, 2016. (Cited on pages 15 and 27.)
- [H *et al.* 2004] H, Daniel A werker, John M Ollinger and Mark D'Esposito. *Variation of BOLD hemodynamic responses across subjects and brain regions and their effects on statistical analyses*. *NeuroImage*, vol. 21, no. 4, pages 1639–1651, 2004. (Cited on page 46.)
- [Hall *et al.* 2014] Catherine N Hall, Clare Reynell, Bodil Gesslein, Nicola B Hamilton, Anusha Mishra, Sutherl, Brad A, Fergus M O 'farrell, Alastair M Buchan, Martin Lauritzen and

- David Attwell. *Capillary pericytes regulate cerebral blood flow in health and disease*. *Nature*, vol. 508, no. 7494, pages 55–60, 2014. (Cited on pages 23 and 32.)
- [Halliday *et al.* 2015] Matthew R Halliday, Sanket V Rege, Qingyi Ma, Zhen Zhao, Carol A Miller, Ethan A Winkler and Berislav V Zlokovic. *Accelerated pericyte degeneration and blood–brain barrier breakdown in apolipoprotein E4 carriers with Alzheimer’s disease*. *Journal of Cerebral Blood Flow & Metabolism*, vol. 36, no. 1, pages 216–227, 2015. (Cited on page 25.)
- [Hamel 2006] Edith Hamel. *Perivascular nerves and the regulation of cerebrovascular tone*. *Journal of Applied Physiology*, vol. 100, no. 3, pages 1059–1064, 2006. (Cited on page 13.)
- [Harris *et al.* 2012] Julia J. Harris, Renaud Jolivet and David Attwell. *Synaptic Energy Use and Supply*. *Neuron*, vol. 75, no. 5, pages 762–777, 2012. (Cited on page 13.)
- [Haselden *et al.* 2020] William Davis Haselden, Ravi Teja Kedarasetti and Patrick J. Drew. *Spatial and temporal patterns of nitric oxide diffusion and degradation drive emergent cerebrovascular dynamics*. *PLOS Computational Biology*, vol. 16, no. 7, page e1008069, 2020. (Cited on page 29.)
- [Hassler 1966] O Hassler. *Deep cerebral venous system in man: A microangiographic study on its areas of drainage and its anastomoses with the superficial cerebral veins*. *Neurology*, vol. 16, no. 5, pages 505–505, 1966. (Cited on page 13.)
- [Hellums 1977] J.D. Hellums. *The resistance to oxygen transport in the capillaries relative to that in the surrounding tissue*. *Microvascular Research*, vol. 13, no. 1, pages 131–136, 1977. (Cited on page 38.)
- [Hingorani *et al.* 2019] Aroon D. Hingorani, Valerie Kuan, Chris Finan, Felix A. Kruger, Anna Gaulton, Sandesh Chopade, Reecha Sofat, Raymond J. MacAllister, John P. Overington, Harry Hemingway, Spiros Denaxas, David Prieto and Juan Pablo Casas. *Improving the odds of drug development success through human genomics: modelling study*. *Scientific Reports*, vol. 9, no. 1, page 18911, 2019. (Cited on page 40.)
- [Hirano *et al.* 2011] Yoshiyuki Hirano, Bojana Stefanovic and Afonso C. Silva. *Spatiotemporal Evolution of the Functional Magnetic Resonance Imaging Response to Ultrashort Stimuli*. *The Journal of Neuroscience*, vol. 31, no. 4, pages 1440–1447, 2011. (Cited on page 30.)
- [Hirbec *et al.* 2019] H el ene Hirbec, Fran ois Rassendren and Etienne Audinat. *Microglia, Methods and Protocols*. *Methods in Molecular Biology*, vol. 2034, pages 41–55, 2019. (Cited on page 33.)
- [Hirsch *et al.* 2012] Sven Hirsch, Johannes Reichold, Matthias Schneider, G abor Sz ekely and Bruno Weber. *Topology and Hemodynamics of the Cortical Cerebrovascular System*. *Journal of Cerebral Blood Flow & Metabolism*, vol. 32, no. 6, pages 952–967, 2012. (Cited on page 16.)
- [Hodge *et al.* 2019] Rebecca D. Hodge, Trygve E. Bakken, Jeremy A. Miller, Kimberly A. Smith, Eliza R. Barkan, Lucas T. Graybuck, Jennie L. Close, Brian Long, Nelson Johansen, Osnat Penn, Zizhen Yao, Jeroen Eggermont, Thomas H ollt, Boaz P. Levi, Soraya I. Shehata, Brian Aevermann, Allison Beller, Darren Bertagnolli, Krissy Brouner, Tamara Casper, Charles Cobbs, Rachel Dalley, Nick Dee, Song-Lin Ding, Richard G. Ellenbogen, Olivia Fong, Emma Garren, Jeff Goldy, Ryder P. Gwinn, Daniel Hirschstein, C. Dirk Keene, Mohamed Keshk,

- Andrew L. Ko, Kanan Lathia, Ahmed Mahfouz, Zoe Maltzer, Medea McGraw, Thuc Nghi Nguyen, Julie Nyhus, Jeffrey G. Ojemann, Aaron Oldre, Sheana Parry, Shannon Reynolds, Christine Rimorin, Nadiya V. Shapovalova, Saroja Somasundaram, Aaron Szafer, Elliot R. Thomsen, Michael Tieu, Gerald Quon, Richard H. Scheuermann, Rafael Yuste, Susan M. Sunkin, Boudewijn Lelieveldt, David Feng, Lydia Ng, Amy Bernard, Michael Hawrylycz, John W. Phillips, Bosiljka Tasic, Hongkui Zeng, Allan R. Jones, Christof Koch and Ed S. Lein. *Conserved cell types with divergent features in human versus mouse cortex*. *Nature*, vol. 573, no. 7772, pages 61–68, 2019. (Cited on page 40.)
- [Hong & Zafar 2018] Keum-Shik Hong and Amad Zafar. *Existence of Initial Dip for BCI: An Illusion or Reality*. *Frontiers in Neurorobotics*, vol. 12, page 69, 2018. (Cited on page 46.)
- [Hosford *et al.* 2021] Patrick S Hosford, Jack A Wells, Iván Ruminot, Isabel N Christie, Shefeeq M Theparambil, Anna Hadjihambi, L Felipe Barros, Mark F Lythgoe and Alexander V Gourine. *CO₂ signalling mediates neurovascular coupling in the cerebral cortex*. *bioRxiv*, page 2020.12.31.424942, 2021. (Cited on pages 25 and 26.)
- [Hu & Yacoub 2012] Xiaoping Hu and Essa Yacoub. *The story of the initial dip in fMRI*. *NeuroImage*, vol. 62, no. 2, pages 1103–1108, 2012. (Cited on pages 46, 47 and 49.)
- [Hu *et al.* 1997] Xiaoping Hu, Tuong Huu Le and Kâmil Uğurbil. *Evaluation of the early response in fMRI in individual subjects using short stimulus duration*. *Magnetic Resonance in Medicine*, vol. 37, no. 6, pages 877–884, 1997. (Cited on page 47.)
- [Huettel *et al.* 2014] Scott A. Huettel, Allen W. Song and Gregory McCarthy. *Functional Magnetic Resonance Imaging*. Oxford University Press, 3 édition, 2014. (Cited on page 41.)
- [Huneau *et al.* 2015] Clément Huneau, Habib Benali and Hugues Chabriat. *Investigating Human Neurovascular Coupling Using Functional Neuroimaging: A Critical Review of Dynamic Models*. *Frontiers in Neuroscience*, vol. 9, page 467, 2015. (Cited on page 26.)
- [Huneau *et al.* 2018] Clément Huneau, Marion Houot, Anne Joutel, Benoit Béranger, Christian Giroux, Habib Benali and Hugues Chabriat. *Altered dynamics of neurovascular coupling in CADASIL*. *Annals of clinical and translational neurology*, vol. 5, no. 7, pages 788–802, 2018. (Cited on page 25.)
- [Huo *et al.* 2015] Bing-Xing Huo, Yu-Rong Gao and Patrick J. Drew. *Quantitative separation of arterial and venous cerebral blood volume increases during voluntary locomotion*. *NeuroImage*, vol. 105, pages 369–379, 2015. (Cited on page 31.)
- [Iadecola *et al.* 1993] Costantino Iadecola, Dale A. Pelligrino, Michael A. Moskowitz and Niels A. Lassen. *Nitric Oxide Synthase Inhibition and Cerebrovascular Regulation*. *Journal of Cerebral Blood Flow & Metabolism*, vol. 14, no. 2, pages 175–192, 1993. (Cited on pages 13 and 29.)
- [Iadecola 2004] Costantino Iadecola. *Neurovascular regulation in the normal brain and in Alzheimer’s disease*. *Nature Reviews Neuroscience*, vol. 5, no. 5, pages 347–360, 2004. (Cited on page 25.)
- [Iadecola 2013] Costantino Iadecola. *The Pathobiology of Vascular Dementia*. *Neuron*, vol. 80, no. 4, pages 844–866, 2013. (Cited on pages 8 and 25.)

- [Iadecola 2017] Costantino Iadecola. *The Neurovascular Unit Coming of Age: A Journey through Neurovascular Coupling in Health and Disease*. *Neuron*, vol. 96, no. 1, pages 17–42, 2017. Concept of NVU from a Conference in 2001. (Cited on pages 8, 13, 14, 15, 17, 20, 23, 25, 26, 29 and 42.)
- [Ianni & Airan 2021] Tommaso Di Ianni and Raag D. Airan. *Deep-fUS: Functional ultrasound imaging of the brain using deep learning and sparse data*. *bioRxiv*, page 2020.09.29.319368, 2021. (Cited on page 59.)
- [Jezzard *et al.* 1997] Peter Jezzard, Josef P. Rauschecker and Dov Malonek. *An in vivo model for functional MRI in cat visual cortex*. *Magnetic Resonance in Medicine*, vol. 38, no. 5, pages 699–705, 1997. (Cited on page 49.)
- [Jezzard *et al.* 2001] Peter Jezzard, Paul M. Matthews and Stephen M. Smith. *Functional Magnetic Resonance Imaging: An Introduction to Methods*. 1 édition, 2001. (Cited on page 42.)
- [Ji *et al.* 2021] Xiang Ji, Tiago Ferreira, Beth Friedman, Rui Liu, Hannah Liechty, Erhan Bas, Jayaram Chandrashekar and David Kleinfeld. *Brain microvasculature has a common topology with local differences in geometry that match metabolic load*. *Neuron*, vol. 109, no. 7, pages 1168–1187.e13, 2021. (Cited on pages 10, 12, 13 and 130.)
- [John *et al.* 2011] Leslie K. John, George Loewenstein and Drazen Prelec. *Measuring the Prevalence of Questionable Research Practices With Incentives for Truth Telling*. *Psychological Science*, vol. 23, no. 5, pages 524–532, 2011. (Cited on page 132.)
- [Jones 1970] E G Jones. *On the mode of entry of blood vessels into the cerebral cortex*. *Journal of anatomy*, vol. 106, no. Pt 3, pages 507–20, 1970. (Cited on pages 10, 12, 13 and 14.)
- [Jordan & Powers 2012] J. Dedrick Jordan and William J. Powers. *Cerebral Autoregulation and Acute Ischemic Stroke*. *American Journal of Hypertension*, vol. 25, no. 9, pages 946–950, 2012. (Cited on page 15.)
- [Kaplan *et al.* 2020] Luke Kaplan, Brian W. Chow and Chenghua Gu. *Neuronal regulation of the blood–brain barrier and neurovascular coupling*. *Nature Reviews Neuroscience*, vol. 21, no. 8, pages 416–432, 2020. (Cited on pages 17 and 42.)
- [Kerr 1998] Norbert L. Kerr. *HARKing: Hypothesizing After the Results are Known*. *Personality and Social Psychology Review*, vol. 2, no. 3, pages 196–217, 1998. (Cited on page 132.)
- [Kety 1950] Seymour S. Kety. *Circulation and metabolism of the human brain in health and disease*. *The American Journal of Medicine*, vol. 8, no. 2, pages 205–217, 1950. (Cited on page 18.)
- [Kim & Ogawa 2012] Seong-Gi Kim and Seiji Ogawa. *Biophysical and Physiological Origins of Blood Oxygenation Level-Dependent fMRI Signals*. *Journal of Cerebral Blood Flow & Metabolism*, vol. 32, no. 7, pages 1188–1206, 2012. (Cited on page 31.)
- [Kim *et al.* 2000] Dae-Shik Kim, Timothy Q. Duong and Seong-Gi Kim. *High-resolution mapping of iso-orientation columns by fMRI*. *Nature Neuroscience*, vol. 3, no. 2, pages 164–169, 2000. (Cited on page 49.)
- [Kim *et al.* 2016] Ki Jung Kim, Juan Ramiro Diaz, Jennifer A. Iddings and Jessica A. Filosa. *Vasculo-Neuronal Coupling: Retrograde Vascular Communication to Brain Neurons*. *Journal of Neuroscience*, vol. 36, no. 50, pages 12624–12639, 2016. (Cited on pages 25 and 29.)

- [Kirst *et al.* 2020] Christoph Kirst, Sophie Skriabine, Alba Vieites-Prado, Thomas Topilko, Paul Bertin, Gaspard Gerschenfeld, Florine Verny, Piotr Topilko, Nicolas Michalski, Marc Tessier-Lavigne and Nicolas Renier. *Mapping the Fine-Scale Organization and Plasticity of the Brain Vasculature*. *Cell*, vol. 180, no. 4, pages 780–795.e25, 2020. (Cited on pages 12 and 13.)
- [Klein *et al.* 1986] B. Klein, W. Kuschinsky, H. Schrock and F. Vetterlein. *Interdependency of local capillary density, blood flow, and metabolism in rat brains*. *American Journal of Physiology-Heart and Circulatory Physiology*, vol. 251, no. 6, pages H1333–H1340, 1986. Significant differences were found among brain structures investigated; the lowest density of perfused capillaries was found in the white matter (e.g., corpus callosum 162 fragments/mm²), whereas the highest values were determined in the structures of the auditory system (e.g., inferior colliculus 810 fragments/mm²). Density of perfused capillaries correlated well with LCBF ($r = 0.93$) and even better with LCGU ($r = 0.97$). In addition to the relationship between LCGU and LCBF established by earlier studies, these data show the intimate interrelationship between LCGU, density of perfused capillaries, and LCBF. (Cited on page 12.)
- [Kleinfeld *et al.* 1998] David Kleinfeld, Partha P. Mitra, Fritjof Helmchen and Winfried Denk. *Fluctuations and stimulus-induced changes in blood flow observed in individual capillaries in layers 2 through 4 of rat neocortex*. *Proceedings of the National Academy of Sciences*, vol. 95, no. 26, pages 15741–15746, 1998. (Cited on page 35.)
- [Knowles & Moncada 1994] R G Knowles and S Moncada. *Nitric oxide synthases in mammals*. *Biochemical Journal*, vol. 298, no. 2, pages 249–258, 1994. (Cited on page 29.)
- [Koekkoek *et al.* 2018] S.K.E. Koekkoek, S. SoloukeyTbalvandany, B.S. Generowicz, W.S. Vanhoogstraten, N.L. Deoude, H.J. Boele, C. Strydis, G. Leus, J. G. Bosch, A.F.W. Vander Steen, C. I. De Zeeuw and P. Kruizing. *High Frequency Functional Ultrasound in Mice*. 2018 IEEE International Ultrasonics Symposium (IUS), vol. 00, pages 1–4, 2018. (Cited on page 53.)
- [Krueger & Bechmann 2010] Martin Krueger and Ingo Bechmann. *CNS pericytes: Concepts, misconceptions, and a way out*. *Glia*, vol. 58, no. 1, pages 1–10, 2010. (Cited on page 23.)
- [Kuhn 1962] Thomas S. Kuhn. *The Structure of Scientific Revolutions*. 4th édition, 1962. (Cited on page 4.)
- [Kılıç & Akakın 2007] Türker Kılıç and Akın Akakın. *Anatomy of Cerebral Veins and Sinuses*. *Frontiers of Neurology and Neuroscience*, vol. 23, pages 4–15, 2007. (Cited on page 13.)
- [Lacroix *et al.* 2015] Alexandre Lacroix, Xavier Toussay, Eitan Anenberg, Clotilde Lecrux, Nerea Ferreirós, Anastassios Karagiannis, Fabrice Plaisier, Patrick Chausson, Frédéric Jarlier, Sean A. Burgess, Elizabeth M. C. Hillman, Irmgard Tegeder, Timothy H. Murphy, Edith Hamel and Bruno Cauli. *COX-2-Derived Prostaglandin E2 Produced by Pyramidal Neurons Contributes to Neurovascular Coupling in the Rodent Cerebral Cortex*. *The Journal of Neuroscience*, vol. 35, no. 34, pages 11791–11810, 2015. (Cited on page 22.)
- [Lalзад *et al.* 2017] Assema Lalзад, Flora Wong and Michal Schneider. *Neonatal Cranial Ultrasound: Are Current Safety Guidelines Appropriate?* *Ultrasound in Medicine & Biology*, vol. 43, no. 3, pages 553–560, 2017. (Cited on page 57.)

- [Lancaster 1994] J R Lancaster. *Simulation of the diffusion and reaction of endogenously produced nitric oxide*. Proceedings of the National Academy of Sciences, vol. 91, no. 17, pages 8137–8141, 1994. (Cited on page 29.)
- [Larrivée *et al.* 2009] Bruno Larrivée, Catarina Freitas, Steven Suchting, Isabelle Brunet and Anne Eichmann. *Guidance of Vascular Development*. Circulation Research, vol. 104, no. 4, pages 428–441, 2009. Ref for high similarity between organ-specific vascular pattern across vertebrates. (Cited on page 11.)
- [Lassen *et al.* 1978] Nils A. Lassen, David H. and Erik Skinhøj. *Brain Function and Blood Flow*. Scientific American, no. 239, pages 62–71, 1978. (Cited on pages 18 and 20.)
- [Lecoq *et al.* 2009] Jérôme Lecoq, Pascale Tiret, Marion Najac, Gordon M. Shepherd, Charles A. Greer and Serge Charpak. *Odor-Evoked Oxygen Consumption by Action Potential and Synaptic Transmission in the Olfactory Bulb*. The Journal of Neuroscience, vol. 29, no. 5, pages 1424–1433, 2009. (Cited on pages 13, 47, 62, 64 and 129.)
- [Lecoq *et al.* 2011] Jérôme Lecoq, Alex Parpaleix, re, Emmanuel Roussakis, Mathieu Ducros, Yannick Goulam Houssen, Sergei A Vinogradov and Serge Charpak. *Simultaneous two-photon imaging of oxygen and blood flow in deep cerebral vessels*. Nature Medicine, vol. 17, no. 7, pages 893–898, 2011. (Cited on pages 25 and 37.)
- [Lecrux & Hamel 2016] C. Lecrux and E. Hamel. *Neuronal networks and mediators of cortical neurovascular coupling responses in normal and altered brain states*. Philosophical Transactions of the Royal Society B: Biological Sciences, vol. 371, no. 1705, page 20150350, 2016. (Cited on page 22.)
- [Lin & Schnitzer 2016] Michael Z Lin and Mark J Schnitzer. *Genetically encoded indicators of neuronal activity*. Nature Neuroscience, vol. 19, no. 9, pages 1142–1153, 2016. (Cited on page 34.)
- [Lindauer *et al.* 2009] Ute Lindauer, Christoph Leithner, Heike Kaasch, Benjamin Rohrer, Marco Foddis, Martina Fächtemeier, Nikolas Offenhauser, Jens Steinbrink, Georg Roysl, Matthias Kohl-Bareis and Ulrich Dirnagl. *Neurovascular Coupling in Rat Brain Operates Independent of Hemoglobin Deoxygenation*. Journal of Cerebral Blood Flow & Metabolism, vol. 30, no. 4, pages 757–768, 2009. (Cited on page 137.)
- [Lindquist *et al.* 2009] Martin A. Lindquist, Ji Meng Loh, Lauren Y. Atlas and Tor D. Wager. *Modeling the hemodynamic response function in fMRI: Efficiency, bias and mis-modeling*. NeuroImage, vol. 45, no. 1, pages S187–S198, 2009. (Cited on page 46.)
- [Logothetis *et al.* 1999] Nikos K. Logothetis, Heinz Guggenberger, Sharon Peled and Jon Pauls. *Functional imaging of the monkey brain*. Nature Neuroscience, vol. 2, no. 6, pages 555–562, 1999. (Cited on page 49.)
- [Logothetis *et al.* 2001] Nikos K. Logothetis, Jon Pauls, Mark Augath, Torsten Trinath and Axel Oeltermann. *Neurophysiological investigation of the basis of the fMRI signal*. Nature, vol. 412, no. 6843, pages 150–157, 2001. (Cited on page 32.)
- [Logothetis 2008] Nikos K. Logothetis. *What we can do and what we cannot do with fMRI*. Nature, vol. 453, no. 7197, pages 869–878, 2008. (Cited on page 20.)

- [Lohr *et al.* 2014] Christian Lohr, Antje Grosche, Andreas Reichenbach and Daniela Hirnet. *Purinergic neuron-glia interactions in sensory systems*. Pflügers Archiv - European Journal of Physiology, vol. 466, no. 10, pages 1859–1872, 2014. (Cited on page 62.)
- [Longden *et al.* 2015] Thomas A Longden, David C Hill-Eubanks and Mark T Nelson. *Ion channel networks in the control of cerebral blood flow*. Journal of Cerebral Blood Flow & Metabolism, vol. 36, no. 3, pages 492–512, 2015. (Cited on page 14.)
- [Longden *et al.* 2017] Thomas A Longden, Dabertr, Fabrice, Masayo Koide, Albert L Gonzales, Nathan R Tykocki, Joseph E Brayden, David Hill-Eubanks and Mark T Nelson. *Capillary K⁺-sensing initiates retrograde hyperpolarization to increase local cerebral blood flow*. Nature Neuroscience, vol. 20, no. 5, pages 717–726, 2017. (Cited on page 23.)
- [Mace *et al.* 2013] Emilie Mace, Gabriel Montaldo, Bruno-Felix Osmanski, Ivan Cohen, Mathias Fink and Mickael Tanter. *Functional Ultrasound Imaging of the Brain : Theory and Basic Principles*. IEEE Transactions on Ultrasonics, Ferroelectrics and Frequency Control, vol. 60, no. 3, pages 492–506, 2013. (Cited on pages 53 and 54.)
- [Macé *et al.* 2011] Emilie Macé, Gabriel Montaldo, Ivan Cohen, Michel Baulac, Mathias Fink and Mickael Tanter. *Functional ultrasound imaging of the brain*. Nature Methods, vol. 8, no. 8, pages 662–664, 2011. (Cited on pages 20, 53, 55 and 58.)
- [Macé *et al.* 2018] Émilie Macé, Gabriel Montaldo, Stuart Trenholm, Cameron Cowan, Alexandra Brignall, Alan Urban and Botond Roska. *Whole-Brain Functional Ultrasound Imaging Reveals Brain Modules for Visuomotor Integration*. Neuron, vol. 100, no. 5, pages 1241–1251.e7, 2018. (Cited on page 58.)
- [Malonek & Grinvald 1996] Dov Malonek and Amiram Grinvald. *Interactions Between Electrical Activity and Cortical Microcirculation Revealed by Imaging Spectroscopy: Implications for Functional Brain Mapping*. Science, vol. 272, no. 5261, pages 551–554, 1996. (Cited on page 46.)
- [Mandeville *et al.* 1999] Joseph B. Mandeville, John J.A. Marota, C. Ayata, Michael A. Moskowitz, Robert M. Weisskoff and Bruce R. Rosen. *MRI measurement of the temporal evolution of relative CMRO₂ during rat forepaw stimulation*. Magnetic Resonance in Medicine, vol. 42, no. 5, pages 944–951, 1999. (Cited on page 49.)
- [Marota *et al.* 1999] John J.A. Marota, C. Ayata, Michael A. Moskowitz, Robert M. Weisskoff, Bruce R. Rosen and Joseph B. Mandeville. *Investigation of the early response to rat forepaw stimulation*. Magnetic Resonance in Medicine, vol. 41, no. 2, pages 247–252, 1999. (Cited on page 49.)
- [Maršál 2010] Karel Maršál. *Exposure to Ultrasound in Utero: Epidemiology and Relevance of Neuronal Migration Studies*. Ultrasound in Medicine & Biology, vol. 36, no. 8, pages 1221–1223, 2010. (Cited on page 57.)
- [Masatoshi 2020] Inoue Masatoshi. *Genetically Encoded Calcium Indicators to Probe Complex Brain Circuit Dynamics in vivo*. Neuroscience Research, 2020. (Cited on page 34.)
- [Mayhew *et al.* 2001] John Mayhew, David Johnston, John Martindale, Myles Jones, Jason Berwick and Ying Zheng. *Increased Oxygen Consumption Following Activation of Brain:*

- Theoretical Footnotes Using Spectroscopic Data from Barrel Cortex*. NeuroImage, vol. 13, no. 6, pages 975–987, 2001. (Cited on pages 49 and 135.)
- [Mehta *et al.* 2019] Arpan R Mehta, Puja R Mehta, Stephen P Anderson, Barbara L H MacKinnon and Alastair Compston. *Etymology and the neuron(e)*. Brain, vol. 143, no. 1, pages 374–379, 2019. Ref for Willis as the origin of the prefix neuro. (Cited on page 8.)
- [Menon *et al.* 1995] Ravi S. Menon, Seiji Ogawa, Xiaoping Hu, John P. Strupp, Peter Anderson and Kāmil Uğurbil. *BOLD Based Functional MRI at 4 Tesla Includes a Capillary Bed Contribution: Echo-Planar Imaging Correlates with Previous Optical Imaging Using Intrinsic Signals*. Magnetic Resonance in Medicine, vol. 33, no. 3, pages 453–459, 1995. (Cited on page 47.)
- [Michaloudi *et al.* 2005] Helen Michaloudi, Ioannis Grivas, Christos Batzios, Maria Chiotelli and Georgios C. Papadopoulos. *Areal and laminar variations in the vascularity of the visual, auditory, and entorhinal cortices of the developing rat brain*. Developmental Brain Research, vol. 155, no. 1, pages 60–70, 2005. (Cited on page 12.)
- [Mik *et al.* 2004] Egbert G. Mik, Ton G. van Leeuwen, Nicolaas J. Raat and Can Ince. *Quantitative determination of localized tissue oxygen concentration in vivo by two-photon excitation phosphorescence lifetime measurements*. Journal of Applied Physiology, vol. 97, no. 5, pages 1962–1969, 2004. (Cited on page 37.)
- [Mishra 2017] Anusha Mishra. *Binaural blood flow control by astrocytes: listening to synapses and the vasculature*. The Journal of Physiology, vol. 595, no. 6, pages 1885–1902, 2017. (Cited on page 23.)
- [Mombaerts 2006] Peter Mombaerts. *Axonal Wiring in the Mouse Olfactory System*. Annual Review of Cell and Developmental Biology, vol. 22, no. 1, pages 713–737, 2006. (Cited on page 64.)
- [Monti 2011] Martin M. Monti. *Statistical Analysis of fMRI Time-Series: A Critical Review of the GLM Approach*. Frontiers in Human Neuroscience, vol. 5, page 28, 2011. (Cited on pages 42, 44 and 46.)
- [Mosso 1880] Angelo Mosso. *Sulla circolazione del cervello dell'uomo*. Accademia dei Lincei, vol. 5, page 237–358, 1880. (Cited on page 18.)
- [Munafò *et al.* 2017] Marcus R. Munafò, Brian A. Nosek, Dorothy V. M. Bishop, Katherine S. Button, Christopher D. Chambers, Nathalie Percie du Sert, Uri Simonsohn, Eric-Jan Wagenmakers, Jennifer J. Ware and John P. A. Ioannidis. *A manifesto for reproducible science*. Nature Human Behaviour, vol. 1, no. 1, page 0021, 2017. (Cited on pages 132 and 133.)
- [Nagayama *et al.* 2014] Shin Nagayama, Ryota Homma and Fumiaki Imamura. *Neuronal organization of olfactory bulb circuits*. Frontiers in Neural Circuits, vol. 8, page 98, 2014. (Cited on pages 63 and 64.)
- [Nakai *et al.* 2001] Junichi Nakai, Masamichi Ohkura and Keiji Imoto. *A high signal-to-noise Ca²⁺ probe composed of a single green fluorescent protein*. Nature Biotechnology, vol. 19, no. 2, pages 137–141, 2001. (Cited on page 34.)

- [Nara *et al.* 2011] Kiyomitsu Nara, Luis R. Saraiva, Xiaolan Ye and Linda B. Buck. *A Large-Scale Analysis of Odor Coding in the Olfactory Epithelium*. The Journal of Neuroscience, vol. 31, no. 25, pages 9179–9191, 2011. (Cited on page 62.)
- [Netter 2019] Frank H. Netter. Atlas of Human Anatomy. 7th édition, 2019. (Cited on pages 9 and 10.)
- [Nishimura *et al.* 2007] Nozomi Nishimura, Chris B. Schaffer, Beth Friedman, Patrick D. Lyden and David Kleinfeld. *Penetrating arterioles are a bottleneck in the perfusion of neocortex*. Proceedings of the National Academy of Sciences, vol. 104, no. 1, pages 365–370, 2007. (Cited on pages 10 and 12.)
- [Norman *et al.* 2021] Sumner L. Norman, David Maresca, Vassilios N. Christopoulos, Whitney S. Griggs, Charlie Demene, Mickael Tanter, Mikhail G. Shapiro and Richard A. Andersen. *Single-trial decoding of movement intentions using functional ultrasound neuroimaging*. Neuron, vol. 109, no. 9, pages 1554–1566.e4, 2021. (Cited on page 58.)
- [Nunez-Elizalde *et al.* 2021] Anwar O. Nunez-Elizalde, Michael Krumin, Charu Bai Reddy, Gabriel Montaldo, Alan Urban, Kenneth D. Harris and Matteo Carandini. *Neural basis of functional ultrasound signals*. bioRxiv, page 2021.03.31.437915, 2021. (Cited on page 58.)
- [Oberheim *et al.* 2009] Nancy Ann Oberheim, Takahiro Takano, Xiaoning Han, Wei He, Jane H. C. Lin, Fushun Wang, Qiwu Xu, Jeffrey D. Wyatt, Webster Pilcher, Jeffrey G. Ojemann, Bruce R. Ransom, Steven A. Goldman and Maiken Nedergaard. *Uniquely Hominid Features of Adult Human Astrocytes*. The Journal of Neuroscience, vol. 29, no. 10, pages 3276–3287, 2009. (Cited on page 40.)
- [Ogawa & Lee 1990] Seiji Ogawa and Tso-Ming Lee. *Magnetic resonance imaging of blood vessels at high fields: In vivo and in vitro measurements and image simulation*. Magnetic Resonance in Medicine, vol. 16, no. 1, pages 9–18, 1990. (Cited on page 41.)
- [Ogawa *et al.* 1990a] S Ogawa, T M Lee, A R Kay and D W Tank. *Brain magnetic resonance imaging with contrast dependent on blood oxygenation*. Proceedings of the National Academy of Sciences, vol. 87, no. 24, pages 9868–9872, 1990. (Cited on pages 20 and 41.)
- [Ogawa *et al.* 1990b] Seiji Ogawa, Tso-Ming Lee, Asha S. Nayak and Paul Glynn. *Oxygenation-sensitive contrast in magnetic resonance image of rodent brain at high magnetic fields*. Magnetic Resonance in Medicine, vol. 14, no. 1, pages 68–78, 1990. (Cited on page 41.)
- [Osmanski *et al.* 2014] Bruno-F'elix Osmanski, Sophie Pezet, Ana Ricobaraza, Zsolt Lenkei and Mickael Tanter. *Functional ultrasound imaging of intrinsic connectivity in the living rat brain with high spatiotemporal resolution*. Nature communications, vol. 5, no. 1, page 5023, 2014. (Cited on page 58.)
- [Otsu *et al.* 2015] Yo Otsu, Kiri Couchman, Declan G Lyons, Mayeul Collot, Amit Agarwal, Jean-Maurice Mallet, Frank W Pfrieger, Dwight E Bergles and Serge Charpak. *Calcium dynamics in astrocyte processes during neurovascular coupling*. Nature neuroscience, vol. 18, no. 2, pages 210–8, 2015. (Cited on page 23.)
- [Parpaleix *et al.* 2013] Alex Parpaleix, re, Yannick Goulam Houssen and Serge Charpak. *Imaging local neuronal activity by monitoring PO transients in capillaries*. Nature medicine, vol. 19, no. 2, pages 241–6, 2013. (Cited on pages 22, 25, 38, 47 and 49.)

- [Peppiatt *et al.* 2006] Claire M Peppiatt, Clare Howarth, Peter Mobbs and David Attwell. *Bidirectional control of CNS capillary diameter by pericytes*. *Nature*, vol. 443, no. 7112, pages 700–704, 2006. (Cited on page 23.)
- [Phillips & Whisnant 1992] Stephen J. Phillips and Jack P. Whisnant. *Hypertension and the Brain*. *Archives of Internal Medicine*, vol. 152, no. 5, pages 938–945, 1992. (Cited on page 15.)
- [Pichardo *et al.* 2010] Samuel Pichardo, Vivian W Sin and Kullervo Hynynen. *Multi-frequency characterization of the speed of sound and attenuation coefficient for longitudinal transmission of freshly excised human skulls*. *Physics in Medicine and Biology*, vol. 56, no. 1, pages 219–250, 2010. (Cited on page 58.)
- [Poldrack *et al.* 2009] Russell A. Poldrack, Thomas Nichols and Jeanette Mumford. *Handbook of Functional MRI Data Analysis*. pages 53–69, 2009. (Cited on page 42.)
- [Pontika *et al.* 2015] Nancy Pontika, Petr Knoth, Matteo Cancellieri and Samuel Pearce. *Fostering open science to research using a taxonomy and an eLearning portal*. *Proceedings of the 15th International Conference on Knowledge Technologies and Data-driven Business*, pages 1–8, 2015. (Cited on page 132.)
- [Pries & Secomb 2005] A. R. Pries and T. W. Secomb. *Microvascular blood viscosity in vivo and the endothelial surface layer*. *American Journal of Physiology-Heart and Circulatory Physiology*, vol. 289, no. 6, pages H2657–H2664, 2005. (Cited on page 16.)
- [Purdon & Weisskoff 1998] Patrick L. Purdon and Robert M. Weisskoff. *Effect of temporal autocorrelation due to physiological noise and stimulus paradigm on voxel-level false-positive rates in fMRI*. *Human Brain Mapping*, vol. 6, no. 4, pages 239–249, 1998. (Cited on page 46.)
- [Rabut *et al.* 2020a] Claire Rabut, Jérémy Ferrier, Adrien Bertolo, Bruno Osmanski, Xavier Mousset, Sophie Pezet, Thomas Deffieux, Zsolt Lenkei and Mickaël Tanter. *PharmacofUS: Quantification of pharmacologically-induced dynamic changes in brain perfusion and connectivity by functional ultrasound imaging in awake mice*. *NeuroImage*, vol. 222, page 117231, 2020. (Cited on page 59.)
- [Rabut *et al.* 2020b] Claire Rabut, Sangjin Yoo, Robert C. Hurt, Zhiyang Jin, Hongyi Li, Hongsun Guo, Bill Ling and Mikhail G. Shapiro. *Ultrasound Technologies for Imaging and Modulating Neural Activity*. *Neuron*, vol. 108, no. 1, pages 93–110, 2020. (Cited on page 51.)
- [Raichle & Mintun 2006] Marcus E. Raichle and Mark A. Mintun. *BRAIN WORK AND BRAIN IMAGING*. *Annual Review of Neuroscience*, vol. 29, no. 1, pages 449–476, 2006. (Cited on pages 20 and 25.)
- [Raichle 2000] Marcus E. Raichle. *Brain Mapping: The Systems*. SECTION I: Types of Maps, no. J. *Nucl. Med.*321991, pages 33–75, 2000. (Cited on page 18.)
- [Richard *et al.* 2010] Marion B. Richard, Seth R. Taylor and Charles A. Greer. *Age-induced disruption of selective olfactory bulb synaptic circuits*. *Proceedings of the National Academy of Sciences*, vol. 107, no. 35, pages 15613–15618, 2010. (Cited on page 64.)
- [Robson *et al.* 1998] Matthew D. Robson, Jennifer L. Dorosz and John C. Gore. *Measurements of the Temporal fMRI Response of the Human Auditory Cortex to Trains of Tones*. *NeuroImage*, vol. 7, no. 3, pages 185–198, 1998. (Cited on page 46.)

- [Roche *et al.* 2019] Morgane Roche, Emmanuelle Chaigneau, Ravi L Rungta, Davide Boido, Bruno Weber and Serge Charpak. *In vivo imaging with a water immersion objective affects brain temperature, blood flow and oxygenation*. *eLife*, vol. 8, 2019. (Cited on pages 32, 37 and 57.)
- [Roggendorf & Cervós-Navarro 1977] W. Roggendorf and J. Cervós-Navarro. *Ultrastructure of arterioles in the cat brain*. *Cell and Tissue Research*, vol. 178, no. 4, pages 495–515, 1977. (Cited on pages 13 and 14.)
- [Rolfe & Brown 1997] D. F. Rolfe and G. C. Brown. *Cellular energy utilization and molecular origin of standard metabolic rate in mammals*. *Physiological Reviews*, vol. 77, no. 3, pages 731–758, 1997. Brain 20% of total oxygen consumption. (Cited on page 8.)
- [Ross *et al.* 2020] Jayden M. Ross, Chang Kim, Denise Allen, Elizabeth E. Crouch, Kazim Narsinh, Daniel L. Cooke, Adib A. Abla, Tomasz J. Nowakowski and Ethan A. Winkler. *The Expanding Cell Diversity of the Brain Vasculature*. *Frontiers in Physiology*, vol. 11, page 600767, 2020. (Cited on page 13.)
- [Roy & Sherrington 1890] C. S. Roy and C. S. Sherrington. *On the Regulation of the Blood-supply of the Brain*. *The Journal of Physiology*, vol. 11, no. 1-2, pages 85–158, 1890. (Cited on pages 18 and 19.)
- [Rungta *et al.* 2017] Ravi L Rungta, Bruno-F'elix Osmanski, Davide Boido, Mickael Tanter and Serge Charpak. *Light controls cerebral blood flow in naive animals*. *Nature communications*, vol. 8, page 14191, 2017. (Cited on pages 32 and 58.)
- [Rungta *et al.* 2018] Ravi L. Rungta, Emmanuelle Chaigneau, Bruno-Félix Osmanski and Serge Charpak. *Vascular Compartmentalization of Functional Hyperemia from the Synapse to the Pia*. *Neuron*, vol. 99, no. 2, pages 362–375.e4, 2018. (Cited on pages 23, 24, 27, 32, 65 and 136.)
- [Sakadžić *et al.* 2010] Sava Sakadžić, Emmanuel Roussakis, Mohammad A Yaseen, Emiri T Mandeville, Vivek J Srinivasan, Ken Arai, Svetlana Ruvinskaya, Anna Devor, Eng H Lo, Sergei A Vinogradov and David A Boas. *Two-photon high-resolution measurement of partial pressure of oxygen in cerebral vasculature and tissue*. *Nature Methods*, vol. 7, no. 9, pages 755–759, 2010. (Cited on page 37.)
- [Schaffer *et al.* 2006] Chris B Schaffer, Beth Friedman, Nozomi Nishimura, Lee F Schroeder, Philbert S Tsai, Ford F Ebner, Patrick D Lyden and David Kleinfeld. *Two-Photon Imaging of Cortical Surface Microvessels Reveals a Robust Redistribution in Blood Flow after Vascular Occlusion*. *PLoS Biology*, vol. 4, no. 2, page e22, 2006. (Cited on page 11.)
- [Schaller 2004] B. Schaller. *Physiology of cerebral venous blood flow: from experimental data in animals to normal function in humans*. *Brain Research Reviews*, vol. 46, no. 3, pages 243–260, 2004. (Cited on page 13.)
- [Schmid *et al.* 2015] Franca Schmid, Johannes Reichold, Bruno Weber and Patrick Jenny. *The impact of capillary dilation on the distribution of red blood cells in artificial networks*. *American Journal of Physiology-Heart and Circulatory Physiology*, vol. 308, no. 7, pages H733–H742, 2015. (Cited on pages 27 and 28.)

- [Schmid *et al.* 2019] Franca Schmid, Matthew J.P. Barrett, Patrick Jenny and Bruno Weber. *Vascular density and distribution in neocortex*. *NeuroImage*, vol. 197, pages 792–805, 2019. (Cited on page 12.)
- [Schmid 2017] Franca Schmid. *Cerebral Blood Flow Modeling with Discrete Red Blood Cell Tracking*. PhD thesis, 2017. (Cited on page 26.)
- [Schmidt & Hendrix 1938] Schmidt and J. P. Hendrix. *The action of chemical substances on cerebral blood vessels*. *Res Publ Assoc Res Nerv Ment Dis*, 1938. (Cited on page 18.)
- [Segal 2015] Steven S. Segal. *Integration and Modulation of Intercellular Signaling Underlying Blood Flow Control*. *Journal of Vascular Research*, vol. 52, no. 2, pages 136–157, 2015. (Cited on page 23.)
- [Sela & Sobel 2010] Lee Sela and Noam Sobel. *Human olfaction: a constant state of change-blindness*. *Experimental Brain Research*, vol. 205, no. 1, pages 13–29, 2010. (Cited on page 61.)
- [Shaw *et al.* 2021] K. Shaw, L. Bell, K. Boyd, D. M. Grijseels, D. Clarke, O. Bonnar, H. S. Crombag and C. N. Hall. *Neurovascular coupling and oxygenation are decreased in hippocampus compared to neocortex because of microvascular differences*. *Nature Communications*, vol. 12, no. 1, page 3190, 2021. (Cited on page 29.)
- [Shih *et al.* 2015] Andy Y. Shih, Charlotta Rühlmann, Pablo Blinder, Anna Devor, Patrick J. Drew, Beth Friedman, Per M. Knutsen, Patrick D. Lyden, Céline Matéo, Lisa Mellander, Nozomi Nishimura, Chris B. Schaffer, Philbert S. Tsai and David Kleinfeld. *Robust and Fragile Aspects of Cortical Blood Flow in Relation to the Underlying Angioarchitecture*. *Microcirculation*, vol. 22, no. 3, pages 204–218, 2015. (Cited on pages 10, 13, 27 and 46.)
- [Sieu *et al.* 2015] Lim-Anna Sieu, Antoine Bergel, Elodie Tiran, Thomas Deffieux, Mathieu Pernot, Jean-Luc Gennisson, Mickaël Tanter and Ivan Cohen. *EEG and functional ultrasound imaging in mobile rats*. *Nature Methods*, vol. 12, no. 9, pages 831–834, 2015. (Cited on page 58.)
- [Silva *et al.* 1999] Afonso C. Silva, Sang-Pil Lee, Costantino Iadecola and Seong-Gi Kim. *Early Temporal Characteristics of Cerebral Blood Flow and Deoxyhemoglobin Changes during Somatosensory Stimulation*. *Journal of Cerebral Blood Flow & Metabolism*, vol. 20, no. 1, pages 201–206, 1999. (Cited on page 49.)
- [Silva *et al.* 2007] Afonso C Silva, Alan P Koretsky and Jeff H Duyn. *Functional MRI impulse response for BOLD and CBV contrast in rat somatosensory cortex*. *Magnetic Resonance in Medicine*, vol. 57, no. 6, pages 1110–1118, 2007. (Cited on page 30.)
- [Sloun *et al.* 2021] Ruud J. G. van Sloun, Oren Solomon, Matthew Bruce, Zin Z. Khaing, Hessel Wijkstra, Yonina C. Eldar and Massimo Mischi. *Super-Resolution Ultrasound Localization Microscopy Through Deep Learning*. *IEEE Transactions on Medical Imaging*, vol. 40, no. 3, pages 829–839, 2021. (Cited on page 57.)
- [Soares *et al.* 2016] José M. Soares, Ricardo Magalhães, Pedro S. Moreira, Alexandre Sousa, Edward Ganz, Adriana Sampaio, Victor Alves, Paulo Marques and Nuno Sousa. *A Hitchhiker’s Guide to Functional Magnetic Resonance Imaging*. *Frontiers in Neuroscience*, vol. 10, page 515, 2016. (Cited on page 42.)

- [Souza *et al.* 2019] Annie C. Souza, Bruna D.V. Koike, Rafael Pedrosa, Adriano B.L. Tort, Claudio M. Queiroz and Sidarta Ribeiro. *Chapter 2 Recording Day and Night: Advice for New Investigators in the Sleep and Memory Field*. Handbook of Behavioral Neuroscience, vol. 28, pages 43–62, 2019. (Cited on page 33.)
- [Stefanovic *et al.* 2006] Bojana Stefanovic, Wolfram Schwindt, Mathias Hoehn and Afonso C Silva. *Functional Uncoupling of Hemodynamic from Neuronal Response by Inhibition of Neuronal Nitric Oxide Synthase*. Journal of Cerebral Blood Flow & Metabolism, vol. 27, no. 4, pages 741–754, 2006. (Cited on page 29.)
- [Stefanovic *et al.* 2007] Bojana Stefanovic, Elizabeth Hutchinson, Victoria Yakovleva, Vincent Schram, James T Russell, Leonardo Belluscio, Alan P Koretsky and Afonso C Silva. *Functional Reactivity of Cerebral Capillaries*. Journal of Cerebral Blood Flow & Metabolism, vol. 28, no. 5, pages 961–972, 2007. (Cited on page 12.)
- [Steinmetz *et al.* 2017] Nicholas A. Steinmetz, Christina Buetfering, Jerome Lecoq, Christian R. Lee, Andrew J. Peters, Elina A. K. Jacobs, Philip Coen, Douglas R. Ollerenshaw, Matthew T. Valley, Saskia E. J. de Vries, Marina Garrett, Jun Zhuang, Peter A. Groblewski, Sahar Manavi, Jesse Miles, Casey White, Eric Lee, Fiona Griffin, Joshua D. Larkin, Kate Roll, Sissy Cross, Thuyanh V. Nguyen, Rachael Larsen, Julie Pendergraft, Tanya Daigle, Bosiljka Tasic, Carol L. Thompson, Jack Waters, Shawn Olsen, David J. Margolis, Hongkui Zeng, Michael Hausser, Matteo Carandini and Kenneth D. Harris. *Aberrant Cortical Activity in Multiple GCaMP6-Expressing Transgenic Mouse Lines*. eNeuro, vol. 4, no. 5, pages ENEURO.0207–17.2017, 2017. (Cited on page 34.)
- [Stephan *et al.* 1981] Heinz Stephan, Heiko Frahm and Georg Baron. *New and Revised Data on Volumes of Brain Structures in Insectivores and Primates*. Folia Primatologica, vol. 35, no. 1, pages 1–29, 1981. Average brain weight: 1.3kg. (Cited on page 8.)
- [Stettler & Axel 2009] Dan D. Stettler and Richard Axel. *Representations of Odor in the Piriform Cortex*. Neuron, vol. 63, no. 6, pages 854–864, 2009. (Cited on page 58.)
- [Stodden *et al.* 2018] Victoria Stodden, Jennifer Seiler and Zhaokun Ma. *An empirical analysis of journal policy effectiveness for computational reproducibility*. Proceedings of the National Academy of Sciences, vol. 115, no. 11, page 201708290, 2018. (Cited on page 133.)
- [Strevens 2020] Michael S. Strevens. *The Knowledge Machine: How an Unreasonable Idea Created Modern Science*. 1st édition, 10 2020. (Cited on page 4.)
- [Stromberg & Fox 1972] Don D. Stromberg and James R. Fox. *Pressures in the Pial Arterial Microcirculation of the Cat during Changes in Systemic Arterial Blood Pressure*. Circulation Research, vol. 31, no. 2, pages 229–239, 1972. (Cited on page 15.)
- [Tang *et al.* 2020] Jianbo Tang, Dmitry D. Postnov, Kivilcim Kilic, Sefik Evren Erdener, Blaire Lee, John T. Giblin, Thomas L. Szabo and David A. Boas. *Functional Ultrasound Speckle Decorrelation-Based Velocimetry of the Brain*. Advanced Science, vol. 7, no. 18, page 2001044, 2020. (Cited on page 59.)
- [Tasic *et al.* 2018] Bosiljka Tasic, Zizhen Yao, Lucas T. Graybiuck, Kimberly A. Smith, Thuc Nghi Nguyen, Darren Bertagnolli, Jeff Goldy, Emma Garren, Michael N. Economo, Sarada Viswanathan, Osnat Penn, Trygve Bakken, Vilas Menon, Jeremy Miller, Olivia Fong,

- Karla E. Hirokawa, Kanan Lathia, Christine Rimorin, Michael Tieu, Rachael Larsen, Tamara Casper, Eliza Barkan, Matthew Kroll, Sheana Parry, Nadiya V. Shapovalova, Daniel Hirschstein, Julie Pendergraft, Heather A. Sullivan, Tae Kyung Kim, Aaron Szafer, Nick Dee, Peter Groblewski, Ian Wickersham, Ali Cetin, Julie A. Harris, Boaz P. Levi, Susan M. Sunkin, Linda Madisen, Tanya L. Daigle, Loren Looger, Amy Bernard, John Phillips, Ed Lein, Michael Hawrylycz, Karel Svoboda, Allan R. Jones, Christof Koch and Hongkui Zeng. *Shared and distinct transcriptomic cell types across neocortical areas*. *Nature*, vol. 563, no. 7729, pages 72–78, 2018. (Cited on page 22.)
- [Thakore *et al.* 2021] Pratish Thakore, Michael G Alvarado, Sher Ali, Amreen Mughal, Paulo W Pires, Evan Yamasaki, Harry A T Pritchard, Brant E Isakson, Cam Ha T Tran and Scott Earley. *Brain endothelial cell TRPA1 channels initiate neurovascular coupling*. *eLife*, vol. 10, page e63040, 2021. (Cited on pages 23 and 32.)
- [Thompson *et al.* 2003] Jeffrey K. Thompson, Matthew R. Peterson and Ralph D. Freeman. *Single-Neuron Activity and Tissue Oxygenation in the Cerebral Cortex*. *Science*, vol. 299, no. 5609, pages 1070–1072, 2003. (Cited on pages 47 and 48.)
- [Thompson *et al.* 2004] Jeffrey K Thompson, Matthew R Peterson and Ralph D Freeman. *High-resolution neurometabolic coupling revealed by focal activation of visual neurons*. *Nature Neuroscience*, vol. 7, no. 9, pages 919–920, 2004. (Cited on page 47.)
- [Thompson *et al.* 2005] Jeffrey K. Thompson, Matthew R. Peterson and Ralph D. Freeman. *Separate Spatial Scales Determine Neural Activity-Dependent Changes in Tissue Oxygen within Central Visual Pathways*. *The Journal of Neuroscience*, vol. 25, no. 39, pages 9046–9058, 2005. (Cited on page 47.)
- [Tian *et al.* 2010] Peifang Tian, Ivan C Teng, Larry D May, Ronald Kurz, Kun Lu, Miriam Scadeng, Elizabeth M C Hillman, Alex J De Crespigny, H. E. D’Arceuil, M, Joseph B eville, John J A Marota, Bruce R Rosen, Thomas T Liu, David A Boas, Richard B Buxton, Anders M Dale and Anna Devor. *Cortical depth-specific microvascular dilation underlies laminar differences in blood oxygenation level-dependent functional MRI signal*. *Proceedings of the National Academy of Sciences*, vol. 107, no. 34, pages 15246–15251, 2010. (Cited on page 49.)
- [Tiran *et al.* 2017] Elodie Tiran, Jérémy Ferrier, Thomas Deffieux, Jean-Luc Gennisson, Sophie Pezet, Zsolt Lenkei and Mickaël Tanter. *Transcranial Functional Ultrasound Imaging in Freely Moving Awake Mice and Anesthetized Young Rats without Contrast Agent*. *Ultrasound in Medicine & Biology*, vol. 43, no. 8, pages 1679–1689, 2017. (Cited on page 59.)
- [Todorov *et al.* 2020] Mihail Ivilinov Todorov, Johannes Christian Paetzold, Oliver Schoppe, Giles Tetteh, Suprosanna Shit, Velizar Efremov, Katalin Todorov-Völgyi, Marco Düring, Martin Dichgans, Marie Piraud, Bjoern Menze and Ali Ertürk. *Machine learning analysis of whole mouse brain vasculature*. *Nature Methods*, vol. 17, no. 4, pages 442–449, 2020. (Cited on page 12.)
- [Tran *et al.* 2018] Cam Ha T. Tran, Govind Peringod and Grant R. Gordon. *Astrocytes Integrate Behavioral State and Vascular Signals during Functional Hyperemia*. *Neuron*, vol. 100, no. 5, pages 1133–1148.e3, 2018. (Cited on page 23.)
- [Tsai *et al.* 2005] Amy G Tsai, Pedro Cabrales, Paul C Johnson and Marcos Intaglietta. *Effect of oxygen consumption by measuring method on Po₂ transients associated with the passage*

- of erythrocytes in capillaries of rat mesentery*. American Journal of Physiology-Heart and Circulatory Physiology, vol. 289, no. 4, pages H1777–H1779, 2005. (Cited on page 38.)
- [Tsai *et al.* 2009] Philbert S. Tsai, John P. Kaufhold, Pablo Blinder, Beth Friedman, Patrick J. Drew, Harvey J. Karten, Patrick D. Lyden and David Kleinfeld. *Correlations of Neuronal and Microvascular Densities in Murine Cortex Revealed by Direct Counting and Colocalization of Nuclei and Vessels*. The Journal of Neuroscience, vol. 29, no. 46, pages 14553–14570, 2009. (Cited on pages 12 and 13.)
- [Urban *et al.* 2015] Alan Urban, Clara Dussaux, Guillaume Martel, Clément Brunner, Emilie Mace and Gabriel Montaldo. *Real-time imaging of brain activity in freely moving rats using functional ultrasound*. Nature Methods, vol. 12, no. 9, pages 873–878, 2015. (Cited on page 58.)
- [Vazquez & Noll 1998] Alberto L. Vazquez and Douglas C. Noll. *Nonlinear Aspects of the BOLD Response in Functional MRI*. NeuroImage, vol. 7, no. 2, pages 108–118, 1998. (Cited on page 46.)
- [Wachowiak & Shipley 2006] Matt Wachowiak and Michael T. Shipley. *Coding and synaptic processing of sensory information in the glomerular layer of the olfactory bulb*. Seminars in Cell & Developmental Biology, vol. 17, no. 4, pages 411–423, 2006. (Cited on page 64.)
- [Wager *et al.* 2005] Tor D. Wager, Alberto Vazquez, Luis Hernandez and Douglas C. Noll. *Accounting for nonlinear BOLD effects in fMRI: parameter estimates and a model for prediction in rapid event-related studies*. NeuroImage, vol. 25, no. 1, pages 206–218, 2005. (Cited on page 46.)
- [Waldorp 2009] Lourens Waldorp. *Robust and Unbiased Variance of GLM Coefficients for Misspecified Autocorrelation and Hemodynamic Response Models in fMRI*. International Journal of Biomedical Imaging, vol. 2009, page 723912, 2009. (Cited on page 44.)
- [Walpole *et al.* 2012] Sarah Catherine Walpole, David Prieto-Merino, Phil Edwards, John Cleland, Gretchen Stevens and Ian Roberts. *The weight of nations: an estimation of adult human biomass*. BMC Public Health, vol. 12, no. 1, page 439, 2012. Average Body Weight over the world: 62kg. (Cited on page 8.)
- [Watanabe *et al.* 2013] Masataka Watanabe, Andreas Bartels, Jakob H. Macke, Yusuke Murayama and Nikos K. Logothetis. *Temporal Jitter of the BOLD Signal Reveals a Reliable Initial Dip and Improved Spatial Resolution*. Current Biology, vol. 23, no. 21, pages 2146–2150, 2013. (Cited on pages 49 and 50.)
- [Weber *et al.* 2008] Bruno Weber, Anna Lena Keller, Johannes Reichold and Nikos K. Logothetis. *The Microvascular System of the Striate and Extrastriate Visual Cortex of the Macaque*. Cerebral Cortex, vol. 18, no. 10, pages 2318–2330, 2008. (Cited on page 13.)
- [Wellerstein 2018] Alex Wellerstein. *The myth of apolitical science*. Science, vol. 362, no. 6418, pages 1006–1006, 2018. (Cited on page 51.)
- [Willis 1664] Thomas Willis. *Cerebri Anatome: Cui Accessit Nervorum Descriptio Et Usus*. London, 1664. (Cited on page 8.)

- [Winder *et al.* 2017] Aaron T Winder, Christina Echagarruga, Qingguang Zhang and Patrick J Drew. *Weak correlations between hemodynamic signals and ongoing neural activity during the resting state*. *Nature Neuroscience*, vol. 20, no. 12, pages 1761–1769, 2017. (Cited on pages 30 and 31.)
- [Winkler *et al.* 2013] Ethan A. Winkler, Jesse D. Sengillo, John S. Sullivan, Jenny S. Henkel, Stanley H. Appel and Berislav V. Zlokovic. *Blood–spinal cord barrier breakdown and pericyte reductions in amyotrophic lateral sclerosis*. *Acta Neuropathologica*, vol. 125, no. 1, pages 111–120, 2013. (Cited on page 25.)
- [Xiong *et al.* 2017] Benyi Xiong, Anan Li, Yang Lou, Shangbin Chen, Ben Long, Jie Peng, Zhongqin Yang, Tonghui Xu, Xiaquan Yang, Xiangning Li, Tao Jiang, Qingming Luo and Hui Gong. *Precise Cerebral Vascular Atlas in Stereotaxic Coordinates of Whole Mouse Brain*. *Frontiers in neuroanatomy*, 12 2017. (Cited on pages 11, 12 and 13.)
- [Yu *et al.* 2014] Xin Yu, Chunqi Qian, Der-yow Chen, Stephen J Dodd and Alan P Koretsky. *Deciphering laminar-specific neural inputs with line-scanning fMRI*. *Nature Methods*, vol. 11, no. 1, pages 55–58, 2014. (Cited on page 49.)
- [Zhang *et al.* 1997] Fangyi Zhang, Chris Eckman, Steven Younkin, Karen K. Hsiao and Costantino Iadecola. *Increased Susceptibility to Ischemic Brain Damage in Transgenic Mice Overexpressing the Amyloid Precursor Protein*. *Journal of Neuroscience*, vol. 17, no. 20, pages 7655–7661, 1997. (Cited on pages 13 and 14.)
- [Zhang *et al.* 2020] Y. Zhang, M. Rózsa, D. Bushey, J. Zheng, D. Reep, G. J. Broussard, A. Tsang, G. Tsegaye, R. Patel, S. Narayan, J. X. Lim, R. Zhang, M. B. Ahrens, G. C. Turner, S. S.-H. Wang, K. Svoboda, W. Korff, E. R. Schreiter, J. P. Hasseman, I. Kolb and L. L. Looger. *jRCaMP8 Fast Genetically Encoded Calcium Indicators*. 2020. (Cited on page 34.)
- [Zhu *et al.* 2006] Mingming Zhu, Joseph J. H. Ackerman, Alexander L. Sukstanskii and Dmitriy A. Yablonskiy. *How the body controls brain temperature: the temperature shielding effect of cerebral blood flow*. *Journal of Applied Physiology*, vol. 101, no. 5, pages 1481–1488, 2006. (Cited on page 25.)
- [Şencan *et al.* 2020] İkbâl Şencan, Tatiana Esipova, Kivılcım Kılıç, Baoqiang Li, Michèle Desjardins, Mohammad A Yaseen, Hui Wang, Jason E Porter, Sreekanth Kura, Buyin Fu, Timothy W Secomb, David A Boas, Sergei A Vinogradov, Anna Devor and Sava Sakadžić. *Optical measurement of microvascular oxygenation and blood flow responses in awake mouse cortex during functional activation*. *Journal of Cerebral Blood Flow & Metabolism*, page 0271678X2092801, 2020. (Cited on page 50.)